3D GEOPHYSICAL ELECTROMAGNETIC FORWARD MODELING OF COMPLEX GRAPHITIC FAULT ZONES.

By

©Drew J. Jones

Supervisor: Colin G. Farquharson

A thesis submitted to the School of Graduate Studies in partial fulfillment of the requirements for the degree of

Master of Science

Department of Earth Sciences
Memorial University of Newfoundland
St. John`s Newfoundland Canada A1B 3X5
May, 2017

Abstract

Uranium exploration in the Athabasca Basin, Canada, has been compared to finding a needle in a haystack as the typical targets are thin, near-vertical graphitic faults buried under thick sedimentary cover. Time domain electromagnetic (EM) exploration methods are commonly used in the detection of these conductive graphitic fault zones. A method of using many three-dimensional (3D) frequency-domain EM forward responses, computed over a wide range of frequencies, to construct an accurate 3D time-domain forward response is presented. The application of 3D forward modeling using unstructured tetrahedral meshes provides a more precise means of replicating EM responses of targets like those in the Athabasca Basin with complicated, challenging geometries. Results for synthetic and real-world scenarios demonstrate the ability of the approach in accurately modeling simple or complex conductors and sets of conductors in 3D. Results also demonstrate the application of the method to model realistic geologic situations with many individual model regions based on actual geologic data.

Acknowledgements

Funding for this project was provided by ARC Resources Canada Inc. (ARC) and I would very much like to thank Patrick Ledru for his support of this project, and Robert Hearst for his support and regular helpful advice on many topics regarding EM exploration and my thesis research. I'd like to thank Dr. Colin Farquharson, my advisor on this project. He took a chance inviting a crazy American out to Newfoundland to study EM with him, and his constant happy nature, willingness to help, and intelligence on the subject have been invaluable to me throughout my master's work. I simply can't thank him enough for everything he has done, and all I've learned in these two years. I'd like to thank Dr. Alison Leitch, my co-advisor for her help and support with this project. Dr. Chuck Hurich, for his help and advice on a variety of topics. I'd like to thank Peter Lelièvre for providing access to his FacetModeller program as well as a variety of support codes, and for his help in their use and willingness to quickly modify his program to better suit my needs. Paul Sherren, for his aid in creating a reliable method for running multiple models on a remote server. Pierre Martz for providing geochemical information and some ideas for interesting models. I'd like to thank each and every member of Colin's research group at MUN, particularly Seyedmasoud Ansari for his help and advice in the use of his CSEM3DFWD code. I'd like to thank all of the other geophysics grad students, there's a lot of you, but each of you has inspired me in some way. You guys were my co-advisors, friends, fishing buddies, and more and I appreciate it. I'd like to thank all the great people I met in Newfoundland who became like a second family

to me here, your support and friendship made it all possible for me. Finally, I'd like to thank my family, who thoroughly supported me when I wanted to travel far from home to pursue my dream, I did it with you all in mind!

To all of you, I will always be grateful.

Table of Contents

5. Simple Conductor Models 95

6. Geologically Realistic Models 132

List of Figures

Chapter 1

Introduction

The Athabasca Basin is a vast sedimentary basin located in northern Saskatchewan, and partially in Alberta, Canada. The Basin is host to the highest-grade uranium deposits in the world, showing grades up to 18% U_3O_8 (World Nuclear Assn. 2015). Monometallic uranium deposits are generally basement-hosted ore pods, veins, and breccia occurring mainly in reactivated fault zones located close to basal unconformities between basin sediments and metamorphic basement rocks (Jefferson et al. 2007). Particularly important are units of gneiss with graphitic metapelite. These constitute weak areas between competent units and were the focus of local deformation during regional tectonics and also perhaps conduits for ore-forming hydrothermal fluids (Jefferson et al. 2007). While typically of high-grade, the deposits are often of small scale, and the thin graphitic faults with which they are associated can have steep near-vertical dips making them challenging targets for drilling (Figure 1.1). Additionally, deposits may lie under thick sedimentary sequences up to 1000 m below the surface. Typical strike lengths for graphitic fault zones are on the order of hundreds of metres to kilometres with similar depth extent while the thickness of individual faults may be only a few metres to 10’s of metres. Graphitic fault zones often show a marked contrast in resistivity with their host rocks. The fault zones range between 30 Ohm-m and 300 Ohm-m but can be higher or lower, generally with resistivity decreasing as graphite content increases.

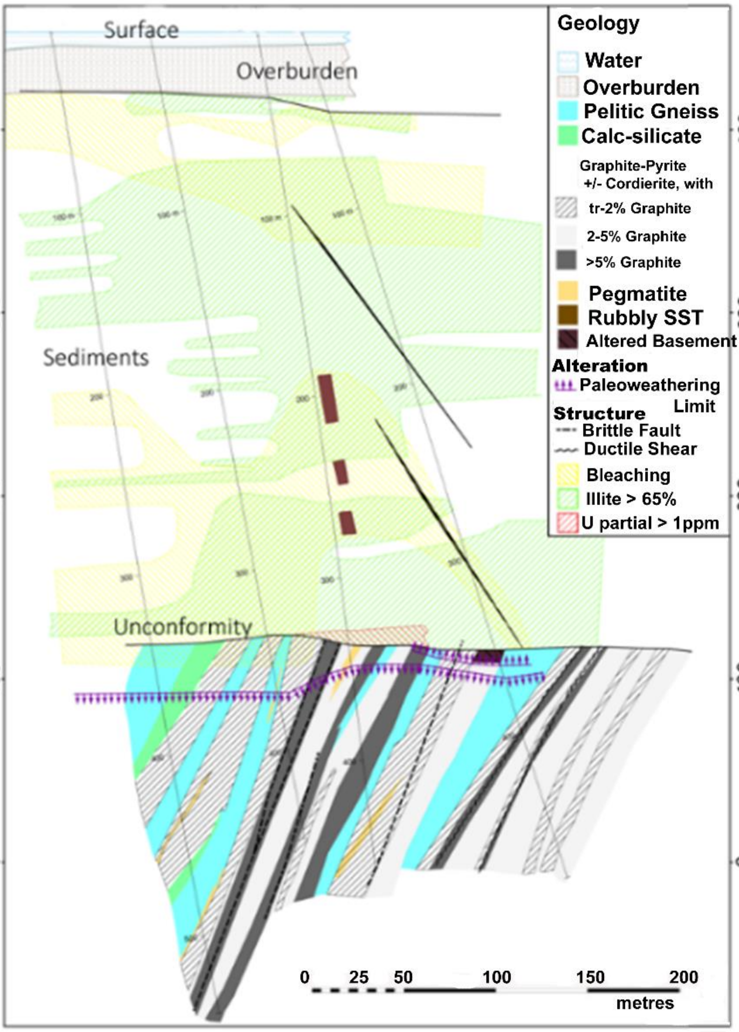

Figure 1.1: Cross-section of graphitic fault zone showing multiple, closely related graphitic zones, those in dark gray contain greater than 5% graphite (provided by ARC Resources Canada Inc.).

Basin sediments and basement rocks have highly varied resistivity values depending on the rock type and geologic setting but are most often much more resistive than the graphitic zones.

Time-domain electromagnetic (TDEM) surveys, both airborne and ground-based, have played a significant role in the discovery of many known deposits in the Athabasca Basin (Powell & Wood 2007). Large loop ground TDEM surveys, in particular, can image deep into the subsurface and are currently one of the most common means of detecting graphitic conductors in the Basin. Typically, a large loop with a diameter on the order of the expected target depth is used, in either a fixed or moving loop configuration at various offsets from the receiver. Measurements are collected in a grid or series of lines over the area of interest.

Recent advances in the 3D finite element forward modeling of EM data on unstructured meshes (e.g. Ansari and Farquharson 2014; Jahandari and Farquharson 2014; Puzyrev et al. 2013; Ren et al. 2014; Schwarzbach et al. 2011), have shown the ability to model the frequency-domain EM response due to bodies of complex shape, without the pixelation effect or blockiness commonly seen in a rectilinear mesh. Methods also exist for incorporating real structural geologic data, in a variety of forms, into these 3D meshes (e.g. Lelièvre et al., 2012). At least one method of forward modeling time-domain EM data on unstructured meshes has been developed by Um et al. (2010) and has been successfully applied to petroleum exploration. Still lacking is an application with specific attention to mining exploration scenarios.

It is possible by use of a Fourier transform to take many individual frequency-domain responses computed for a single 3D model and from them obtain a time-domain response (e.g. Newman et al. 1986). The method presented here has made use of this approach as well as the 3D finite-element code of Ansari and Farquharson (2014), and successfully reproduced known time-domain results for 1D half-spaces and a 3D conductor in a half-space. Simple conductor models were created to demonstrate the response curves for a variety of conductor geometries and conductivities. Realistic models that incorporate actual drill log data were created and demonstrate the full advantage of the capabilities of unstructured tetrahedral meshes in replicating real exploration targets in the Athabasca Basin.

1.1 Motivation

Uranium exploration began in the Athabasca Basin (Figure 1.2) in only the mid-1960's, but currently between 15-20% of the world's uranium supply comes from the Basin (Witherly & Kosteniuk 2010), making it a valuable resource not only in Canada but worldwide. The McArthur River mine, which became operational in the year 2000, currently produces nearly 20 million pounds of uranium per year (13% of world supply) making it the largest high-grade uranium mine in the world. Probable reserves for the mine are over 360 million pounds at grades averaging 15% U_3O_8 (World Nuclear Assn. 2015). Cigar Lake, considered the world's largest undeveloped high-grade uranium deposit, became operational in mid-2014 with probable reserves of nearly 220 million pounds averaging 18% U_3O_8 (World Nuclear Assn. 2015).

ARC Resources Canada Inc. (ARC) is one of Canada`s leading uranium producers, responsible for uranium exploration, development, mining and milling operations in Saskatchewan and Nunavut. With a long history of uranium exploration in the Athabasca Basin dating back to 1964, ARC has a significant presence in the Basin with ongoing joint operations at the McArthur River, Cigar Lake, McClean Lake, and Key Lake mines (Figure 1.3). ARC is also currently

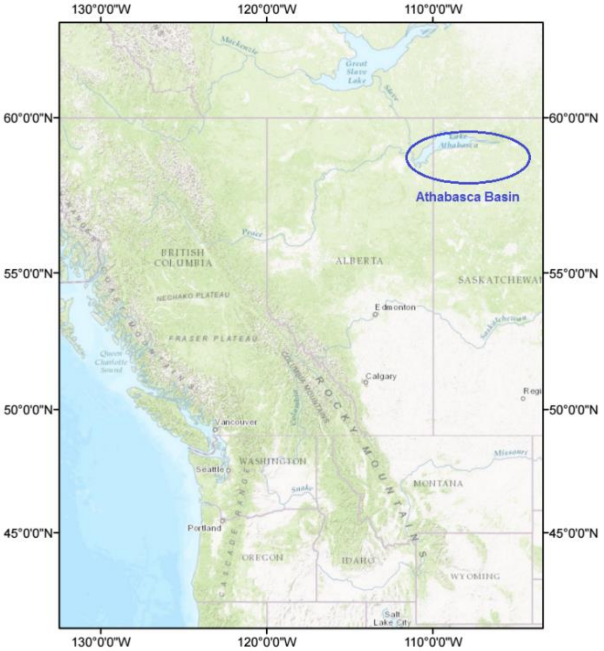

Figure 1.2: Location of the Athabasca Basin within north-western North America, the Basin is in northern Saskatchewan and partially in Alberta, Canada.

invested in the exploration of other potential properties in the Basin and has a continued interest in the development of improved methods for detecting and differentiating these complex and lucrative deposits. ARC`s geophysical exploration team has shown a continued interest in improving results from forward and inverse modeling of time-domain EM data collected over its prospects in the Basin. The company approached Memorial University to determine if current research in the modeling of 3D frequency-domain EM data (e.g. Ansari & Farquharson 2014; Jahandari & Farquharson 2014) might be applied to the time domain. This project was sponsored by ARC with the goal of investigating a method of forward modeling time-domain data in 3D on unstructured model meshes that realistically replicate the challenging exploration scenarios ARC is currently facing in the Athabasca Basin.

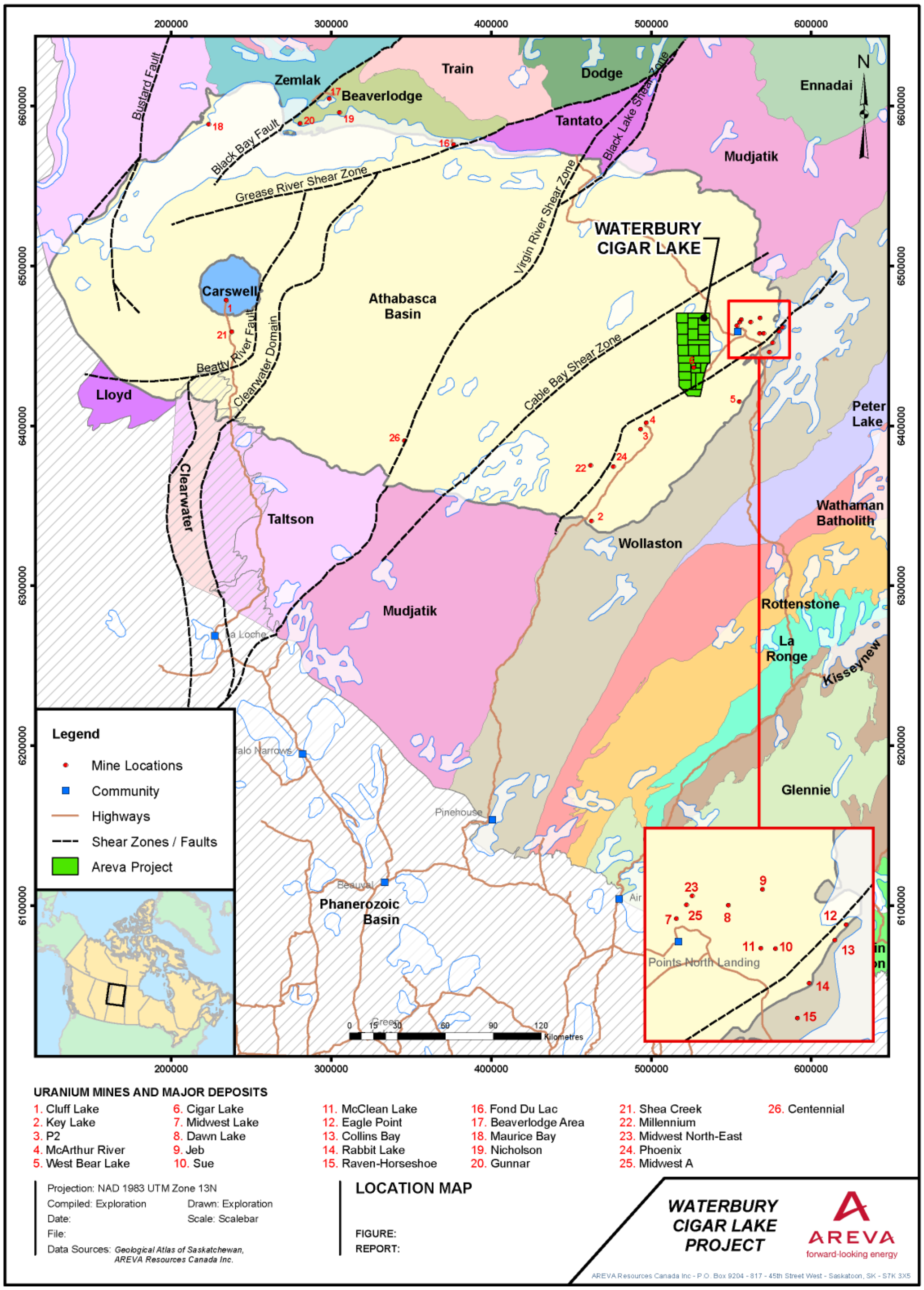

Figure 1.3: Location of important uranium mines in the Athabasca Basin in which ARC has joint ownership.

1.2 Project Goals

Broadly, the goal of this project is to create realistic forward models that can determine the limits of time-domain EM data in differentiating distinct targets with a potential for uranium deposition. In the Athabasca Basin, conductive graphitic units associated with uranium deposition can exist in closely related sets of faults, 10`s of metres apart, and each with varied graphite content, and not all hosting uranium (Figure 1.1). Differentiating single units in a broad conductive package can be incredibly difficult using current methods of TDEM data collection and interpretation. Often simplified interpretations must be made that can overlook important targets, especially when information from drilling does not exist. Also, complex conductor geometries and the presence of moderately conductive metasediment units adjacent to graphitic units can complicate interpretation of TDEM data. Successful completion of this project will result in a method of forward modeling time-domain EM data that can aid in a more accurate and complete interpretation of complicated deposits. This work will also attempt to answer a major question regarding the current means for ground TDEM data collection: is it even possible to obtain the resolution necessary to distinguish individual targets and determine their complex geometries under increasing depths of overburden.

1.3 Project Overview

The project began in May of 2015 with initial work focused on understanding the 3D finite element frequency-domain forward modeling code of Ansari & Farquharson (2014). The code was run for a range of individual frequencies and with varied parameters and input models, to determine its characteristics and best use practices. Next, a method was developed to parallelize the running of code allowing for the computation of the multiple frequency-domain models necessary to form a complete time-domain response in a simple manner. Running models in this way required the use of a remote computing cluster and much work was done to understand cluster computing and develop a system to efficiently move large amounts of data to and from the cluster and synchronize the computation of multiple models simultaneously. Cluster computing was a constant aspect of the project and effort was continuously given to the better management of data on and off the cluster. After a system was in place to produce a range of frequency-domain results for a model, a similar system was developed to transform the frequency data into the time domain.

A series of investigations were then conducted to determine the number of frequency-domain models and the range of frequencies covered necessary to produce an accurate time-domain response for a half-space. Preliminary investigations into mesh refinement methods and other model characteristics were also conducted to examine their effects on the time-domain response. After an accurate half-space response could be reliably produced in the time-domain, the method was tested on models containing a simple rectilinear conductor in a half-space. The process was again verified for accuracy through comparison to published results, and further investigations into the effects of model and computation parameters were performed to refine results and improve computation time. A set of different conductor-in-half-space models were then generated to determine the effects of conductor geometry and conductivity. Altering parameters such as the dip, thickness, and the separation of two conductors allows for determining the ability of the process to resolve such differences while at the same time creating a reference for use in future interpretation. With successful results for a variety of simple conductors, effort was turned to the creation of more complex and geologically accurate models that demonstrate the advantage of using unstructured 3D meshes in accurately modeling the uranium mining scenarios important to ARC.

1.4 Thesis Organization

In the following chapter a variety of background information concerning the geology of unconformity-type uranium deposits in the Athabasca Basin, the theory and methods behind time-domain electromagnetic exploration for mineral deposits, as well as the concepts of geophysical forward modeling and the methods used in this project are presented. Chapter Three will cover in detail the methodologies applied in this project including topics such as model construction and mesh refinement, as well as the procedures for forward modeling the frequency-domain data and subsequent transform into the time-domain. Chapter Four will discuss results from modeling of simple resistive half-spaces, and investigations into important model properties like the total volume and mesh refinement, and most importantly the number and range of frequencies used in the time-domain transform. Chapter Five will cover the results of conductor in half-space models, including investigations into the dip, depth, thickness, and conductivity of a single or pair of conductors. Chapter Six will discuss the results of realistic models, some based on drill-core information provided by ARC, and will demonstrate the ability of this method to model complicated geologic features with realistic geophysical properties. Finally, Chapter Seven will conclude and summarize the project as well as the insights gained from the research and some thoughts on what may still be done to progress this research further in the future.

Chapter 2

Background

2.1 Geology

Uranium mineralization in the Athabasca Basin occurs as unconformity-associated deposits consisting of pods, veins, and semimassive replacements of mainly uraninite, located close to basal unconformities between Proterozoic redbed basins and metamorphosed basement rocks, especially supracrustal gneiss with graphitic metapelite (Jefferson et al. 2007). Monometallic deposits are generally basement-hosted ore pods, veins, and breccia occurring mainly in reactivated fault zones. Polymetallic deposits are commonly subhorizontal ore lenses that straddle the unconformity, replacing sandstone and altered basement rock with variable amounts of U, Ni, Co, and As, and traces of Au, PGE's, Cu, REE's, and Fe.

Sedimentary basins hosting unconformity-associated uranium such as the Athabasca, as well as other analogous basins in northern Canada and Australia, all meet a similar geologic criteria consisting of a few key features: Proterozoic unmetamorphosed sedimentary rocks unconformably overlying deformed and metamorphosed Paleoproterozoic and Archean basement, reactivated basement faulting, and an elevated concentration of uranium in basement rocks (Crowe et al. 2013). In Athabasca, many of the most significant deposits occur in the eastern portion of the basin near the unconformity between the unmetamorphosed detrital units of the Athabasca group where they overlie the transition between the Mudjatik

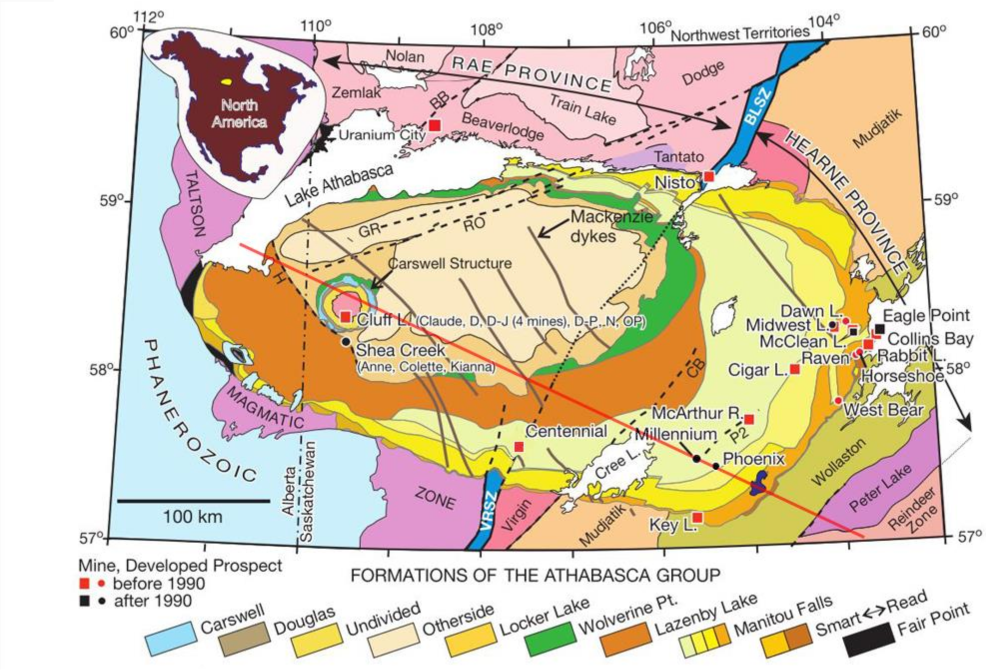

Figure 2.1: Stratigraphic map of the Athabasca Group in Athabasca Basin, underlying domains, and major unconformity uranium deposits. Major brittle reactivated shear zones: BB = Black Bay, BLSZ = Black Lake Shear Zone, CB = Cable Bay, GR = Grease River, H = Harrison, RO = Robillard, VRSZ = Virgin River Shear Zone. Modified from Reid et al. (2014), after Jefferson et al. (2007).

and Wollaston basement domains (Jefferson et al. 2007), as seen in Figures 2.1 and 2.2. The Athabasca group is of Middle Proterozoic age and comprised of redbed sandstones, conglomerates, minor shales, and dolomites. This group makes up the lower portion of the sediment filling the Athabasca Basin, which at its maximum is roughly 1500 metres deep (Bruneton 1993). The basement immediately below the Athabasca group has a vertical paleoweathered profile ranging from a few centimetres up to 220 metres thick. The Mudjatik-Wollaston basement domain transition (Figure 2.1, 2.2) contains high proportions of pelitic, quartzose and arkosic paragneiss (sedimentary derived) that are isoclinally folded and interfingered with

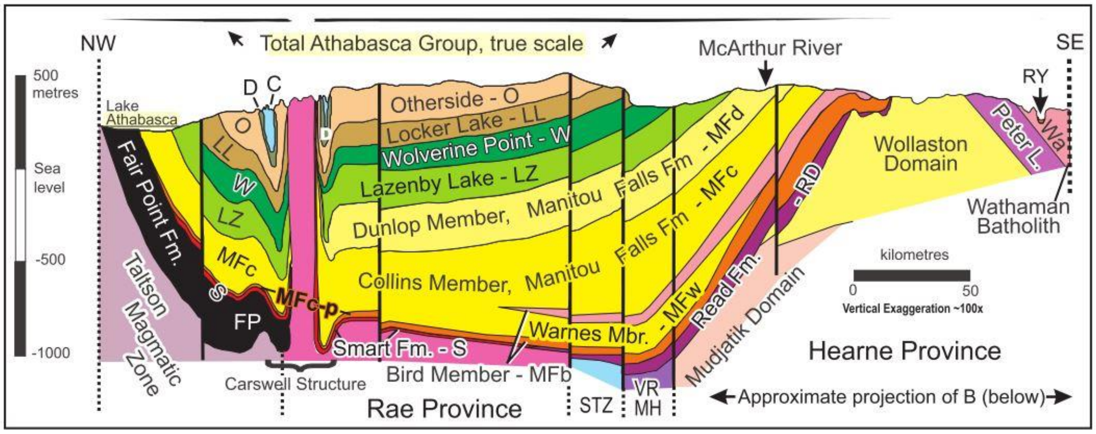

Figure 2.2: Lithostratigraphic cross section of Athabasca Basin (Jefferson et al. 2007), approximate location of cross section is represented by a red line in Figure 2.1.

Archean orthogneiss (igneous derived) and intruded by abundant pegmatite (Jefferson et al. 2007). Also, many significant deposits in the eastern basin are located at the metamorphosed unconformable contact between the Archean granitoid gneiss and late Paleoproterozoic basal Wollaston group, where it contains graphitic metapelitic gneiss. Graphitic metapelitic gneiss units constitute weak zones between competent units and were the focus of local deformation during regional folding, thrusting, and later brittle deformation. Similar graphitic units underlie deposits in areas of the western Athabasca Basin where they are detectable as conductors and were perhaps conduits for deep crustal heat to move upward and drive convection of ore-forming hydrothermal fluids (Jefferson et al. 2007). The graphitic metapelitic gneiss units are not only electrically conductive exploration targets and the sites of reactivated faults, but are also widely regarded as a source of reductant in geochemical process models for unconformity-associated uranium. Significant uranium deposits can form in the absence of graphitic units, however these are in the minority and it is not known whether super high-grade deposits, such as MacArthur River, can form without graphite. Aquifers along the unconformity, brittle reactivated faults, crosscutting local structures and alteration (e.g. silicification, clay minerals, and dissolution) were the main controls on fluid flow at uranium deposition sites (Jefferson et al. 2007). Faults in the Athabasca Basin constitute a number of arrays with different attributes, such as dextral or sinistral, extensional or transpressional, and ductile or brittle. The close association between faulting and unconformity-associated uranium deposits has been known since the initial uranium discoveries in Athabasca, and these faults are important targets for mineral exploration both at the district and deposit scale. A number of originally ductile faults underwent repeated brittle reactivation, with offsets on the order of tens to hundreds of metres, and were important for focusing mineralizing fluids.

The morphology of individual deposits within the Athabasca Basin are varied but tend to range between two end-member types (Jefferson et al. 2007):

1. Fracture-controlled and breccia-hosted replacement, dominantly basement hosted.
2. Clay-bounded, massive ore developed along the unconformity and just above it in the overlying conglomerate and sandstone of the Athabasca group.

The fracture-controlled basement hosted ore (Figure 2.3a), typically occupies steeply to moderately dipping brittle shear, fracture, and breccia zones hundreds of metres in strike length that extend down dip for tens to hundreds of metres into basement rocks below the unconformity. Both disseminated and massive uraninite occupies these fractures and the breccia matrix, as well as smaller near vertical ore lenses within the hanging wall. The high-grade ore lenses are bounded by sheared and

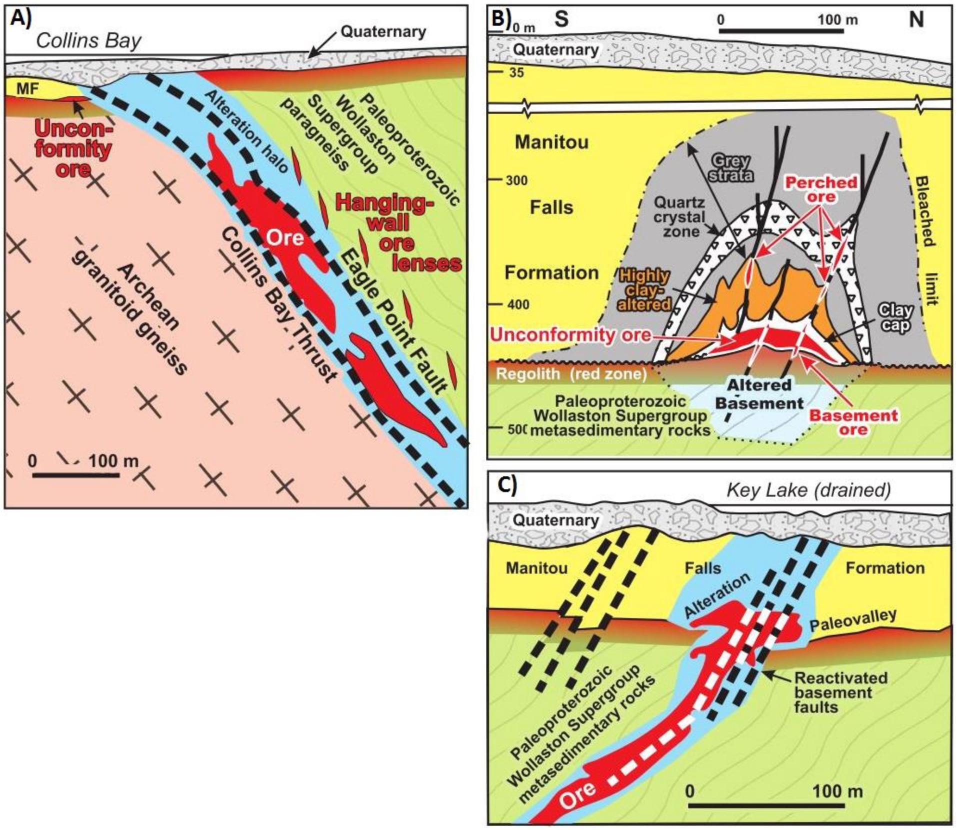

Figure 2.3: Examples of unconformity-associated uranium deposits of two end-member types. A) Basement hosted Eagle Point deposit. B) Unconformity hosted Cigar Lake deposit. C) Key Lake deposit showing traits of both types. Modified from Jefferson et al. (2007).

brecciated graphitic schist that contains smaller lenses of similar material, forming an envelope of lower grade ore. In contrast, clay-bound ore (Figure 2.3b) develops along the basement-sandstone unconformity and forms flattened elongate pods and linear orebodies typically characterized by a high-grade core surrounded by a lower grade halo. Many clay-bound ore bodies show traits of both end-member types, having root-like extensions into the basement (Figure 2.3c), and in places mineralization also extending up into the overlying conglomeratic sandstone along fracture and brecciated zones (Jefferson et al. 2007). The unconformity-hosted ore is sometimes broken into two distinct groups (Powell & Wood 2007) and a distinction is made between unconformity and sandstone-hosted deposits, which include perched ore lenses (Figure 2.3b). Both the unconformity and basement hosted deposit end-member types typically have similar size ranges, however, in different dimensions. Many conventional genetic models employed today in the Athabasca Basin describe late diagenetic to hydrothermal processes with ore formation being spatially and temporally focused by the reactivation of pre-Athabasca Group structures (Jefferson et al. 2007). These models suggest that oxidizing, uranium-bearing, basin fluids heated by geothermal gradients to 200 ºC at the unconformity reacted with reducing fluids coming out of reactivated basement shear zones. Uranium precipitated as uraninite in fault zones where reduced and oxidized fluids were mixed. Uraninite filled tension gashes and other structural traps during active faulting and was repeatedly brecciated while new uraninite precipitated. Ore deposits accumulated where these conditions were focused for very long periods of time, perhaps hundreds of millions of years (Jefferson et al. 2007).

Finally, it is important to discuss briefly the electrical properties of Athabasca Basin rock types since their resistivity, and/or its inverse conductivity are the basis of interpreting EM responses. Figure 2.4 shows the range of resistivity values for many of the common rock types related to unconformity-associated uranium deposits in the Basin. Overburden and lake water are relatively conductive compared to deeper sandstones but are typically thin and do not generally affect EM methods. Lake sediments, on the other hand, can be fairly conductive and in some cases, decrease the depth of penetration of EM systems (Irvine & Witherly 2006). Basin sandstones are generally highly resistive, alteration zones can also be highly resistive

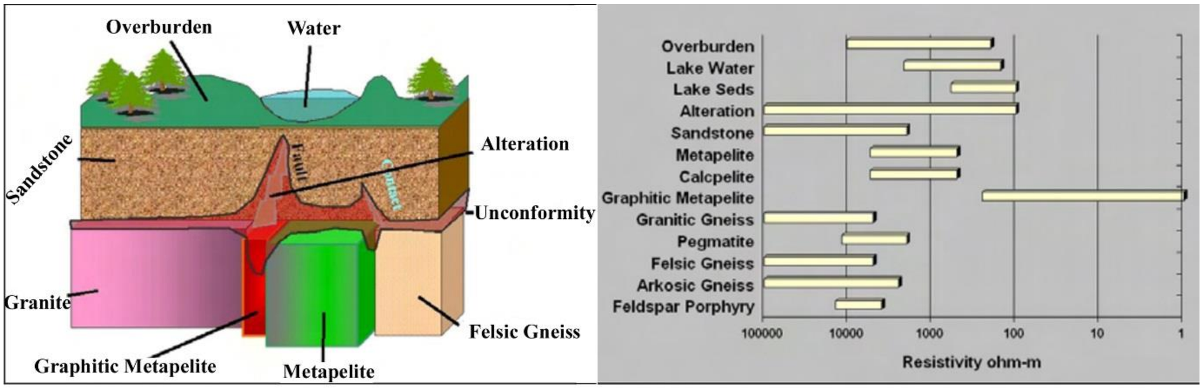

Figure 2.4: Conductivities of general rock types related to uranium deposition in the Athabasca Basin. Modified from Irvine & Witherly (2006).

but are variable and can sometimes be moderately conductive. At the unconformity the paleoweathered regolith is not a significant conductor, and the basement rock types (granite, gneiss, metapelite) are all resistive. The graphitic metapelites, which are the regions of greatest interest, are highly conductive and so can be detected and imaged well even at considerable depth in this otherwise mostly resistive environment.

2.2 Electromagnetic Geophysical Exploration Methods

2.2.1 Introduction

The use of electromagnetic prospecting has been an essential component of uranium exploration in the Athabasca Basin since just after initial discoveries were made there. A variety of techniques have been utilized to image the conductive graphitic metapelite units hosting or related to uranium deposition. Modern techniques for electromagnetic exploration can be separated into two main groups: time-domain and frequency-domain EM. Time-domain or transient EM prospecting (TEM/TDEM) is the most popular method employed in the Athabasca Basin today, due to its ability to image deep conductors successfully and at a relatively low cost compared to other methods. However, other methods such as magnetotellurics (Crowe et al. 2013; Hautot et al. 2011), audiomagnetotellurics (Tuncer & Unsworth 2006; Tuncer et al. 2006), as well as audio-frequency magnetics (Legault et al., 2009a; Lo et al. 2008; Legault et al., 2009b), and more have been used successfully in Athabasca to image conductors from shallow depths, to depths approaching 1000 metres.

2.2.2 EM Induction Theory

The basic principles of the EM exploration methods are based on Maxwell's Equations, namely Ampere's law, and Faraday's law, shown here in the differential form.

$$\text{Ampere's law:} \qquad \nabla X\, \boldsymbol{H} = (\boldsymbol{J} + \varepsilon_0 \frac{\partial \boldsymbol{E}}{\partial t})$$

$$\text{Faraday's law:} \qquad \nabla \mathrm{X}\, \boldsymbol{E} = -\frac{\partial \boldsymbol{B}}{\partial t}$$

$$\text{where} \qquad \mathbf{B} = \boldsymbol{\mu_0}\mathbf{H}$$

Here **H** is the magnetic field (A/m), **J** is the current density (A/m^2), **E** is the electric field (V/m), **B** is the magnetic induction (T), μ_0 and ε_0 are the permeability and permittivity of free space respectively; bold characters indicate vector quantities. Ampere's law states that a magnetic field can be caused by either an electric current or a changing electric field. Faraday's law states that a changing magnetic field will induce an electric field. Also important is Ohm's law:

$$\text{Ohm's law:} \qquad \mathbf{J} = \sigma\mathbf{E}$$

Here σ is the conductivity of the material. Very simply, and regarding its application to exploration geophysics, the primary magnetic field created by a current in a transmitter coil on or near the earth's surface induces electric eddy currents in subsurface conductors. The induced eddy currents will, in turn, generate secondary magnetic fields that can be measured as a current or voltage in a receiver coil (Figure 2.5).

To examine this in more detail, the response of a fixed-coil, frequency-domain prospecting system to a single, closed, buried conductive circuit is summarized from Grant and West (1965). Figure 2.6 shows the situation being considered, and we start with an alternating current $I_o e^{i\omega t}$ in the transmitter coil. The current generates an alternating magnetic field in the surrounding environment which then induces

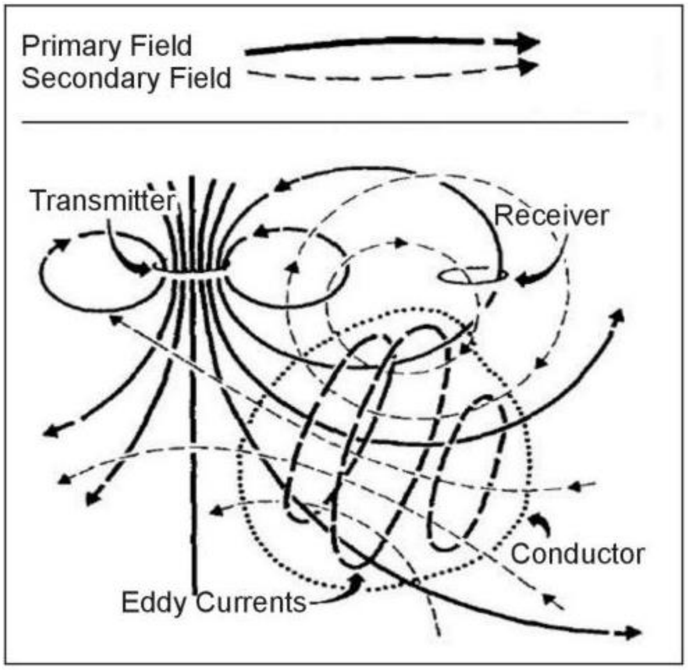

Figure 2.5: Generalized picture of electromagnetic induction prospecting (Grant and West 1965).

and electromotive force (emf) in the buried circuit as well as in the receiver coil. This follows Faradays Law:

$$\varepsilon_j = -M_{ij}\frac{dI_i}{dt},$$

where ε_j is the emf induced in one circuit by a current of I_i flowing in another,

and M_{ij} is the mutual inductance between the two. The emf induced in the receiver by the primary field (transmitter) is:

$$\varepsilon_2{}^{(P)} = -M_{02}\frac{d}{dt}I_o e^{i\omega t} = -i\omega M_{02}\, I_o e^{i\omega t},$$

and the emf induced in the underground circuit is:

$$\varepsilon_1 = -i\omega M_{01}\, I_o e^{i\omega t}.$$

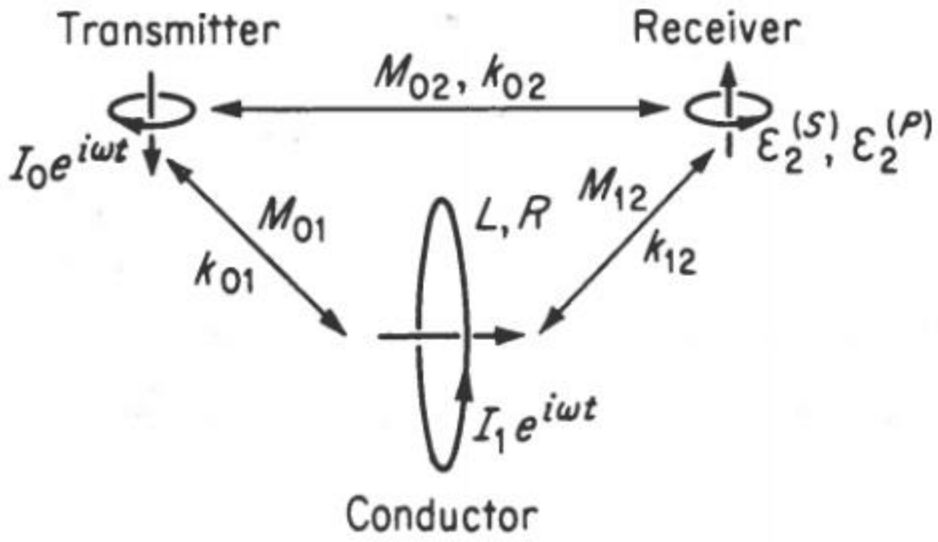

Figure 2.6: Circuit representation of a simple EM prospecting system (Grant and West, 1965).

The quantity $\varepsilon_1{}^{\dagger}$, which is the sum of the voltage drop across the resistance of the circuit and the back emf generated by the self-inductance when the current $I_o e^{i\omega t}$ flows around the loop, must be added to the current induced in the buried circuit ε_1, Grant and West (1965).

$$\varepsilon_1{}^{\dagger} = -RI_1 e^{i\omega t} - L\frac{d}{dt}I_1 e^{i\omega t} = -(R + i\omega L)I_1 e^{i\omega t}$$

The total emf must vanish around any closed circuit, so to find I_1,

$$\varepsilon_1 + \varepsilon_1{}^{\dagger} = 0,$$

and

$$I_1 e^{i\omega t} = -\frac{i\omega M_{01}}{R + i\omega L} I_0 e^{i\omega t} = -\frac{M_{01}}{L}\left[\frac{i\omega L(R - i\omega L)}{R^2 + \omega^2 L^2}\right] I_0 e^{i\omega t}.$$

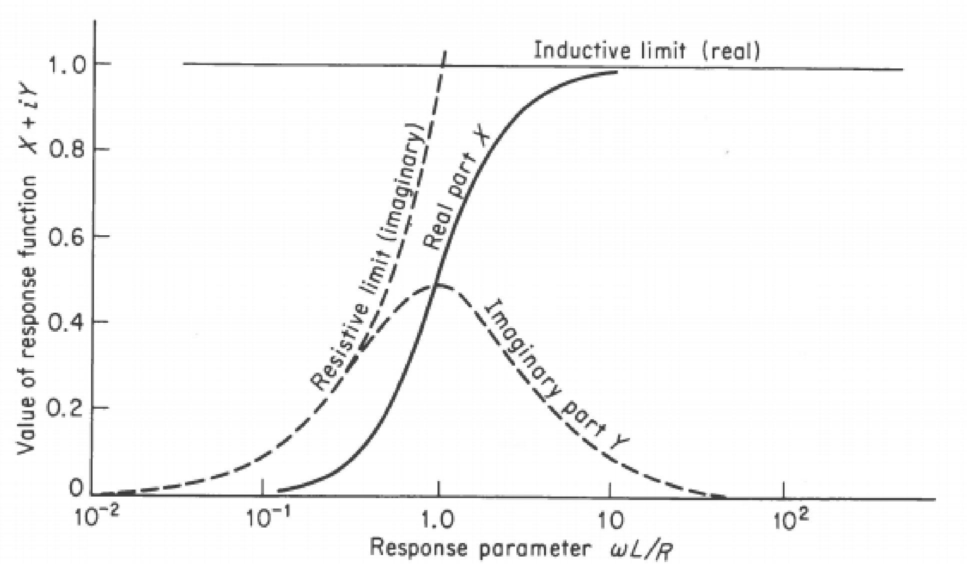

Figure 2.7: Frequency-domain response function of a simple circuit (Grant and West, 1965).

This equation gives the solution for induced eddy currents in the buried circuit, but of most interest is the secondary magnetic field produced by this current, and particularly in the emf induced by the magnetic field in the receiver coil. This emf is given by:

$$\varepsilon_2{}^{(S)} = -i\omega M_{12}\, I_1 e^{i\omega t},$$

where M_{12} is the mutual inductance of the buried vertical circuit and the receiver coil (Grant and West, 1965). In the frequency domain, the response is often measured as:

$$\frac{\varepsilon_2{}^{(S)}}{\varepsilon_2{}^{(P)}} = -\frac{M_{01}\, M_{12}}{M_{02}\, L}\left(\frac{\alpha^2 + i\alpha}{1 + \alpha^2}\right),$$

Where $\alpha = \omega L/R$. The remainder of the equation above is a complex function of the dimensionless quantity α, called the response parameter, which depends upon the frequency of the field as well as on the electrical properties of the buried loop (Grant

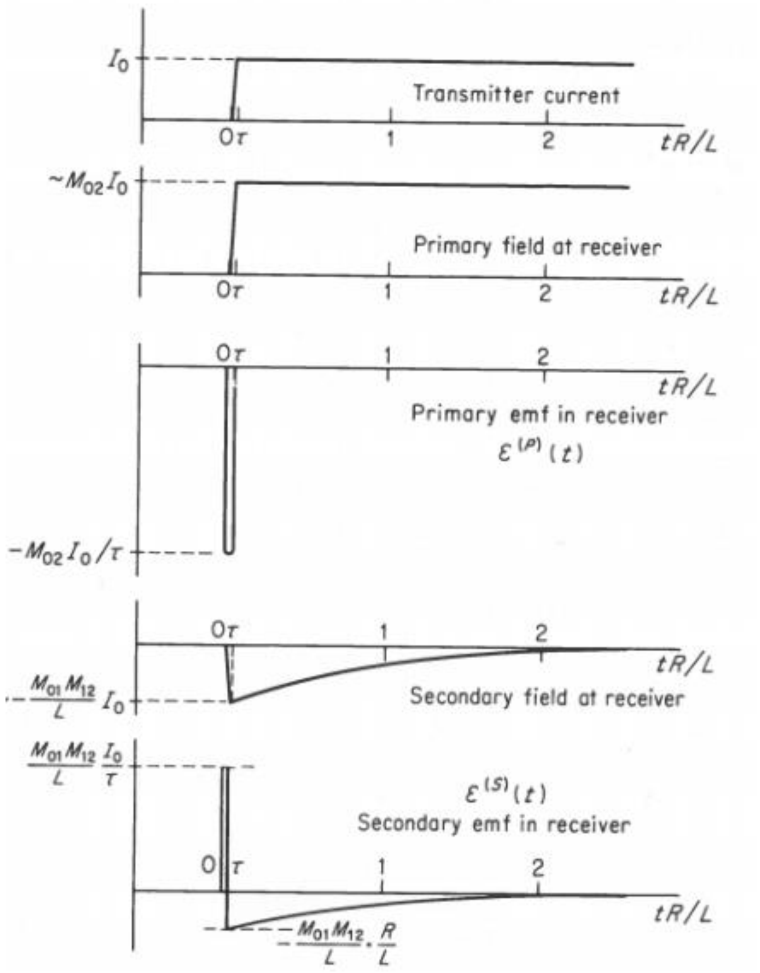

Figure 2.8: Time-domain response of a simple circuit (Grant and West, 1965).

and West, 1965). The complex function $f(\alpha) = (\alpha^2 + i\alpha)/(1 + \alpha^2)$, is called the response function and is responsible for the real and imaginary, or also called the in-phase and quadrature components of the frequency response, see Figure 2.7.

In the time domain, the equations can be formed in a similar way as for the frequency-domain case, see Figure 2.8 for the time-domain response of a simple circuit. Again, summarizing Grant and West (1965), the equations for $\varepsilon_1(t)$ and $\varepsilon_1{}^{\dagger}(t)$ induced in the underground buried circuit by a current $I_0u(t)$ in the transmitter and the current *I(t)* in the buried circuit are:

$$\varepsilon_1(t) = \; -M_{01}\,\frac{d}{dt}[I_0 u(t)],$$

$$\varepsilon_1{}^{\dagger}(t) = -RI(t) - \; L\frac{d}{dt}[I(t)].$$

The function $u(t)$ is the step function:

$$u(t) = 0 \quad t < 0$$

$$= \frac{t}{\tau} \quad 0 \; \leq t < \tau$$

$$= 1 \quad t > \tau$$

The emf's induced in the receiving coil by the transmitter and the buried circuit are:

$$\varepsilon_2{}^{(P)} = \; -M_{02}\,\frac{d}{dt}[I_0 u(t)] = -M_{02}\,I_0\delta(t),$$

$$\varepsilon_2{}^{(S)} = \; -M_{12}\,\frac{d}{dt}I(t) = -\frac{M_{01}M_{12}}{L}\;I_0\left[\delta(t) - \frac{R}{L}e^{-\frac{Rt}{L}}\right],$$

where

$$\delta(t) = 0 \quad t < 0$$

$$= \frac{t}{\tau} \quad 0 \; \leq t < \tau$$

$$= 1 \quad t > \tau.$$

An example of the delta-function response for $\varepsilon_2{}^{(P)}$ can be seen in the middle panel of Figure 2.8. The similar delta-function response, including the exponential decay, of $\varepsilon_2{}^{(S)}$ can be seen in the bottom panel of Figure 2.8.

2.2.3 EM Skin Depth

A brief explanation is necessary to understand the electromagnetic "skin depth" and its effect on frequency-domain EM systems. The skin depth is defined as the depth of penetration at which amplitude of a plane-wave electric or magnetic field traveling in a homogeneous half-space falls to $1/e$ of its surface value (Reid & Macnae 1999). Shown here for the frequency domain the skin depth δ is given by,

$$\delta = \sqrt{\frac{2}{\sigma\mu\omega}}$$

where σ is the conductivity of the half-space, ω is the angular frequency, and μ is the magnetic permeability. Holding all else constant the skin depth decreases as frequency increases and this plays an important role in geophysical exploration, governing the type of equipment used in a survey. It is also an important consideration in the forward model design process as the model space must be made large enough to accommodate a range of frequencies.

The decay of an EM field away from a localized source, like that of a typical time or frequency-domain survey, is more complicated than this simplified plane-wave case. However, the place-wave skin-depth is still a quick and useful way of determining the necessary size of the model domain.

2.2.4 Frequency-Domain EM Method

Frequency-domain exploration techniques, while not explicitly studied in this project, are important to briefly cover because the forward modeling method described in subsequent chapters is based on a FDEM code. Frequency-domain methods are popular for use in situations where target depths are shallow and have a moderate to strong conductivity/resistivity contrast with the surrounding rock types (Peltoniemi 1998). The method is often used in environmental geophysical applications such as mapping shallow aquifers, locating buried pipes or unexploded munitions, monitoring leakages of dangerous chemicals in the subsurface, etc. The actual depth of investigation of FDEM varies depending on the system but is almost always much less than a few hundred meters, this governed by the frequency used, geologic setting, and most importantly contamination by the primary field.

In the frequency-domain, a continuous sinusoidal alternating current is driven through the transmitter coil at a single frequency (see the left side of Figure 2.9). This creates an alternating primary magnetic field which as above induces alternating currents in the subsurface as well as an alternating secondary magnetic field when a subsurface conductor is present. Because the transmitter current is continuous, both primary and secondary fields are measured simultaneously by the receiver coil making separation of the fields difficult. This limitation can be a major drawback of the frequency-domain method because the secondary EM fields from underground bodies are orders of magnitude smaller than the primary transmitted field (Nabighian, 1988). In most FDEM systems, there is some contamination of the secondary field by the primary field that varies in sign and magnitude from station

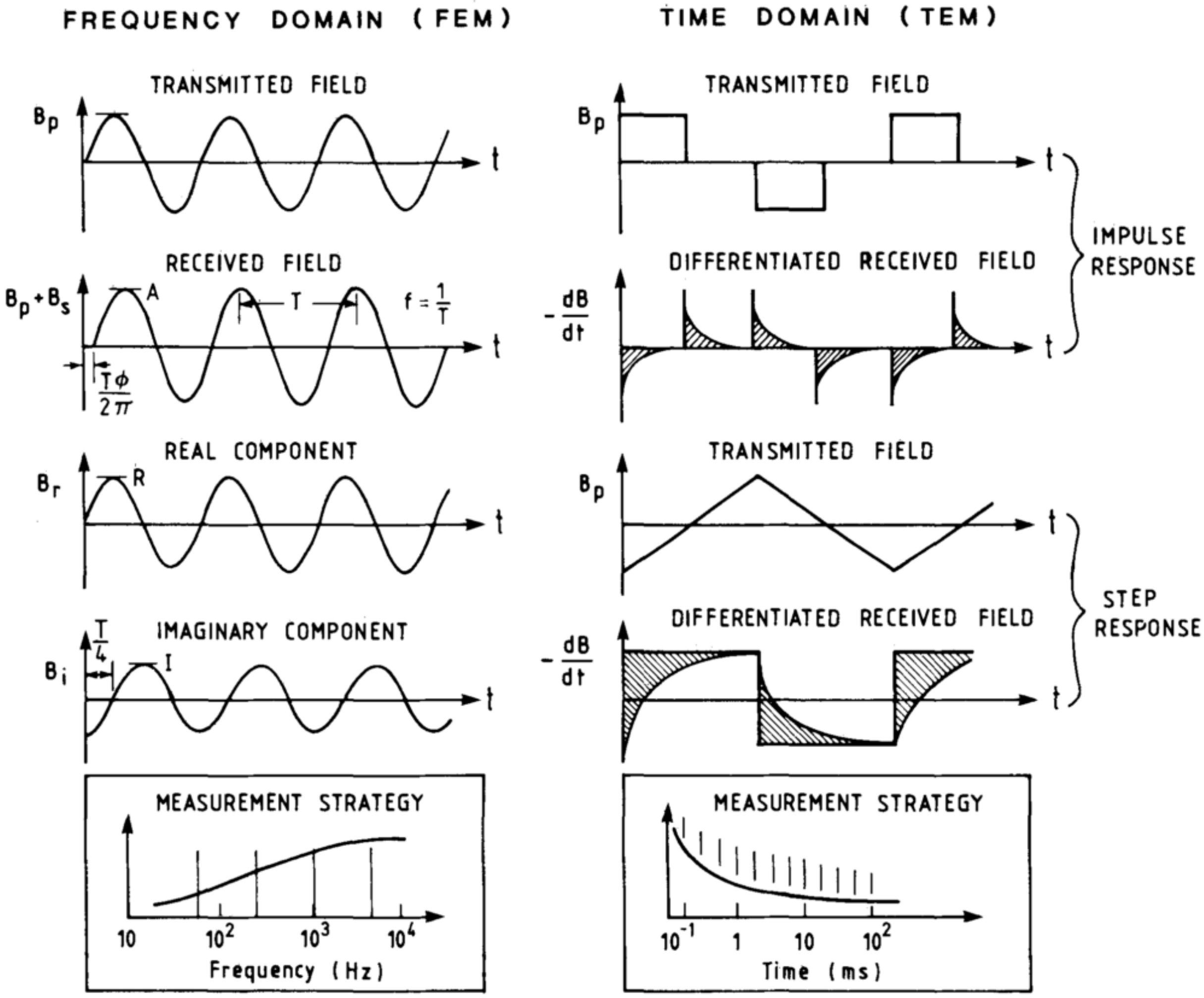

Figure 2.9: Input and output relations for FDEM and TDEM. Cross-hatched regions indicate secondary fields in the TDEM cases. The measurement strategy box illustrates the manner in which measurements are made, at different frequencies or at different times (Mccracken 1986).

to station. This source of noise ultimately sets the limit to exploration at depth (Mccracken 1986).

Operating frequencies for FDEM systems are roughly between 100 Hz and 130,000 Hz but vary considerably depending on equipment design and whether it is a ground-based or airborne system. Ground FDEM systems are smaller in scale than TDEM systems and often can be carried by a single operator as the transmitter and receiver coils are only on the order of a few meters apart and contained within the same unit in many cases (e.g. Reid & Howlett 2001; Won et al. 1996). The transmitter and receiver coils may have different geometries based on the type of survey and the desired results. Coils can be placed in a coaxial or coplanar arrangement or some combination of these to measure different directional components of the secondary field. Multiple coils can also be used in configurations that allow for simultaneous measurement of multiple directional components and or multiple frequencies. Airborne frequency-domain systems come in many forms but are classified typically by whether they are towed by a fixed wing aircraft or helicopter. Airborne systems often look like scaled up versions of ground FDEM systems (Figure 2.10) and house transmitter and receiver coils within a tubular shaft ("bird") approximately 3-10 metres in length. Typically, multiple coils and frequencies are used to maximize data acquisition at various depths. The bird is towed from the aircraft at some height above the Earth's surface, typically as low as possible for safe operation of the aircraft. Fixed-wing systems are less common in FDEM and do not always employ a bird but instead may affix the transmitter and receiver to opposite wingtips on the plane. Since many of the actual survey methods are similar to TDEM methods, more information of survey design and implementation will be covered in the following section.

Figure 2.10: Examples of ground and airborne FDEM systems. At top left is the GEM-2 from Geophex Ltd., top right is the EM-31 from Geonics Ltd., bottom right is the SGFEM fixed-wing system from Sander Geophysics, and at the bottom right is the RESOLVE heliborne system from CGG.

2.2.5 Time-Domain EM Method

Time-domain EM was initially developed to get around the complexities in separating the primary and secondary field response experienced in frequency-domain EM (Nabighian and Macnae, 1991). With TDEM methods, the transmitted direct current is most commonly in the form of a modified square wave (Figure 2.9), or in some "on-time" systems a triangular wave, each typically driven at a 50% duty cycle. For a square wave, every quarter period the current is abruptly reduced to zero (off-time) for one-quarter period before reversing direction. The response is determined by the decay of the receiver voltage and is measured in a series of time bins or channels that increase exponentially in length with time. The principle behind TDEM is that the current is on for a period of time then abruptly shuts off causing the primary magnetic field to decrease rapidly and inducing secondary currents in subsurface bodies. One benefit of this method is that the secondary field is measured in the absence of the primary field, and so in most cases not distorted by it (possibly at early times or in very conductive rock types). For a triangular waveform, the current is never truly off: it is only ramping up to some maximum then down to some minimum value. This creates a linearly varying primary field for which d**B**/dt is constant, and so the receiver coil is only measuring the time variation of the secondary field. The use of a continuous triangular waveform effectively simulates a pure step function in the primary transmitted field and reduces or removes contamination of the secondary field response by the primary field (Mccracken 1986).

The use of modified square or triangular waveforms depends on the type of receiver used and the desired measurement. The voltage measured by an induction coil receiver is proportional to the change in the secondary magnetic induction over time ($d\mathbf{B}/dt$); this is explained by the principles of induction in the section 2.2.2. Typical ways of presenting the response include $d\mathbf{B}/dt$, the derived magnetic induction **B**, and the time constant or tau, which relates conductivity to the measured voltage decay (Wightman et al. 2003). In recent years the development of high sensitivity SQUID magnetometers (e.g. Foley & Leslie 1998; Foley et al. 2006) has allowed for direct measurement of the magnetic induction **B**. These SQUID **B**-field measurements are desirable for many reasons including an improvement in the signal to noise ratio and the conductance discrimination capabilities needed to detect small, long-time constant (>>10ms) targets at depth (Osmond et al. 2002). By measuring **B**, better conductors yield larger measured voltage values immediately after the current is shut off, whereas for d**B**/dt measurements it takes more time for a good conductor to yield larger voltages. Another important difference is the nearly six orders of magnitude in variation of d**B**/dt decay curves vs. only nearly three orders of magnitude difference for **B**-field measurements (per. Comm. Misac Nabighian, 2017). Finally, **B**-field measurements also provide the benefits of measuring a step response as opposed to an impulse response as with induction coil receivers (Mccracken 1986).

The basic configuration for TEM systems, both airborne and ground-based, consists of a large primary transmitter coil and an equally sized or smaller secondary receiver coil or high sensitivity magnetometer. The depth of exploration with time-domain techniques is determined by factors such as the diameter of the transmitter loop and its magnetic dipole moment among others. A variety of airborne TEM systems exist to handle a broad range of geophysical exploration scenarios. In recent years the fixed wing MEGATEM system (Smith et al. 2003), and the heliborne VTEM system (Witherly et al. 2004) were the most commonly used in the Athabasca Basin (Irvine & Witherly 2006). Both systems employ a large transmitter coil approximately 30-40 metres in diameter and a smaller receiver coil, or system of coils. For the fixed wing MEGATEM, the transmitter encircles the entire plane and the receiver bird is towed by cable some distance behind and below the aircraft. With the heliborne VTEM, the transmitter is coincident with the receiver coil and both are suspended by a cable beneath the helicopter. The basic configurations of these systems represent the general layout of other, similar, fixed wing and heliborne EM systems (Figure 2.11). Steady increases in transmitter size, as well as transmitted currents, have allowed for these systems to achieve dipole moments of 1.5-2 million Am^2, giving the greatest depths of penetration possible for current airborne TEM systems. This along with a steady increase in the signal-to-noise ratio and the ability to collect data quickly and inexpensively have made airborne TEM very popular for use in the Athabasca Basin (e.g. Irvine and Witherly 2006; Smith and Lemieux 2003; Legault et al. 2010; Witherly 2009; Smith and Koch 2006). Despite the growing popularity of airborne systems and their ability to successfully image large and intermediate scale geology, there is still need for ground-based TEM techniques to more precisely image complex conductors on local scales, for example, to improve drill hole targeting (Powell & Wood 2007).

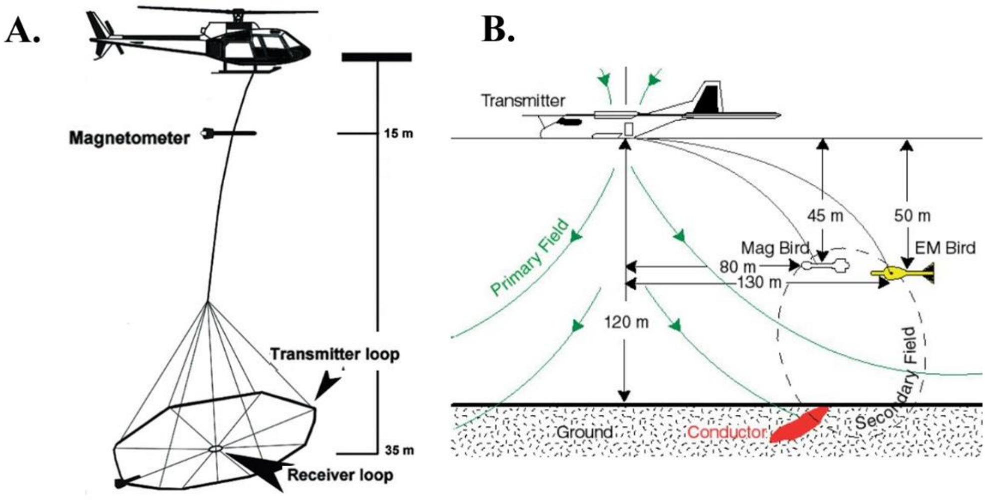

Figure 2.11: Generalized airborne TDEM systems. A) Heliborne (Witherly & Irvine 2006). B) Fixed wing (Smith & Lemieux 2003).

Ground-based TEM systems work on the same principles as airborne systems with the major difference being the much larger transmitter coil, which can be on the order of a few hundred metres in diameter on the ground. A variety of configurations exist for transmitter and receiver arrangement during data acquisition as seen in Figure 2.12. In the simplest of these, the transmitter coil is kept in a fixed location while the receiver is moved throughout the survey area (2.12a). Another method holds the receivers at a fixed distance from a moving transmitter coil (2.12b), this is commonly referred to as the Slingram method. Another technique used in the Athabasca Basin is the Stepwise Moving Loop method (2.10c), which is a hybrid between fixed and moving transmitter methods and is applied in a fashion similar to seismic surveys with the transmitter coil centered between a line of receivers at each measurement location (Powell & Wood 2007). This technique can image embedded and multiple conductor systems, masked hanging wall conductors, and other complex conductor environments, making it ideal for the challenges faced in unconformity-associated uranium exploration. However, in current practice, the Slingram style moving loop survey offers the best results for the cost of the survey and is the design most commonly used for ground TDEM exploration in the Athabasca Basin (per. comm. Robert Hearst, 2016). The hybrid style transmitter-receiver layout was not tested during the course of this project; however it would certainly be possible to carry out using this forward-modeling method. Figure 2.13 shows the Slingram-style survey layout used for modeling purposes in this project. A 400 x 400-metre square transmitter coil was located at an offset of 800 m from the receiver which in terms of this project can be thought of as a $d\mathbf{B}/dt$ induction coil of unit area, and/or a **B**-

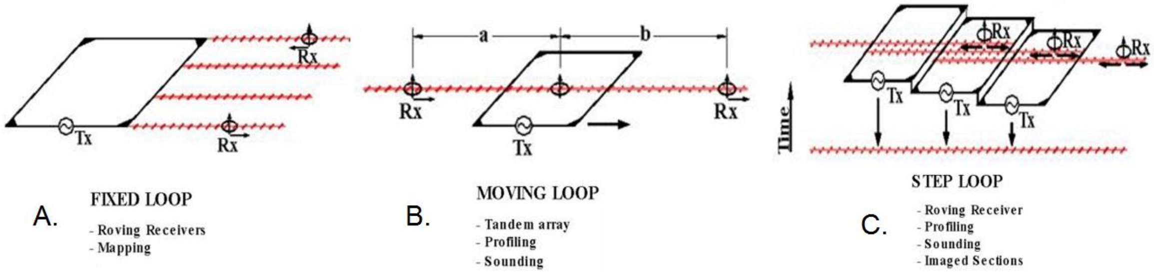

Figure 2.12: Large loop EM configurations common in Athabasca Basin (Powell & Wood 2007).

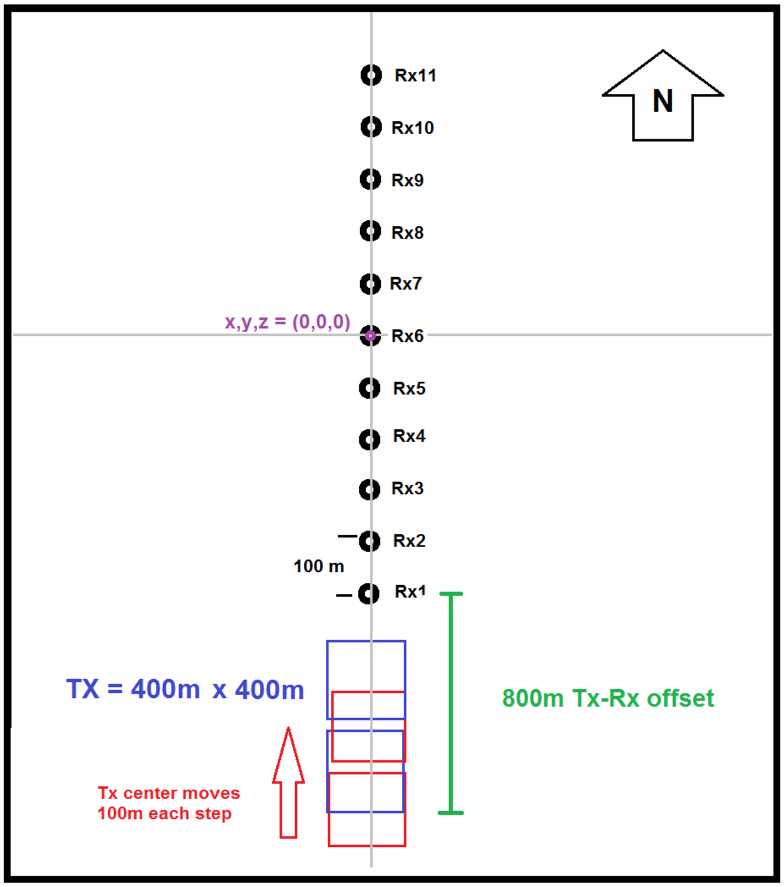

Figure 2.13: Slingram-style survey layout used for this project.

field magnetometer type sensor. The transmitter and receiver are stepped together along the receiver line at increments of 100 m over the target of interest.

2.2.6 Frequency to Time-Domain Transformation Method

The method of transformation from the frequency-domain to time-domain used in this project follows that of Newman et al. (1986), and makes use of sine and cosine transforms. Namely the time derivative of the magnetic field ($d\mathbf{h}_z/dt$), can be obtained from the imaginary part of the frequency-domain magnetic field

[Im($\mathbf{H}_z(\omega)$)]. A Fast Fourier Transform (FFT) could also be used for the transformation into the time domain. However, the FFT requires a large number of component frequencies and simple interpolation over a sparsely sampled frequency response does not give accurate results (Newman et al. 1986). The calculated time-domain response is equivalent to that of an impulse response caused by a step-off, or square transmitter waveform (Newman et al. 1986):

$$\frac{\partial \boldsymbol{h_z}(t)}{\partial t} = \frac{2}{\pi}\int_0^\infty Im\,[H(\omega)]\sin(\omega t)\;d\omega$$

$$and\quad \frac{\partial \boldsymbol{B_z}}{\partial t} = \mu_0 \frac{\partial \boldsymbol{h_z}}{\partial t}$$

It is also possible to obtain the time-domain **H**-field (or **B**-field) response by use of a cosine transform:

$$\boldsymbol{h_z}(t) = -\frac{2}{\pi}\int_0^\infty \frac{Im[\boldsymbol{H_z}(\omega)]}{\omega}\cos(\omega t)\;d\omega$$

$$and\quad \boldsymbol{B_z} = \mu_0 \boldsymbol{H_z}$$

The calculations necessary to carry out both of the transforms follow Anderson's digital filtering routine and are described in detail by Newman et al. (1986). The code used in this project was obtained (per. comm. Colin Farquharson, 2014) in a ready to use form that only required minor updates to compute the cosine transform. The equations are shown here for the *z*-component only but the process is exactly the same for the *x*- and *y*-components.

2.2.7 Interpretation of Time- and Frequency-domain Responses

The interpretation of time- and frequency-domain responses for identification of conductor properties such as depth, dip, etc., is a topic that is well covered in the literature (e.g. West et al. 1984; Keller 1997; Lamontagne 1975; Newman et al. 1986; Newman & Hohmann 1988; Nabighian, 1988; Ogilvy, 1986; etc.) and will not be discussed in detail here. It is necessary however to briefly describe the types of results displayed in the following chapters and their significance. In the frequency-domain, the real and imaginary (also referred to as in-phase and quadrature) components of the response at each frequency are plotted vs. distance along the receiver line (Figure 2.14 A and B). The magnitude of the response is also plotted over the range of frequencies used in the model, again for the in-phase and quadrature components (Figure 2.14 C). For the time-domain it is similar, with the response plotted vs. time, which is called the time decay curve (2.14 F and 2.14 G). The response of each time channel is also plotted vs. distance for each receiver along the survey line (2.14 C and 2.14 D). In the frequency domain, the units are amps per metre (A/m) and the response is equivalent to the magnetic field **H**. In the time domain, the time derivative of the magnetic induction ($d\mathbf{B}/dt$) is plotted in micro Volts (µV), or, more or less equivalently in nV/Am^2, after normalizing by the magnetic moment of the transmitter. The magnetic induction (**B**) response is plotted in units of pico-Tesla per Ampere (pT/A) which is common in industry survey reports and is also obtained after normalizing by the magnetic moment of the transmitter.

In practice, both the time decay curve and the response over the survey line are commonly used to identify conductors. Frequency domain responses are not typically used in uranium exploration, at least not over the broad range of frequencies seen here, but are similar in some respects to the time-domain response and are examined here mainly to understand and monitor the results of the frequency-domain forward modeling code. At the center right of Figure 2.14 is the model mesh used to produce these responses: it is a 10m thick 3 Ohm-m body in a 3500 Ohm-m half space. This model also illustrates well the standard response shape of a thin vertical conductor detected with a Slingram-style survey.

The presence of a conductor is detected as a trough with the minimum over the conductor; this, of course, can become much more complicated as the conductor is varied from a simple vertical position, or when multiple conductors are present. The trough response is used by convention and is common in the mineral exploration industry (e.g. Ogilvy 1986), however the actual frequency-domain result of CSEM3DFWD has a positive peak response and so the values are multiplied by negative one before transformation into the time domain. This has no effect on the result besides reversing the sign, and is done only for consistency in interpretation of the responses when comparing them to actual exploration data. The manual sign reversal is only done for the *z*-component; the polarity of the *x* and *y*-components are in practice based on the direction in which the transmitter-receiver pair is moved along the survey line, i.e. north to south or south to north, and must be adjusted individually (per comm. Robert Hearst, 2016). On the *x*-axis of the plots is the center location between the transmitter and receiver, *not* the location of the receiver itself. This is common in practice due to the geometry of the transmitter-receiver pair and

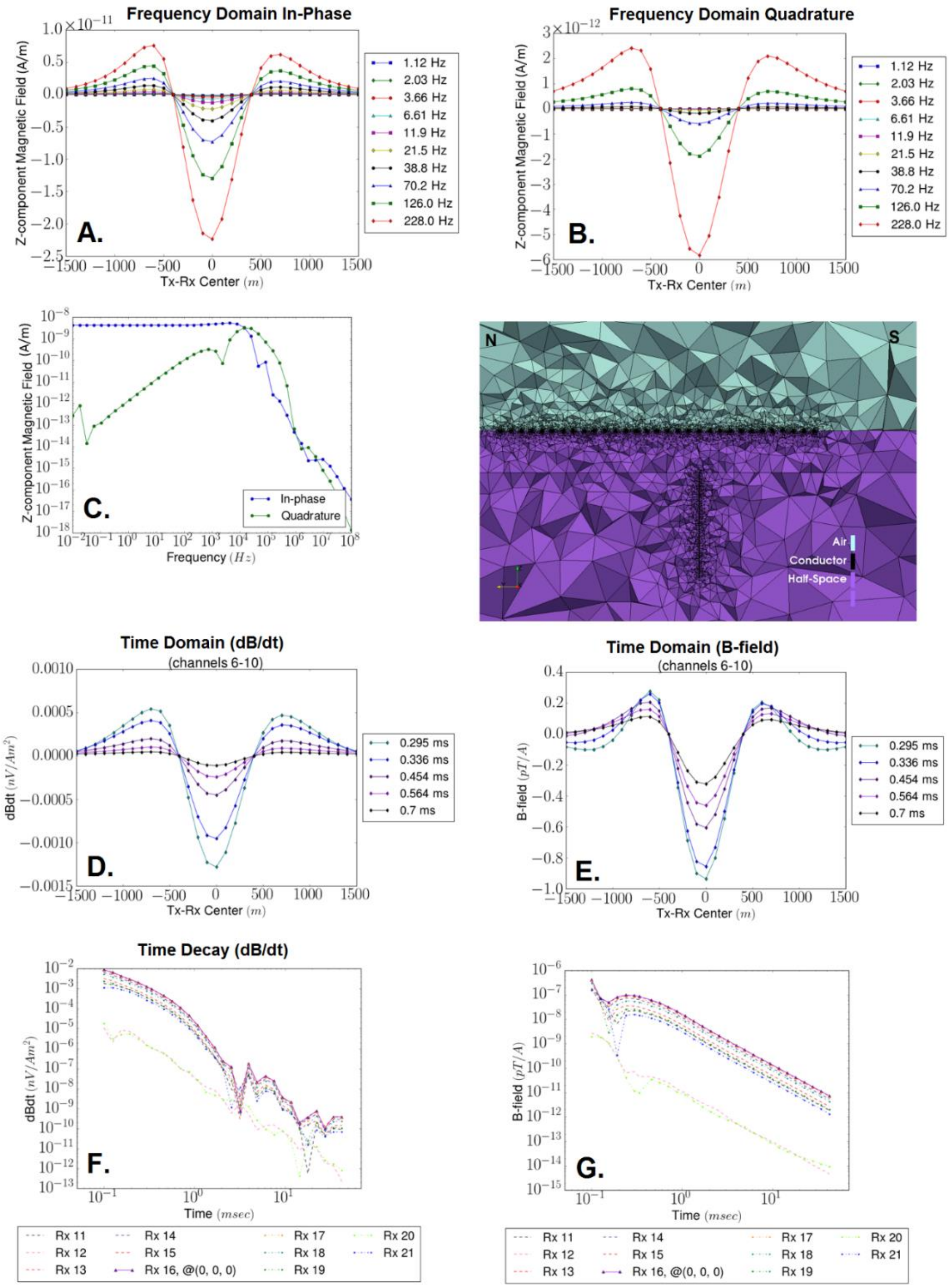

Figure 2.14: Selected time- and frequency-domain results for the vertical 3 Ohm-m conductor in a 3500 Ohm-m half space. A) In-phase (real component) of the frequency-domain response plotted for each frequency vs. distance along the survey line. B) Quadrature (imaginary component) of the frequency response. C) Amplitude of all model frequencies for a single receiver. D) Time-domain dB/dt response along the survey line. E) Time-domain B-field response along the survey line. F) dB/dt time decay curves for a selected group of receivers along the survey line. G) B-field time decay curves. Seen at the center is a cutaway image of the model mesh.

the conductor (e.g. Figure 2.6). More on these responses and their interpretation will be discussed in following chapters.

2.3 Geophysical Modeling

Geophysical forward modeling is a process by which a subsurface model is constructed and given physical properties, such as electrical resistivity, then using a mathematical algorithm a response is calculated for the model that is ideally equivalent to data collected in a field situation over a similar geologic scenario. It is very useful for testing geophysical hypotheses quickly and inexpensively as well as attempting to recreate and thus identify the characteristics of responses collected in the field over, for example, valuable uranium deposits.

Geophysical inversion, while not explicitly a part of this project, is still an important topic to understand. Inversion in many ways is the opposite of the forward-modeling process. In simple terms, inversion takes data collected in the field and through various means determines the physical properties and attempts to create a model that could have produced the measured response. Inversion is a very complicated process with many considerations. Inversion of EM data is also non-unique, meaning that there are infinitely many situations that may produce a single response, and so careful computation choices and geologic knowledge are necessary to accurately create and interpret inversion results.

2.3.1 Finite-Element Method on Unstructured Tetrahedral Meshes

A variety of methods currently exist for the 3D finite-element forward modeling of electromagnetic data (e.g. Ansari and Farquharson 2014; Puzyrev et al. 2013; Ren et al. 2014; Schwarzbach et al. 2011; Fu et al. 2015). In particular, Ansari and Farquharson, (2014) present a finite-element approach using vector and scalar potentials and unstructured meshes to solve the 3D EM forward problem in the frequency domain. Very simply, the finite-element method (FE) is a technique used to obtain approximate solutions to partial differential equations (PDE's) with specific boundary conditions, also called boundary value problems. In many situations involving PDE's, although an equation may be known for a problem, due to the complexity of the problem domain it cannot be directly solved. The FE technique was devised to discretize the domain into a mesh of many finite elements, or cells. In each cell the approximate solution can be expressed in simple terms, and thus an approximate solution can be built up for the entire problem domain. In the EM geophysical context, the boundaries of these cells, or even groups of cells, can represent lithological boundaries between rocks with different electrical properties. The benefit of the FE method over other traditional methods like finite difference (FD), is its ability to be applied to nonstandard i.e. non-rectilinear, unstructured tetrahedral meshes which are far better suited for modeling complex shapes like those encountered in geophysical scenarios (Figure 2.15). Also, the ability for mesh refinement (Figure 2.16) in regions of interest and coarsening near domain boundaries allows for better discretization of complex domains (Ansari & Farquharson 2014). The application of the FE approach to geophysical EM field problems was first

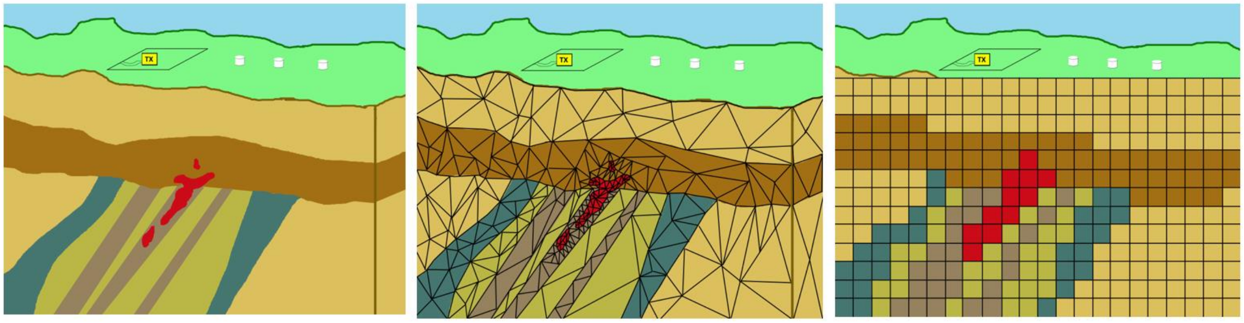

Figure 2.15: A 2D example of a complex geologic scenario discretized on 2 meshes. In the center is an unstructured Delaunay triangular mesh and at the right is a simple rectilinear mesh.

described by Coggon (1971) for the 2D calculation of EM and induced polarization anomalies. Since then the idea has been extended into 3D, and a variety of adjustments and implementation schemes have been used to try and optimize the process. The improvements made to the FE process are complex subjects themselves and represent the work of many authors; only a brief treatment of three of the most important modifications is given below, as they relate to the FE approach of Ansari and Farquharson (2014).

The first improvement was the introduction and use of edge-element basis functions (e.g. Schwarzbach et al. 2011), to approximate the electric field instead of the nodal element functions used previously. Edge element basis functions are defined along edges of cells in the mesh as opposed to at the vertices of cells in nodal element basis functions. By using edge-element basis functions instead of nodal-element basis functions, the normal component of the approximated electric field can be discontinuous across element boundaries, and thus sharp conductivity contrasts and the associated jump in the normal electric field can be better represented. The use of edge element basis functions still preserves the continuity of the tangential electric field at boundaries, and ensures that the divergence is zero within each cell.

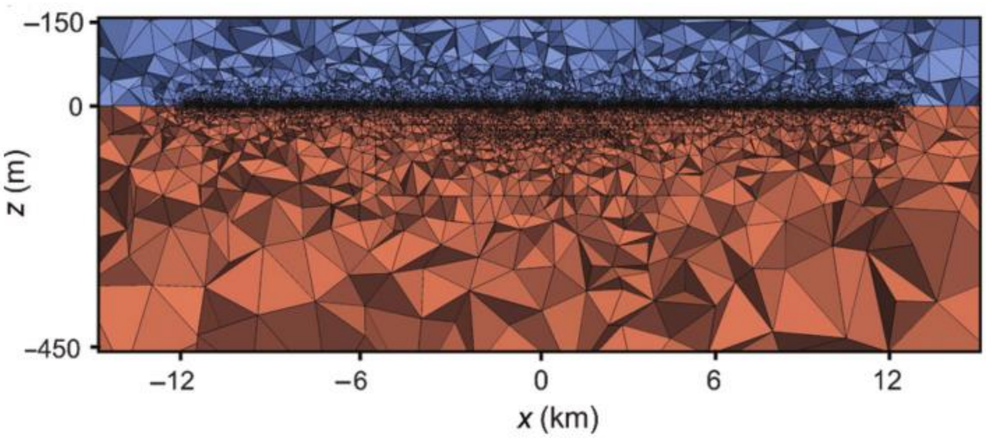

Figure 2.16: Enlarged cross-section of a tetrahedral mesh used for a homogeneous half-space model. The conductive ground and the resistive air are shown in orange and blue, respectively. The earth's surface is flat, and the mesh is refined about the dipole source at the origin and along 24 km of observation locations (Ansari & Farquharson 2014).

Ansari and Farquharson (2014) use a combined approach in which nodal basis functions are used for the electric scalar potential which ensures continuity of the scalar potential, and edge element basis functions are used for the magnetic vector potential.

Ansari and Farquharson (2014) present a method of further decomposing the electric field into its inductive and galvanic components allowing for them to each be analyzed separately. The decomposition of the electric field into the magnetic vector potential **A** and the electric scalar potential φ is used to explicitly separate out the inductive and galvanic effects thus making the equations simpler to solve. This is a better and more efficient forward modeling technique, and it also reduces computing time.

Finally, the EM forward problem itself can be formulated to be solved in terms of just the secondary EM field, or in terms of the total EM field, which would represent the primary source field as well as secondary fields caused by conductive anomalies. Solving for just the secondary field is simpler. However the primary field still must be calculated in some way and the process can become challenging for background models that are more complex than simple homogeneous half-spaces. Another drawback of solving in terms of the secondary field is that changes of elevation within the model are not handled well; when using a total field approach this is not a problem.

2.3.2 Unified Earth Models

The desire for geophysical models to represent subsurface geologic structure as accurately as possible needs no explanation; however, the process of combining these two distinct entities is not simple. The creation of 3D unified earth models that successfully incorporate geophysical and known structural geologic data is a growing area of research (e.g. Lelièvre et al. 2012). Three-dimensional geologic models are typically constructed of connected triangles that form tessellated wireframe surfaces like that in Figure 2.17. The surfaces represent geologic contacts between rock units and are able to accurately represent complex structures as well as topography (Lelièvre et al. 2012). In a mining scenario, data used to construct geologic models typically comes from outcrop mapping done on the surface as well as information obtained from drill core by connecting common units observed over the region of interest. Over a typical prospect, a considerable amount of useful structural data is obtained from drilling. However this data is for the most part not currently used in 3D geophysical forward modeling, which is done on rectilinear meshes that are not compatible with triangular wireframe geologic models. However, with the

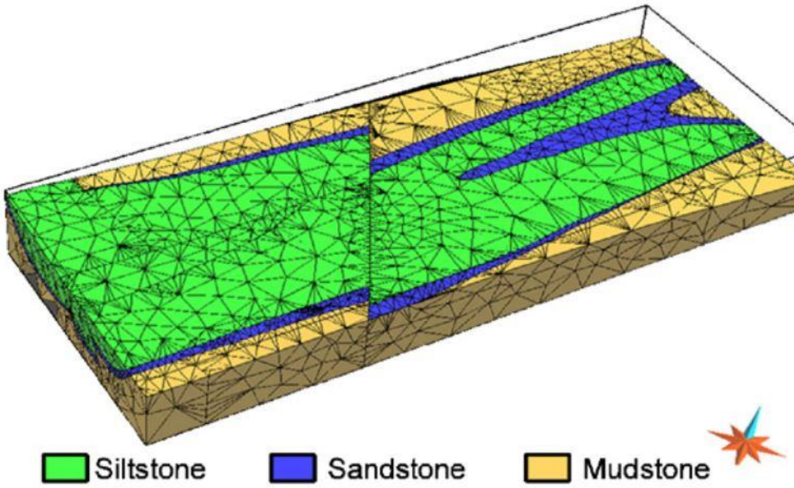

Figure 2.17**:** Example of 3D wireframe geological model on a tetrahedral mesh (Pouliot et al. 2008).

introduction of 3D forward modeling on unstructured tetrahedral meshes, e.g. Ansari and Farquharson (2014), the combination of geologic and geophysical models is achievable, although not without challenges (e.g. Lelievre et al. 2012; Lelièvre et al. 2012). In principle, the process of creating a unified model involves discretizing the regions between the surfaces of the geologic model with unstructured tetrahedra, while still preserving those surfaces, thus creating a forward modeling mesh that is the same as the geologic model. However, this can be made complicated by complex geologic settings or a lack of high-resolution drill core data, requiring hand manipulation of the wire frame model to prepare it for the discretization process. For this project no 3D geologic model was provided by ARC, so models were constructed entirely by hand, but still making use of real geologic drill data.

Another major concern for accurate representation of complex geology in the model mesh is the number of cells necessary to represent the situation. Models can quickly become "too accurate" and require a vast number of cells making computation slow or impossible by current means. A delicate balance is necessary to represent the geology accurately while also limiting cells.

2.3.3 Current Geophysical Modeling Programs

There are several programs and codes currently available for the forward modeling of EM exploration situations. However due to the complex nature of computing EM fields, full 3D forward modeling is often restricted to simple rectilinear meshes and/or the problem is reduced to a 2.5D situation. The benefits of computing models on unstructured tetrahedral meshes over rectilinear meshes were discussed previously in Section 2.3.1, and the improvement in the ability to more accurately model complex shapes is clear in Figure 2.15. Still, use of the 3D integral equation (IE) in forward and inverse modeling on rectilinear meshes, like EMVision® from Technoimaging®, is quite popular and used in many EM exploration situations.

The program Maxwell® from ElectroMagnetic Imaging Technology (EMIT) is also very popular and is the program most commonly used by ARC in their exploration for graphitic conductors. Maxwell offers forward modeling and inversion using a plate approximation that is quick and relatively simple to use. The conductive bodies are approximated by plates that have no finite thickness, and the electrical properties are defined by a conductivity-thickness product rather than a regional conductivity; although to some extent modeling of thick plates is possible using Maxwell. The approximation makes for very fast computations of EM forward responses, but there are some significant limits to Maxwell. For instance, the background half-space used in Maxwell's models is only able to be set to the conductivity of free-space (~10^{-8} mhos), which prevents the accurate modeling of conductors in moderately or highly conductive backgrounds like the Athabasca Basin for example. Despite this and other drawbacks, Maxwell is still a great program for quickly determining the forward response of various simple conductors. Many of the models seen in Chapter 5 and especially Chapter 6 could not be reproduced accurately using the Maxwell software and make the forward modeling method described in this thesis different, and quite valuable.

Chapter 3

Methods

3.1 Model Construction

Model construction begins with the creation of a single file that describes the location of nodes and facets within the model. This file being the key component for later meshing, the model is created in a format used by the tetrahedral mesh generator Tetgen (Si, 2015), which will be discussed in more detail in the following section. The "poly" file (.poly) describes a piecewise linear complex (PLC), and is a set of vertices, edges, polygons, and polyhedra, collectively called cells that satisfy a certain set of properties (Si, 2015; see Figure 3.1). The vertices are commonly referred to as nodes and the planes connecting nodes are called facets and can form any arbitrary polygonal shape, i.e. connect to an arbitrary number of nodes and have any 3D orientation, as long as a single facet only varies in two dimensions and has no curvature.

Figure 3.2 shows an example of a poly file for a simple cube of 10 m^3, skewed somewhat for clarity in showing the typical numbering scheme for node and facet definition. First the total number of nodes and the dimension of the model are defined and then the nodes are defined individually by their x, y, z, locations. Similarly, for the facets, first the total number is defined, then each facet is defined individually

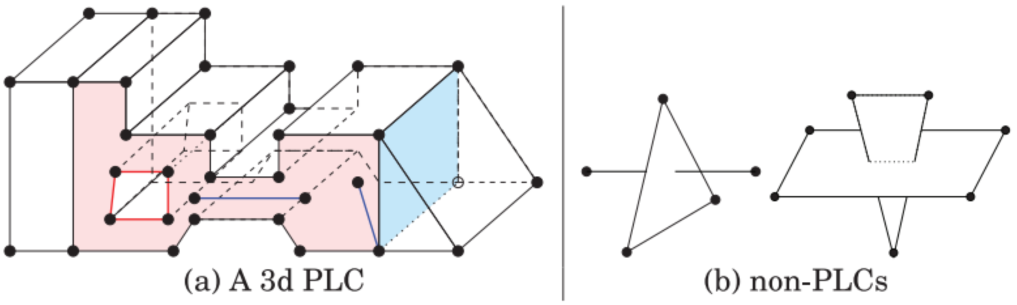

(a) A 3d PLC

(b) non-PLCs

Figure 3.1: (A) 3D piecewise linear complex. The left shaded area shows a polygon which is nonconvex and has a hole in it. It also has edges and vertices floating in it. The right area shows an interior polygon separating two sub-domains. (B) two configurations which are not PLCs. (Si, 2013).

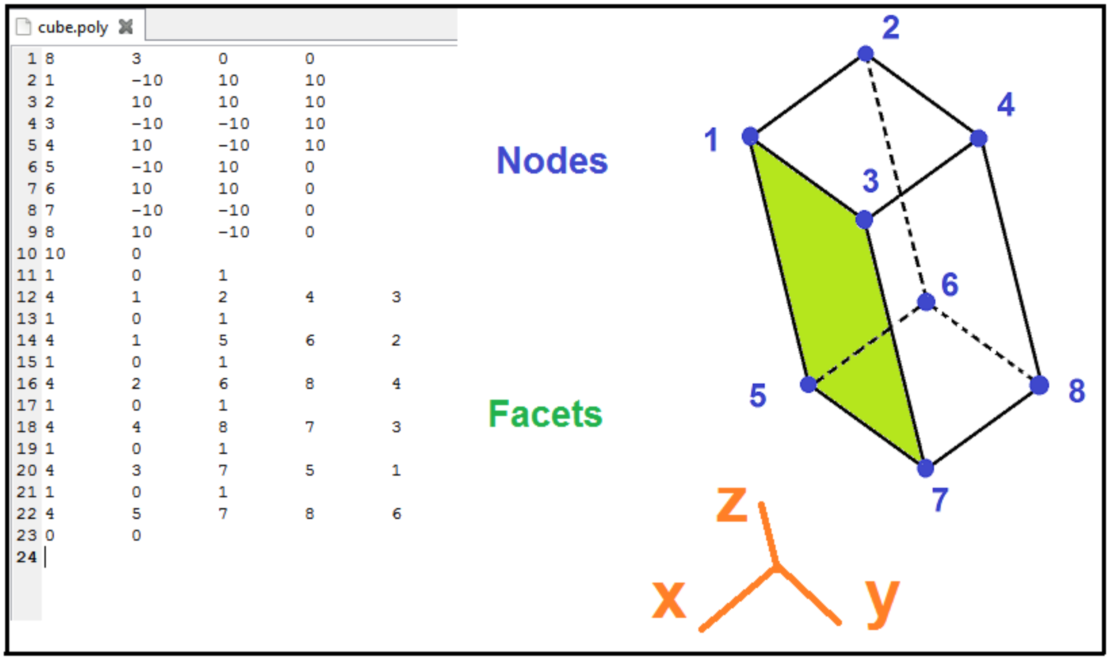

```
8         3         0         0
1         -10       10        10
2         10        10        10
3         -10       -10       10
4         10        -10       10
5         -10       10        0
6         10        10        0
7         -10       -10       0
8         10        -10       0
10        0
1         0         1
4         1         2         4         3
1         0         1
4         1         5         6         2
1         0         1
4         2         6         8         4
1         0         1
4         4         8         7         3
1         0         1
4         3         7         5         1
1         0         1
4         5         7         8         6
0         0

```

Figure 3.2: Example file cube.poly, a piecewise linear complex describing a simple cube with dimensions of 10 m^3. Nodes, in blue, are points in 3D space. Facets, in green, are planar polygons connecting nodes.

by the nodes it connects, using the same numbering used to define the nodes above. Although not necessary in this simple example, any holes in the model are defined next, and finally, the regions are defined, all in the same manner. For simple models, such as half-spaces, and simple rectangular conductors in a half-space the model can be constructed by extending the method of defining the simple cube to all parts of the model, taking care to adhere to the properties of PLCs. It is easy enough to simply write such a file in a text editor. However, this project made use of Microsoft Excel©, which allowed for the easy creation and quick variation of model dimensions. Poly files built in spreadsheets were easily extracted and put into a text format for meshing. Poly files can also be easily combined if they do not contain intersecting facets or duplicate nodes, and in such a way a variety of models can be easily built up from parts that need only be made once.

For a simple model, such as a vertical conductor in a half-space (Figure 3.3), it is first necessary to construct the outer boundaries of the model. For simplicity and the idea that during the forward solving of the electric and magnetic fields it is better to have a model volume of equal proportions (per. comm. Seyedmasoud Ansari, 2014), a cubic boundary is used. The total volume of the boundary cube can vary arbitrarily and for this project was chosen based on the EM skin depth, with the idea that the boundary should be at least eight times the skin depth from the transmitter and receiver locations. Experiments with the total model volume are discussed further in Chapter 4. The outer cube is split in half at $z = 0$ with a facet representing the Earth-air boundary. The air region is included in all models created for this project and is required for the finite-element forward-modelling method. Next, a smaller cubic volume is attached to the Earth-air boundary and extended into the subsurface to a depth corresponding to the unconformity surface in the Athabasca Basin. Depths of 400-500 metres were most often used as they correspond well to measured depths at Waterbury-Cigar Lake. This smaller volume extends for

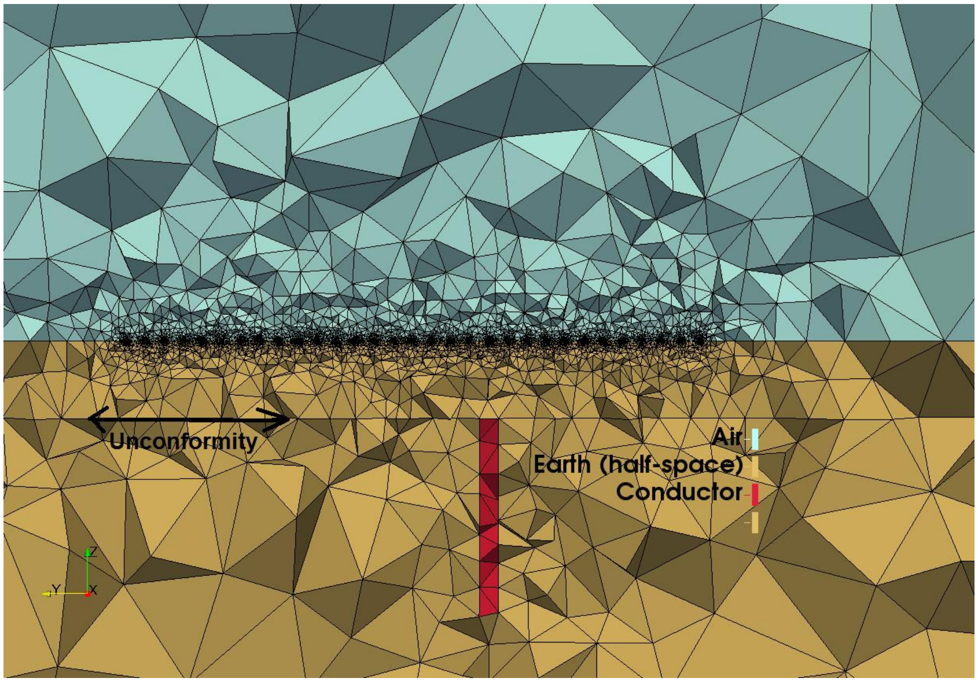

Figure 3.3: 2D slice along the x-axis of a 3D model containing a simple vertical conductor in half-space, the conductor is 10 m thick and has a depth extent of 1000 m.

8-12 km in the x and y directions and serves the purpose of having a space to alter the properties of the sediment layer, without having to extend it to the boundary of the model. Extending this box 8-12 km ensures that it is well beyond the transmitter-receiver line and will show no edge effects in the forward response. This smaller box becomes more important as we consider meshing of the model and the effect that thin layers have on increasing the overall model cells.

Finally, the conductor is attached to the unconformity surface and extended into half-space to any desired depth. It is ideal to extend the conductor to a depth greater than that from the surface to the unconformity to ensure quality late time results in the time-domain response, and this also applies to the conductor's strike length. However, as the conductor is typically thin, to reduce the total number of cells, depth and strike lengths may be shortened from what may be ideal. Even for a single conductor in half-space, when the conductor is thin, extending the strike length and depth extent to values approaching 1000 metres can quickly lead to models with over 500,000 cells.

The last step in model design is defining regions; this is done very similarly to defining the location of nodes. Region points simply contain the geophysical property value, in this case, the conductivity, of the group of cells bounded by some region in the model enclosed by facets. For example, the air, sediment, basement, and conductor are all separate regions in the model. Region points must be defined before the model is meshed and do not necessarily have to define different conductivities, they also offer the ability for volume constraint refinement of regions in chosen parts the model during meshing.

3.1.1 FacetModeller

Although all simple models seen in Chapters 4 and 5 were created as described above using a method of manually writing poly files, the more complex and geologically realistic models seen in Chapter 6 were created using the software FacetModeller which was obtained for use in this project (per. comm. Peter Lelièvre, 2014). FacetModeller allows for the visual construction of models on a series of 2D sections (Figure 3.4). Models are constructed one node and one facet at a time, but the process can be shortened with features that allow for the insertion of node and element (facet) files that were designed previously or by other means. A 3D viewer makes visualization of the model building process more manageable. When model

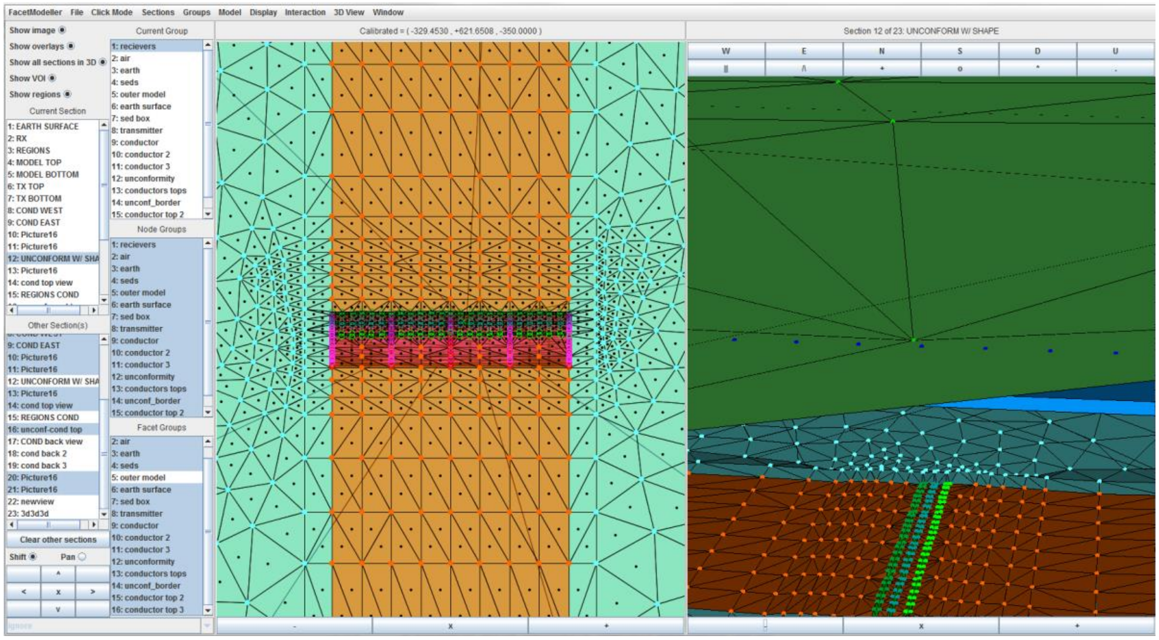

Figure 3.4: FacetModeller model building window, showing at left the 2D section where the model is constructed, and at right the 3D viewer which aids in construction of complex surfaces.

features such as the conductor or the unconformity or sediment boundaries become more complex and stray from a simple rectangular shape large rectangular and polygonal facets that allowed for quick construction of simple models are no longer viable. It is necessary instead to build these complicated features from many small triangular facets. Because triangular facets cannot have curvature, constructing models in this way avoids problems when meshing the model. On the left side of Figure 3.4 is a view of the triangular facets that form the unconformity surface for a complex model with three conductors attached to the unconformity, which itself has varied topography. The process of creating surfaces like this is time-consuming, and care must be given to creating triangular facets with internal angles that are not too small, leading to sharp needle like triangles and tetrahedra (Figure 3.5). Poor tetrahedra can cause problems in the computation of the forward results, especially

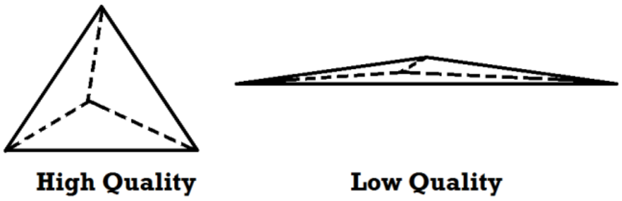

Figure 3.5: Example of high-quality and low-quality tetrahedra. Triangular facets of a high quality tetrahedra have near equal face angles and a good aspect ratio. The needle-like low-quality tetrahedra have face/internal angles that are very small.

when the iterative solve approach is used. In some cases, this cannot be avoided for surfaces such as the edges of conductors that are very thin, on the order of 10 metres, but from experience, a small amount of poor tetrahedra does not detrimentally affect the forward response, especially when using the direct solve approach that is favored by this method. Despite the time-consuming nature of the process, the software is fairly straight forward and even quite complex models can be built one feature at a time starting at the center of the model volume and building out, finishing with the boundary cube. The process of working from the center out is beneficial for a few reasons. Namely, when working from the outside in, inevitably there may be need to add facets or change a particular surface inside the model and that change has a tendency to propogate outward to all exterior surfaces, requiring the addition of facets, reconstruction of surfaces, and loss of time. The software allows for easy export of the data to a poly file that is ready for the meshing process. Also there are means to discover errors in the mesh caused by intersections and duplicates of nodes and facets. Figure 3.6 shows another valuable feature of FacetModeller in that it allows for the direct import of geologic cross sections into the 2D model building pane. Models can be built right on top of these sections allowing for a quick method of simply tracing the features with nodes and facets. By placing many similar

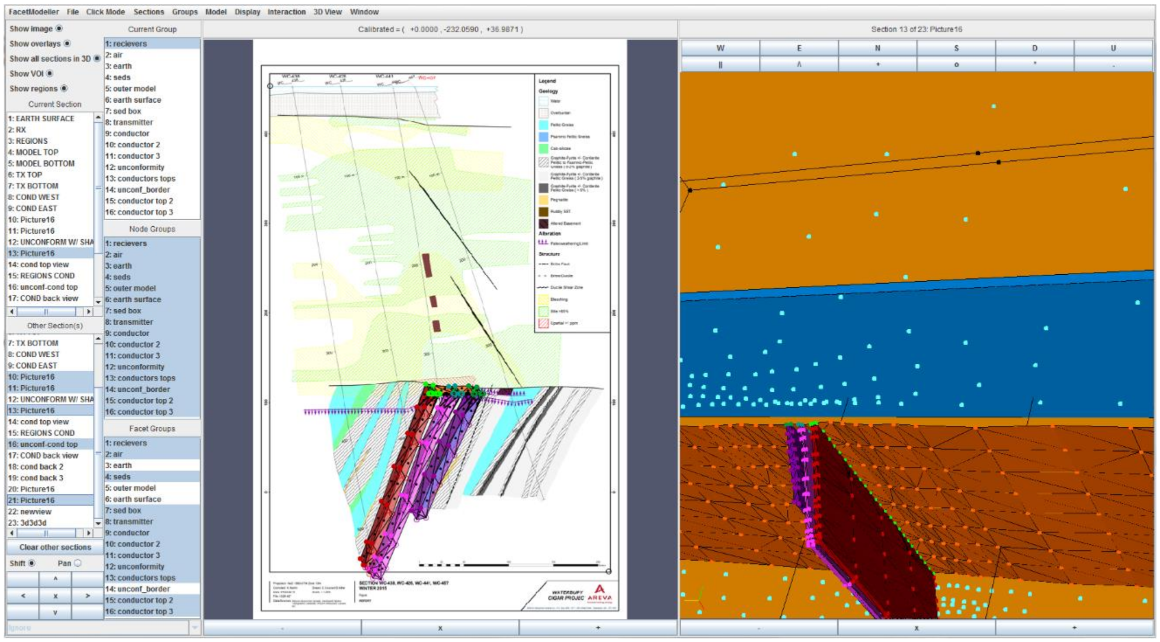

Figure 3.6: FacetModeller model building window, showing at left the ability to bring geologic cross sections directly into the model building process.

sections in series along one axis a set of 2D sections can be expanded into a 3D model with relative ease.

3.2 Model Meshing Process

Once a model is constructed the next step is creating the unstructured tetrahedral mesh that fills the model. This process is carried out with *TetGen*, a quality tetrahedral mesh generator and a 3D Delaunay triangulator (Si, 2015). This code is freely available and is fast and simple to use. TetGen takes a PLC poly file as input and outputs five new files required for the forward modeling computations. These files (.ele, .node, .neigh, .face, .edge) describe various aspects of the mesh which is created and refined by TetGen automatically. TetGen can take various input parameters which allow for different types of mesh refinement and mesh quality constraints. Standard TetGen constraints used for this project included automatic refinement to improve mesh quality by limiting tetrahedra in the mesh to those with dihedral angles greater than 14 degrees and aspect ratios greater than 1.4. Occasionally volume constraint refinement has also been used; this limits the volume of tetrahedra within a defined region of the model thereby increasing the number of tetrahedra within a region. Figure 3.7 shows the TetGen output of mesh quality statistics for a thin vertical conductor model like that shown in Figure 3.8; this is a valuable source for determining many properties of a model mesh. As the mesh is created not all tetrahedra comprising the mesh will be perfectly equant or "regular tetrahedra". The aspect ratio, face angle, and dihedral angle histograms outputted by TetGen show at a glance the quality of the mesh, and any concerns can be addressed before moving to the forward modeling computations. Notice that although the input restricts tetrahedra to having aspect ratios above 1.4, it was not successful in achieving this for this example, with the minimum in the mesh being 1.233. The minimum dihedral angle does however meet the criteria of being 14 degrees or greater.

The number of mesh cells, here 433881, governs factors such as the memory required for computation as well as the time necessary to compute the responses in the frequency domain. From experience, models with cells in the 200,000 – 500,000 cell range typically run in 1 - 2 hours per frequency with little issue using a 64 GB computing node. Models with 500,000 – 800,000 cells take longer: 3 - 7 hours per frequency. Models approaching 2 million cells have been run with the iterative solve version of the forward modeling code, and are successful but quite slow, with the solve phase of the forward modeling code alone requiring over 10 hours per frequency.

Using the direct solve version of the code, the limit is closer to 1 million cells, and computation of a model that large requires an enormous amount of available RAM, approaching 80-100GB. The number of model cells is an ever-present concern when designing complex models and/or batches of simple models and will be discussed further in the following sections.

TetGen is also a useful if not required tool for identifying problems in mesh design such as intersecting facets and duplicate facets or nodes. TetGen will not run if the poly file used as input is not by definition a PLC. There are also options to help identify the source of the problem, which can sometimes be a complicated task even when dealing with relatively simple models.

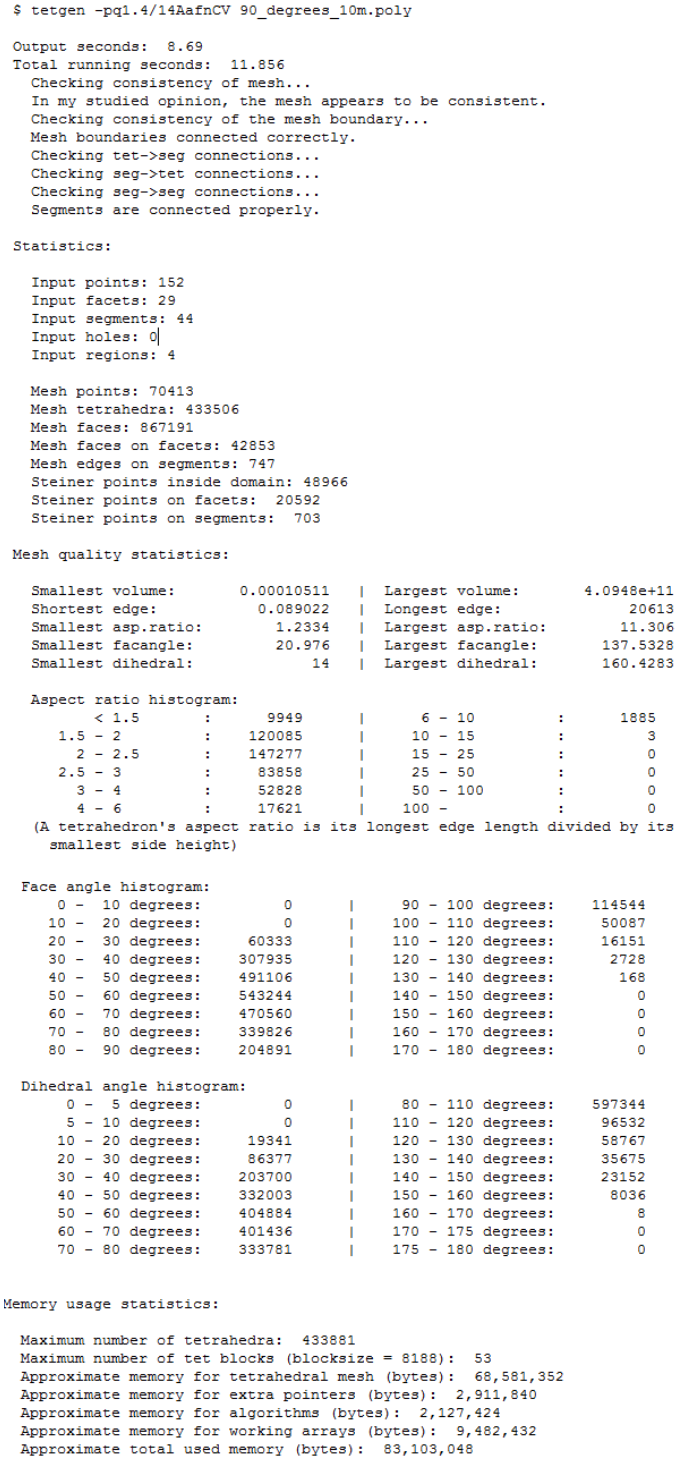

```
 $ tetgen -pq1.4/14AafnCV 90_degrees_10m.poly

 Output seconds:  8.69
 Total running seconds:  11.856
   Checking consistency of mesh...
   In my studied opinion, the mesh appears to be consistent.
   Checking consistency of the mesh boundary...
   Mesh boundaries connected correctly.
   Checking tet->seg connections...
   Checking seg->tet connections...
   Checking seg->seg connections...
   Segments are connected properly.

 Statistics:

   Input points: 152
   Input facets: 29
   Input segments: 44
   Input holes: 0
   Input regions: 4

   Mesh points: 70413
   Mesh tetrahedra: 433506
   Mesh faces: 867191
   Mesh faces on facets: 42853
   Mesh edges on segments: 747
   Steiner points inside domain: 48966
   Steiner points on facets:  20592
   Steiner points on segments:  703

 Mesh quality statistics:

   Smallest volume:       0.00010511   |  Largest volume:       4.0948e+11
   Shortest edge:           0.089022   |  Longest edge:              20613
   Smallest asp.ratio:        1.2334   |  Largest asp.ratio:        11.306
   Smallest facangle:         20.976   |  Largest facangle:       137.5328
   Smallest dihedral:             14   |  Largest dihedral:       160.4283

   Aspect ratio histogram:
          < 1.5       :      9949      |      6 - 10         :      1885
      1.5 - 2         :    120085      |     10 - 15         :         3
        2 - 2.5       :    147277      |     15 - 25         :         0
      2.5 - 3         :     83858      |     25 - 50         :         0
        3 - 4         :     52828      |     50 - 100        :         0
        4 - 6         :     17621      |    100 -            :         0
   (A tetrahedron's aspect ratio is its longest edge length divided by its
     smallest side height)

  Face angle histogram:
      0 -  10 degrees:         0      |     90 - 100 degrees:    114544
     10 -  20 degrees:         0      |    100 - 110 degrees:     50087
     20 -  30 degrees:     60333      |    110 - 120 degrees:     16151
     30 -  40 degrees:    307935      |    120 - 130 degrees:      2728
     40 -  50 degrees:    491106      |    130 - 140 degrees:       168
     50 -  60 degrees:    543244      |    140 - 150 degrees:         0
     60 -  70 degrees:    470560      |    150 - 160 degrees:         0
     70 -  80 degrees:    339826      |    160 - 170 degrees:         0
     80 -  90 degrees:    204891      |    170 - 180 degrees:         0

  Dihedral angle histogram:
       0 -  5 degrees:         0      |     80 - 110 degrees:    597344
       5 - 10 degrees:         0      |    110 - 120 degrees:     96532
      10 - 20 degrees:     19341      |    120 - 130 degrees:     58767
      20 - 30 degrees:     86377      |    130 - 140 degrees:     35675
      30 - 40 degrees:    203700      |    140 - 150 degrees:     23152
      40 - 50 degrees:    332003      |    150 - 160 degrees:      8036
      50 - 60 degrees:    404884      |    160 - 170 degrees:         8
      60 - 70 degrees:    401436      |    170 - 175 degrees:         0
      70 - 80 degrees:    333781      |    175 - 180 degrees:         0


Memory usage statistics:

  Maximum number of tetrahedra:  433881
  Maximum number of tet blocks (blocksize = 8188):  53
  Approximate memory for tetrahedral mesh (bytes):  68,581,352
  Approximate memory for extra pointers (bytes):  2,911,840
  Approximate memory for algorithms (bytes):  2,127,424
  Approximate memory for working arrays (bytes):  9,482,432
  Approximate total used memory (bytes):  83,103,048
```

Figure 3.7: TetGen mesh statistics output for a vertical conductor in half-space model.

3.3 Mesh Refinement Methods

Before moving on to the forward modeling, it is important to cover mesh refinement methods which have evolved greatly over the course of this project and are still an active area of research. Mesh refinement can be thought of as methods of increasing the density of tetrahedral cells within a specific region of the model. Mesh refinement is most important near the receiver locations, and for a time it was thought to be at least somewhat important near transmitter locations and possibly deeper in the subsurface near the conductor. Methods of refining the mesh vary from the insertion of subsurface boxes of varied dimensions, insertion of nodes, insertion of regular tetrahedra, and volume constraint refinement.

Figure 3.8 shows many of the early refinement methods used in the research. "Boxes" or cubes of different sizes were placed in the model before meshing with TetGen to refine some combination of the shallow or deep subsurface and always near the receiver locations. At receiver locations, small boxes on the order of 1 – $3m^3$ were placed 1 – 3 m above their locations on the Earth-air boundary at which the receiver measurement locations were placed. For the shallow subsurface a roughly 10 – 50 m box was used to refine the region below the transmitter location(s). Finally, a 100 m thick box was used to give coarse refinement to the subsurface at depths of 400 – 500 metres. This method of box refinement was successful but cumbersome to employ when creating models manually, especially for multiple receiver locations which each required a full cube of facets and nodes. Figure 3.9 shows the next evolution in mesh refinement: the receiver refinement boxes were replaced by single nodes which provided nearly identical refinement with much less effort. A thin

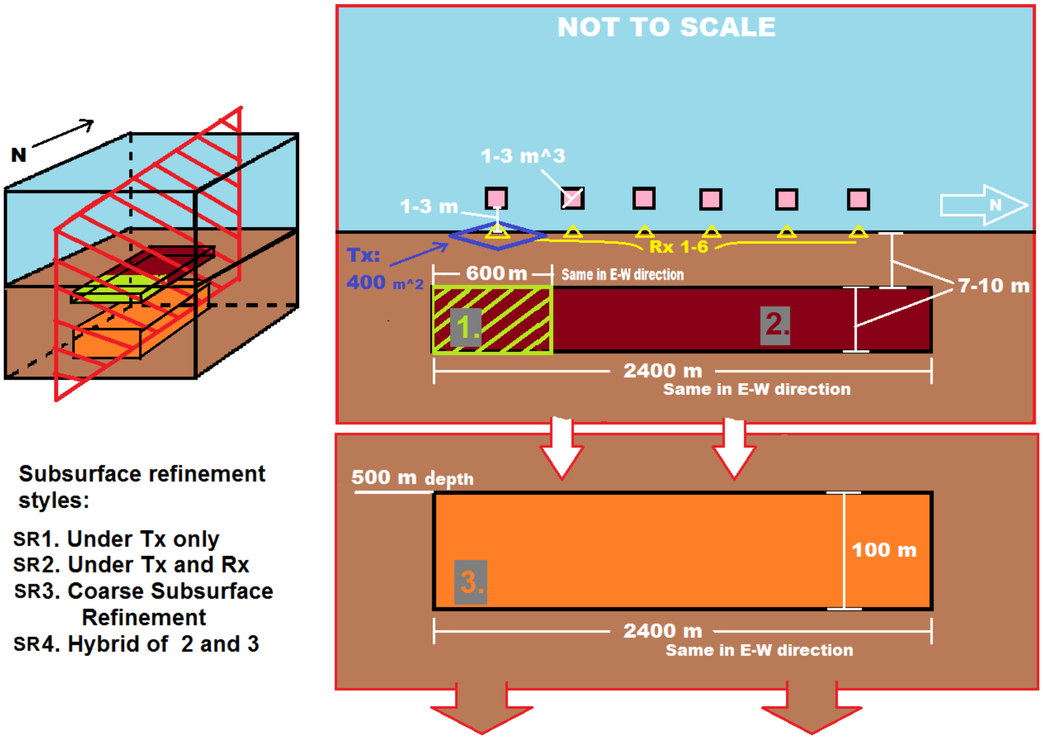

Figure 3.8: Examples of early box style mesh refinement methods at various depths and positions within the model.

subsurface transmitter refinement box was still used, and some degree of volume constraint refinement was implemented in the sediment box and the distant half-space. These changes did in fact improve results to some degree (see Appendix F), but use of the volume constraint needs to be moderate otherwise it will quickly increase the number of cells in the mesh. Over time it has been realized through this research and that of others (per. comm. Seyedmasoud Ansari, Michael Dunham, Chelsea Squires, 2015-2016) that refinement is indeed very important near receivers, but not as necessary elsewhere. Figure 3.10 shows an x-axis cutaway through a 100m thick vertical conductor model mesh made using the most recent refinement methods. A code was obtained (per. comm. Seyedmasoud Ansari, 2016), that allowed for the

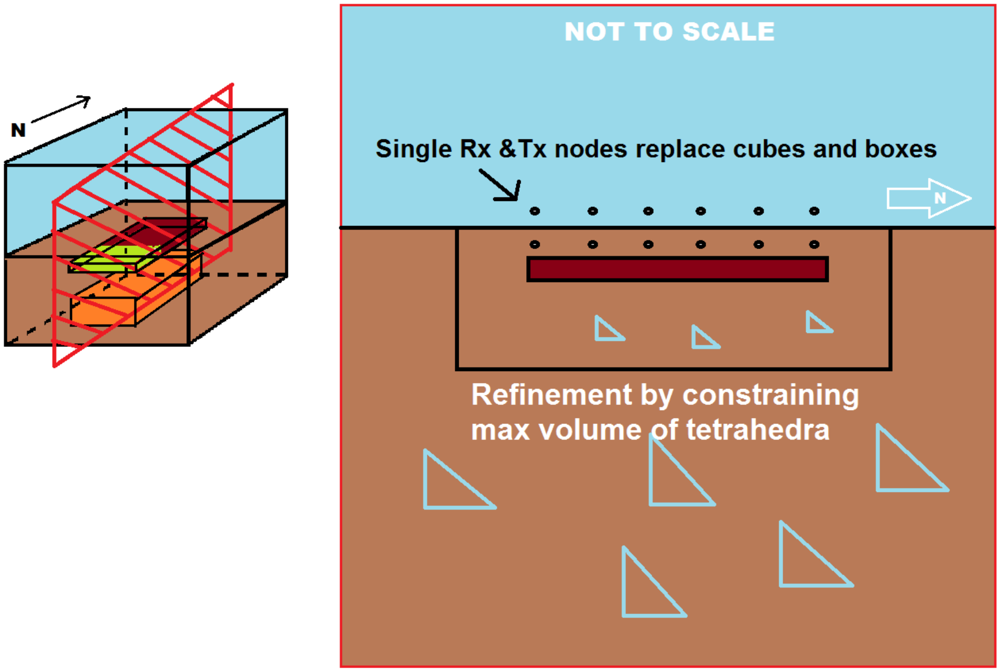

Figure 3.9: Example of improved mesh refinement methods. Boxes have been replaced by inserted nodes and volume constrain refinement.

insertion of regular tetrahedra around the receiver location, i.e. the measurement location is exactly at the center of the tetrahedral cell. Use of tetrahedra over nodes alone was thought to be the ideal way to refine receiver locations for accurate results for the EM fields in the forward modeling calculations (per. comm. Seyedmasoud Ansari, 2015). To some degree this is true, and modest improvement over insertion of nodes alone was achieved, but this was highly dependent on the edge length chosen for the tetrahedra surrounding the receivers. Edge lengths between 0.5 and 1 m proved most effective for this work, with longer edge lengths being about as effective as a single node at the receiver location. Use of the regular tetrahedra method increased the total model cells by only up to 80,000 cells even for small edge lengths, so it is a process worth using. The major improvement was the confirmation that transmitter refinement boxes used previously in mesh refinement were not necessary and did not affect results at all. Eliminating any specific transmitter refinement could remove close to 200,000 cells from even simple conductor models. Overall the idea of minimalism in mesh refinement has made improvements not only in the calculated forward response, but in decreasing the runtime of models of all complexity levels, especially the smaller models that need to be run multiple times for a variety of parameters. A decrease from only 500,000 to 300,000 models cells offers a substantial improvement to total runtime over all model frequencies; it amounts to a complete time-domain response in less than a day vs. 2-3 days, which is significant.

As models become more complex, the problem in meshing becomes that of finding ways to minimize the refinement that is naturally caused by the features of complex shape, thin bodies, angular bodies or geologic pinch-outs, etc. in the model. These features can all require vast amounts of cells in the mesh, and when you begin to combine these features into a single model the problem only compounds. Care must be taken in finding ways to accurately represent the features of the desired model while controlling the number of cells created in the TetGen process.

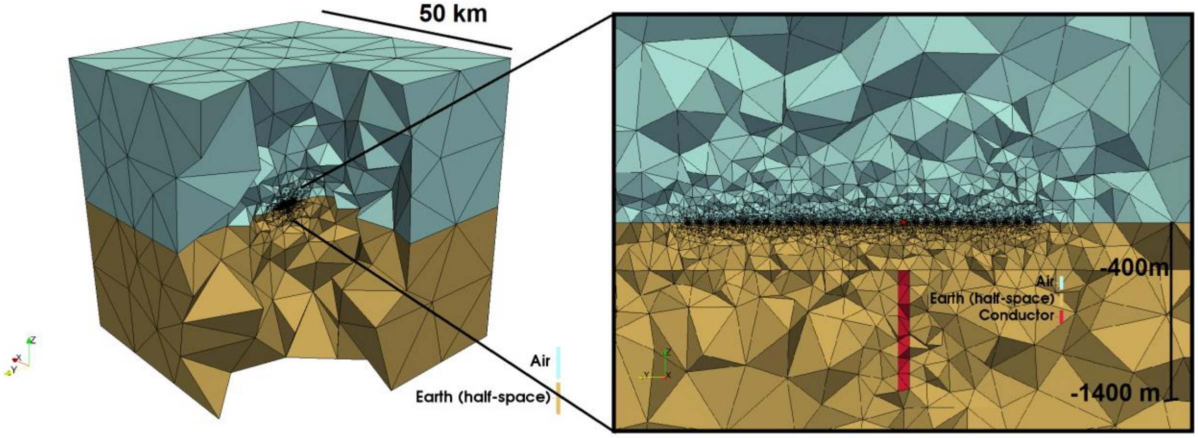

Figure 3.10: Example of a 3D model mesh created using current methods of minimal refinement. Regular tetrahedra replace nodes at receiver locations; no other refinement is used. The conductor is 100 m thick with 1000 m depth extent.

3.4 Forward Modeling

Forward modeling is carried out in the frequency domain using the 3D finite-element code CSEM3DFWD of Ansari & Farquharson (2014). The FORTRAN based code can solve the system of equations resulting from the finite element method either iteratively or directly, and both methods were explored in this project. The iterative method has the benefit of requiring less memory, but there are also many drawbacks including longer solution times, higher possibility of an incorrect solution, and the fact that each transmitter-receiver pair must be solved for independently, which reduces the ability to model long survey lines with many transmitter locations. The direct solve method does require more memory to solve an equivalently sized mesh but has the advantage of being faster and can provide the solutions for multiple transmitters at not much more cost than for a single transmitter. This change alone drastically reduced the total solve times for a time-domain model over using the iterative solver, and after the direct solve version of the code became available (per. comm. Seyedmasoud Ansari, 2015), the iterative version was no longer used. However, because both methods were used in this project, in the following sections descriptions of both the iterative and direct solvers will be provided.

3.4.1 CSEM3DFWD

3.4.1.1 General Use for Iterative Solve

Regardless of the choice of iterative or direct solving, models must be prepared in the same way. Use of the CSEM3DFWD code is relatively simple but requires a few files that must be set up properly to ensure a successful run of the code. The five mesh files output from TetGen after meshing are required (.ele, .node, .neigh, .face, .edge). Two files, csem3dfwd.in and physical_property.in, are also both required and often must be updated for each model. Figure 3.11 shows the two input files, and it is worth describing their content. The csem3dfwd.in file (3.11 top) is used to define the major parameters of the model and some specifics of the solving routine. First, the frequency of the desired response is defined (see (i) in Figure 3.11). Models in this project have used 20-60 frequency forward responses to construct a single time-domain result, and each frequency response requires its own in-file. Next, the source type is defined (ii in Figure 3.11) the combination seen here (3 2 3) indicates a z-directed moving loop source. Below that the source location and dimensions of the transmitter coil are defined (iii in Figure 3.11). If the survey being modeled is a moving loop survey, this defines the initial transmitter location, and the subsequent locations are defined below by their center points, using the same dimensions define here. Current and magnetic moment values of 25 A and 400,000 $\mathrm{A} \cdot m^2$ (iv.) are chosen to be similar to field TDEM systems used in the Athabasca Basin. The magnetic moment here, and for most geophysical equipment, is defined simply as the current in the transmitter multiplied by the area of the transmitter loop and the number of wire turns (NIA). Next, the model boundary values (Figure 3.11, v) are given for the *x, y,* and *z* directions. Iterative solver type (1) indicates the use of GMRES (Figure 3.11, vi) or generalized minimum residual method (Saad, 2003); this is never changed for standard use of the code. The number of iterations (Figure 3.11, vii) is typically set to 1000 for use in this project. However, this is dependent on the model and the level of decrease in the residual norm of the solution that is desired. Tolerances (Figure 3.11, viii) of the solver indicate again what level of decrease in the residual norm of the solution is desired before the code will stop iterations. This is set to a very low value of 10^{-17} to ensure the code will only stop before 1000 iterations if the solution is of good quality. Low-frequency models tend to reach this value before 1000 iterations, higher frequency models typically do not. The Krylov subspace dimension is an aspect of the iterative solver that affects things like the solution time, the decrease in the residual norm, and memory required for solving the system. Krylov methods are used to solve large sparse systems of linear equations (e.g. Ipsen & Meyer 1998), the specifics of which are beyond the scope of this thesis, but the ability to alter the dimension of the subspace is a useful tool in practice. Some effects of altering the Krylov subspace dimension on half-space model results can be found in Appendix B. Similar results may be obtained with the use of high

csem3dfwd.in

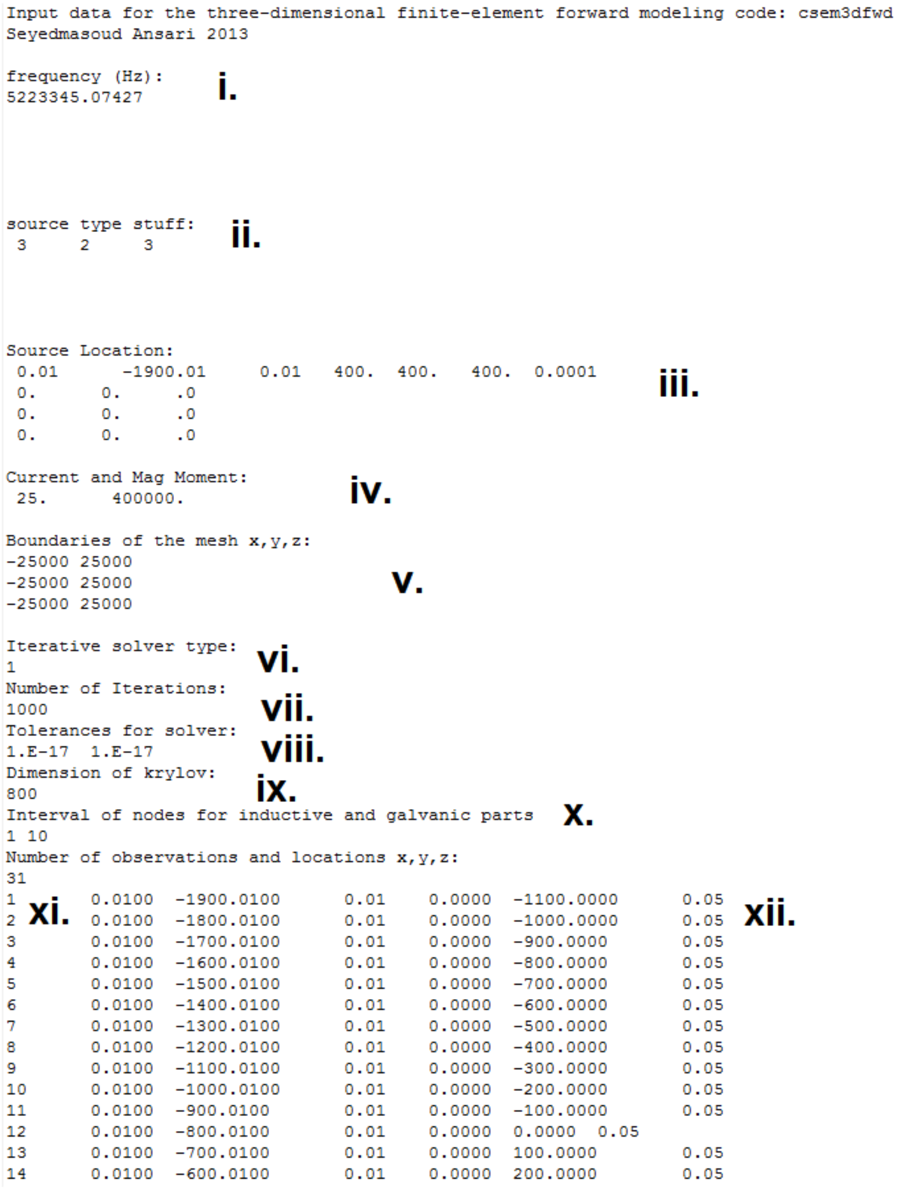

```
Input data for the three-dimensional finite-element forward modeling code: csem3dfwd
Seyedmasoud Ansari 2013

frequency (Hz):
5223345.07427




source type stuff:
 3     2     3




Source Location:
 0.01      -1900.01     0.01   400.  400.   400.  0.0001
 0.      0.     .0
 0.      0.     .0
 0.      0.     .0

Current and Mag Moment:
 25.      400000.

Boundaries of the mesh x,y,z:
-25000 25000
-25000 25000
-25000 25000

Iterative solver type:
1
Number of Iterations:
1000
Tolerances for solver:
1.E-17  1.E-17
Dimension of krylov:
800
Interval of nodes for inductive and galvanic parts
1 10
Number of observations and locations x,y,z:
31
1       0.0100  -1900.0100      0.01    0.0000  -1100.0000      0.05
2       0.0100  -1800.0100      0.01    0.0000  -1000.0000      0.05
3       0.0100  -1700.0100      0.01    0.0000  -900.0000       0.05
4       0.0100  -1600.0100      0.01    0.0000  -800.0000       0.05
5       0.0100  -1500.0100      0.01    0.0000  -700.0000       0.05
6       0.0100  -1400.0100      0.01    0.0000  -600.0000       0.05
7       0.0100  -1300.0100      0.01    0.0000  -500.0000       0.05
8       0.0100  -1200.0100      0.01    0.0000  -400.0000       0.05
9       0.0100  -1100.0100      0.01    0.0000  -300.0000       0.05
10      0.0100  -1000.0100      0.01    0.0000  -200.0000       0.05
11      0.0100  -900.0100       0.01    0.0000  -100.0000       0.05
12      0.0100  -800.0100       0.01    0.0000  0.0000  0.05
13      0.0100  -700.0100       0.01    0.0000  100.0000        0.05
14      0.0100  -600.0100       0.01    0.0000  200.0000        0.05
```

physical_property.in

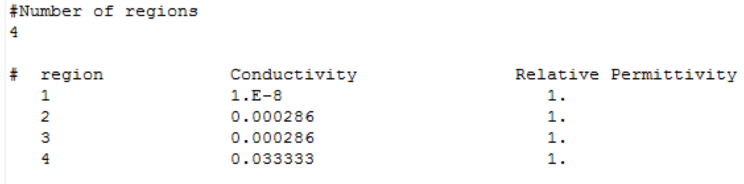

```
#Number of regions
4

#  region             Conductivity              Relative Permittivity
   1                  1.E-8                        1.
   2                  0.000286                     1.
   3                  0.000286                     1.
   4                  0.033333                     1.
```

Figure 3.11: Example input files for CSEM3DFWD forward modeling code.

or low values, but for models with many cells, lowering the subspace dimension may help the model to run more successfully when memory is a concern. For this project, a moderate subspace dimension of 800 was used as the memory was often not a major concern when using the iterative solver, which was primarily used for half-space modeling. The node interval for inductive and galvanic parts (Figure 3.11, x) is an additional component of CSEM3DFWD that is not used in this research. Finally, the transmitter (Figure 3.11, xi) and receiver (Figure 3.11, xii) locations are defined. For moving loop surveys each unique transmitter and receiver pair must be defined. For a fixed loop survey, it is sufficient to define the transmitter location in the section above (Figure 3.11, xiii) and define unique receiver locations in this section.

The second file (Figure 3.11, bottom), physical_property.in, is relatively simple and is used to define the conductivity in Siemens per metre (S/m) of the regions previously defined at the end of model construction. Although this thesis tends to refer to the electrical properties of the subsurface as resistivity, which is often the convention in mineral exploration, CSEM3DFWD uses conductivity (1/resistivity), and it is important to note and differentiate the two. Each region is assigned a conductivity value and a magnetic permeability value. For purposes of this research the magnetic permeability was kept constant at its free-space value for all models.

3.4.1.2 Direct Solve

Transition to use of the direct solve version of CSEM3DFWD occurred during the initial stages of modeling simple conductors in half-spaces (Chapter 5) and was done for a few reasons. First it was thought that use of the direct solve code had the potential for increased accuracy of results over the iterative version due to the decrease in sensitivity of the solution to mesh quality. This change was thought to be particularly important for improving the frequency-domain response at higher frequencies (per comm. Seyedmasoud Ansari, 2015). Another major benefit of the direct approach is the ability to calculate the solution for all transmitter-receiver (Tx-Rx) pairs simultaneously using the same decomposition of the finite-element matrix as opposed to the iterative method which required separate calculations for each transmitter, offering a significant decrease in total computation time for each time-domain response. Depending on the number of model cells, each frequency-domain response can take multiple hours to solve, and when using the iterative code the number of individual solves is equivalent to the 40 (80 total) frequencies multiplied by the number of transmitter locations (i.e. 80 x (11, 31, …, n)). This can quickly result in a situation where a single time-domain response could potentially take weeks or months to run, which is unacceptable. The direct solve code requires only 40 (80 total) solves of the forward code with any arbitrary number of transmitters. The direct solve approach is also in general faster than the iterative approach even for a single transmitter location, which again speeds up the modeling process by one or more hours per solution. Use of the direct solve approach became a necessity in this project to create time-domain results efficiently, and arguably modeling large Slingram-style surveys promptly may not have been possible at all using the iterative method.

The potential downside to the direct approach is that more memory is required to compute the solution by comparison to the iterative approach. However, on a 64 GB RAM computing node with 30 GB swap memory, this only becomes a concern when models contain close to 1 million cells. However, this can be mitigated with intelligent model design and adjustments to the mesh quality requirements used with TetGen in the meshing process. Because mesh quality is less important with the direct solve code, it is possible to decrease the quality of even modestly complex models to a degree that they can be computed and still offer accurate results (See Appendix E). Overall the transition to use of the direct solve version of the code was a major improvement to this forward-modeling process.

Set-up of the direct solve code is done in the same manner as for the iterative solver above, with the exception that sections of the csem3dfwd.in file concerning the iterations, tolerances, and Krylov dimension (Figure 3.11 vi-ix) have no effect and are of no concern. The direct solve CSEM3DFWD code makes use of the Multifrontal Massively Parallel sparse direct Solver (MUMPS; Amistoy et al., 2006) to compute the forward solution and there are no additional inputs necessary for this version of the code.

3.4.2 Total Field Solutions and Calculation of the Secondary Field

CSEM3DFWD outputs the total magnetic field (**H**) in amps/metre for each receiver location specified in the input file. Figure 3.12 shows the standard output file ‘obs_magneticfield.txt’ for a Slingram-style survey of 31 Tx-Rx locations over a conductor in half-space model at a single transmitter frequency. The output contains the *x*-*y*-*z* locations of the receiver as well as the real and imaginary (in-phase and quadrature) parts of all three components of **H** (H_x, H_y, H_z). All components of the response are examined, but the **H**z component is of particular importance in EM exploration. The crossline component, whether it be H_x or H_y is also of moderate importance in exploration situations. The inline component of the response may contain some valuable information but is typically noisy and of limited use. The secondary magnetic field, $\mathbf{H}_s$, is the typical final data type in actual field situations, and for forward modeling programs it is imperative to calculate this value when modeling anything besides simple half-spaces. The secondary field is that of the earth or conductors only, and does not contain the transmitted primary field. To obtain the secondary field using this forward modeling method it is necessary to compute the forward response for two versions of each model mesh, each at 40 frequencies. The model for the first 40 frequency responses contains the various resistivity values of the conductor and in later models the other geologic features, and the background resistivity of the half-space. These 40 frequency responses thus form the total magnetic field response of the model in the time domain. The model for the second group of 40 frequencies contains only the half-space resistivity in all subsurface model cells and the computed response corresponds to the half-space total-field response. By a simple subtraction of the half-space response from the full total-field response,

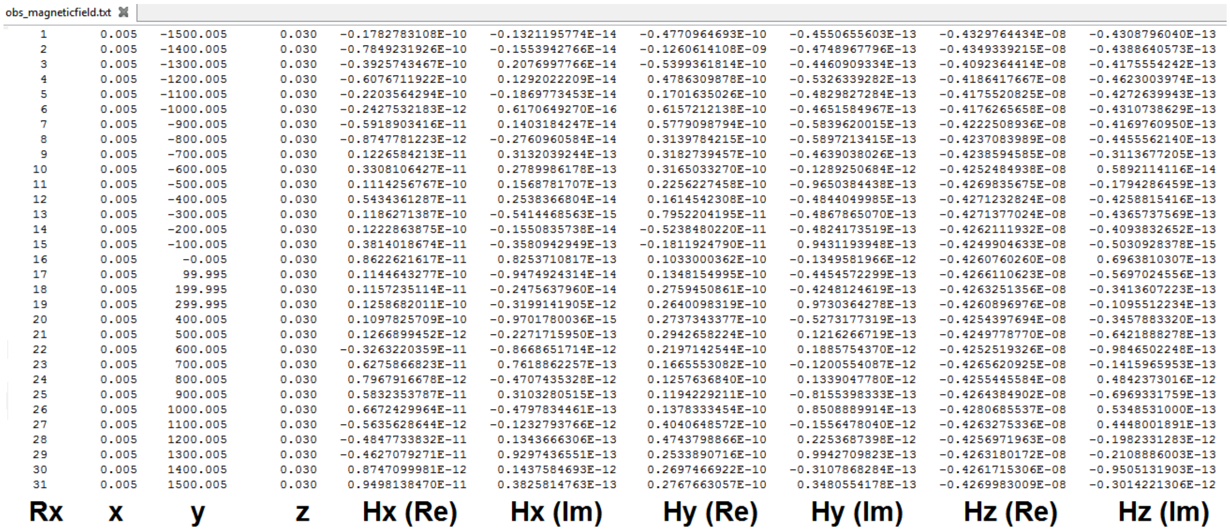

```
 1   0.005  -1500.005   0.030  -0.1782783108E-10  -0.1321195774E-14  -0.4770964693E-10  -0.4550655603E-13  -0.4329764434E-08  -0.4308796040E-13
 2   0.005  -1400.005   0.030  -0.7849231926E-10  -0.1553942766E-14  -0.1260614108E-09  -0.4748967796E-13  -0.4349339215E-08  -0.4388640573E-13
 3   0.005  -1300.005   0.030  -0.3925743467E-10   0.2076997766E-14  -0.5399361814E-10  -0.4460909334E-13  -0.4092364414E-08  -0.4175554242E-13
 4   0.005  -1200.005   0.030  -0.6076711922E-10   0.1292022209E-14   0.4786309878E-10  -0.5326339282E-13  -0.4186417667E-08  -0.4623003974E-13
 5   0.005  -1100.005   0.030  -0.2203564294E-10  -0.1869773453E-14   0.1701635026E-10  -0.4829827284E-13  -0.4175520825E-08  -0.4272639943E-13
 6   0.005  -1000.005   0.030  -0.2427532183E-12   0.6170649270E-16   0.6157212138E-10  -0.4651584967E-13  -0.4176265658E-08  -0.4310738629E-13
 7   0.005   -900.005   0.030  -0.5918903416E-11   0.1403184247E-14   0.5779098794E-10  -0.5839620015E-13  -0.4222508936E-08  -0.4169760950E-13
 8   0.005   -800.005   0.030  -0.8747781223E-12  -0.2760960584E-14   0.3139784215E-10  -0.5897213415E-13  -0.4237083989E-08  -0.4455562140E-13
 9   0.005   -700.005   0.030   0.1226584213E-11   0.3132039244E-13   0.3182739457E-10  -0.4639038026E-13  -0.4238594585E-08  -0.3113677205E-13
10   0.005   -600.005   0.030   0.3308106427E-11   0.2789986178E-13   0.3165033270E-10  -0.1289250684E-12  -0.4252484938E-08   0.5892114116E-14
11   0.005   -500.005   0.030   0.1114256767E-10   0.1568781707E-13   0.2256227458E-10  -0.9650384438E-13  -0.4269835675E-08  -0.1794286459E-13
12   0.005   -400.005   0.030   0.5434361287E-11   0.2538366804E-14   0.1614542308E-10  -0.4844049985E-13  -0.4271232824E-08  -0.4258815416E-13
13   0.005   -300.005   0.030   0.1186271387E-10  -0.5414468563E-15   0.7952204195E-11  -0.4867865070E-13  -0.4271377024E-08  -0.4365737569E-13
14   0.005   -200.005   0.030   0.1222863875E-10  -0.1550835738E-14  -0.5238480220E-11  -0.4824173519E-13  -0.4262111932E-08  -0.4093832652E-13
15   0.005   -100.005   0.030   0.3814018674E-11  -0.3580942949E-13  -0.1811924790E-11   0.9431193948E-13  -0.4249904633E-08  -0.5030928378E-15
16   0.005     -0.005   0.030   0.8622621617E-11   0.8253710817E-13   0.1033000362E-10  -0.1349581966E-12  -0.4260760260E-08   0.6963810307E-13
17   0.005     99.995   0.030   0.1144643277E-10  -0.9474924314E-14   0.1348154995E-10  -0.4454572299E-13  -0.4266110623E-08  -0.5697024556E-13
18   0.005    199.995   0.030   0.1157235114E-11  -0.2475637960E-14   0.2759450861E-10  -0.4248124619E-13  -0.4263251356E-08  -0.3413607223E-13
19   0.005    299.995   0.030   0.1258682011E-10  -0.3199141905E-12   0.2640098319E-10   0.9730364278E-13  -0.4260896976E-08  -0.1095512234E-13
20   0.005    400.005   0.030   0.1097825709E-10  -0.9701780036E-15   0.2737343377E-10  -0.5273177319E-13  -0.4254397694E-08  -0.3457883320E-13
21   0.005    500.005   0.030   0.1266899452E-12  -0.2271715950E-13   0.2942658224E-10   0.1216266719E-13  -0.4249778770E-08  -0.6421888278E-13
22   0.005    600.005   0.030  -0.3263220359E-11  -0.8668651714E-12   0.2197142544E-10   0.1885754370E-12  -0.4252519326E-08  -0.9846502248E-13
23   0.005    700.005   0.030   0.6275866823E-11   0.7618862257E-13   0.1665553082E-10  -0.1200554087E-12  -0.4265620925E-08  -0.1415965953E-13
24   0.005    800.005   0.030   0.7967916678E-12  -0.4707435328E-12   0.1257636840E-10   0.1339047780E-12  -0.4255445584E-08   0.4842373016E-12
25   0.005    900.005   0.030   0.5832353787E-11   0.3103280515E-13   0.1194229211E-10  -0.8155398333E-13  -0.4264384902E-08  -0.6969331759E-13
26   0.005   1000.005   0.030   0.6672429964E-11  -0.4797834461E-13   0.1378333454E-10   0.8508889914E-13  -0.4280685537E-08   0.5348531000E-13
27   0.005   1100.005   0.030  -0.5635628644E-12  -0.1232793766E-12   0.4040648572E-10  -0.1556478040E-12  -0.4263275336E-08   0.4448001891E-13
28   0.005   1200.005   0.030  -0.4847733832E-11   0.1343666306E-13   0.4743798866E-10   0.2253687398E-12  -0.4256971963E-08  -0.1982331283E-12
29   0.005   1300.005   0.030  -0.4627079271E-11   0.9297436551E-13   0.2533890716E-10   0.9942709823E-13  -0.4263180172E-08  -0.2108886003E-13
30   0.005   1400.005   0.030   0.8747099981E-12   0.1437584693E-12   0.2697466922E-10  -0.3107868284E-13  -0.4261715306E-08  -0.9505131903E-13
31   0.005   1500.005   0.030   0.9498138470E-11   0.3825814763E-13   0.2767663057E-10   0.3480554178E-13  -0.4269983009E-08  -0.3014221306E-12
Rx     x        y        z        Hx (Re)            Hx (Im)            Hy (Re)            Hy (Im)            Hz (Re)            Hz (Im)
```

Figure 3.12: Example output file of CSEM3DFWD showing the frequency-domain magnetic field response at a single transmitter frequency for typical Slingram-style survey layout of 31 transmitter-receiver locations.

the secondary field of the conductor can be obtained. In actual field practices, the secondary field is obtained directly. However, in synthetic forward modeling cases like this, it can be necessary to subtract the response for the background half-space resistivity. Testing has shown that it is necessary to compute a unique half-space or background version of each model using the same mesh as for the full model. The difference in meshing between models makes the use of some generic common half-space model for computation of the secondary field problematic and commonly leads to errors or an inadequate removal of the background field.

The secondary field calculation can be carried out either in the frequency-domain before the time-domain transform, or in the time-domain after the transform.

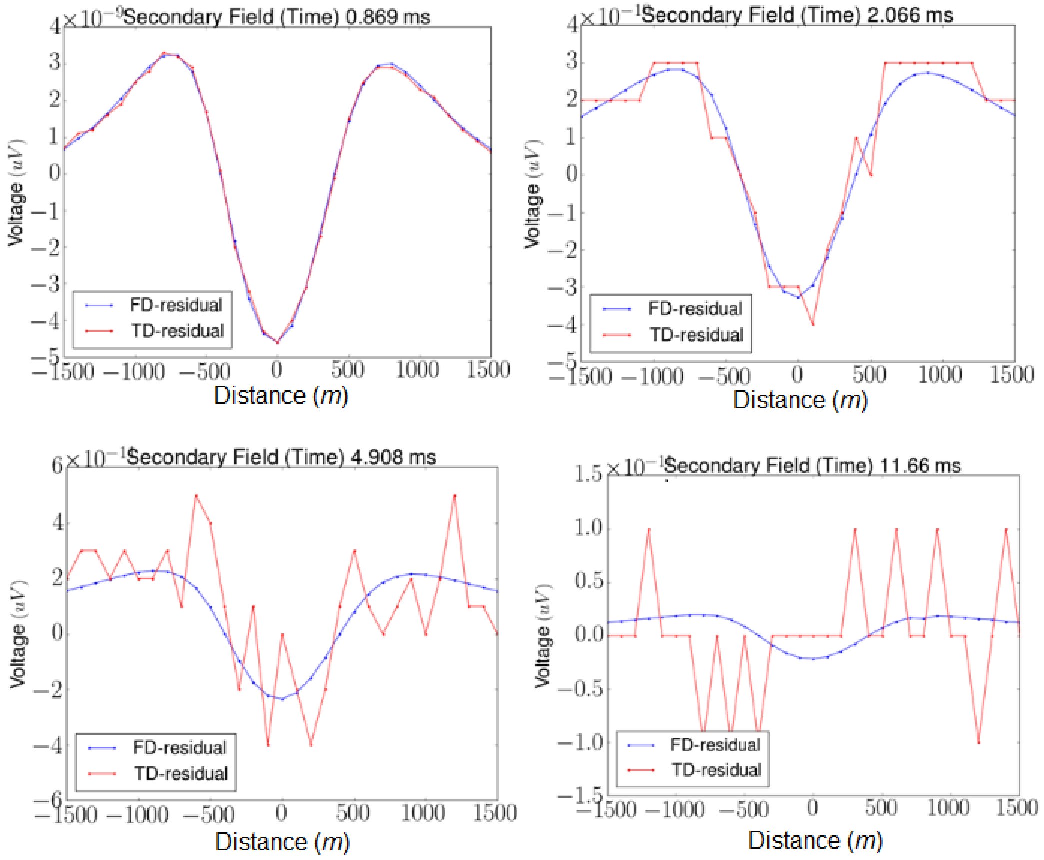

Figure 3.13: Time-domain secondary magnetic field vs. distance at four time gates illustrating the benefit of computing the secondary field in the frequency domain (blue) over computing it in the time domain (red), for this forward modeling method.

Experience has shown that calculating the secondary field in the frequency domain before the transform improves the time-domain result quite drastically especially at later times. Figure 3.13 shows a set of time-domain response vs. distance plots for just four of the 29 time gates typically used in transformation. In blue is the result when the secondary field is computed in the frequency domain before the transform, and in red is the result when it is computed in the time-domain after the transform. The benefit of calculating the secondary field before the transform is clear. However this issue may be due to a discrepancy in numerical precision between the forward modeling and time-domain transform codes, meaning the time-domain transform code has less precision than the CSEM3DFWD. The computation of the secondary field in this way is thus very important for this project and this forward modeling method, but perhaps not necessarily in general.

3.5 Time-Domain Transform

The time-domain transform is carried out using a subroutine (per. comm. Colin Farquharson, 2014) of the 1-dimensional (1D) time-domain EM inversion code EM1DTM developed at the University of British Columbia Geophysical Inversion Facility (UBCGIF). The subroutine is fast and simple to use but requires some consideration in making sure that for a chosen number of time gates, there are a sufficient number of frequencies to properly compute the transform. Figure 3.14 shows an example of the simple input and output files of the subroutine. Inputs are the frequency domain forward model results for each frequency at each receiver and the desired time gates for the transform. The transform is carried out once for each component of the frequency-domain forward response (H_x, H_y, H_z) at each receiver location separately using the same time gates. The sine transform is used to obtain the standard d**B**/dt results and for many of the models, the cosine transform is also separately carried out on the data to obtain the **B**-field results. For a standard Slingram-style model of 31 receiver locations, this amounts to 186 separate transforms required to obtain a full 3D data set in the time domain. Despite the large number of transforms, this process is fast and the number of frequencies and or time gates and their ranges can be easily varied to explore a variety of possible

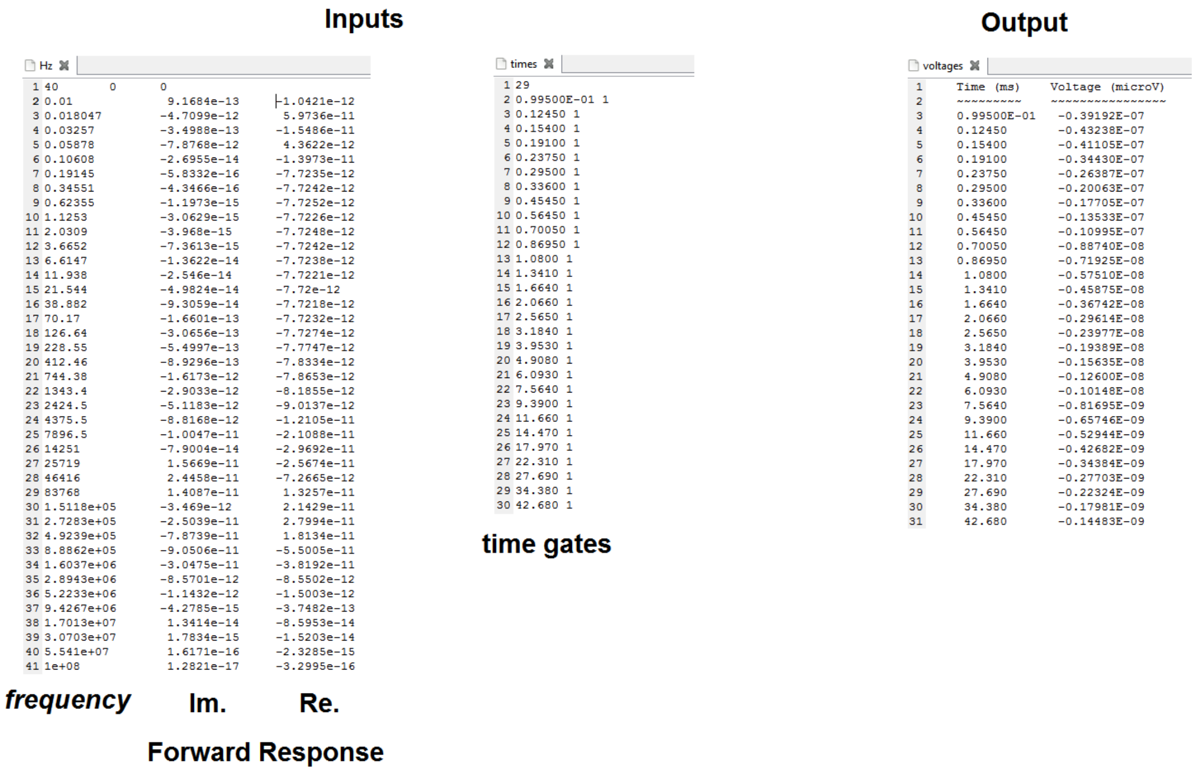

```
40        0         0
0.01                 9.1684e-13      -1.0421e-12
0.018047            -4.7099e-12       5.9736e-11
0.03257             -3.4988e-13      -1.5486e-11
0.05878             -7.8768e-12       4.3622e-12
0.10608             -2.6955e-14      -1.3973e-11
0.19145             -5.8332e-16      -7.7235e-12
0.34551             -4.3466e-16      -7.7242e-12
0.62355             -1.1973e-15      -7.7252e-12
1.1253              -3.0629e-15      -7.7226e-12
2.0309              -3.968e-15       -7.7248e-12
3.6652              -7.3613e-15      -7.7242e-12
6.6147              -1.3622e-14      -7.7238e-12
11.938              -2.546e-14       -7.7221e-12
21.544              -4.9824e-14      -7.72e-12
38.882              -9.3059e-14      -7.7218e-12
70.17               -1.6601e-13      -7.7232e-12
126.64              -3.0656e-13      -7.7274e-12
228.55              -5.4997e-13      -7.7747e-12
412.46              -8.9296e-13      -7.8334e-12
744.38              -1.6173e-12      -7.8653e-12
1343.4              -2.9033e-12      -8.1855e-12
2424.5              -5.1183e-12      -9.0137e-12
4375.5              -8.8168e-12      -1.2105e-11
7896.5              -1.0047e-11      -2.1088e-11
14251               -7.9004e-14      -2.9692e-11
25719                1.5669e-11      -2.5674e-11
46416                2.4458e-11      -7.2665e-12
83768                1.4087e-11       1.3257e-11
1.5118e+05          -3.469e-12        2.1429e-11
2.7283e+05          -2.5039e-11       2.7994e-11
4.9239e+05          -7.8739e-11       1.8134e-11
8.8862e+05          -9.0506e-11      -5.5005e-11
1.6037e+06          -3.0475e-11      -3.8192e-11
2.8943e+06          -8.5701e-12      -8.5502e-12
5.2233e+06          -1.1432e-12      -1.5003e-12
9.4267e+06          -4.2785e-15      -3.7482e-13
1.7013e+07           1.3414e-14      -8.5953e-14
3.0703e+07           1.7834e-15      -1.5203e-14
5.541e+07            1.6171e-16      -2.3285e-15
1e+08                1.2821e-17      -3.2995e-16
```

```
29
0.99500E-01 1
0.12450 1
0.15400 1
0.19100 1
0.23750 1
0.29500 1
0.33600 1
0.45450 1
0.56450 1
0.70050 1
0.86950 1
1.0800 1
1.3410 1
1.6640 1
2.0660 1
2.5650 1
3.1840 1
3.9530 1
4.9080 1
6.0930 1
7.5640 1
9.3900 1
11.660 1
14.470 1
17.970 1
22.310 1
27.690 1
34.380 1
42.680 1
```

```
    Time (ms)     Voltage (microV)
    ~~~~~~~~~~    ~~~~~~~~~~~~~~~~~
    0.99500E-01    -0.39192E-07
    0.12450        -0.43238E-07
    0.15400        -0.41105E-07
    0.19100        -0.34430E-07
    0.23750        -0.26387E-07
    0.29500        -0.20063E-07
    0.33600        -0.17705E-07
    0.45450        -0.13533E-07
    0.56450        -0.10995E-07
    0.70050        -0.88740E-08
    0.86950        -0.71925E-08
     1.0800        -0.57510E-08
     1.3410        -0.45875E-08
     1.6640        -0.36742E-08
     2.0660        -0.29614E-08
     2.5650        -0.23977E-08
     3.1840        -0.19389E-08
     3.9530        -0.15635E-08
     4.9080        -0.12600E-08
     6.0930        -0.10148E-08
     7.5640        -0.81695E-09
     9.3900        -0.65746E-09
     11.660        -0.52944E-09
     14.470        -0.42682E-09
     17.970        -0.34384E-09
     22.310        -0.27703E-09
     27.690        -0.22324E-09
     34.380        -0.17981E-09
     42.680        -0.14483E-09
```

Figure 3.14: Example input and output files for the time-domain transform subroutine.

transform results. The output file contains the time gates and the d**B**/dt (outputted as μ₀ d**H**/dt) magnetic field results in units of microvolts (μV, or equivalently μV/Am^2), and in a separate file the **B**-field results in microvolt-seconds which is equivalent in this case to micro Tesla (μV-s, or equivalently μV-s/Am^2 = μT). For clarification the units of Am^2 coming from the transmitter current and transmitter area are normalized out of the results in the CSEM3DFWD code and the time domain transform assumes a transmitter of unit area. These outputs are the final results of the forward modeling process described in this thesis; they contain the time decay curves for an individual receiver and the results from all receivers can be combined to examine the time-domain response vs. distance along the modeled survey line.

3.6 Plotting

A major component of this project was the development of many plotting codes for use in displaying multiple aspects of the vast data sets generated for every model. Plotting codes were written in the Python computing language which is easily adapted for data management, plotting, and the combination and arrangement of multiple plots, all in the same code. Plotting codes were developed for both research and comparison purposes, and in creating a deliverable product for ARC that covers all relevant information in each model. Appendix A shows what is termed a ‘full output’ of plots for a thin vertical conductor in a half-space. This collection of plots covers all important aspects of a model, demonstrating the time- and frequency-domain responses in a variety of forms and for each frequency, time gate, and receiver location.

3.6.1 A Note on Figures Used in This Work

The amount of data created by this method is substantial, with 40 frequencies, 29 time gates, 31 receiver locations, and total and secondary fields. The reader will notice, especially in later chapters, that figures are often composed of multiple plots, and it is noted that this may be overwhelming to the eye at first. When such plots are made use of it is done to compare the effects of some parameter on multiple similar models. In this format, the idea is to examine the shape of the various response curves, and not to dwell on response amplitude values and transmitter locations, the text for which may be quite small. It is hoped that the standard type of outputs seen in this work will be well established in Chapters 4-5, and the reader will seamlessly be able to interpret the meaning of the results seen in the many full page figures in Chapter 6. In situations where the response amplitude is the focus of the comparison in the figure, readability is hopefully not an issue. These larger figures are available in full size in the digital version of the Appendix for this work.

3.7 Data Management and Parallelization Methods

By the very nature of this project, a lot of data is generated for each complete model. This includes frequency-domain results for both the real and imaginary parts for typically 40 individual frequencies at 31 receiver locations, as well as the resulting time-domain results at these locations. This number is doubled when the half-space version of each model necessary to compute the secondary magnetic field is also considered. A variety of methods were used to simplify, streamline, and speed up the process as well as to reduce the amount of manual manipulation of results necessary throughout the course of the forward modeling procedure. These methods included the use of a variety of Python scripts and command line shell scripts. These scripts ensured that all data from any given model were created and processed in the same way in both the frequency and time domains, and accidental operator error in the forward modeling process was substantially reduced.

The initial frequency-domain forward modeling stage of this process is by far the most computationally intensive and time-consuming portion of the process. The forward code CSEM3DFWD runs one frequency at a time, and 40 frequencies are required for a time-domain response. This requires that the code be run 80 (including half-space version) times per example. Since somewhere between 2 GB and 60+ GB of RAM is necessary to compute each response, this may not be possible on a standard desktop or laptop computer. Furthermore, at typically 1 – 10 hours (or more) of solve time per frequency, if a desktop computer could run one or two models at a time, the process could still take days or weeks to obtain a single time-domain result. To decrease the time necessary to compute the required frequency-domain responses the process was adapted to run CSEM3DFWD in parallel on the "torngat" cluster of MUN's Computational Applied Geophysics Group, containing multiple computing nodes each with adequate memory for running one or more individual frequency responses at a time, depending on the model cell size.

Initially, each frequency-domain model was set-up and run separately using all or part of a single computation node. This sped up the modeling process by allowing up to 20 or more frequencies to be run simultaneously but required a great deal of manipulation of individual model results, and careful management of the runs on each node to ensure that the available memory was not exceeded. It was often difficult to assess the memory requirement as models with the same mesh but of different frequency could potentially have different spikes in memory usage. These spikes would often cause failure of the other model running on the node.

Eventually, a specialized Grid Engine script was obtained (per. comm. Paul Sherren, 2015), that made it possible to set up all the individual frequency-domain models necessary for one time-domain result as a group and then run them together in parallel in smaller groups continuously until each frequency was computed. The script simplified the memory assignment problems and allowed for any arbitrary number of nodes to be used in computing a single model. This advancement made it possible to begin to run the necessary sets of frequency-domain models for multiple time-domain models at the same time. Careful management of jobs was still necessary as far as moving datasets on and off the cluster, and timing the running of jobs to create what was essentially a model production line that was continuously running and creating results. For simple conductor models especially, model building takes a small fraction of the time that running the frequency-domain models requires. By taking advantage of this, many models could be built at once and then placed on the cluster where they simply wait their turn to run.

3.8 Computational Requirements

Due to the high number of examples that were considered during this project, the individual memory requirements for each frequency model were not kept track of in detail. As mentioned in above sections, for the direct solve version of the CSEM3DFWD forward modeling code, anywhere from 2 GB to 60+ GB of RAM was necessary to compute a single frequency-domain model, depending on the number of cells in the mesh. Only models at or above 1 million cells have been

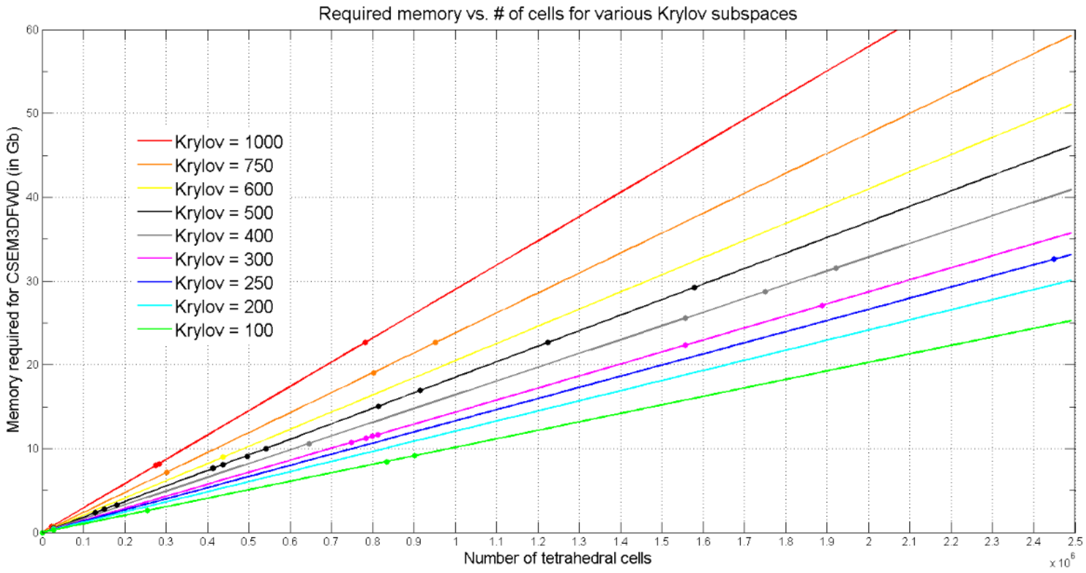

Figure 3.15: Comparison of the memory requirements in GB for models with various numbers of cells, and computed at different Krylov subspace dimensions. Obtained through personal communication with Michael Dunham, 2016.

observed, in this work and others (per. comm. Seyedmasoud Ansari, Michael Dunham, 2016), to crash due to lack of available memory when using the direct solve version of the code, meaning they exceeded the 60 GB RAM and 30 GB swap available on the computing nodes used in this project. For the iterative solve version of the code, results were obtained (per comm. Michael Dunham, 2016) that do well to demonstrate the relationship between mesh cells and memory usage. Figure 3.15 shows these results for a variety of Krylov subspace dimensions, important to the iterative code, with individual points representing individual models and lines representing predicted trends. Overall the iterative version uses less memory for meshes with a similar number of cells, but this example does well to show generally what can be expected as far as memory requirements are concerned for running the frequency-domain computations.

Chapter 4

Half-Space Modeling

4.1 Introduction

The primary goal of this stage of the project was to build the necessary framework for computing multiple time-domain responses, with each of those responses being generated from many individual frequency-domain responses. It was also crucial to test the forward response obtained from these models to ensure that no errors were occurring in the process. For that reason, a series of tests were run on simple homogeneous half-spaces, and the results were compared to independent results obtained from the 1D time-domain electromagnetic forward modeling and inversion code, EM1DTM, developed at the University of British Columbia Geophysical Inversion Facility (UBCGIF). Of primary importance was determining the number and range of frequencies necessary to properly construct the time-domain response. A variety of model design and forward modeling code parameters were also tested to determine their possible effects on the forward response in both the time and frequency domains. The correct reproduction of simple half-space models is a fundamental task for any forward modeling method before moving on to more complex modeling involving conductors.

4.2 Half-Space Model Design

Models were constructed in the same manner as described in Chapter 3, however, for these initial tests half-space models with total volumes of 100 km^3, 50 km^3, 14 km^3, and 8 km^3 were constructed for comparison. Models at each volume were constructed using multiple refinement methods, typically at this stage achieved through insertion of boxes in the model before meshing. These variations focused on determining the effects of refinement around transmitters and receivers, as well as coarse refinement boxes inserted either in the shallow or deep subsurface. In time, boxes were replaced with nodes and volume refinement methods and eventually, as seen in later chapters, all refinement was reduced to regular tetrahedra inserted at receiver locations only.

For initial models, the transmitter and receivers were set up in a simple way that is comparable to a single sounding of a fixed loop TEM survey, or one station of a moving loop TEM survey. The receiver line extends 2000 metres along the North-South axis with receivers spaced 400 metres apart. The transmitter loop is 400 x 400 metres, see Figure 4.1 below. Receiver 3, at an offset of 800 metres from the transmitter is of primary importance as it is a common Tx-Rx offset for Slingram-style moving loop surveys used in Athabasca Basin uranium exploration. For that reason, most model comparisons in the following results are based on the response at Receiver 3 only.

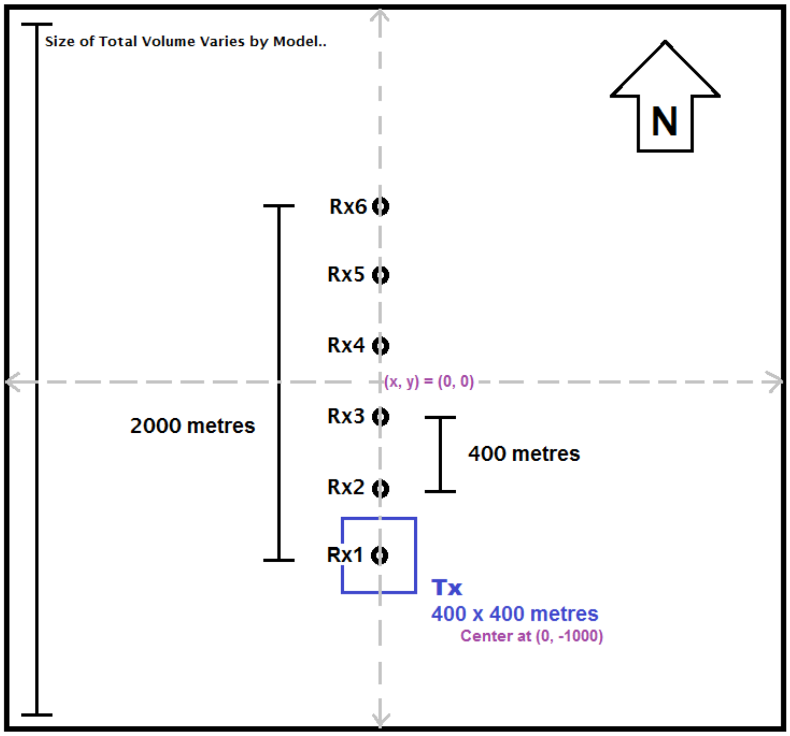

Figure 4.1: The standard transmitter-receiver layout used in half-space modeling. Receiver 3 at an offset of 800 metres from the transmitter center is of most importance in this project.

4.3 Results

It is important to mention that nearly all results of initial half-space models were computed using the iterative version of the CSEM3DFWD forward modeling code. The direct solve version did not become available until initial conductor models were being computed. However, it was beneficial that these early models were computed using the iterative approach as it allowed for an examination of the residual norm of the solution over the range of frequencies modeled. CSEM3DFWD was written for use in modeling of controlled-source EM, which makes use of low frequencies typically less than 1 Hz, and the behavior of the code at high frequencies up to 100 MHz had not previously been tested in this manner. In Chapter 5, results comparing the iterative and direct solve approaches will be presented.

In this section, the results of tests regarding the number and range of frequencies necessary for the time-domain transform will be of primary focus, with model parameters such as refinement and model volume being secondary and incidental in these comparisons. The total model volume does have important effects on the forward results and so will also be covered briefly. The effect of mesh refinement style was eventually determined to be minimal and of little importance beyond ensuring a quality mesh was created, and the receiver locations are well refined. Some information regarding the effects of the old refinement methods can be found in Appendix F. Additionally, the effect of variation in the Krylov subspace dimension, an important parameter only used with the iterative version of the code, can be found in Appendix B.

4.3.1 Total Model Volume

The volume of the 3D cube that bounds the model space has a significant effect on the forward results in both the frequency and time domains. Figure 4.2 shows the z-component of the magnetic field (**H**) vs frequency for both the real and imaginary parts for four half-space models of different volume. In these four models, total model domain sizes of 100 km^3, 50km^3, 14km^3, and 8km^3, were tested. The half-space resistivity was chosen to be 1500 Ohm-m, a value chosen based on averages of measurements obtained by ARC in the Athabasca Basin. Figure 4.3 shows the percent error (left) and residual (right) of the frequency-domain forward responses vs. the verified 1D response of EM1DTM computed for the half-space. The effect of model volume on the frequency-domain response is best observed in the imaginary component of the response. Both the percent error and the residual between the models and the 1D response are seen to increase at low frequencies as the model volume is decreased. This effect is thought to be due to the skin-depth relation at low frequencies: low frequencies have larger skin depths, and it is likely that the error seen here is due to the fact that as the model volume decreases it is simply too small to accommodate a corresponding range of low frequencies. Figure 4.4 shows the time-domain, time decay curves for these four models as well as the 1D response at 200 representative frequencies. The effect of small model volumes is quite pronounced in the time-domain results, and as the model volume is decreased significant error is introduced at late times. This is not exactly a surprise as the time-domain transform makes use of the imaginary component of the frequency-domain results, the error at late times is directly related to the error at low frequencies in the imaginary component. The time-domain results also show error at early times (Figure 4.5) for the larger 100 km^3 model, this likely corresponds to some degree to the errors seen at high frequencies.

The model volume is clearly an important consideration in model design, and it appears best to choose a model volume based on the skin-depth of a mid-range frequency when attempting to model a variety of frequencies over a larger range. For this project, all subsequent models created after the half-space testing phase were created using a volume of 50 km^3. This is based on 8x the skin depth of a frequency of approximately 100 Hz calculated with a half-space resistivity based on averages of Athabasca Basin rock types. This volume, when compared to the others

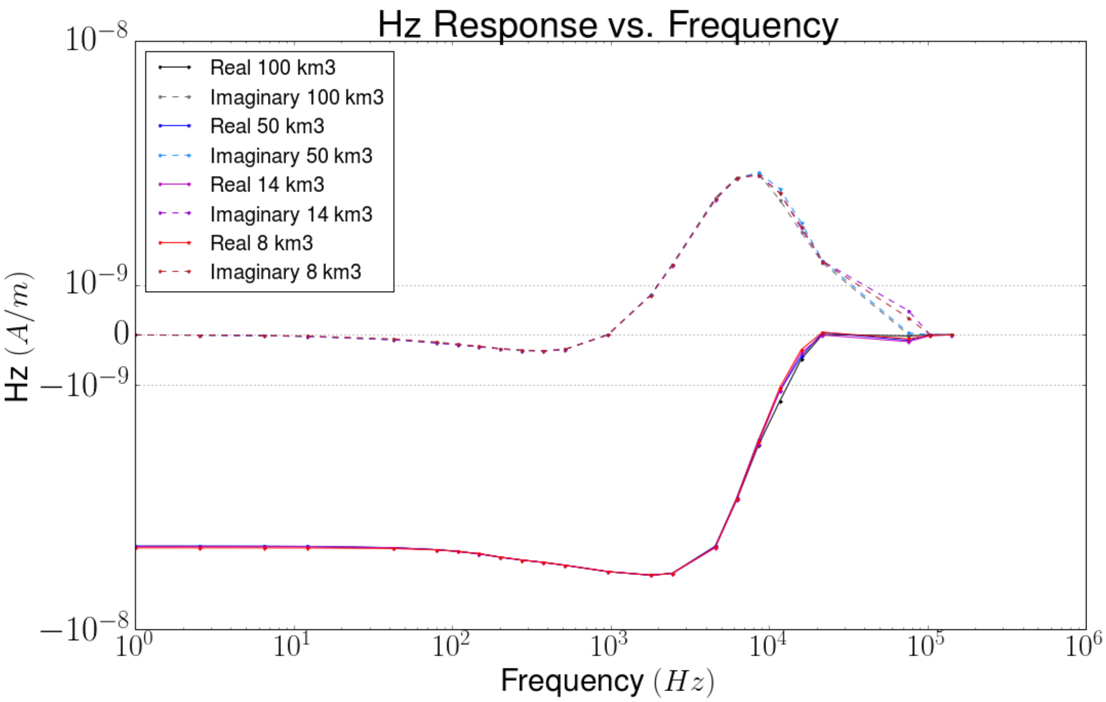

Figure 4.2: Z-component of the magnetic field strength (**H**) vs. frequency for both the real and imaginary parts for four half-space models of different volume.

tested, could accurately represent the 1D time-domain response over the entire time window considered (i.e. .09 ms – 42ms). It is interesting to note that changes in the model volume have no apparent effect on the creation or reduction of error in the higher frequencies in either the real or imaginary components. High frequency error remains prevalent at frequencies above 10^4 Hz regardless of changes in the model volume or refinement method. This apparently significant error (Figure 4.3) is likely due to the fact that the response approaches zero at high frequencies (see Figure 4.2). Small discrepancies between the 3D and 1D results at higher frequencies appear to be significant yet due to their very low amplitude are likely unimportant to the overall accuracy of the resulting time-domain response (Figure 4.4).

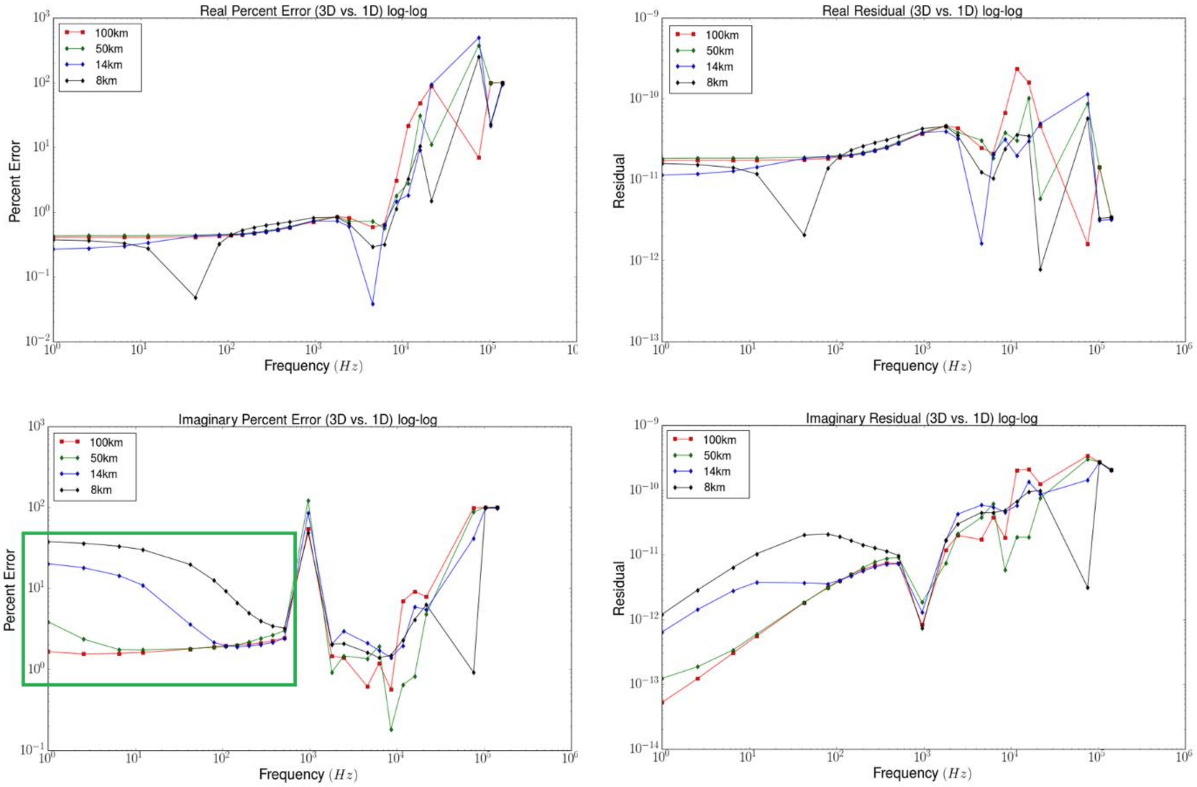

Figure 4.3: Percent error (left) and residual (right) for the real (top) and imaginary (bottom) parts of the modeled forward responses vs. the verified 1D response of EM1DTM computed for the same half-space resistivity. Highlighted in green is the primary effect on the imaginary response due to altering the model volume.

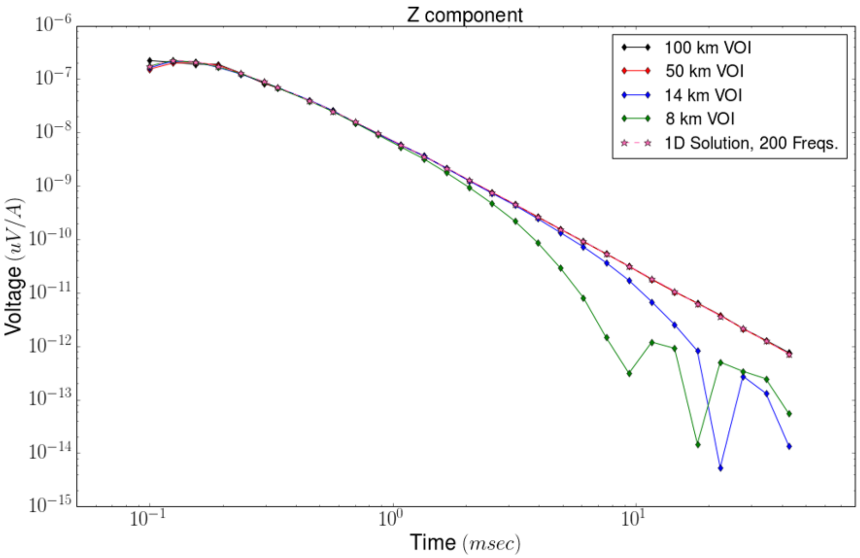

Figure 4.4: Time-domain decay curves of half-space models of four different volumes as well as the verified 1D response of EM1DTM using 200 representative frequencies.

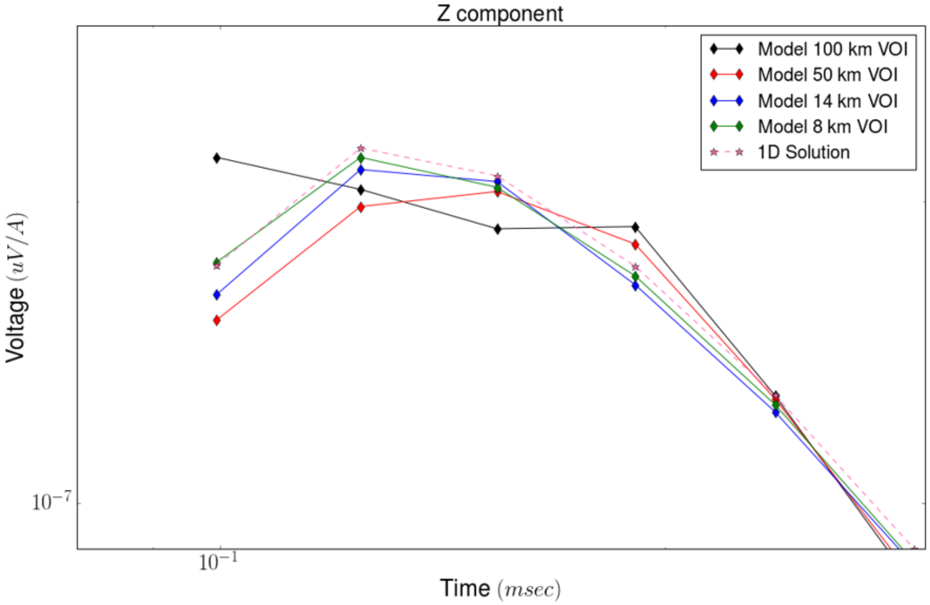

Figure 4.5: Time-domain decay curves at *early times only*, for the half-space models seen in Figure 4.4.

4.3.2 Number and Range of Frequencies for Time-Domain Transform

Newman et al. (1986) suggest that between 20 and 40 frequency-domain values, with 5-8 representative frequencies per decade over the frequency range covered, is necessary to accurately create a time-domain response via the sine transform. With the goal of minimizing computation time and resources, 24 frequencies were used initially covering a frequency range from 1 Hz to 142 kHz. These values were chosen to be the approximate inverse of the minimum and maximum time gates used in standard ARC TDEM data collection. Figures 4.6 and 4.7 show the time-domain decay curves of four responses computed using 24 frequencies. The specific variation in these responses is caused by variations in the mesh refinement method and the volume of the mesh, but are unimportant in this case. As seen in previous examples the responses show the majority of variation from the 1D response at early times, but for the most part, the results are fairly accurate in reproducing the 1D result over the entire time window.

To determine whether the addition of more frequencies and/or broadening the frequency range covered could improve the time decay curves and more accurately reproduce the 1D response, the forward method was upgraded to allow for models of 40 and 57 representative frequencies to be computed. Figures 4.8 and 4.9 show time-domain decay curves for six variations of a half-space model computed using 24, 40, and 57 frequencies, over two frequency ranges $10^{-2} - 10^{6}$ Hz and $10^{-2} - 10^{8}$ Hz. The models computed using only 24 frequencies show the most error over the entire time decay and most significantly at the earliest times. Responses computed using 40 and 57 frequencies are within a reasonable range of error when compared to the 1D solution, but due to the reduced time necessary for computing only 40 frequencies that method is preferable. These results confirm the results of Newman et al. (1986), suggesting that 20-40 frequencies are adequate to create an accurate time-domain response. Although Newman et al. (1986) do not explicitly mention the frequency range used in their calculations, aadditional evidence that approximately 20 frequencies over a reduced frequency range can accurately represent the time-domain response can be seen in Appendix D. Wanting to ensure accurate results, 40 frequencies became the standard for all subsequent time-domain models created for this project.

Additional testing was performed to determined the effect of high-pass, low-pass, and band-pass style filtering on the half-space frequency domain results before the transformation into the time domain. These results can be seen in Appendix C and further demonstrate the importance of specific frequency ranges on certain time windows in the time decay curve.

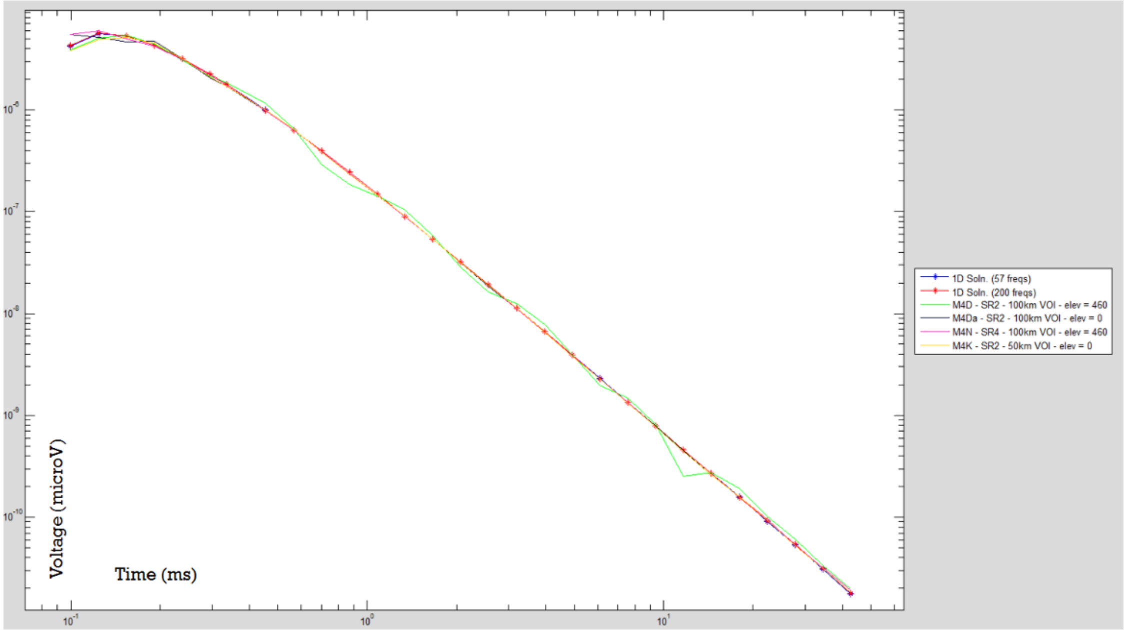

Figure 4.6: Time-domain decay curves of four half-space models computed using 24 frequencies, also the verified 1D response of EM1DTM using 57 and 200 representative frequencies.

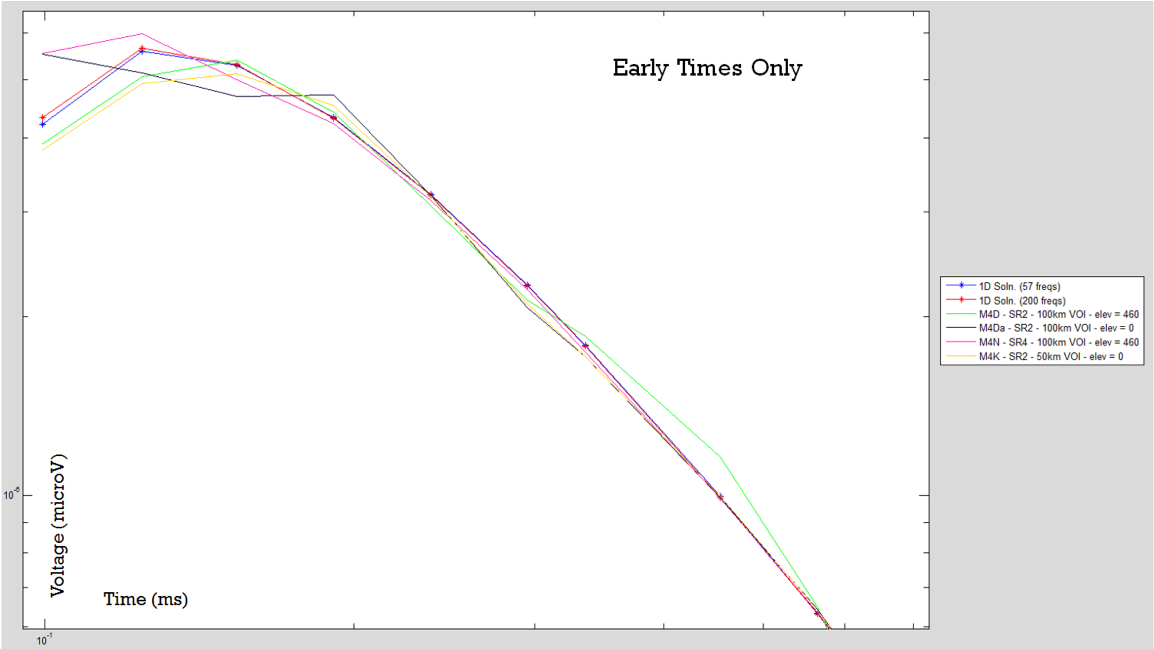

Figure 4.7: Time-domain decay curves at *early times only*, for the half-space models.

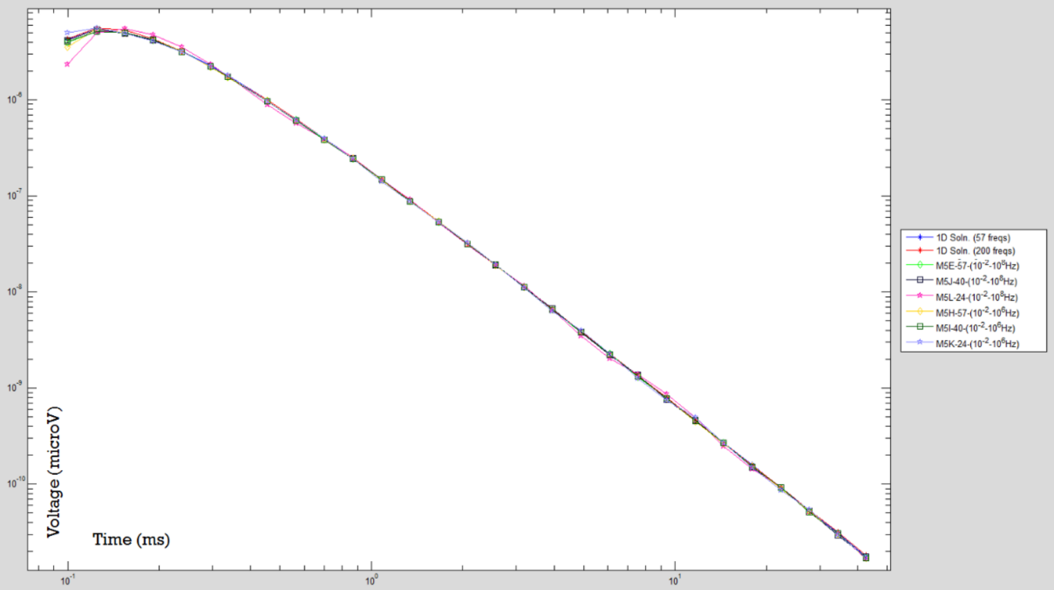

Figure 4.8: Time-domain decay curves of six variations of a half-space model computed using 24, 40, and 57 frequencies, over two frequency ranges $10^{-2} - 10^{6}$ Hz and $10^{-2} - 10^{8}$ Hz. The 1D response of EM1DTM calculated using 57 and 200 representative frequencies from $10^{-2} - 10^{8}$ Hz is also shown.

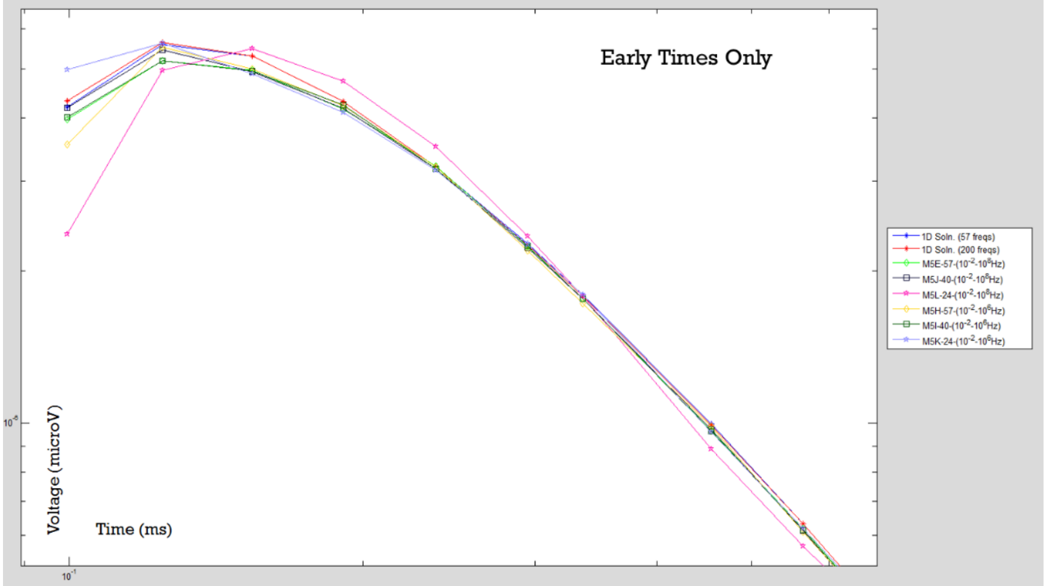

Figure 4.9: Time-domain decay curves at *early times only*, for the half-space models seen in Figure 4.8.

4.3.3 B-Field Decay Curve

Although all initial testing carried out on simple half-space models was done using the d**B**/dt response obtained through use of the sine transform from the frequency to the time domain, it is useful also to examine the **B**-field time-decay curve obtained with the cosine transform. Differences in the **B-**field and d**B**/dt responses have been discussed previously, but as the results of both response types will be examined for many of the models in the following chapters it is necessary to first compare the 1D and 3D **B**-field decay curves to ensure accuracy. Figure 4.10 shows a side-by-side comparison of the **B-**field and d**B**/dt time-decay curves for both the 3D half-space and the 1D half-space results of the EM1DTM code. In this case, the frequency-domain responses from the same 1500 Ohm-m half-space model were used to compute the time decay curves. The results highlight the differences in the decay behavior between the two response types and show that the method can reproduce **B**-field half-space responses as accurately as the d**B**/dt response discussed in detail in the previous sections.

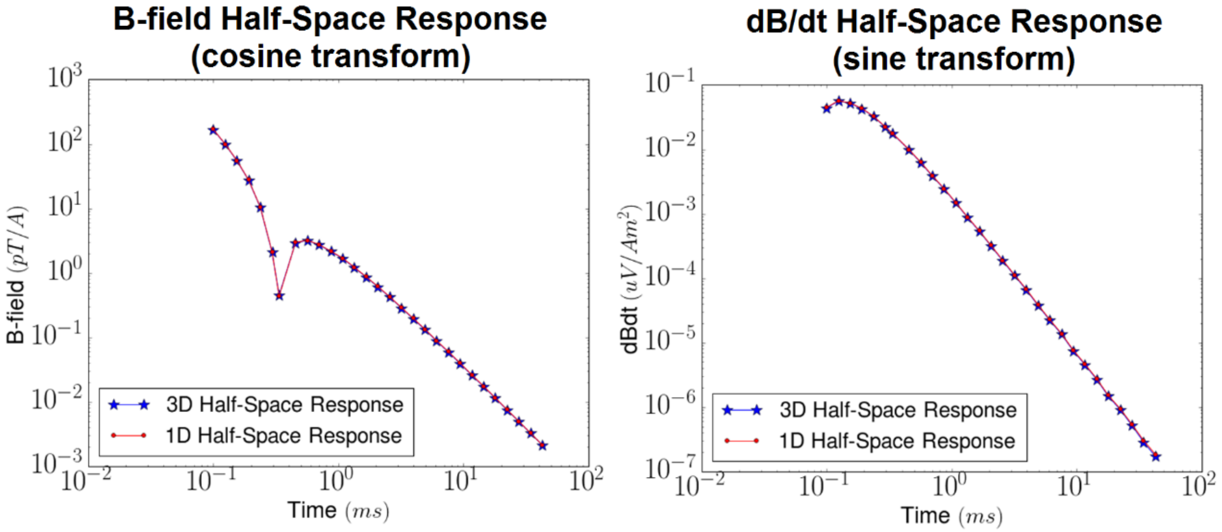

Figure 4.10: Comparison of **B**-field and d**B**/dt time-decay curves for the same 1500 Ohm-m homogeneous half-space model. Results of a 1D 1500 Ohm-m half-space computed using EM1DTM are also shown to demonstrate the accuracy of the responses.

4.4 Conclusions

The results demonstrate the ability of this forward modeling approach to successfully reproduce the time-decay curve for a 1-D resistive half-space from a set of 3D frequency-domain responses. The use of 40 model frequencies over a wide frequency range has been shown to be able to reproduce the 1D results within an acceptable range of error. The results have shown the importance of the total volume of the model-space, and that a volume based on the skin-depth of a mid-range frequency is the best choice when modeling over a wide range of frequencies in a resistive half-space. Additional results seen in Appendix B-D demonstrate the effect of a variety of other modeling parameters on the forward modeling process. In all, a great deal of information regarding the behavior of the half-space magnetic field in both the frequency and time domains was obtained in this stage of the research. With the successful reproduction of the 1D results, the method was ready to be applied to models containing simple conductors.

Chapter 5

Simple Conductor Models

5.1 Introduction

With confirmation that the forward modeling process could accurately produce time-domain magnetic field responses for homogeneous half-spaces, the addition of simple conductors to the models was the next step in testing the method before attempting to reproduce actual geologic situations. The addition of conductors to the models required changes in the model design process, as well as an upgrade of the modeling procedures. A switch from an iterative to direct solve version of the CSEM3DFWD forward modeling code was made to improve the accuracy of the results as well as to decrease overall computation time. In this chapter, the results of two models built to replicate published time-domain responses are presented as another check on the accuracy of the method. A comparison of the half-space resistivity used in conductor models and its relation to the polarity of the frequency- and time-domain responses will also be discussed. Finally, the response of a simple vertical conductor and simple dipping conductors will be presented. Additionally, an investigation into the resolution of the time-domain response will be presented in the form of a conductor of varying thickness and a set of two conductors at increasing depths. These results allow for the comparison of time-domain responses in a few simple situations and aid in the interpretation and comparison of the more complex geologic model results seen in the next chapter.

5.2 Simple Conductor Modeling

It is necessary to discuss briefly some of the changes made to both the modeling process and the model design when simple conductors were introduced. All simple conductor models were constructed manually as described in Chapter 3, conductors are all represented by rectangular prisms, and thus are considered “simple” by comparison to later models. The major change to model design for this stage of the process was the addition of the Slingram-style transmitter and receiver layout necessary to obtain the magnetic field vs. distance style measurements that are most common in mineral exploration. The Slingram layout used is seen in Figure 5.1 and consisted initially of 11 receiver locations spaced 100 m apart, creating a 1.1 km survey line. Each receiver was paired with a unique 400 by 400-m transmitter loop, at an offset of 800 m from the center of the transmitter to the receiver. The transmitter-receiver pair stepped up the survey line 100 m at a time, from south to north along the y-axis. After several models were computed, it was determined that a 1.1 km survey line could not get a complete background-to-background response (i.e. half-space value response at the ends of the survey line) for thin conductors. For this reason, models were upgraded to allow for 31 transmitter-receiver locations and a 3.1 km survey line that could capture the full response. An upgrade of the modeling process was also necessary to be able to compute 80 frequency-domain responses for each desired time-domain response, instead of the 40 used for half-space modeling, to compute the secondary field. Finally, it is also important to note that results of Slingram style surveys are typically plotted vs. distance using the center point between the transmitter and receiver, rather than the receiver location itself. When

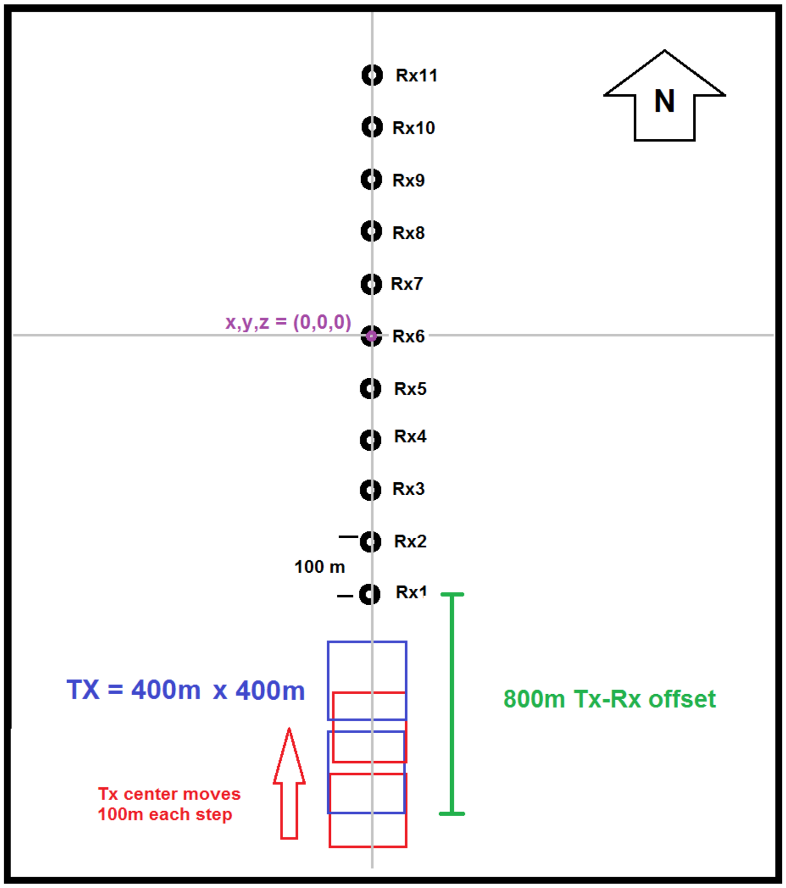

Figure 5.1: Slingram-style transmitter-receiver layout used for models containing conductors.

plotted in this way the response is centered over the conductor rather than being shifted along the survey line and is thus ideal for interpretation purposes.

5.3 Iterative vs. Direct Solve Results

The direct solve version of the CSEM3DFWD code became available for use in this project conveniently at the time when simple conductor models were initially being run. Specific differences in the solve method are covered in Chapter 3, but the

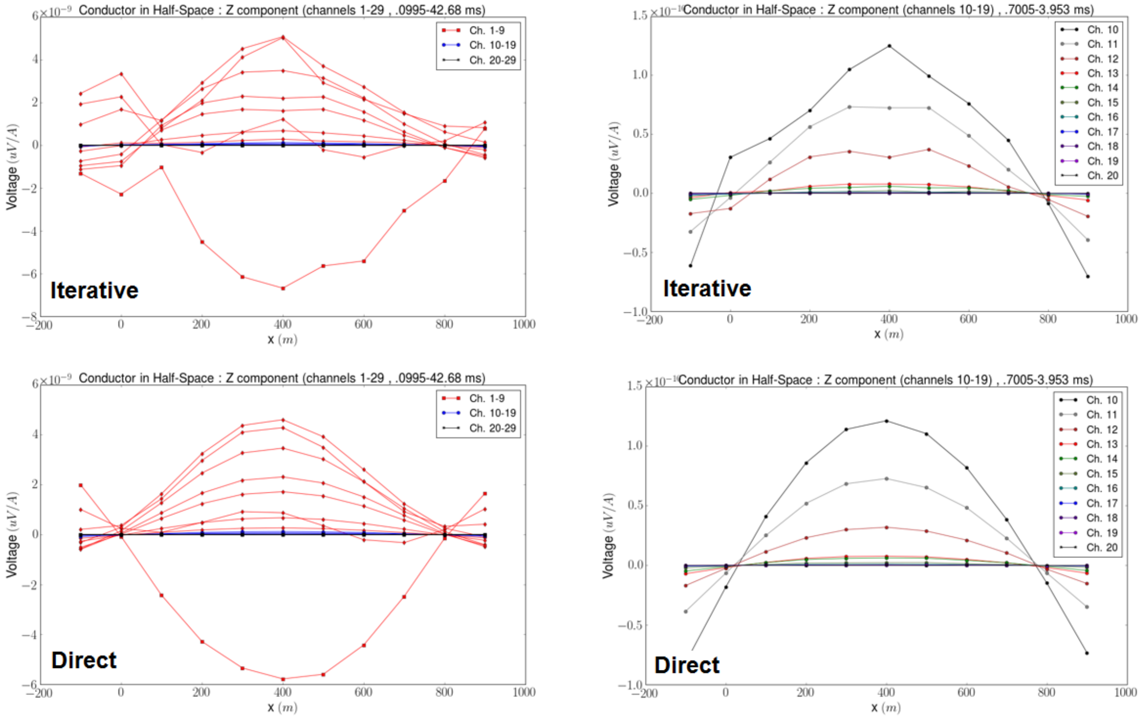

Figure 5.2: Secondary magnetic field vs. distance response for a simple vertical conductor in half-space model computed with the iterative solver (top) and the direct solver (bottom). Shown at the left are the results for the entire time window at 29 time channels, at the right is a smaller selection of channels covering middle-times.

direct solve code offered advantages in decreased computation time and increased accuracy of results and was able to improve the forward modeling process. Figure 5.2 shows the secondary field d$\mathbf{B}$/dt vs. distance response for a simple vertical conductor in half-space model computed with the iterative solver (top) and the direct solver (bottom). Shown at the left are the results for the entire time window from .09 ms to 42 ms, at 29 time channels; at the right is a smaller selection of channels covering middle-times from 0.7 ms to 3.9 ms. Figure 5.3 shows the model mesh used to compute the responses in Figure 5.2. The 30 Ohm-m conductor is at a depth of 500 m in a resistive half-space of 1500 Ohm-m. The thickness, strike length, and depth extent of the conductor are 100 m, 200 m, and 400 m respectively. Responses

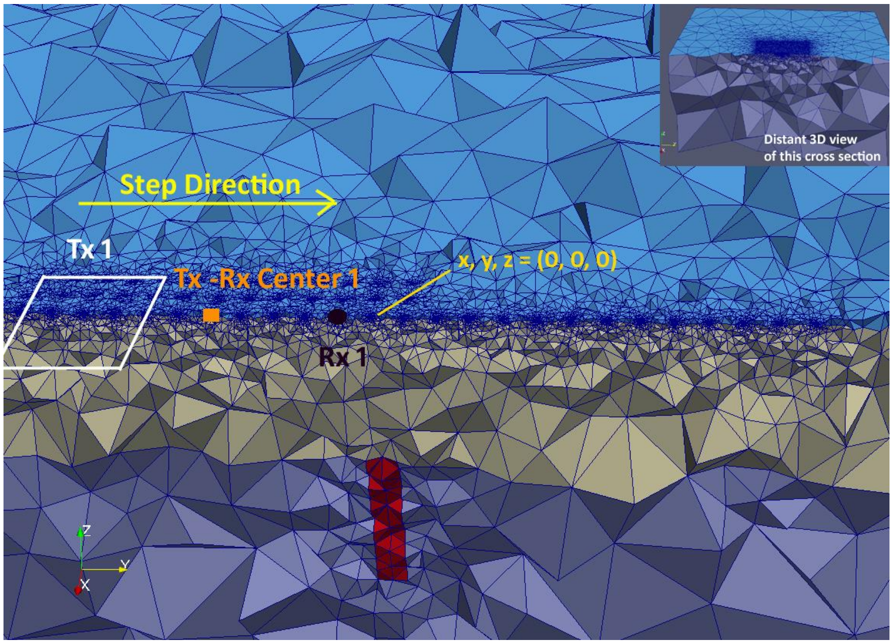

Figure 5.3: Vertical conductor in half-space model used to compute responses seen in Figure 5.2.

were computed at 11 transmitter-receiver locations, and the convention of conductors giving a negative minimum response rather than a positive peak response over the conductor was not applied in this case. The difference in results is quite clear, and it is apparent that more accurate and consistent responses are obtained via use of the direct solve code. Again, this is likely due to the decreased sensitivity of the solver to mesh quality. Although the mesh, in this case, was believed to be of good quality before computing the models, at this point in the research mesh refinement was much more variable, and the effect is apparent in the accuracy of the iterative results in the time- and frequency-domains. It is believed that with more careful attention to mesh refinement the iterative results could be improved to some degree. However, the benefit of the decreased model run time alone dissuaded the further use of the iterative solve code and improving the iterative results was not further pursued. The direct solve code produced more accurate results in less time, and memory was most often not an issue, and so it was used in the computation of all further models created for this project.

5.4 Comparison of Forward Method to Published Results

To further check the accuracy of the forward method on models that contain conductors, two results were chosen from the published literature to be reproduced for comparison. Both models chosen were simple conductor in half-space models and the parameters originally used to construct and run the models were replicated as closely as possible.

5.4.1 Newman Model

First, a conductor in half-space model was created to replicate a 3D integral equation result from Newman et al. (1986); the model mesh is seen in Figure 5.4. This is a fixed-loop style survey with a transmitter loop of 500 x 600 m in the x and y directions, and a 300 m offset from the leading edge of the loop along the y-axis from the start of the receiver line. Ten receivers run along the y-axis at 20 m spacing from -90 m to 90 m, centered at the model's origin. The 1 Ohm-m conductor has a width of 20 m, strike length of 600 m, and depth extent of 60 m. The conductor sits at a depth of 40 m in a 100 Ohm-m half-space. The mesh used to recreate the Newman model consisted of 112698 cells, and responses were computed for 40 individual frequencies from $10^{-2} - 10^{8}$ Hz. Figure 5.5 shows comparisons of the

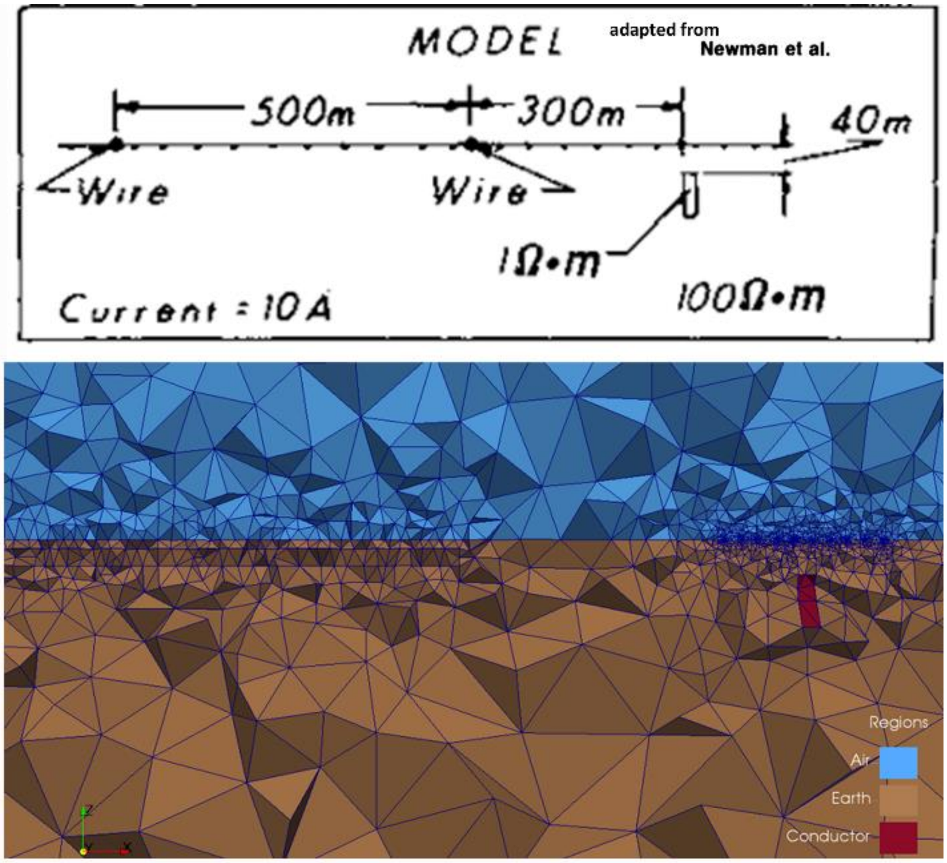

Figure 5.4: Model mesh used in computing the Newman model, with the corresponding description of the original model above, modified from Newman et al. (1986).

time-domain decay curves (bottom) and the secondary magnetic field response vs. distance along the receiver line (top). The results show good agreement between the two methods, and small discrepancies in response are believed to be attributable to the difference in computation methods. Overall this example does well to demonstrate the accuracy of the forward modeling method in reproducing known results for a conductor in a resistive half-space.

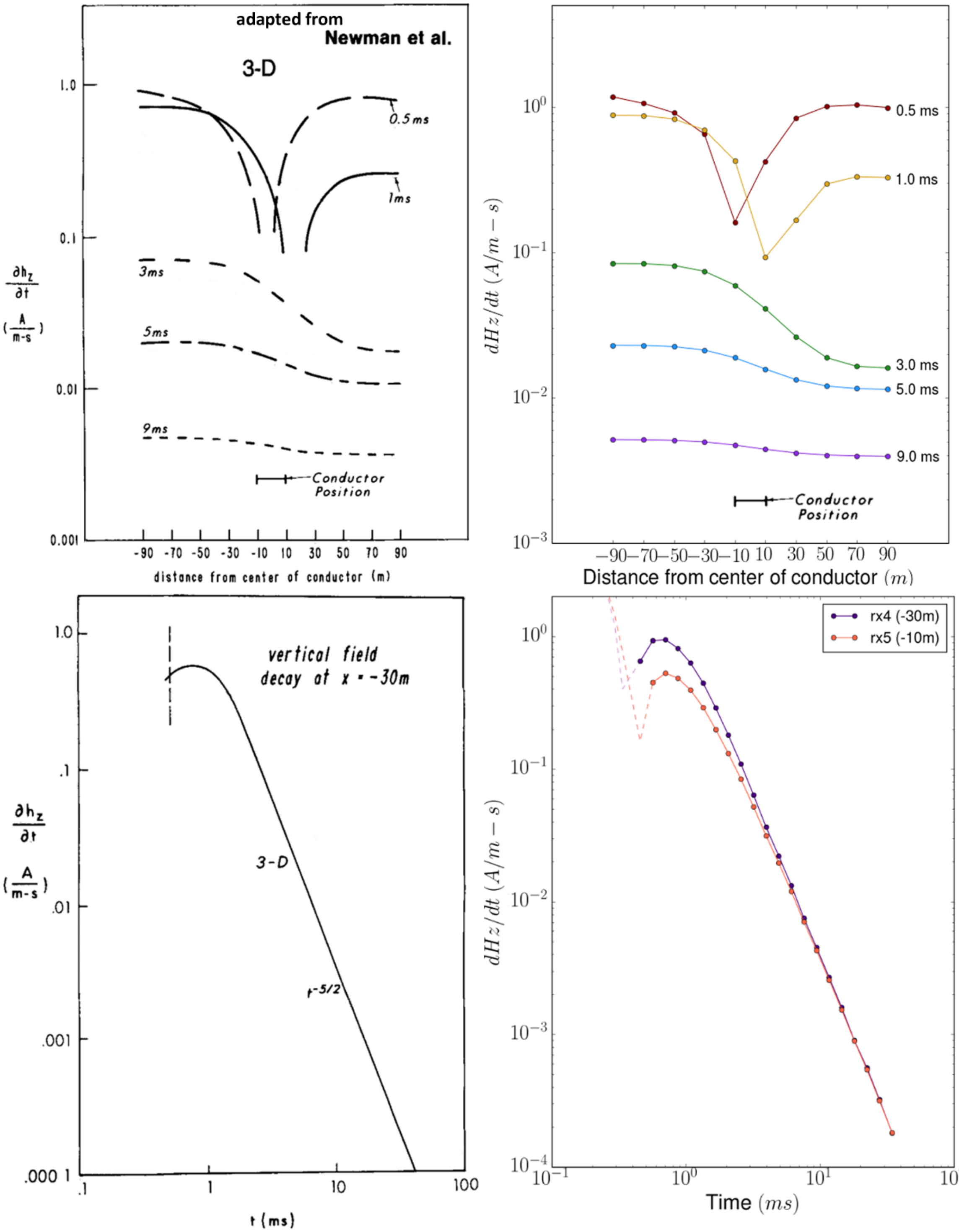

Figure 5.5: Comparison of results from Newman et al. (1986) at left, and from this study at right. At the top are time-domain secondary magnetic field vs. distance plots, and at the bottom are the time decay curves for selected receivers.

5.4.2 Ogilvy Model

Next, a model was created to reproduce the simple vertical conductor in free-space (i.e. air resistivity) example of Ogilvy (1986). In the original example, Ogilvy (1986) made use of the exact formal solution to calculate the response curves, assuming a step-function excitation of the ground and a resulting impulse response measured by an induction coil. The conductor in the original model of Ogilvy (1986) is a conductive sheet with no actual thickness but a specified conductance, and with infinite strike length and depth extent as seen in Figure 5.6. The top of the conductor is at a depth of 25 m below the transmitters and receivers, and the conductivity-thickness product of the conductor is 50 Siemens. The transmitter and receiver are circular loops with a diameter of 2.8 m, the transmitter-receiver offset is 50 m, and the receiver spacing is 10 m. To reproduce the Ogilvy model using this method some approximations and assumptions had to be made. First regarding the conductor dimensions, any infinite dimension is not possible using the method developed here, so the thickness, strike length and depth extent were chosen to be 10 m, 800 m, and 2 km respectively. The conductivity of the conductor was set to 5 S/m to match the 50 S conductivity-thickness product. Half-space resistivity was set to 10^8 Ohm-m. The mesh used consisted of 458377 cells, and responses were computed for 40 individual frequencies from $10^{-2} - 10^8$ Hz. A 5 by 5-m square transmitter was used which is approximately the same as the 2.8 m radius loop used originally. The receiver loop was not reproduced as CSEM3DFWD makes use of receivers that represent point measurements. However this was simply rectified by multiplying the response by 5^2, the diameter of a proportional square receiver loop. No mention of

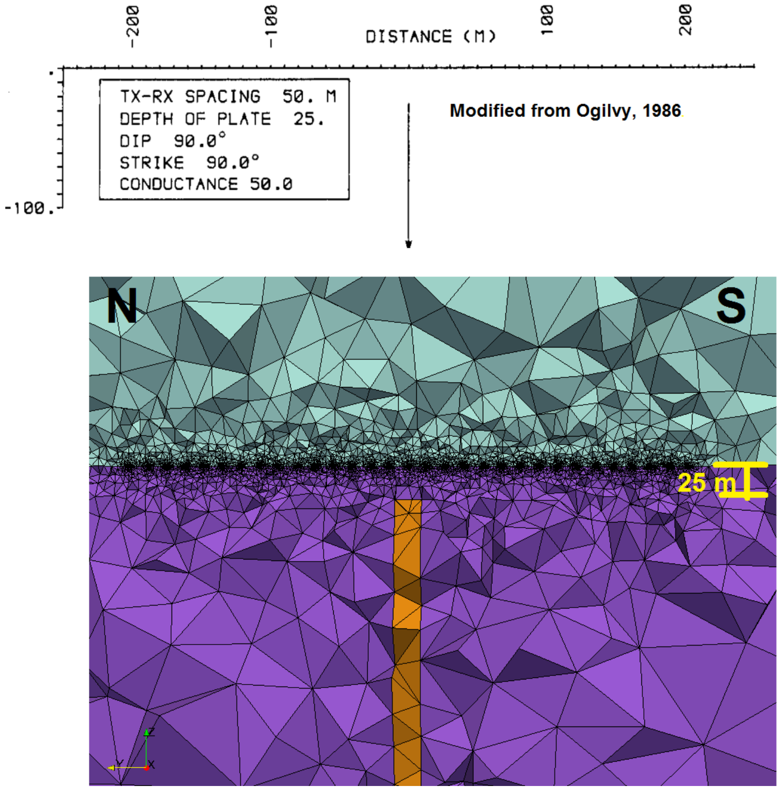

Figure 5.6: Model mesh for Ogilvy model, depth of conductor is 25m, thickness, strike length, and depth extent are 10 m, 800 m, and 2 km respectively. Above is original model cross-section modified from Ogilvy (1986); the conductor in this case has no thickness and is infinite in strike length and depth extent.

the transmitter current is made in Ogilvy (1986), so the model was run with a transmitter current of 10 A, and the response was normalized by this current. The model was run at only 31 transmitter-receiver locations forming a survey line from -150 m to 150 m instead of -200 m to 200 m as seen in the original example. Finally, the time-domain magnetic field responses generated by this method were multiplied by -1 before plotting to correspond to the SIROTEM convention used by Ogilvy (1986). As seen in Figure 5.7 the results of this method show very good agreement with the results of Ogilvy (1986), with minor differences in the minimum trough

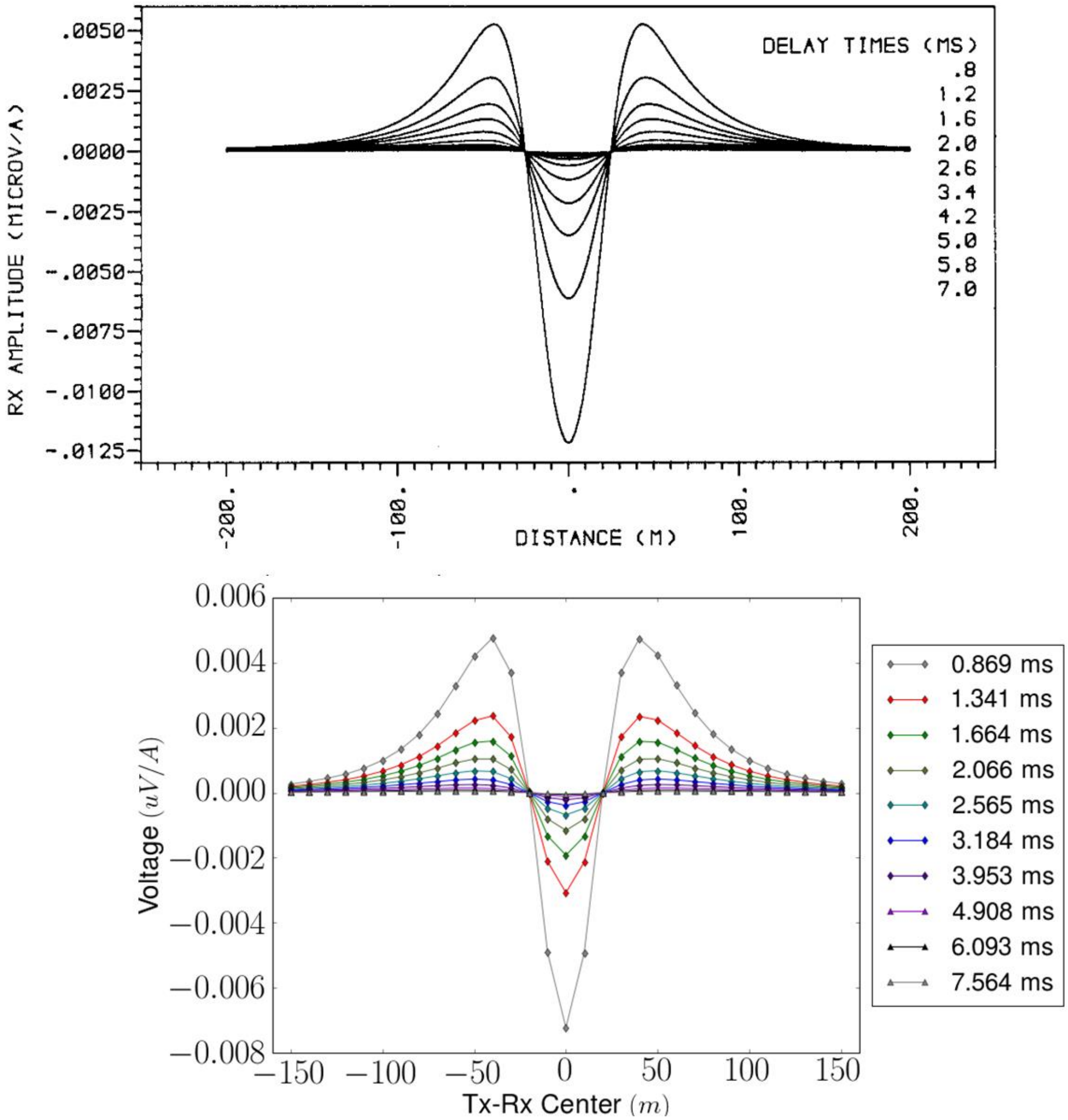

Figure 5.7: Comparison of the z-component magnetic field response vs. distance for a vertical conductor in free space. Original result of Ogilvy (1986) above and the comparable version computed using the method of this research below.

response amplitude likely due to the limited strike length and depth extent of the 3D conductor. The successful reproduction of these responses is encouraging in that, at least for a shallow conductor of finite dimension in free-space, the results of this forward modeling method are confirmed to be accurate.

5.5 Response Polarity and the Effect of Half-Space Resistivity

After reproducing the published results seen in the previous section it became clear that differences in the polarity of the forward responses can occur in both the frequency and time domains. These differences are thought to be caused by variation in the half-space resistivity of the model, as well as other factors such as conductor geometry and transmitter-receiver survey design. It is thus important to briefly discuss the polarity of the forward response before presenting the majority of modeling results seen in the following sections. Figure 5.8 shows the in-phase and quadrature frequency-domain forward responses and the time-domain forward responses at selected frequencies and time-gates for a simple vertical conductor in resistive half-space model. The conductor sits at a depth of 400m below the surface and is 10 m by 800 m by 1 km in thickness, strike length, and depth extent respectively. The conductor resistivity is 3 Ohm-m, and the half-space resistivity is 3500 Ohm-m, these again based on averages of Athabasca Basin rock types.

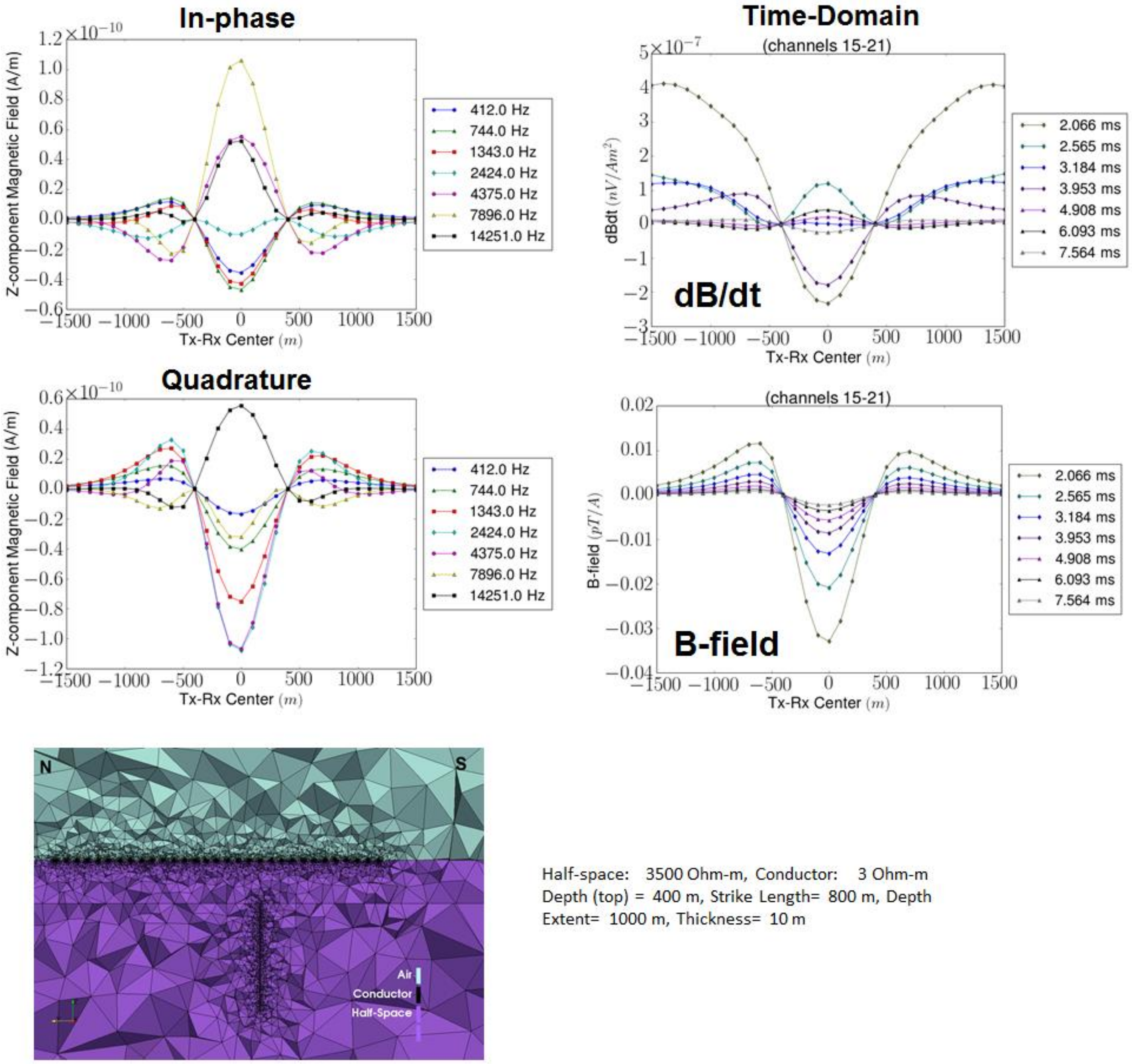

Half-space: 3500 Ohm-m, Conductor: 3 Ohm-m
Depth (top) = 400 m, Strike Length= 800 m, Depth
Extent= 1000 m, Thickness= 10 m

Figure 5.8: Selection of forward modeling results for a simple vertical conductor in half-space model. At upper and lower left are the in-phase and quadrature components of the frequency-domain magnetic field response. At upper and lower right are the time-domain d$\mathbf{B}$/dt and $\mathbf{B}$-field responses for selected time gates. At lower left is a cross-section along the *y*-axis of the model mesh.

5.5.1 Frequency Domain

First it is important to note that the polarity of the response at its peak amplitude over the conductor is actually a negative value commonly called a "trough response." This is the general form of the responses (with some exceptions) in both the time and frequency domains in Figure 5.8. However, as seen in the figure, the frequency-domain results show certain frequencies that are not negative "troughs," but are instead positive "peaks," this possibly most apparent in the selected in-phase results. These sign reversals in the frequency results were the cause of some question as to the accuracy of this modeling method, as well as the effect they may have on apparent sign reversals seen in the time-domain results. Some indication was seen in previous modeling results that these reversals occurred at different frequencies based on the half-space resistivity. To discover the cause of these sign reversals a series of five simple vertical conductor models like that in Figure 5.8, but of varied half-space resistivity, were created to define the bandwidth of the frequency domain response based on this parameter. Figure 5.9 shows the quadrature response vs. distance of these five models at five selected frequencies, seen from top left to bottom right. The half-space resistivities tested were: 100, 1500, 3500, 10,000, and 10^8 Ohm-m. The conductor in air-resistivity model (10^8 Ohm-m, purple curve Fig 5.9, black dotted curve in Fig 5.10) is particularly important as the popular time-domain forward modeling software Maxwell, in addition the calculated response curves of Ogilvy (1986), make use of this approximation. In all cases the resistivity of the conductor was kept at 30 Ohm-m, and only minor variations in the model meshes occurred. In this series of frequencies, the negative trough response for the 3500 Ohm-m half-space seen first

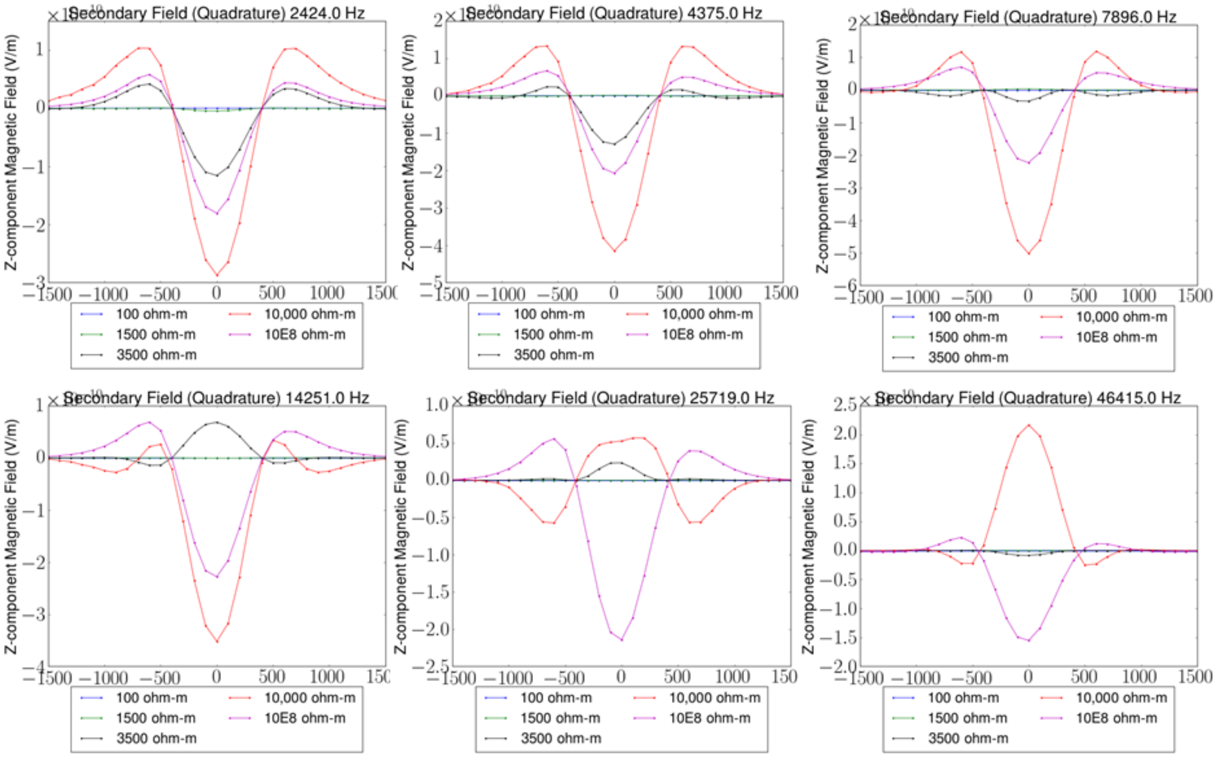
Secondary Field (Quadrature) 2424.0 Hz

Secondary Field (Quadrature) 4375.0 Hz

Secondary Field (Quadrature) 7896.0 Hz

Secondary Field (Quadrature) 14251.0 Hz

Secondary Field (Quadrature) 25719.0 Hz

Secondary Field (Quadrature) 46415.0 Hz

Figure 5.9: Frequency-domain quadrature magnetic field response vs. distance for five simple vertical conductor models of varied half-space resistivity. Six representative frequencies are shown from top left to bottom right and demonstrate the sign reversal of the response at particular frequency ranges.

at the top left transitions to a positive peak response by a frequency of 14 kHz, and then greatly decreases in amplitude. The same change in polarity can be seen in the 10,000 Ohm-m half-space model at frequencies from 14 kHz to 46 kHz. Figure 5.10 shows the magnetic field amplitude vs. frequency for the in-phase and quadrature components of the forward response for these same five models. This example is much more illustrative of the frequency response bandwidth of the five models as well as the shifting of the response envelope depending on the half-space resistivity. The figure shows the response at both receiver 1 and 16 to illustrate the additional fact that when viewing the response in this manner there is not a significant

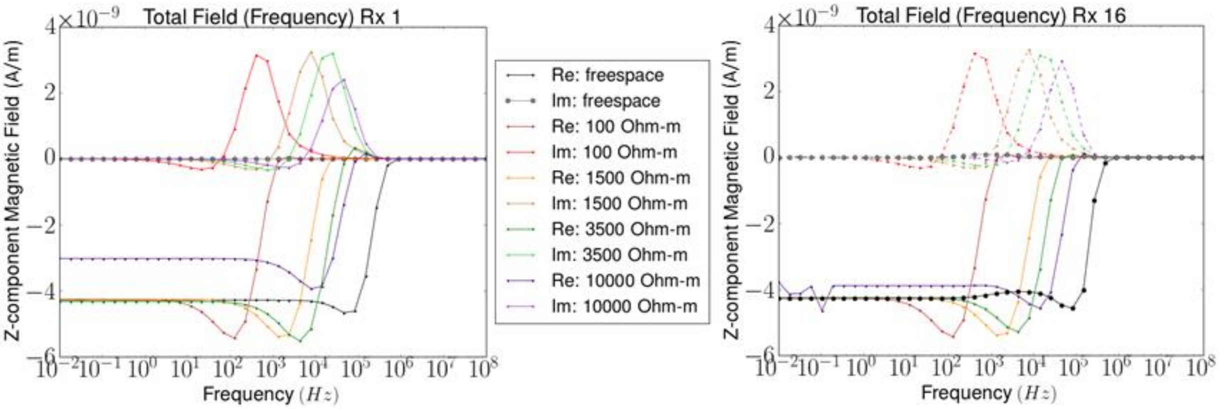

Figure 5.10: Z-component magnetic field amplitude vs. frequency for five vertical conductor in half-space models of varied resistivity. The real and imaginary (in-phase and quadrature) components are shown at receiver 1 (left) far from the conductor, and at receiver 16 (right) centered over the conductor.

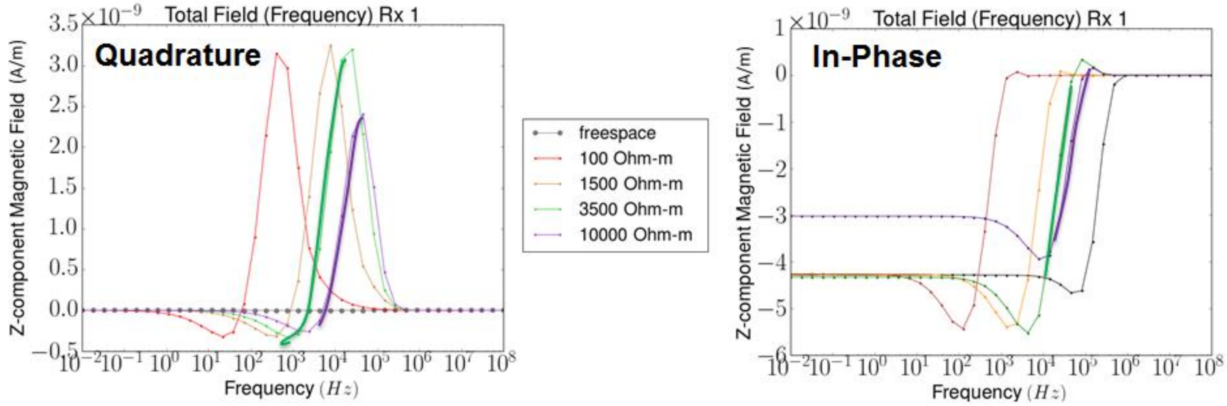

Figure 5.11 Z-component magnetic field amplitude vs. frequency for five vertical conductor in half-space models of varied resistivity. Highlighted are ranges of frequencies where sign reversals occur in response vs. distance plots like Figure 5.9.

difference whether the receiver is far from the conductor (Rx 1), or centered over it (Rx 16). Figure 5.11 highlights at left approximately the range of frequencies of the quadrature response where sign reversals are seen in the quadrature magnetic field vs. distance plots in Figure 5.9. Similar highlighted regions in the in-phase response also occur at frequencies where that component is seen to change response polarity in the response vs. distance plots.

These results indicate that the sign reversals seen in the magnetic field vs. distance plots are in fact related to the amplitude of the response at any particular frequency and in particular the ranges of frequencies where response amplitude transitions from negative to positive. We also see that the position of the response envelope is to some degree based on the resistivity of the model half-space, explaining why the sign reversals are seen to occur over a different range of frequencies in each of the examples.

5.5.2 Time Domain

In the time domain, sign reversals are apparently not correlated with the sign reversals in the frequency domain. According to Ogilvy (1986) and referring to the d**B**/dt response: unlike frequency-domain measurements, the polarity of the anomalous TEM response depends on target conductivity, loop separation, depth of burial, and sample time. Hence, no consistency in response polarity can be assumed, and for real data weak secondary signals can be reduced or even canceled by geometric field reversals. The results of this work show that half-space resistivity is also a parameter that effects the d**B**/dt response polarity. However, the relationship is admittedly not as well understood as in the frequency-domain case. The reversals and double peak style responses seen in the time domain plot in Figure 5.7, when interpreted on a model by model basis, seem to make sense for simple conductor models when the depth and geometry of the conductor, as well as the half-space and conductor resistivity, are considered. Often the reversals occur at time gates that are quite late and not of use typically in interpretations. This is not always the case, however, and more work needs to be done to understand fully the cause of these d**B**/dt response reversals in specific relation to the many factors mentioned above. Except occasionally at the earliest times, the **B**-field response does not undergo sign reversals like the d**B**/dt response. This fact is also not well understood, but perhaps has to do with the background resistivity of the model.

5.6 Simple Conductor Model Results

In the following sections, the results of models containing simple vertical and dipping conductors in resistive half-spaces are presented. Models demonstrate the effects of conductor resistivity, dip, thickness, and depth resolution. Only a selection of time-domain results demonstrating these parameters will be shown here: but the full *Z*-component frequency- and time-domain results as well other model information for all of the simple conductor models are presented in Appendix H.

5.6.1 Vertical Conductor in Half-Space

The vertical conductor in half-space was the simplest model constructed for the project but also the most frequently used for testing a variety of modeling parameters. Here, the conductor sits at a depth of 400m below the surface and is 10 m by 800 m by 1 km in thickness, strike length, and depth extent respectively. The half-space resistivity was kept constant at 3500 Ohm-m, and the conductor resistivity was modeled at 3, 30 and 300 Ohm-m. Figure 5.12 shows the time-domain *z*-component magnetic field response vs. distance for the 3 Ohm-m vertical conductor at all time gates, with the d**B**/dt results at the top of the figure and the **B**-field results at the bottom.

As the results of the Ogilvy model have shown previously, this is the standard response for a thin vertical conductor at depth. Characteristic features are symmetric or mostly symmetric trough responses centered over the conductor. The slight asymmetry seen in the early time responses is due to the large transmitter size compared to the much smaller receiver, and it is common to see a slightly higher amplitude on the approaching side of the conductor. This is due to the distribution of current and EM fields not propagating far enough at early times to lose the influence of the large square loop. In the Ogilvy example, this asymmetry does not occur, because the transmitter and receiver are of the same size. In this case, for a south to north survey line, the higher asymmetric amplitude is seen over the southern portion of the line.

This result also does well to demonstrate the differences in the **B**-field and d**B**/dt response curves for a basic vertical conductor. The **B**-field response of the conductor has higher amplitude even out to the latest times, making the presence of the conductor more apparent over the entire time window, and as mentioned in the previous chapter, the **B**-field shows reversals in response polarity only at early times. Figure 5.13 shows a comparison of the time-domain z-component magnetic field response vs. distance plots for three vertical conductor models of varied conductor resistivity at six selected time gates from upper left to lower right. Overall the 3

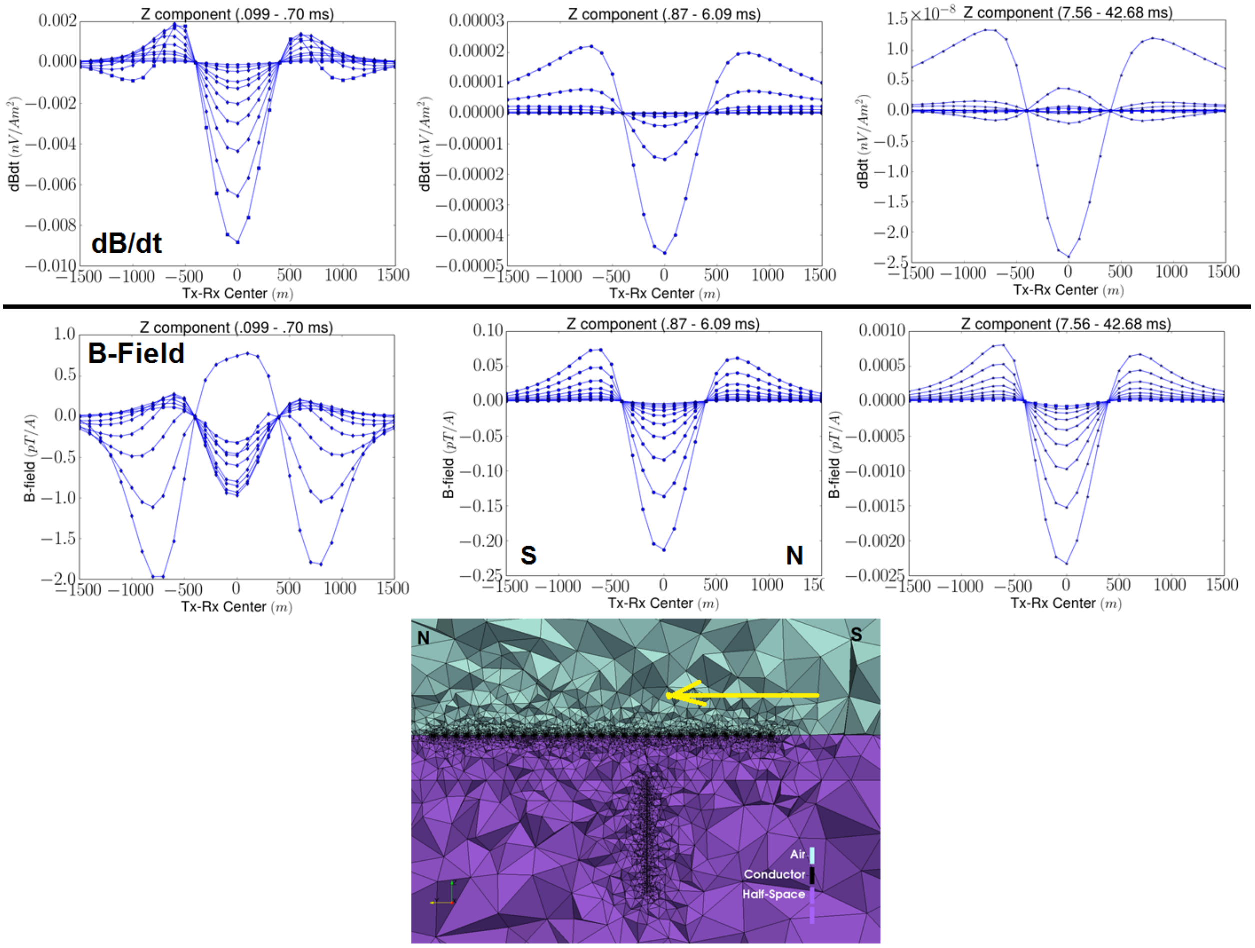

Figure 5.12: Time-domain z-component d$\mathbf{B}$/dt and $\mathbf{B}$-field response vs. distance for the 3 Ohm-m vertical conductor at early and middle-time gates. At top are the dB/dt results and below are the B-field results. At the bottom of the figure is a cross-section along the y-axis of the model mesh.

and 30 Ohm-m conductor models are of higher response amplitude than the 300 Ohm-m model at the time gates shown, and this was to be expected. Also interesting are the differences in the sign reversals of the response seen between these models, doing well to confirm from the section above that conductor resistivity plays an important role in this phenomenon. The $\mathbf{B}$-field response, not shown, is very similar

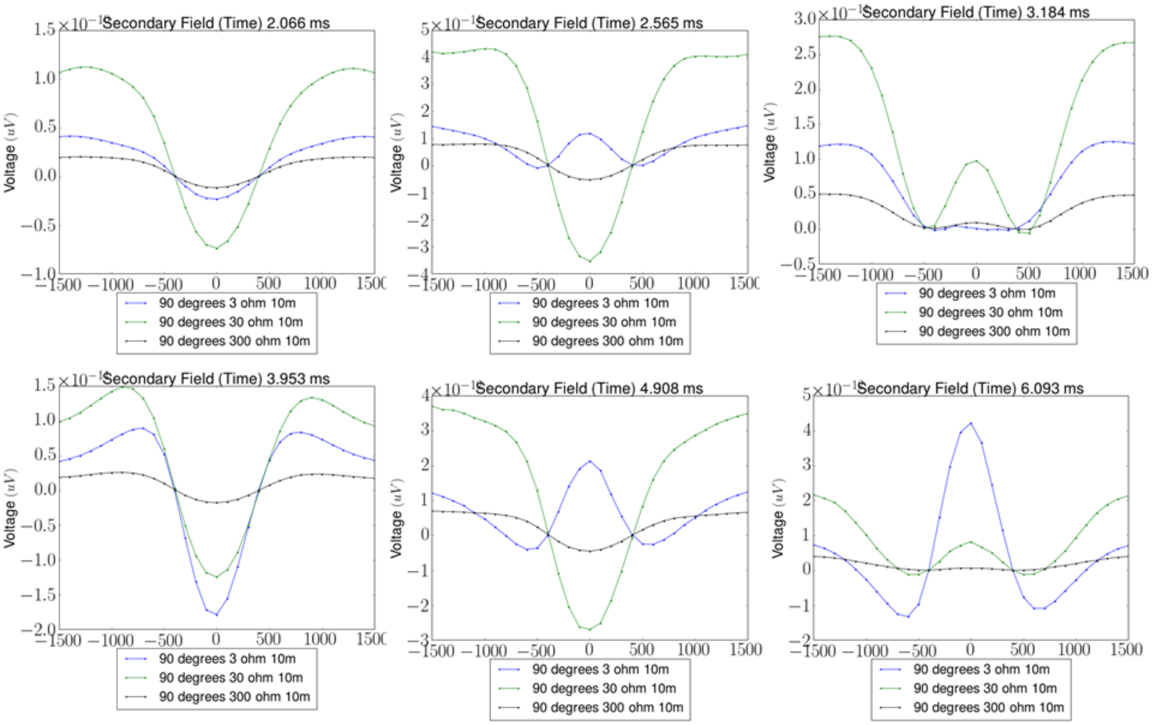

Figure 5.13: Comparison of time-domain z-component d$\mathbf{B}$/dt results for the 10 m thick vertical conductor model with varied conductor resistivity at six selected time gates from upper left to lower right.

regarding changes in response amplitudes over this range of time gates, except without the sign reversals (see Appendix H).

5.6.2 Dipping Conductors

To determine the effect of conductor dip, a set of models with 60-degree dips both to the south and north, and perpendicular to the survey line, were created with conductor thicknesses of both 10 m and 700 m. In all cases strike length and depth extent were 400 m by 1 km respectively for the 10 m thick conductors, and 800 m by 1 km respectively for the 700 m thick conductors. The top of the conductor was located 400 m below the surface. The half-space resistivity was 3500 Ohm-m and three conductor resistivities of 3, 30, and 300 Ohm-m were again tested. Figure 5.14

shows the time-domain z-component d**B**/dt and **B**-field response vs. distance plots for the 3 Ohm-m vertical conductor at all time gates, for the north-dipping and south-dipping conductor models respectively. The response is again broken into groupings of three time windows--early, middle and late--to better observe the varied characteristics of the simple dipping conductor response over time. For these, and all models, the survey line runs from south to north (i.e. -m to +m along the plotting distance axis) as indicated by a yellow arrow in the figure. It is important to note that this is visually opposite of the plotted results.

A few of the important characteristics of dipping conductor models seen in these results are the increase or decrease in the early time asymmetry of the response when compared with the vertical conductor, as well as the increasing asymmetry of the results seen at middle and late times. As seen at mid-times (center of Figure 5.14) the response is asymmetric with the higher amplitude corresponding to the direction in which the conductor is dipping. The d**B**/dt results also do well to reproduce the characteristic response of a thin dipping conductor as seen in Ogilvy (1986), with differences at early times being due to the much greater depth of the conductor in this case. It is also interesting to note that the response of the north-dipping conductor is virtually the mirrored image of the south dipping conductor at all but early times where some variation occurs, this due to the survey geometry. At early times the responses are very similar to that of the vertical conductor model (Figure 5.12) with differences primarily in the amplitude of the two positive peaks of the response and a minor offset of the response minima from zero along the survey line. Figure 5.15 shows the time-domain z-component d**B**/dt and **B**-field response vs. distance plots for the 30 Ohm-m vertical conductor at all time gates, for the north-dipping and south-dipping conductor models respectively. This example is presented as a comparison to the 3 Ohm-m model results to illustrate the fact that as the resistivity of the conductor increases the highly asymmetric d**B**/dt response seen at middle times for the 3 Ohm-m conductor in Figure 5.14 give way to skewed trough responses with response minima progressively offset from zero in the direction of conductor dip at progressively later times. In the **B**-field results, the progressive skewing of the response minima is less apparent, but the minima are offset in the direction of conductor dip. Overall the **B**-field results appear to be somewhat less successful in identifying a dipping conductor as the resistivity increases, and the response is very close in appearance to the response of the vertical conductor. This is especially apparent at middle and late times, and in a situation where the exact location of the conductor is not known, the offset of the minima caused by the dip might be overlooked.

Figures 5.16 and 5.17 are very similar to Figures 5.14 and 5.15, with the only difference being that the thickness of the dipping conductors was increased to 700 m to study the response of a broad dipping conductive package. At a thickness of 700m the conductor is broad enough to give a double trough response, and so the response vs. distance plots are more complicated than the comparable thin conductor models. Of note here is the difference in the response curves as the conductor resistivity is increased, which is quite substantial at middle-times for d**B**/dt and later times for the **B**-field response. The resemblance of the late-time d**B**/dt responses for the 3 Ohm-m conductor (Figures 5.16) to the mid-time responses of the 30 Ohm-m conductor (Figures 5.17) is also interesting.

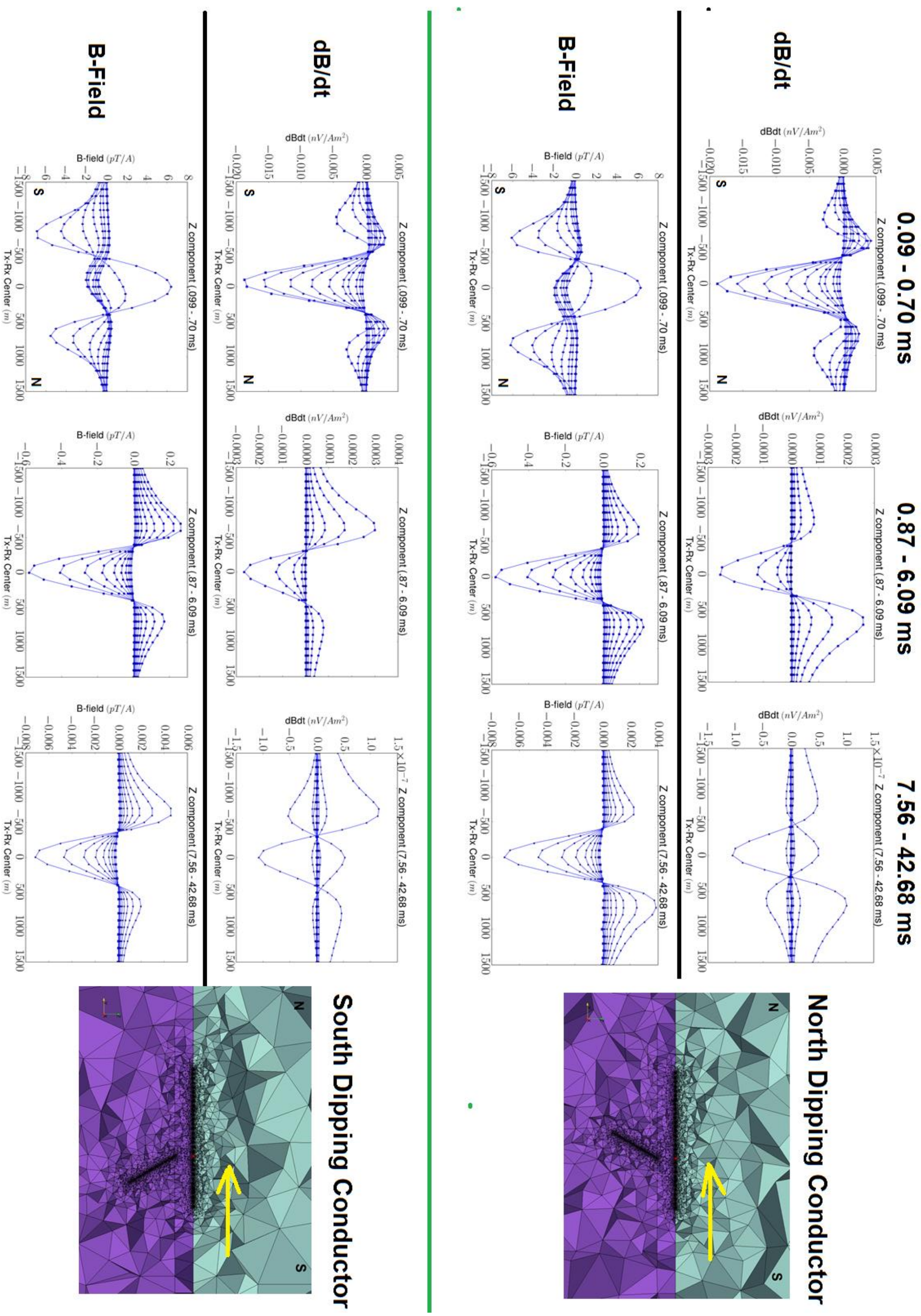

Figure 5.14: See page 122 for full caption.

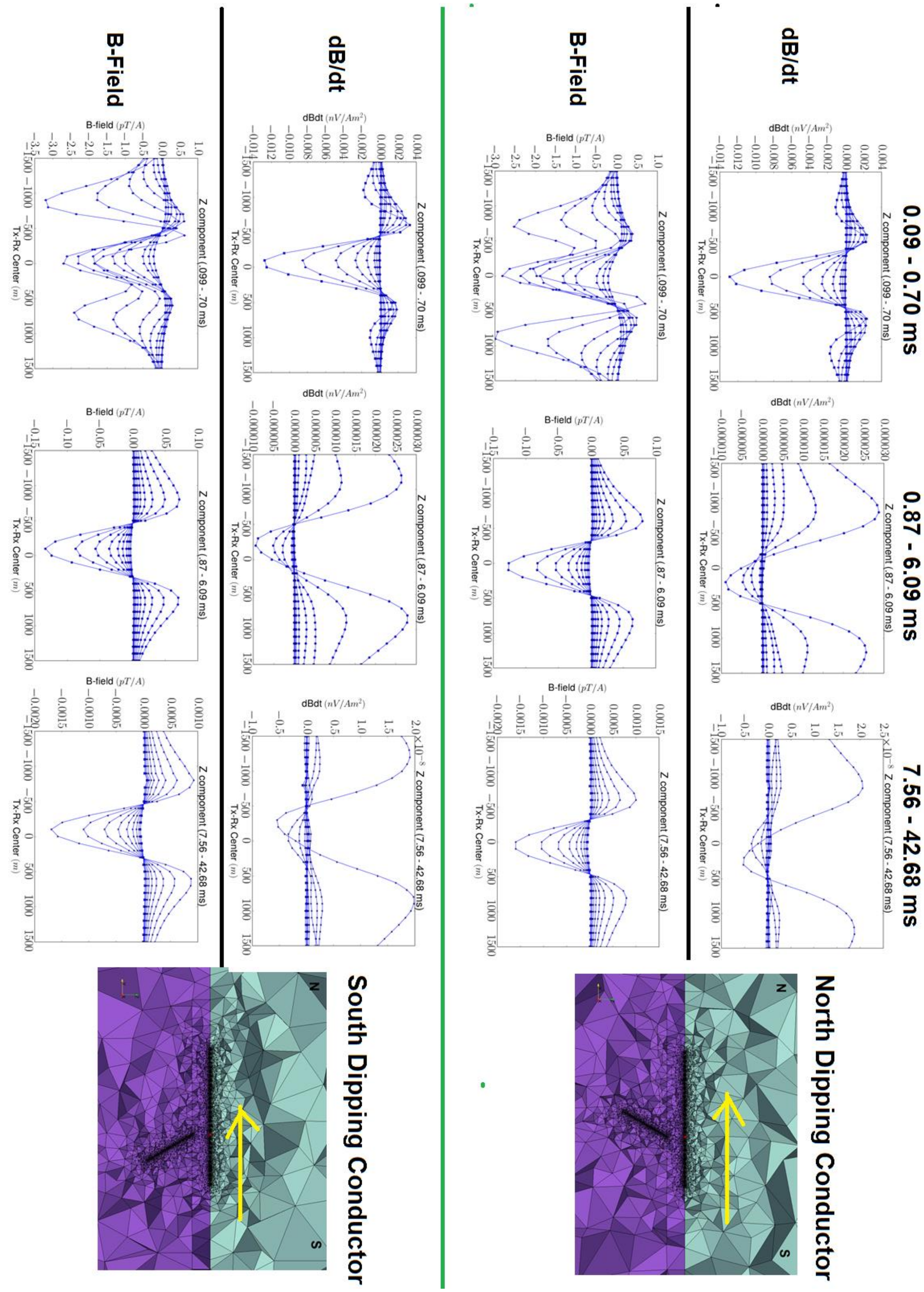

Figure 5.15: See page 122 for full caption.

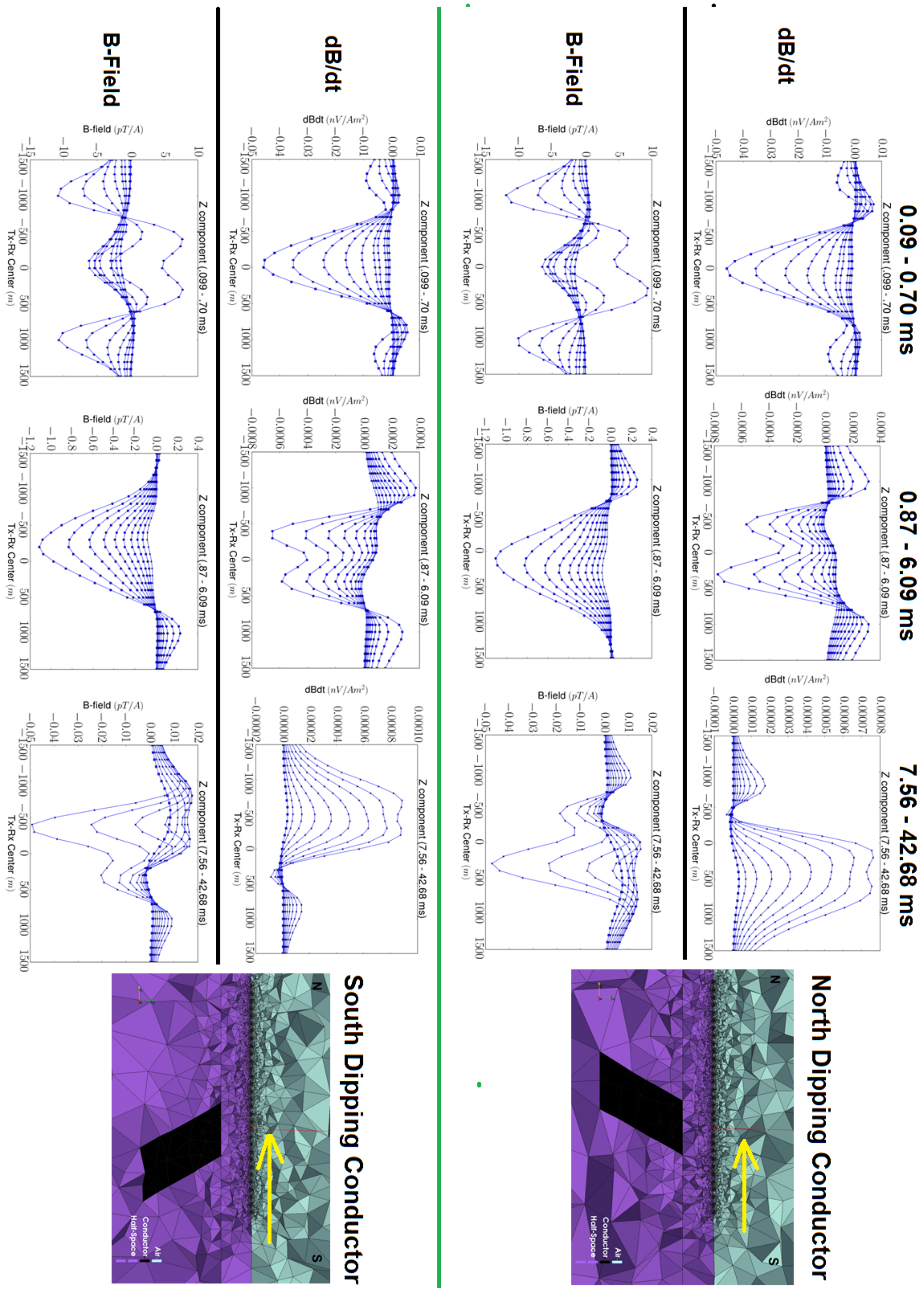

Figure 5.16: See page 122 for full caption.

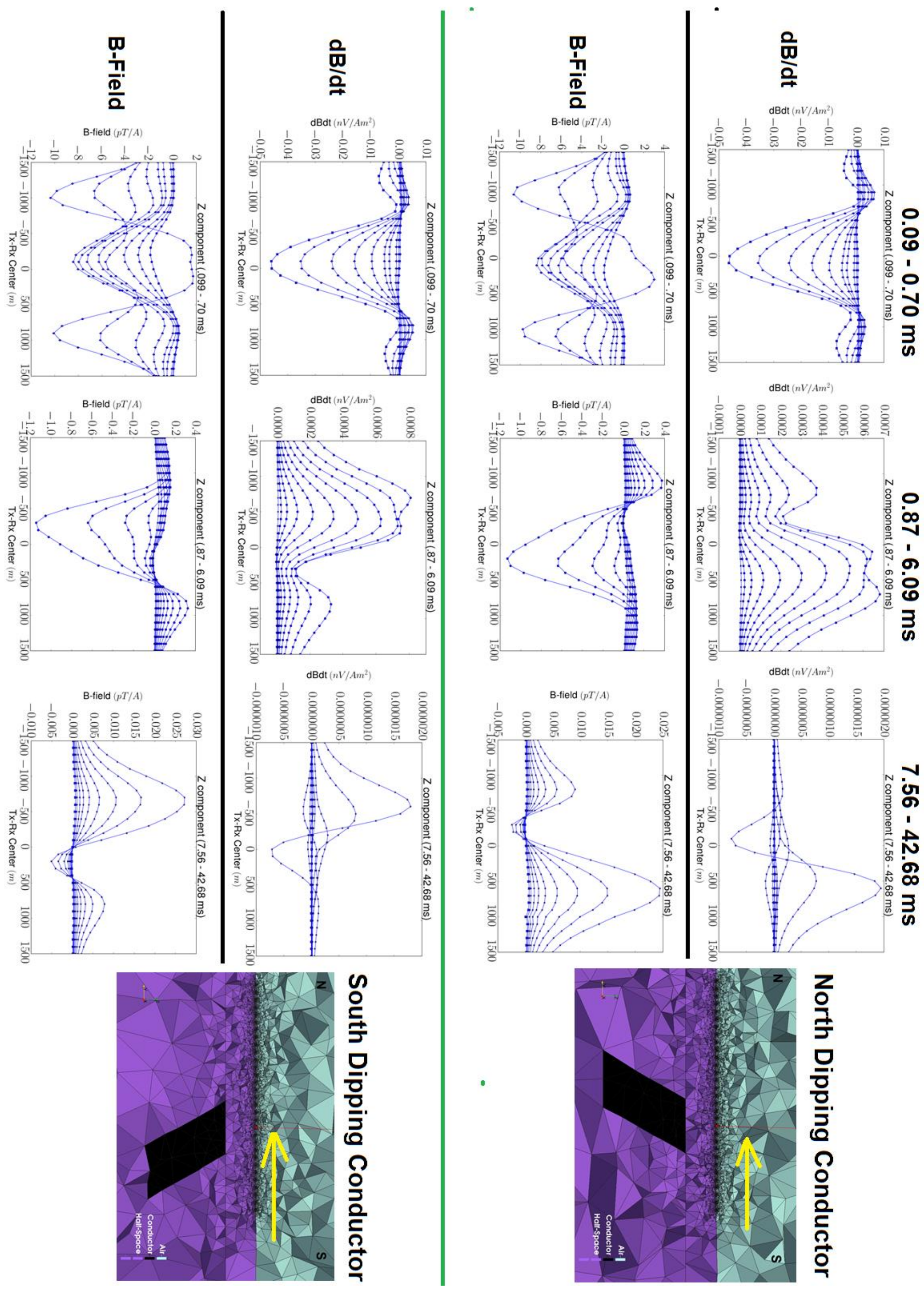

Figure 5.17: See page 122 for full caption.

Figure 5.14: Time-domain *z*-component d**B**/dt and **B**-field response vs. distance for the *3 Ohm-m, 10 m thick,* north and south-dipping conductor models at all time gates. At the right is the cross-section along the *y*-axis of the model mesh, the yellow arrow indicates the direction of data collection.

Figure 5.15: Time-domain *z*-component d**B**/dt and **B**-field response vs. distance for the *30 Ohm-m, 10 m thick*, north and south-dipping conductor models at all time gates. At the right is the cross-section along the *y*-axis of the model mesh, the yellow arrow indicates the direction of data collection.

Figure 5.16: Time-domain *z*-component d**B**/dt and **B**-field response vs. distance for the *3 Ohm-m, 700 m thick,* north and south-dipping conductor models at all time gates. At the right is the cross-section along the *y*-axis of the model mesh, the yellow arrow indicates the direction of data collection

Figures 5.17: Time-domain *z*-component d**B**/dt and **B**-field response vs. distance for the *30 Ohm-m, 700 m thick,* north and south-dipping conductor models at all time gates. At the right is the cross-section along the *y*-axis of the model mesh, the yellow arrow indicates the direction of data collection

5.6.3 Thick Conductors

Next, a series of vertical conductor models of varied thicknesses were constructed to determine, in part, the resolution of the forward modeling method within the constraints of the depths of conductors seen in Athabasca Basin, as well as the Slingram-style survey design typically used there. In each case, the 30 Ohm-m conductor was located at a depth of 400 m in a 3500 Ohm-m half-space. Five models were created with conductor thicknesses of 10, 100, 500, 600, and 700 metres. The strike length and depth extent of the conductors were 800 m and 1 km respectively in each case. Figure 5.18 shows the model meshes for the five thickness models, and Figures 5.19 and 5.20 show comparisons of the time-domain *z*-component d**B**/dt and **B**-field response vs. distance plots for the thickness models at six selected time gates from upper left to lower right. First, it is noted that the response amplitude for the 10 m and 100 m conductors is much lower than for the 500 – 700 m conductors, and so they are hard to interpret in this plot. However,

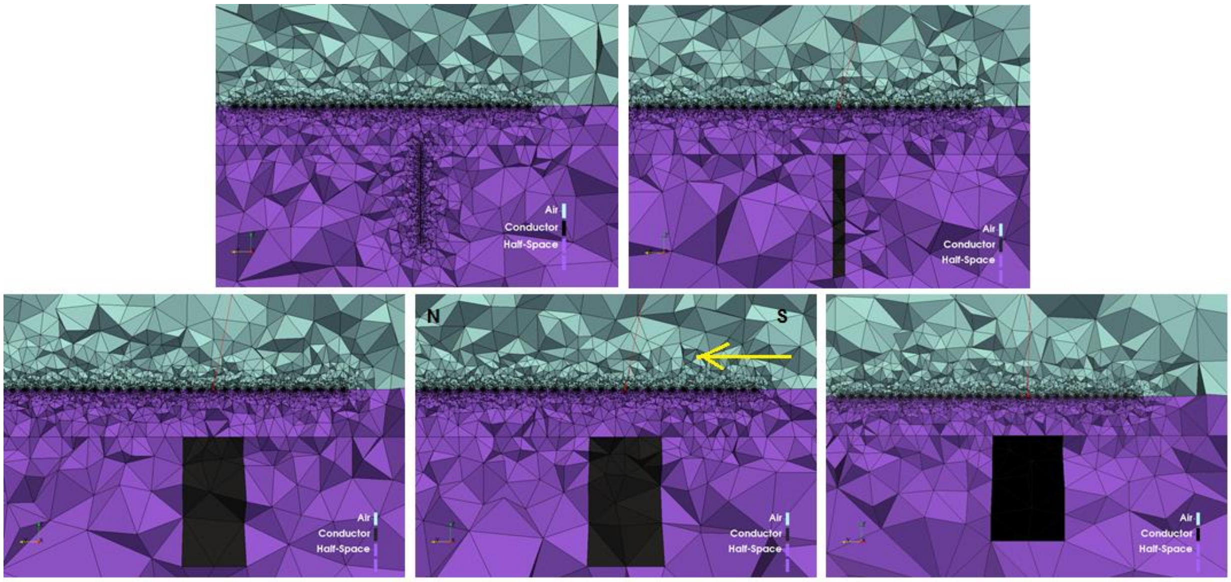

Figure 5.18: Cross-sections along the y-axis of the model meshes for the five conductor thickness models. From top left to bottom right are the 10, 100, 500, 600, and 700-metre-thick conductors respectively, conductor depth extent is 1 km. The yellow arrow indicates the direction of data collection.

additional examination of the results revealed that the responses for the 10 m and 100 m models are nearly identical under these conditions and take the form of the thin vertical conductor in half-space (Figures 5.11 and 5.12). The primary goal of this investigation was to determine the thickness at which the conductor would give a double trough anomaly, meaning that the survey was detecting both the south and north sides of the conductor uniquely. This is an important aspect of the survey resolution and demonstrates to some extent how far apart two conductors might need to be before they can be detected as individual conductors at 400 metres depth, more will be discussed on this later in the two-conductor example. Also, it determines the thickness of an individual conductive unit at which it may appear as two distinct units and possibly confuse interpretation. In Figure 5.19, it can be seen

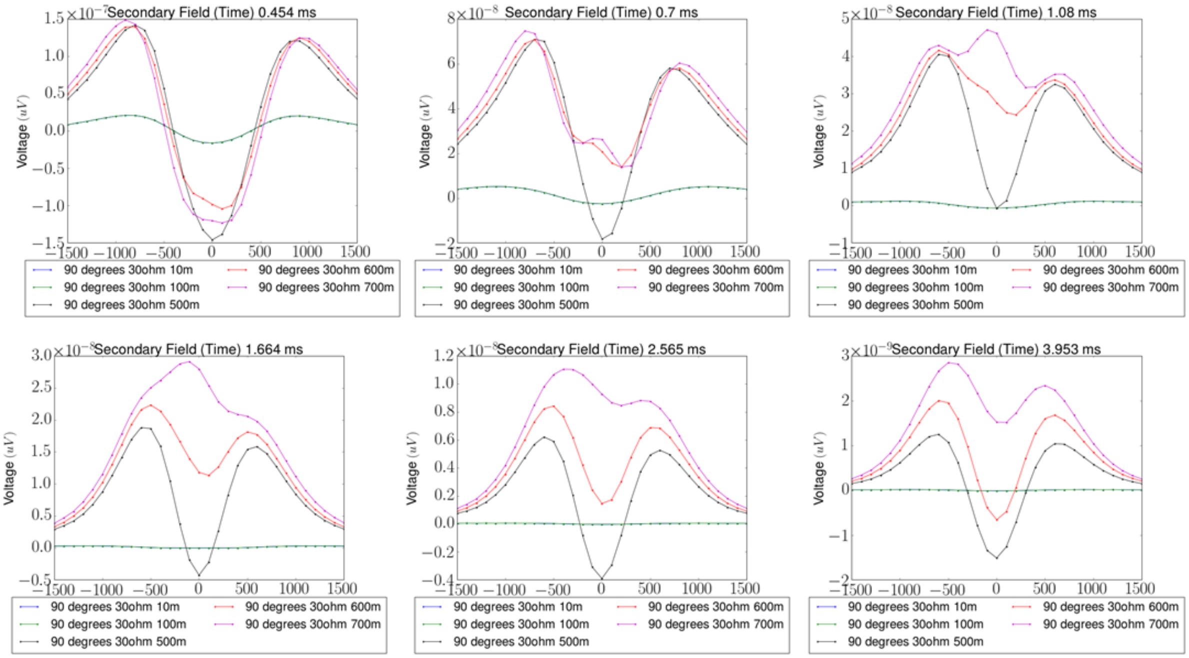

Figure 5.19: Comparison of time-domain z-component d**B**/dt results for five models of varied conductor thickness at six selected time gates from upper left to lower right.

that at early times a double trough anomaly is detected for the 700 m thick conductor in the d**B**/dt response, but by nearly 4 milliseconds this feature has gone. The 600-m conductor also very briefly gives a double trough but only in 2-3 time gates. In Figure 5.20, the **B**-field response shows double trough responses in the 600 m and 700 m models at slightly later time gates, but again this feature is gone by 4 milliseconds. There is, however, good demonstration of other characteristics of increasing conductor thickness seen in these results. It is evident that as thickness increases the trough broadens, the response amplitude increases over the entire survey line, and the difference in amplitude between the two positive peaks and the, typically negative, trough is decreased. As seen in the lower right of Figures 5.19 and 5.20 the minimum response may not even actually be negative for very thick conductors even at late times.

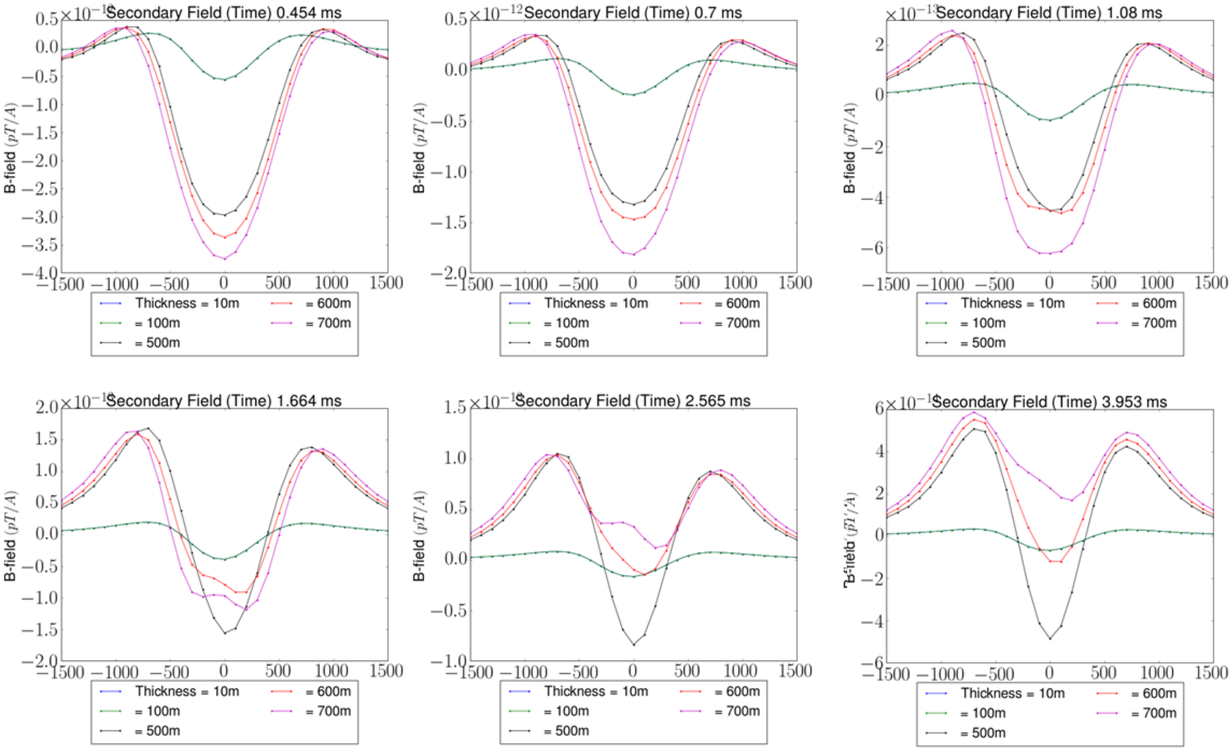

Figure 5.20: Comparison of time-domain z-component **B**-field results for five models of varied conductor thickness at six selected time gates from upper left to lower right.

5.6.4 Two Vertical Conductors at Varied Depths

For the final investigation into simple conductor models, a set of six models containing two thin vertical conductors at a constant separation but, at varied depths were created to further determine the resolution capabilities of the Athabasca Basin style Slingram TEM survey. In each case two 20 m thick, 30 Ohm-m conductors were separated by 100 metres in a 3500 Ohm-m half-space. Each conductor had a strike length of 400 m and the depth to the top of the set of conductors was modeled at six depths: 50, 100, 200, 300, 400, and 500 metres. The depth to the bottom of the conductor was kept at a constant 1400 metres, and so the total depth extent of the conductors varied from 1350 to 900 metres.

Figure 5.21 shows the model meshes for the six models, and Figure 5.22 shows a comparison of the time-domain z-component d$\mathbf{B}$/dt response vs. distance plots for the twin conductor models at six selected time gates from upper left to lower right. As in the previous section, the presence of a double trough response is indicative of the method having the resolution necessary to detect the conductors individually under the conditions being modeled. It was not expected that detection of the individual conductors was possible at depths of 300 - 400 metres using this survey design. However, less was known about the resolution at intermediate depths, and whether, if a double trough is not achieved, there are any other characteristics of the response that may indicate the presence of two conductors at depths beyond 300 metres. Figure 5.22 demonstrates that for some early times the double trough response is observed in the 50 – 200 m conductor depth models, and some flattening of the trough minima in the 300 m depth model may also indicate the two individual conductors. At later times, even the shallower conductors are not able to be individually distinguished, and the d$\mathbf{B}$/dt responses do not vary distinctly from that for single vertical conductor models like those seen in previous sections. Figure 5.23 shows a comparison of the z-component d$\mathbf{B}$/dt response vs. distance plots at six selected time gates from left right to lower right for four models: a single 10 m thick 30 Ohm-m vertical conductor, a 10 m thick 300 Ohm-m vertical conductor, a 100 m thick 30 Ohm-m vertical conductor and the twin 20 m thick 30 Ohm-m vertical conductors. In all four models, the depth to the top of the conductor(s) is 400 m. First, as mentioned in the previous section there is almost no difference in the response of the 10 m and 100 m thick conductors, and this is further illustrated here. The behavior of the twin 30 Ohm-m conductors more closely resembles the response

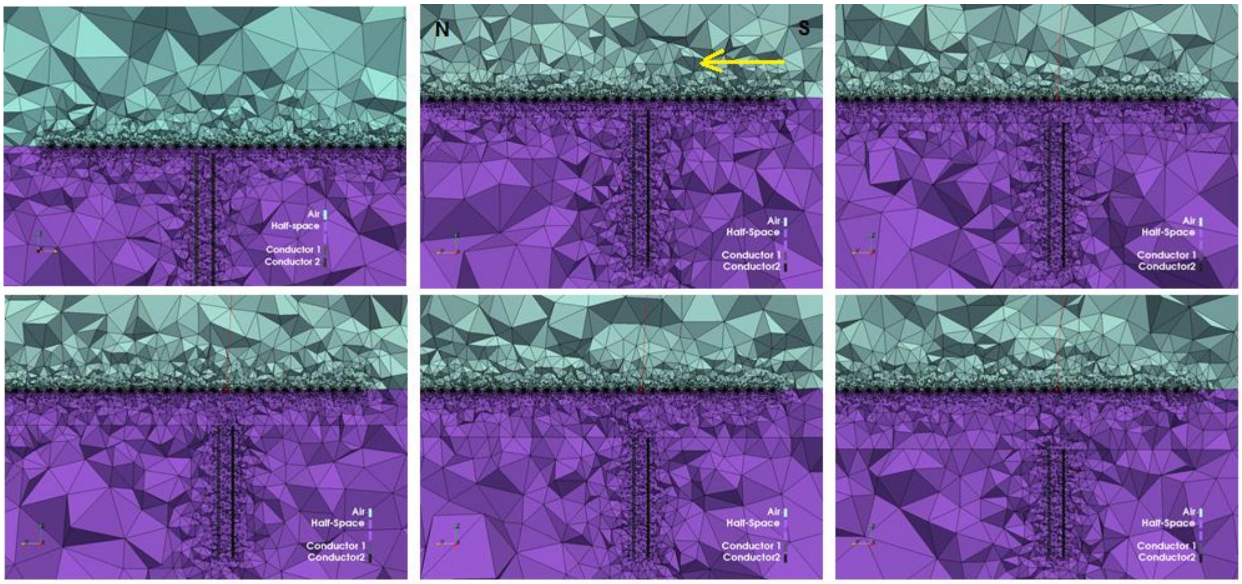

Figure 5.21: Cross-sections along the y-axis of the model meshes for the six twin conductor models. From top left to bottom right depths to the top of the conductors are 50, 100, 200, 300, 400, and 500 metres respectively, conductor depth extent is approximately 1 km. The yellow arrow indicates the direction of data collection.

of the single 300 Ohm-m conductor in most cases, this is likely due to the fact that the cumulative conductance is the same in each case.

Figure 5.23 shows a comparison of the z-component d$\mathbf{B}$/dt response vs. distance plots at six selected time gates from left right to lower right for four models: a single 10 m thick 30 Ohm-m vertical conductor, a 10 m thick 300 Ohm-m vertical conductor, a 100 m thick 30 Ohm-m vertical conductor and the twin 20 m thick 30 Ohm-m vertical conductors. In all four models, the depth to the top of the conductor(s) is 400 m. First, as mentioned in the previous section there is almost no difference in the response of the 10 m and 100 m thick conductors, and this is further illustrated here where they plot directly on top of each other. The behavior of the twin 30 Ohm-m conductors more closely resembles the response of the single

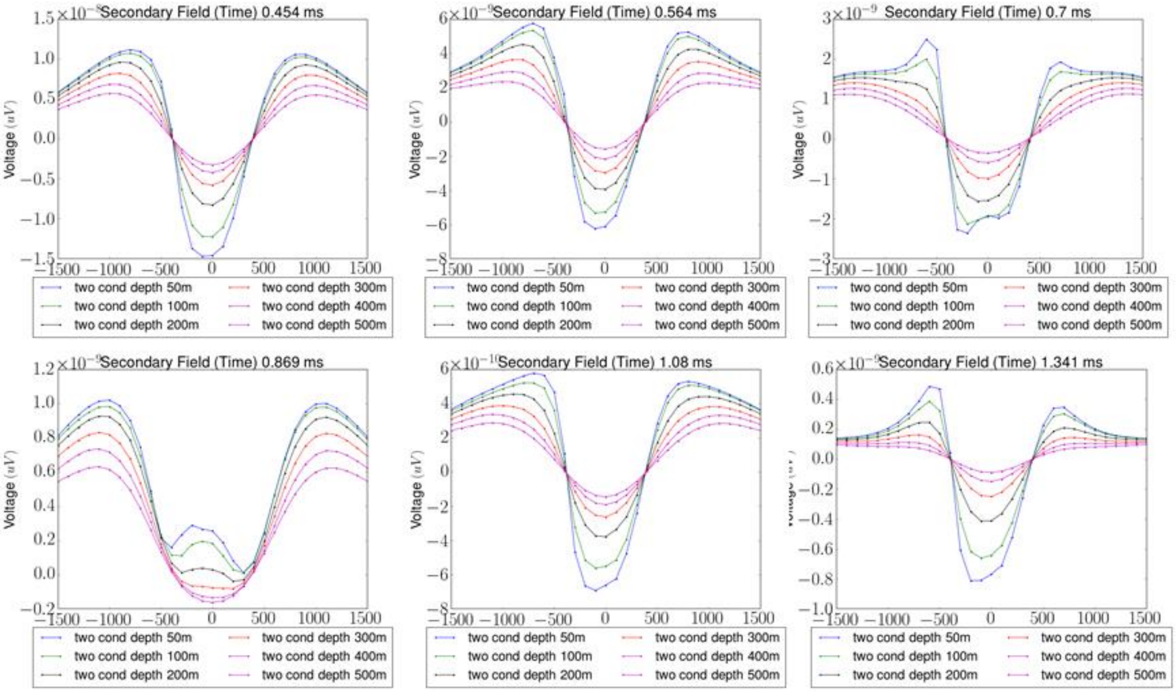

Figure 5.22: Comparison of time-domain z-component d$\mathbf{B}$/dt results for the six twin conductor models of varied depths at six selected time gates from upper left to lower right. Conductor separation is 100m and thickness is 20m.

300 Ohm-m conductor in most cases, this is likely due to the fact that the cumulative conductance is the same in each case.

Figure 5.24 shows a comparison of the time-domain z-component $\mathbf{B}$-field response vs. distance plots for the twin conductor models at six selected time gates from upper left to lower right, like Figure 5.22. For the $\mathbf{B}$-field there is no clear double trough response even for the conductors at 50 m depth and the responses resemble those of a single vertical conductor, except for some skewing of the response minima to the south of the survey line.

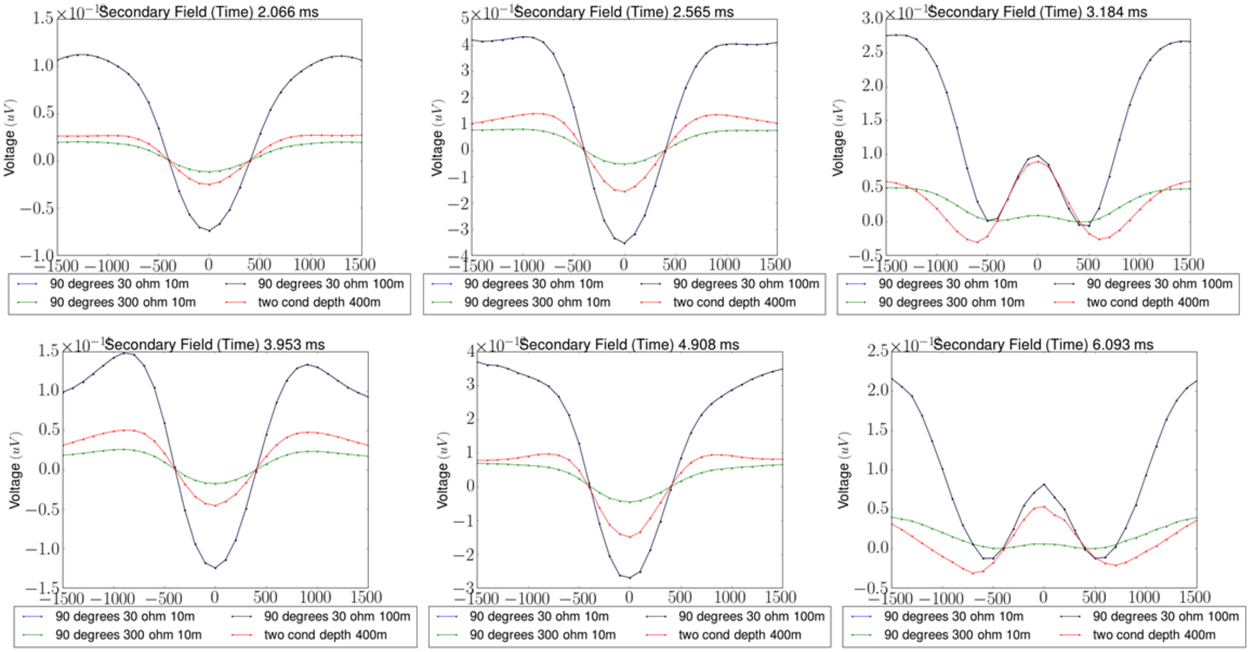

Figure 5.23: Comparison of the time-domain z-component d$\mathbf{B}$/dt response vs. distance plots at six selected time gates from upper left to lower right for four models: a single 10 m thick 30 Ohm-m vertical conductor, a 10 m thick 300 Ohm-m vertical conductor, a 100 m thick 30 Ohm-m vertical conductor and the twin 20 m thick 30 Ohm-m vertical conductors. In all four models, the depth to the top of the conductor(s) is 400 m.

Overall these results do not exactly bode well for the possibility of differentiating individual thin conductors at separations of less than 100 m and depths below even 200 metres using modeling conditions that replicate Athabasca Basin uranium exploration. However, the limits of this type of large offset Slingram-style survey were known before this investigation and rather than being disappointing they simply imply that in order to better distinguish individual thin conductors at depth further investigation into improved survey design for better target resolution is necessary. It is possible that the hybrid style step-wise moving loop transmitter-receiver layout could better define the individual conductors but this remains to be tested.

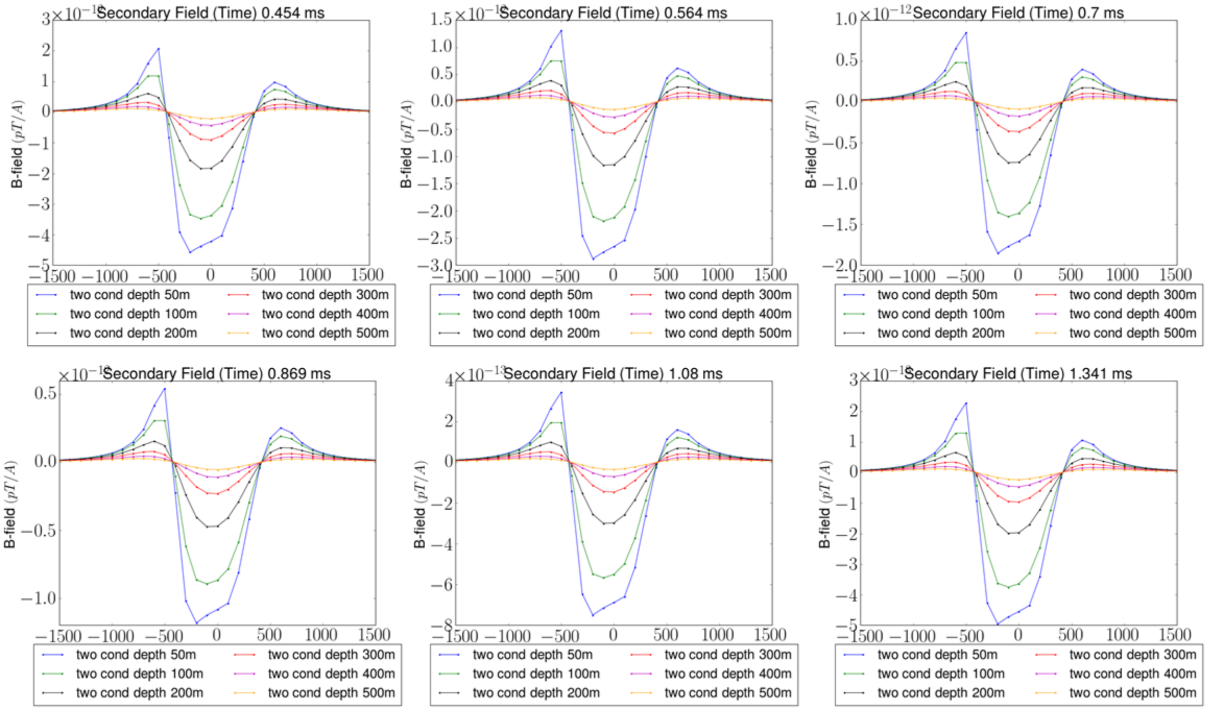
Secondary Field (Time) 0.454 ms

Secondary Field (Time) 0.564 ms

Secondary Field (Time) 0.7 ms

Secondary Field (Time) 0.869 ms

Secondary Field (Time) 1.08 ms

Secondary Field (Time) 1.341 ms

Figure 5.24: Comparison of time-domain z-component $\mathbf{B}$-field results for the six twin conductor models of varied depths at six selected time gates from upper left to lower right. Conductor separation is 100m and thickness is 20m.

5.7 Conclusions

The forward modeling results presented in this chapter do well to demonstrate the ability of this method to accurately produce time-domain EM response curves for simplified conductors in situations representing modern ground TEM uranium exploration methods in the Athabasca Basin. Results of comparisons to the published modeling results of Newman et al. (1986), and Ogilvy (1986), show good agreement and help to establish the accuracy of the method. An investigation into the sign reversals in the frequency-domain response vs. distance plots showed that these are intrinsic properties of the frequency-domain response and occur at varied frequency ranges depending at least partially on the resistivity of the model half-space. Time domain sign reversals were shown to have more complicated origins and depend on a range of factors including the half-space and conductor resistivity, as well as the conductor geometry, survey design, etc. Results of the series of simple conductor models gave insight on the characteristic time-domain z-component magnetic field response vs. distance curves for simple conductors of varied thickness, dip, resistivity, etc. These results establish a means for interpretation of more complicated model responses seen in the final chapter. With success in modeling simple conductors, this method was ready to be applied to more complex models representing actual geologic situations. In the following, and final chapter models designed specifically to address exploration scenarios faced by ARC in the Athabasca Basin are presented, these results will more fully demonstrate the potential of this method in answering pertinent questions in modern TEM exploration.

Chapter 6

Geologically Realistic Models

6.1 Introduction

The final step in this research was to put the forward modeling method to full use in computing synthetic time-domain magnetic field responses for models representing realistic geologic situations faced in the exploration for uranium in the Athabasca Basin. Previous results have shown that this method can accurately reproduce 1D time-domain magnetic field responses for resistive half-spaces, as well as previously published 3D responses for simple conductors in half-space. Although verification of results for more complex models is not possible to the same degree as it was for the simple conductor models in the previous chapter, those results serve as a basis for interpretation and verification as models become more complex. In this chapter, six geologically inspired models will demonstrate the effects on the time-domain magnetic field response of the presence of multiple graphitic conductors, conductive basin sediments and paleoweathered basement over the conductor, faulted and folded conductors, the presence of moderately resistive metasediment units alongside conductors, and the presence of a simplified ore zone and accompanying sediment alteration. Finally, the results will be presented for a complicated reproduction of a 4 km long cross-section through the Athabasca Basin for which actual ground TDEM data has been collected on site and can offer a direct comparison to the modeled response. The geology simulated in these models is for the most part still relatively simple at this stage. However, as the results will show, this forward modeling method can be used successfully to produce synthetic time-domain EM responses that answer specific exploration questions in a variety of situations.

6.2 Complex Model Design

All of the modeling results presented in this chapter were created using the FacetModeller software described in Chapter 3. This program allowed for the construction of the models visually in two and three dimensions, which was very helpful when creating models containing multiple geologic units. As there was not a great deal of detailed 3D geologic data available for the project, the models presented here were designed based on extensions of 2D cross-sections or plan maps, which are easily inserted into the FacetModeller program to be used as guides for model construction. Geologic cross-sections used in modeling were either provided by ARC based on information obtained by drilling done on their prospects in the Athabasca Basin, or created specifically for this project based on simplified situations faced in uranium exploration inspired by communication with ARC geophysicists and geologists.

6.3 Geologic Model Results

In the following sections, the results of the multiple geology inspired models are presented. Only a selection of the time-domain results will be shown here, but the full XYZ-component frequency- and time-domain results as well as the time-domain magnetic field vs. distance response at each time gate, and other relevant model information for these models, are presented in Appendix I.

6.3.1 Three Closely-Spaced, Dipping, Vertical Conductors

The left side of Figure 6.1 shows an ARC cross-section through some part of the Athabasca Basin, containing three closely spaced and slightly dipping graphitic conductors at a depth of approximately 400 m below the surface. The three individual conductors form a broader unit that is approximately 50 m thick overall and has a dip of roughly 80 degrees south. Closely spaced graphitic conductors are common in relation to uranium deposition and determining the possibility of detecting and differentiating multiple conductors in the model response was an important goal of this project. The right side of Figure 6.1 shows a zoomed-in slice along the y-axis of the three-conductor model inspired by the ARC cross-section. At the bottom right of the figure the basement cells have been made transparent from the mesh to show the 3D extent of the dipping conductors. The conductors are all 30 Ohm-m in a 2500 Ohm-m half-space, arguably a low value for Athabasca Basin rocks, but as the secondary field of the conductors only is examined in this case, the effect is minimal. Figure 6.2 shows the time-domain d**B**/dt and **B**-field vs. distance plots for the three-conductor model at 29 time gates from .09 to 42 ms, plotted over three time window groupings. The response curves seen in the figure show at first glance some characteristics of a south dipping conductor which is encouraging, but

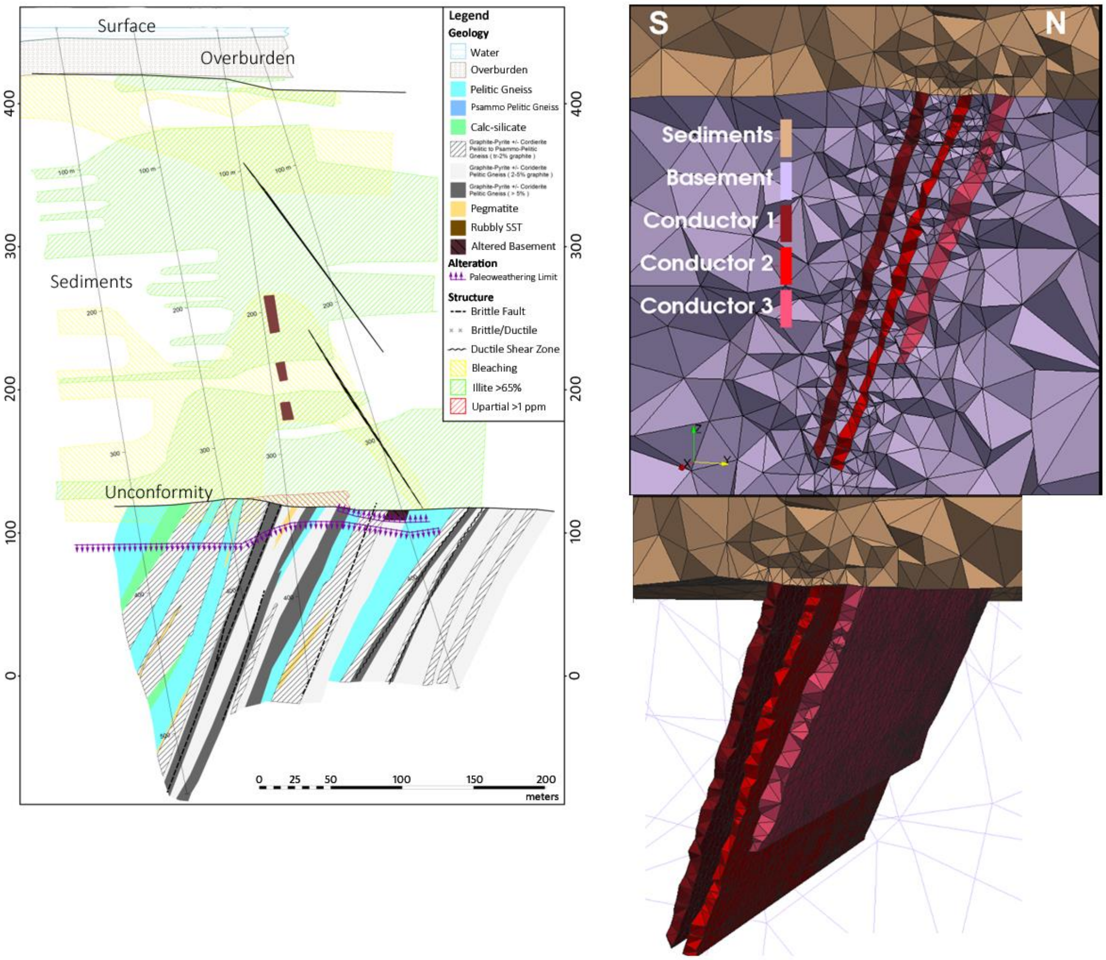

Figure 6.1: On the left is the ARC cross-section showing three closely spaced graphitic conductors. On the right is a close-up slice along the y-axis of the three-conductor model inspired by the ARC cross-section. At the bottom right basement cells have been removed to show the 3D extent of the dipping conductors.

it is harder to determine whether the presence of individual conductors is detectable. Figures 6.3 and 6.4 show the time-domain secondary magnetic field decay curves for d$\mathbf{B}$/dt and the $\mathbf{B}$-field respectively for the three-conductor model at a selection of 11 receiver locations centered over the conductor. The d$\mathbf{B}$/dt decay curve seen in Figure 6.3 is noisy at late times, and although the values are quite small, this is not

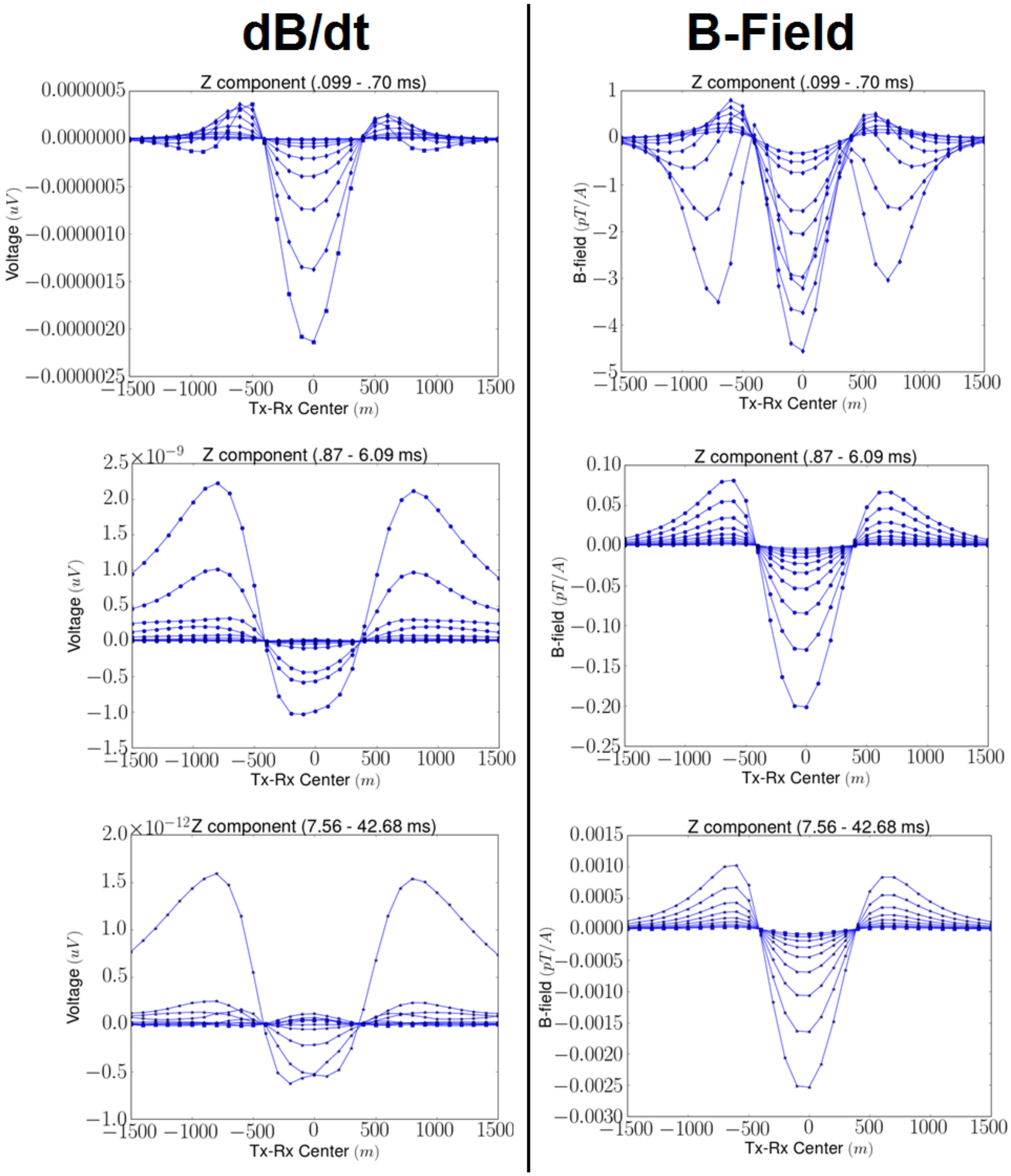

Figure 6.2: Time-domain d**B**/dt and **B**-field vs. distance plots for the three-conductor model at 29 time gates from .09 to 42 ms, plotted over three time window groupings from top to bottom.

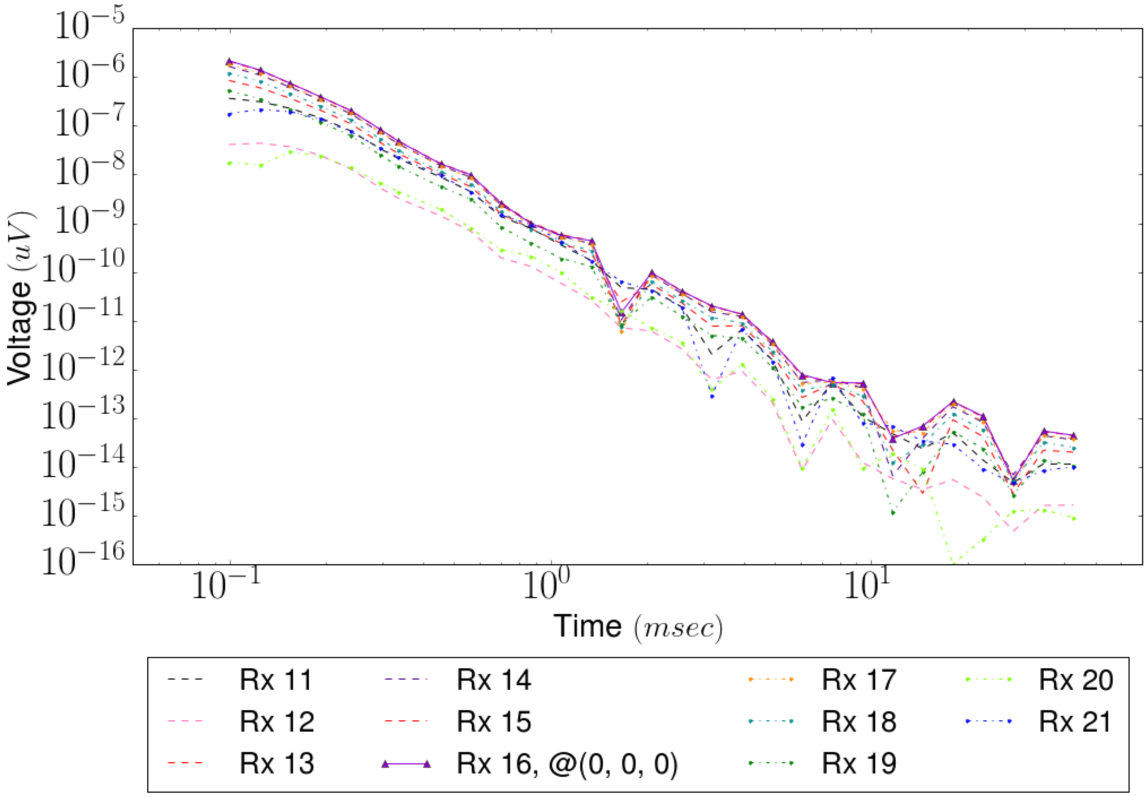

Figure 6.3: Z-component time-domain secondary field d**B**/dt decay curves for the three-conductor model at 11 selected receiver locations centered over the conductor.

exactly understood. However, the **B**-field decay curve in Figure 6.4 shows smooth decay behaviour as desired. Figure 6.5 shows a comparison of the *z*-component d**B**/dt response vs. distance plots at six selected time gates for three models: a single 10 m thick 30 Ohm-m conductor dipping 60 degrees south, a 100 m thick 30 Ohm-m vertical conductor, and in red the three conductor model. Figure 6.6 shows the same comparison but for the **B**-field response. It has been shown in the previous chapter (e.g. Figures 5.19 and 5.20) that there is very minimal difference in the responses of conductors with thicknesses less than 100 m, so the models used in this comparison seek to highlight the difference in response between single vertical and

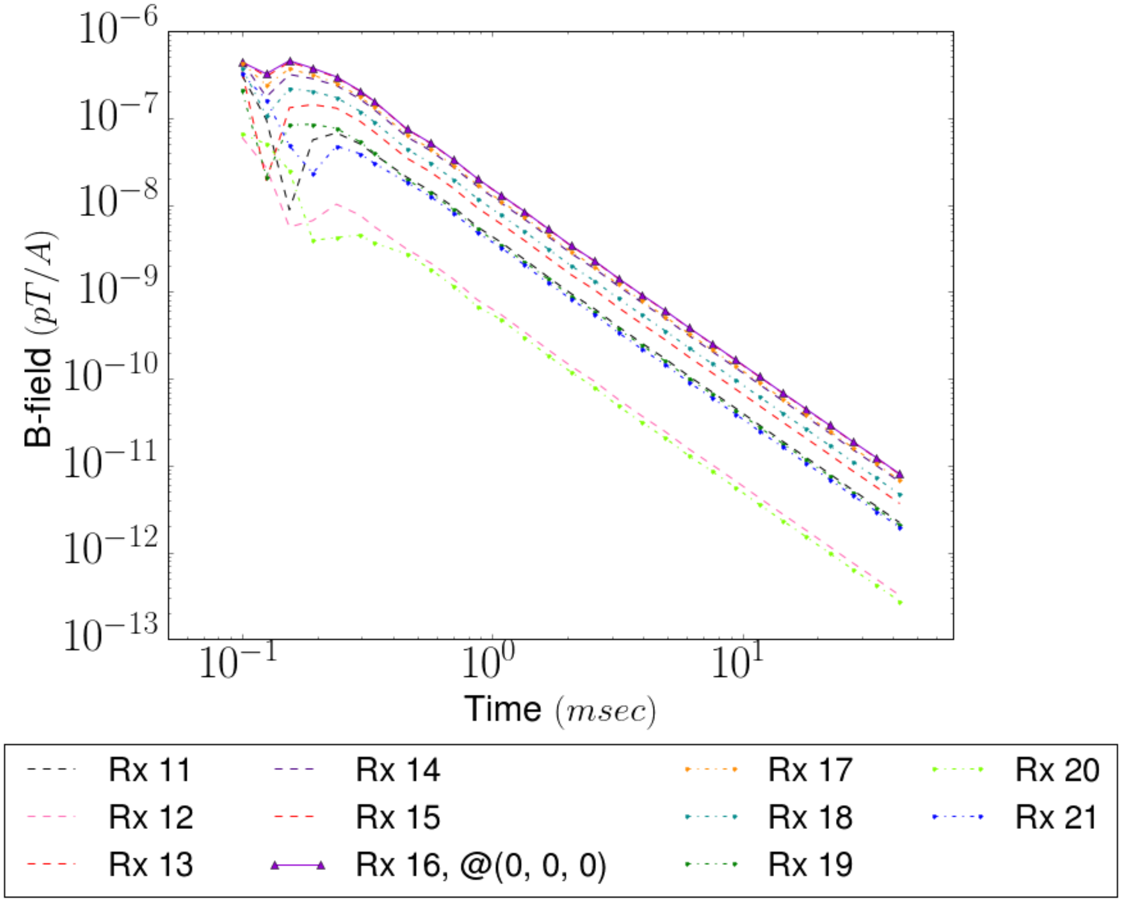

Figure 6.4: Z-component time-domain secondary **B**-field decay curves for the three-conductor model at 11 selected receiver locations centered over the conductor.

dipping conductors and the three moderately dipping conductors in this model. The comparison shows that the d**B**/dt response of the three-conductor model is somewhere between that of the vertical and dipping conductors and that no real indication of the presence of the multiple conductors is evident at these middle (or any) time gates. The **B**-field responses in Figure 6.6 show even less indication of the conductor's dip or the presence of multiple conductors except possibly the higher absolute amplitude of the response minima also seen in the d**B**/dt response. These results and the inability of the modeled survey to detect multiple conductors at 400

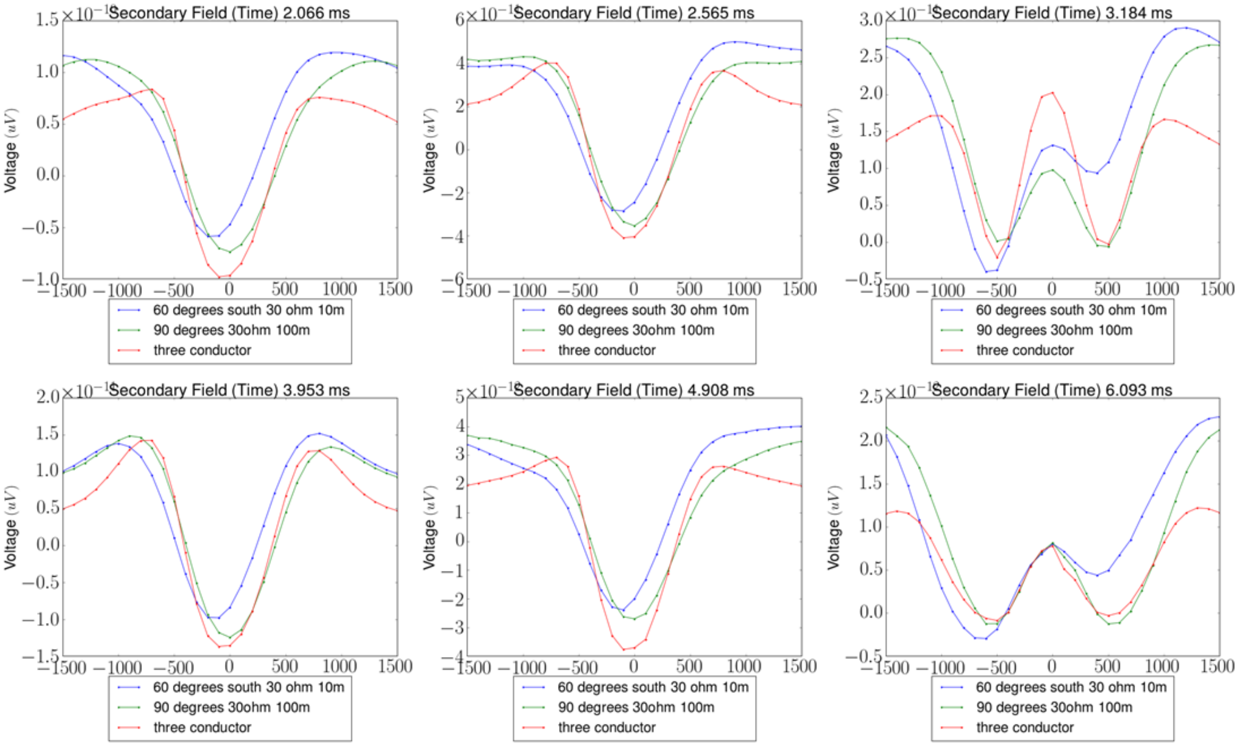

Figure 6.5: Comparison of the time-domain z-component d$\mathbf{B}$/dt response vs. distance plots at six selected time gates from upper left to lower right for three models: a single 10 m thick 30 Ohm-m conductor dipping 60 degrees south, a 100 m thick 30 Ohm-m vertical conductor, and in red the three conductor model.

m depth is perhaps to be expected after examination of the results in section 5.6.4. Although likely not apparent in Figure 6.1, the three-conductor model was the first, and the only, model to attempt to incorporate a somewhat realistic variable topography to the unconformity between the sediment and basement layers, this following the slight variation seen in the ARC cross-section. The addition of a varied topography can be a time consuming and sometimes painstaking process, and, as these results show offers no appreciable change from the flat unconformity contact used in all other models. Of course, in some instances where changes in topography

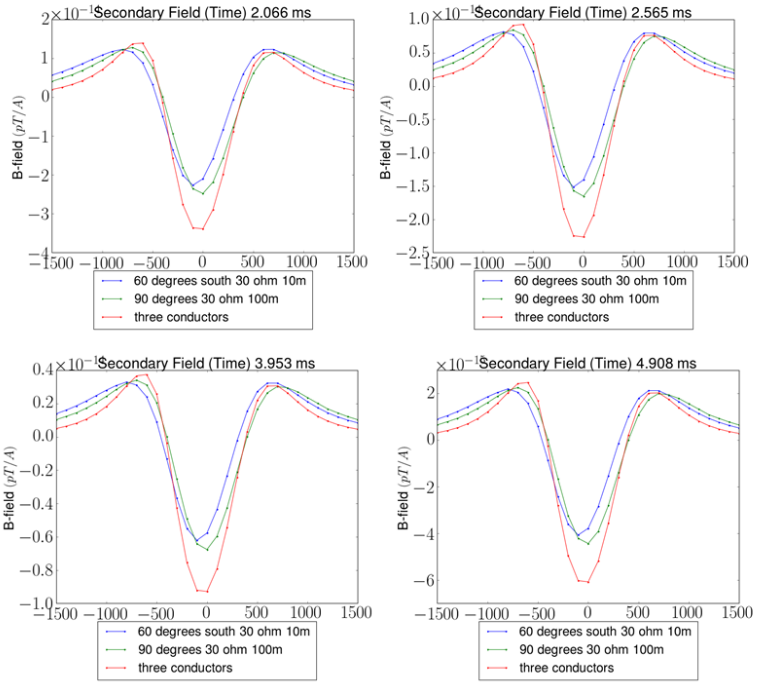

Figure 6.6: Comparison of the time-domain z-component **B**-field response vs. distance plots at six selected time gates from upper left to lower right for three models: a single 10 m thick 30 Ohm-m conductor dipping 60 degrees south, a 100 m thick 30 Ohm-m vertical conductor, and in red the three conductor model.

are within the resolution limits of the survey being modeled, making this effort is important. For this project, the majority of realistic examples obtained from ARC show a relatively flat unconformity in this region of the Athabasca Basin, and so this was not attempted in future models.

6.3.2 Paleoweathered Basement and Vertical Conductor

Another topic of interest in the modeling of graphitic conductors in the Athabasca Basin is the effect of paleoweathering in the first 100 m or so of the basement rocks at and below the unconformity surface. The presence of paleoweathering tends to increase the conductivity of the normally highly resistive basement rocks (per. comm. Pierre Martz, 2016) and there was a question as to the possible effect on the TDEM response. The extent of paleoweathering and the change in resistivity of the basement rocks caused by it are both highly variable spatially, and so only a much-simplified version of this scenario was attempted for modeling in this project. Figure 6.7 shows the model mesh with the region resistivities labeled. Figures 6.8 and 6.9 show comparisons of the secondary d**B**/dt and **B**-field vs. distance plots for three versions of the paleoweathering model. The secondary field is computed by subtracting a half-space model computed on the same mesh but with the homogeneous resistivity of the basement. At the top of each figure, the model contains all regions shown in Figure 6.7, at the center the model contains the sediment and conductor but no paleoweathering, and at the bottom are the results of the conductor in background only. No changes were made to the model mesh from version to version; the resistivity values in each region were simply changed to progressively remove the effects of paleoweathering and the sediments. The responses of the models seen at the bottom of Figures 6.8 and 6.9 are the familiar responses of a vertical conductors in resistive half-space, and by comparison the effect on the response amplitude due to the presence of the sediment and paleoweathering layers is quite pronounced.

For the vertical conductor in half-space, the computed secondary d**B**/dt and **B**-field responses are that of only the conductor, as the half-space response has been totally removed. For that reason, the response is well defined and evenly distributed along the response amplitude axis with a negative minimum over the conductor and positive maxima on the side lobes. For the other two versions of the model, the

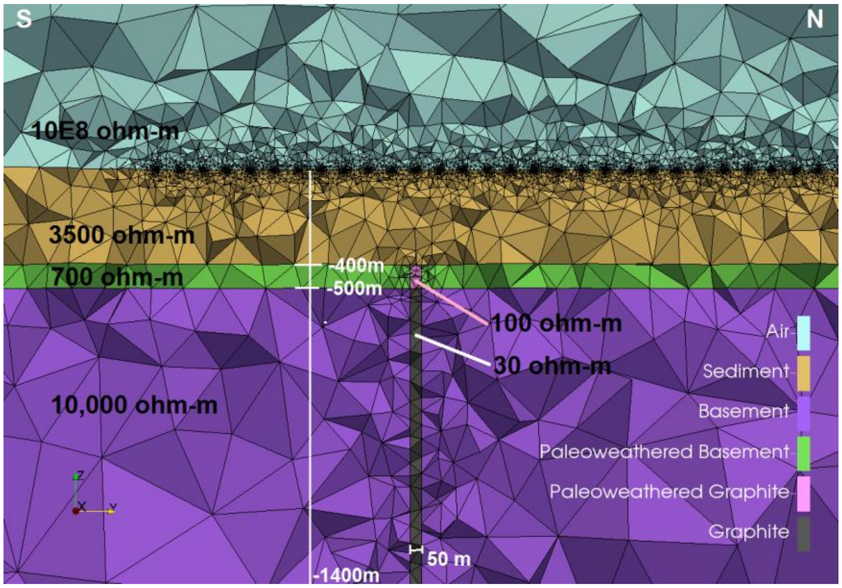

Figure 6.7: Close-up slice along the y-axis of the paleoweathering model mesh. Shown are the resistivity values of the various model regions. Conductor is 50 m by 800 m by 1000 m in thickness, strike length, and depth extent respectively.

secondary field also contains the response of the sediment layer, and the sediment layer and paleoweathering layer respectively. These layers are both resistive in comparison to the conductor but moderately conductive, especially in the case of the paleoweathering layer, when compared to the highly resistive background. The effect of the sediment layer only, as seen in the center of Figures 6.9 and 6.10, is an increased overall response amplitude, with a decrease in the apparent amplitude of the conductor compared to the background response. This effect is compounded by the presence of the paleoweathering layer as seen in the top of Figures 6.9 and 6.10. It can also be seen in both cases that the response minima are no longer negative at middle and late-times. However, the presence of the conductor is still evident even at later times. Figure 6.11 shows a comparison of the time-domain z-component d$\mathbf{B}$/dt response vs. distance plots at six selected time gates from upper left to lower right for the three versions of the weathering model. This is perhaps not the best way to analyze the results in this case, but it does well to illustrate the magnitude of the increase in the background response amplitude when the sediment layer and paleoweathering are included.

Figures 6.11 and 6.12 respectively show comparisons of the secondary field d**B**/dt and **B**-field time-decay curves for the three versions of the model. The d**B**/dt late-time response is seen to degrade as the paleoweathering and then sediment layers are respectively removed. This noisiness in the decay is thought to be occurring because the EM field persists to later times within the more conductive units and so gives a measurable response distinct from background noise. The **B**-field response does not degrade with time but does progressively lose the early time sign reversal seen as a sharp downward spike in the curve.

The effects of the conductive paleoweathering layer over the conductor, as well as the more resistive but still relatively conductive sediment layer above the conductor, can be generalized to many situations where a conductive layer lies over a conductor in a resistive half-space. This includes the thin, but conductive overburden layer often encountered in the Athabasca Basin, which through other experimentation has shown to have similar effects to those described above.

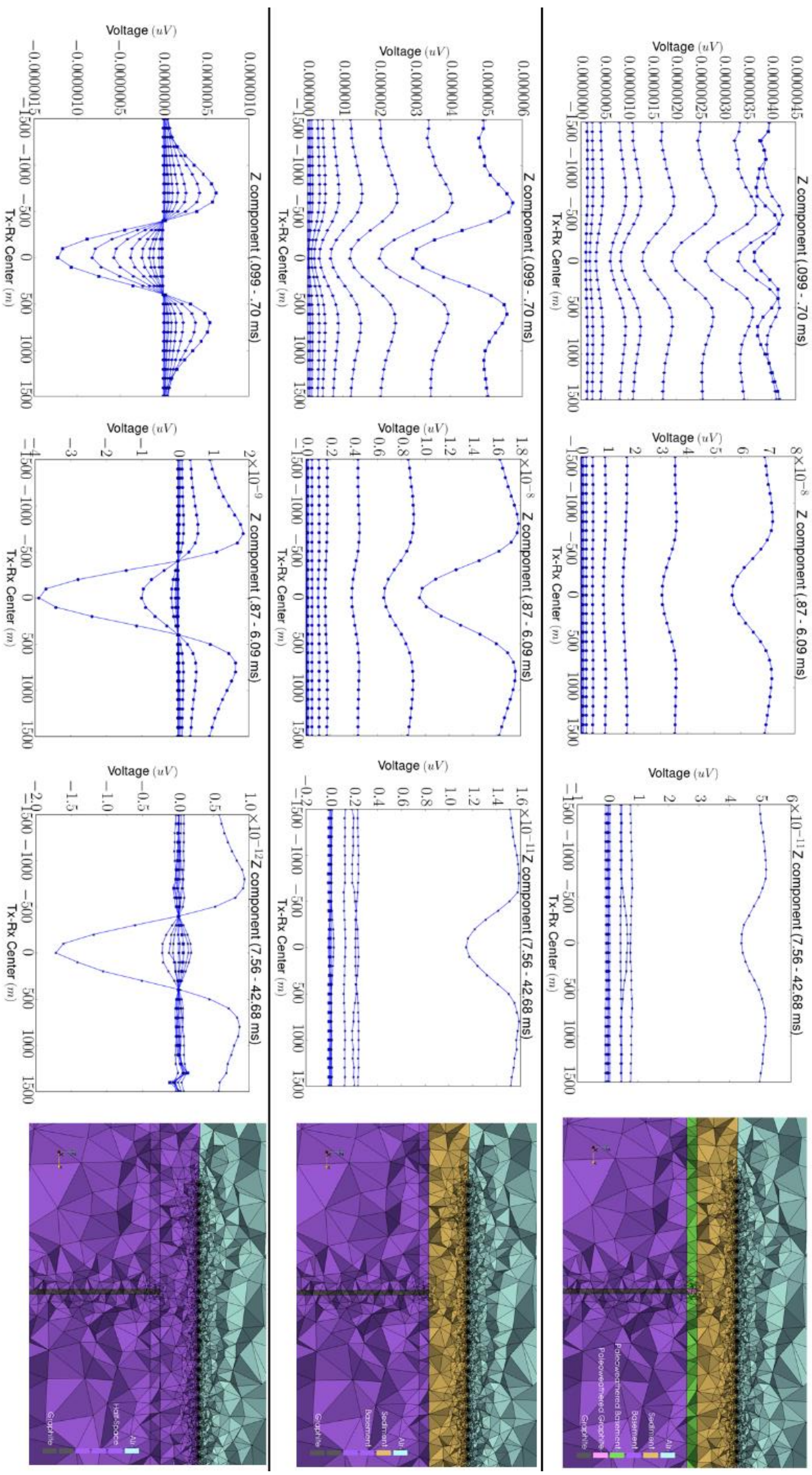

Figure 6.8: See page 147 for full caption.

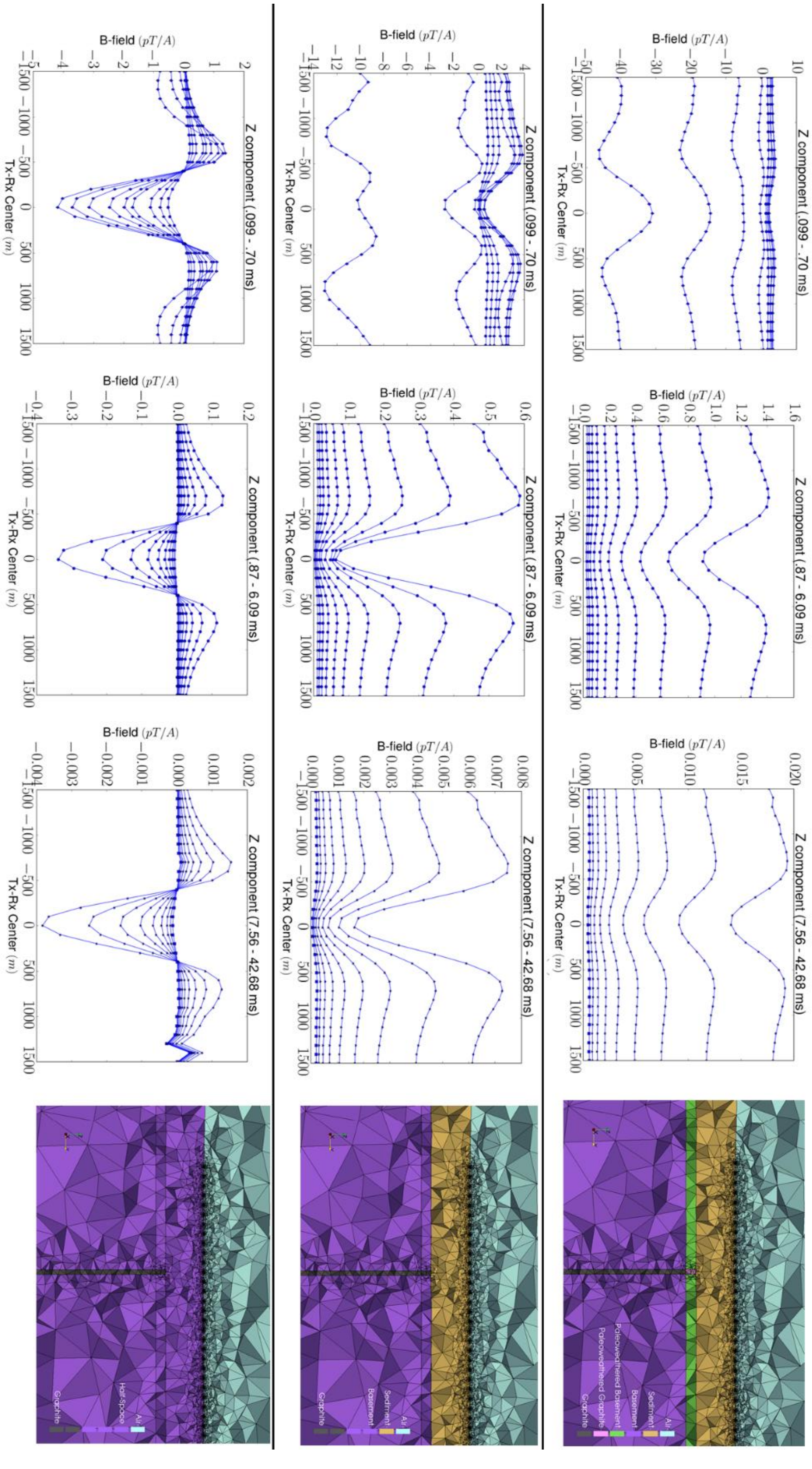

Figure 6.9: See page 147 for full caption.

Figure 6.8: Comparison of z-component time-domain secondary d$\mathbf{B}$/dt vs. distance plots for three versions of the paleoweathering model. At top the model contains all regions, at center the model contains the sediment and conductor but no paleoweathering, at bottom are the results of the conductor in background only. The secondary field is computed by subtracting a half-space model computed on the same mesh but with the homogeneous resistivity of the basement.

Figure 6.9: Comparison of z-component time-domain secondary $\mathbf{B}$-field vs. distance plots for three versions of the paleoweathering model. At top the model contains all regions, at center the model contains the sediment and conductor but no paleoweathering, at bottom are the results of the conductor in background only. The secondary field is computed by subtracting a half-space model computed on the same mesh but with the homogeneous resistivity of the basement.

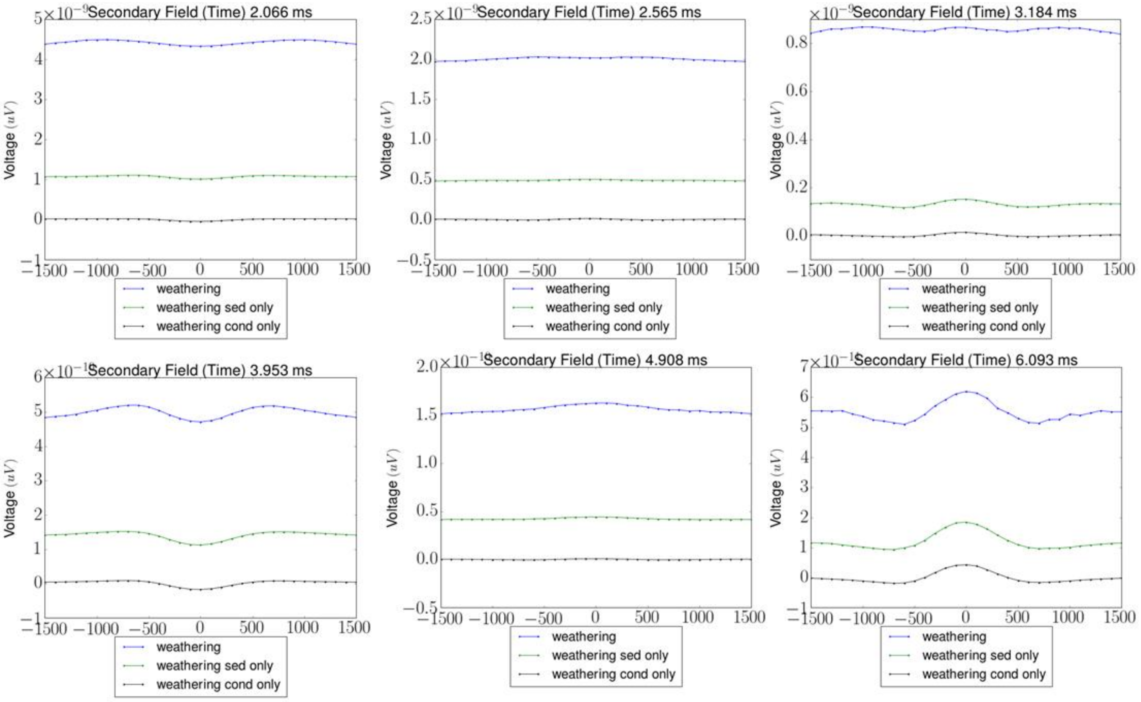
Secondary Field (Time) 2.066 ms
Secondary Field (Time) 2.565 ms
Secondary Field (Time) 3.184 ms
Secondary Field (Time) 3.953 ms
Secondary Field (Time) 4.908 ms
Secondary Field (Time) 6.093 ms

Figure 6.10: Comparison of the time-domain z-component magnetic field response vs. distance plots at six selected time gates from upper left to lower right for the three versions of the weathering model.

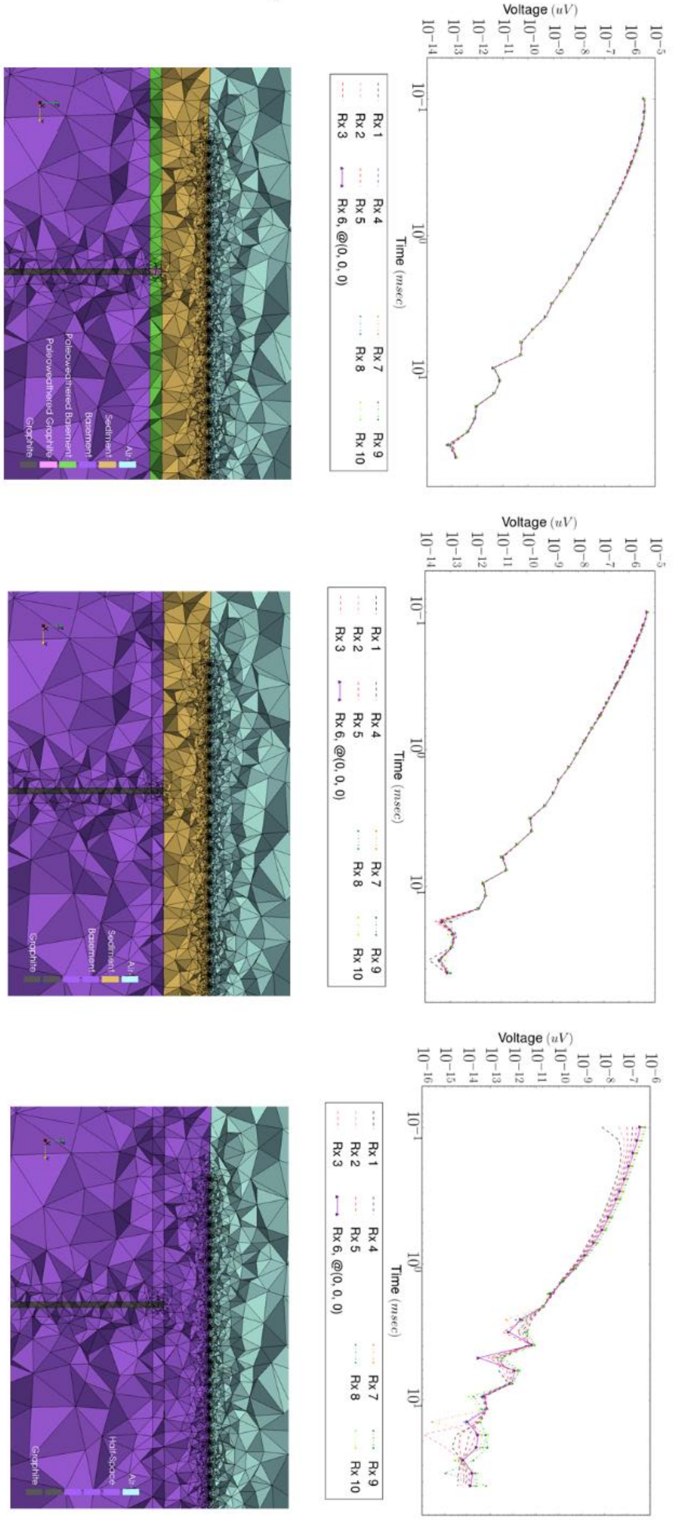

Figure 6.11: Comparison of the secondary field d$\mathbf{B}$/dt time-decay curves for the three versions of the weathering model.

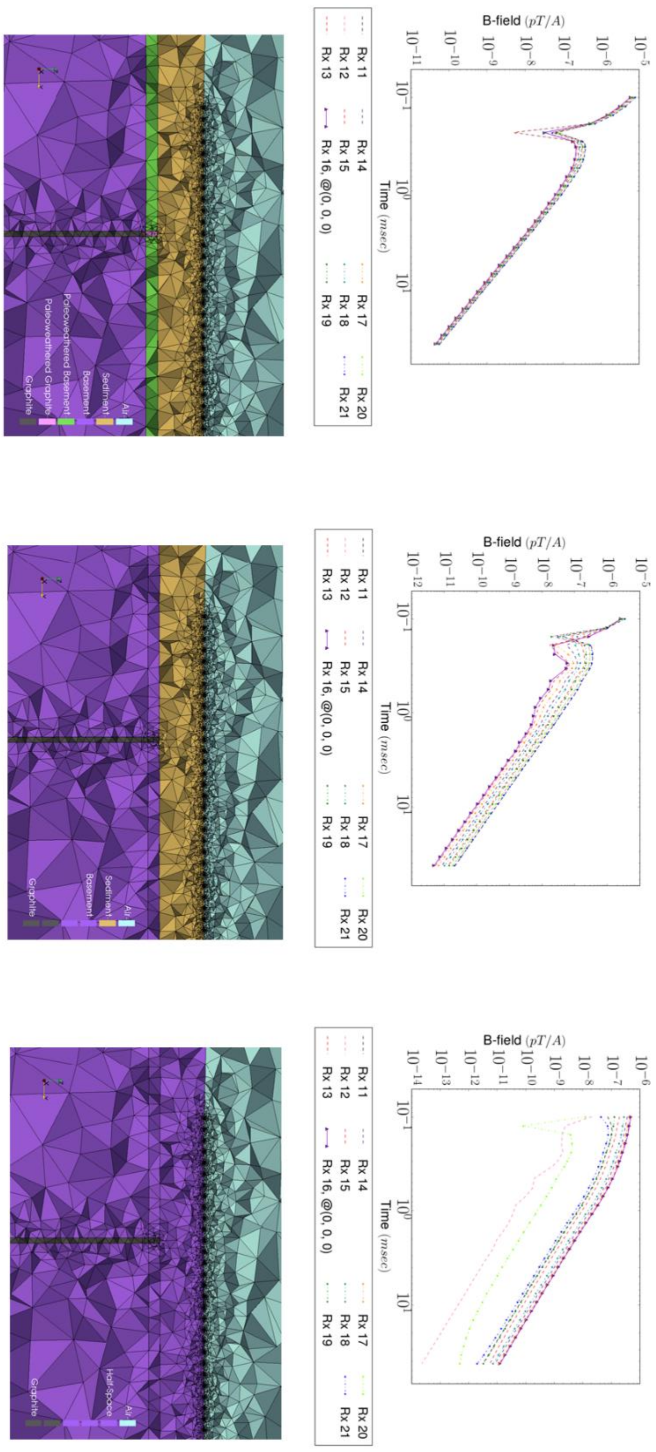

Figure 6.12: Comparison of the secondary field **B**-field time-decay curves for the three versions of the weathering model.

6.3.3 Dipping Metasediment and Conductor

The metasediment and conductor model was created to address a specific question faced by ARC geophysicists. When a dipping graphitic conductor is located next to a moderately conductive metasediment unit, the presence of the metasediment can alter the response in such a way that it would appear that the graphite is dipping in the opposite direction. Figure 6.13 shows close-up cross-sections along the *y*-axis of the four thin-metasediment and conductor models of different dips and arrangements. Two north dipping and two south dipping conductor models were created, one with the metasediment north of and one with the metasediment south of the graphitic conductor. These models cover four simple situations where the reverse dip effect could occur. The graphitic conductor is 10 m thick, and the metasediment unit is 50 m thick, with resistivities of 30 Ohm-m and 1400 Ohm-m respectively. Both units are 400 m x 1000 m in strike length and depth extent, and at a depth of 400 m below surface. Four additional models, seen in Figure 6.14, were created with the same parameters except that the thickness of the metasediment unit was increased to 2500 m to observe any differences in the response when the conductor is located next to a broad and semi-conductive unit. Figure 6.15 shows the z-component secondary **B**-field vs. distance plots for the two north dipping, thin-metasediment and conductor models at left, and the north and south dipping conductor-only models (e.g. Figure 5.14) at right for comparison. It is important to note that the north and south dipping conductor-only models have conductor resistivities of 3 Ohm-m vs. 30 Ohm-m in the metasediment and conductor models. This was done to better compare the dip reversal effect of the metasediment unit which manifests in the positive side peaks of the response. Figure 6.16 shows

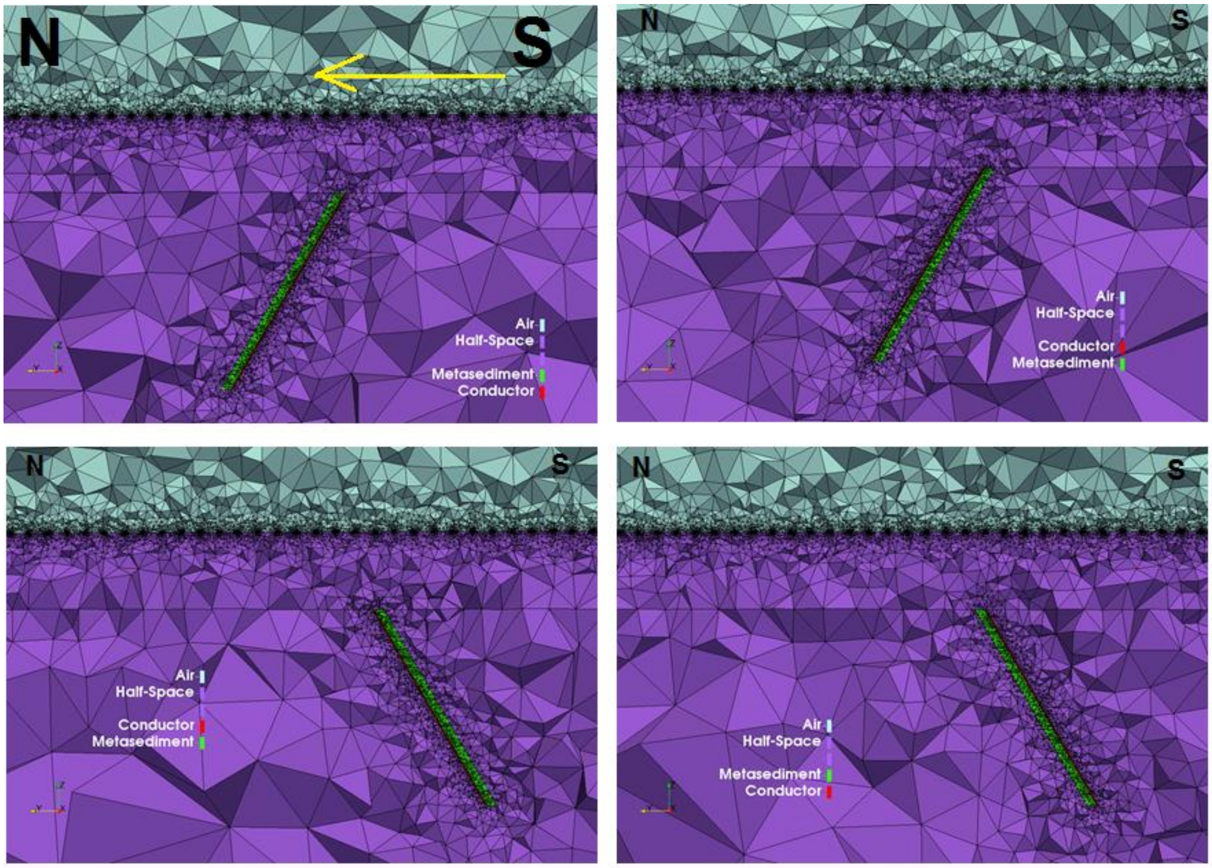

Figure 6.13: Close-up cross-section along the y-axis of the four thin-metasediment and conductor models of different dips and arrangements.

the z-component secondary **B**-field vs. distance plots for the two south dipping, thin-metasediment and conductor models at left, and Figures 6.17 and 6.18 show the z-component secondary **B**-field vs. distance plots for the two north dipping and south dipping, thick-metasediment and conductor models respectively. As for every model created in this project the transmitter-receiver pair moves from south to north along the survey line and that is important in this case. For the north dipping metasediment and conductor models, the apparent dip reversal effect occurs at middle and late times, and is quite pronounced when the metasediment is north of

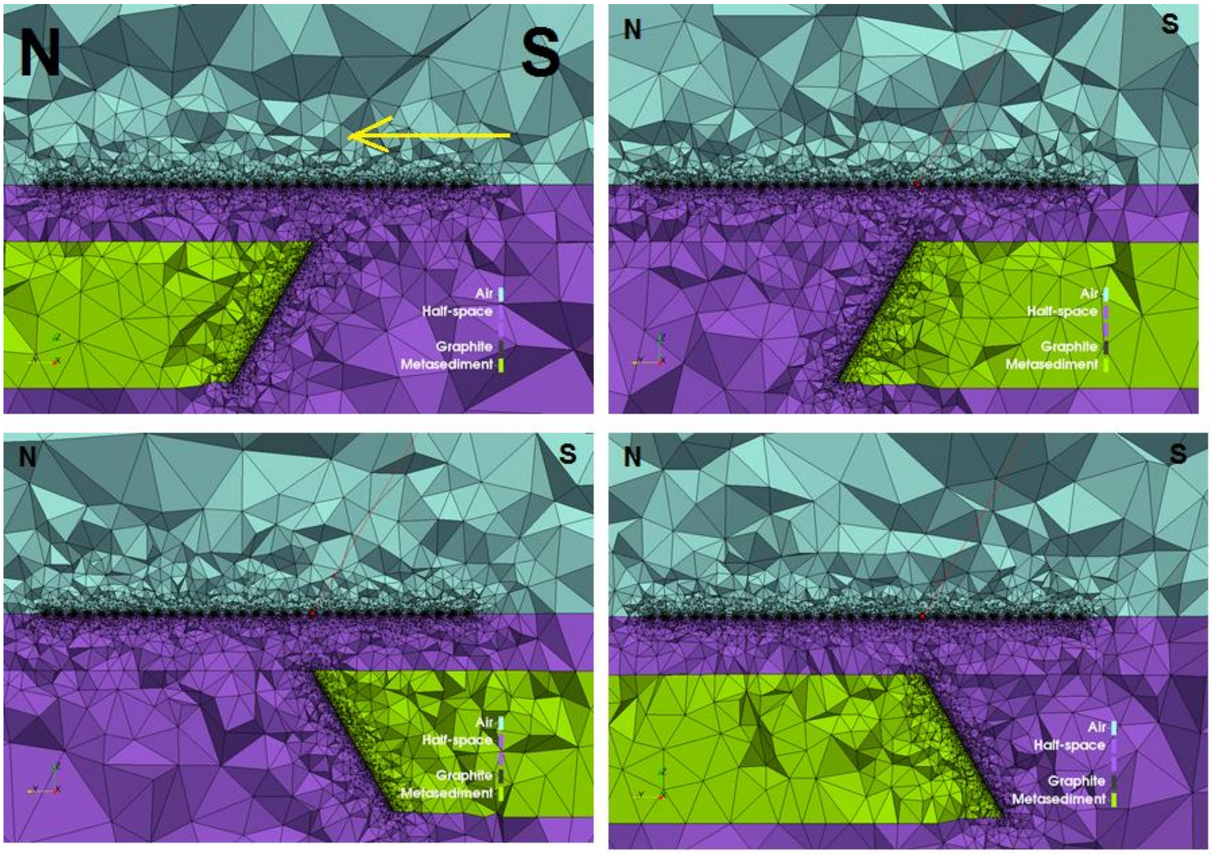

Figure 6.14: Close up cross-section along the y-axis of the four thick-metasediment and conductor models of different dips and arrangements.

the conductor. However, for the south dipping metasediment and conductor models, the effect is much less apparent, demonstrating that the direction of the survey line over the dipping conductor plays a major role in this effect. When the metasediment unit is very thick, the effect occurs very clearly for both north and south dipping conductors, with the placement of the conductor north or south of the metasediment being the most important factor. For a south dipping thick-metasediment and conductor (Figure 6.18), the effect will occur at middle and late times if the metasediment is south of the conductor but not when it is to the north. The dip reversal effect of the metasediment, when located next to a dipping conductor, is an interesting and important result that could clearly have significant effects on interpretation and possibly even lead to the misplacement of drill holes when planning exploration programs. This further illustrates the complexity of time-domain EM responses when realistic geologic situations are considered. Type curves for simple conductors are no longer enough to interpret the response successfully by comparison alone, and one may be easily fooled if not careful.

Finally, these results show only the **B**-field responses of these models and this for a few reasons. First, the ARC geophysicists commonly collect **B**-field data and so for comparison and to limit the number of plots in this section the d**B**/dt response is excluded. More importantly, the dip reversal effect is not present to the same extent if at all in the d**B**/dt data. The metasediment does cause some changes in the response curve vs. the single dipping conductor, but only when it is very thick. For the thin-metasediment and conductor models, the difference in the response when compared to the single dipping conductor is minimal, with the major change being a decrease in amplitude for the metasediment-conductor pair. The d**B**/dt results can be found in Appendix I, and demonstrate that in a situation where there is some possible confusion in interpreting responses of complex units of dipping conductors, if accessible, the d**B**/dt data can help to identify a false dip in the **B**-field response.

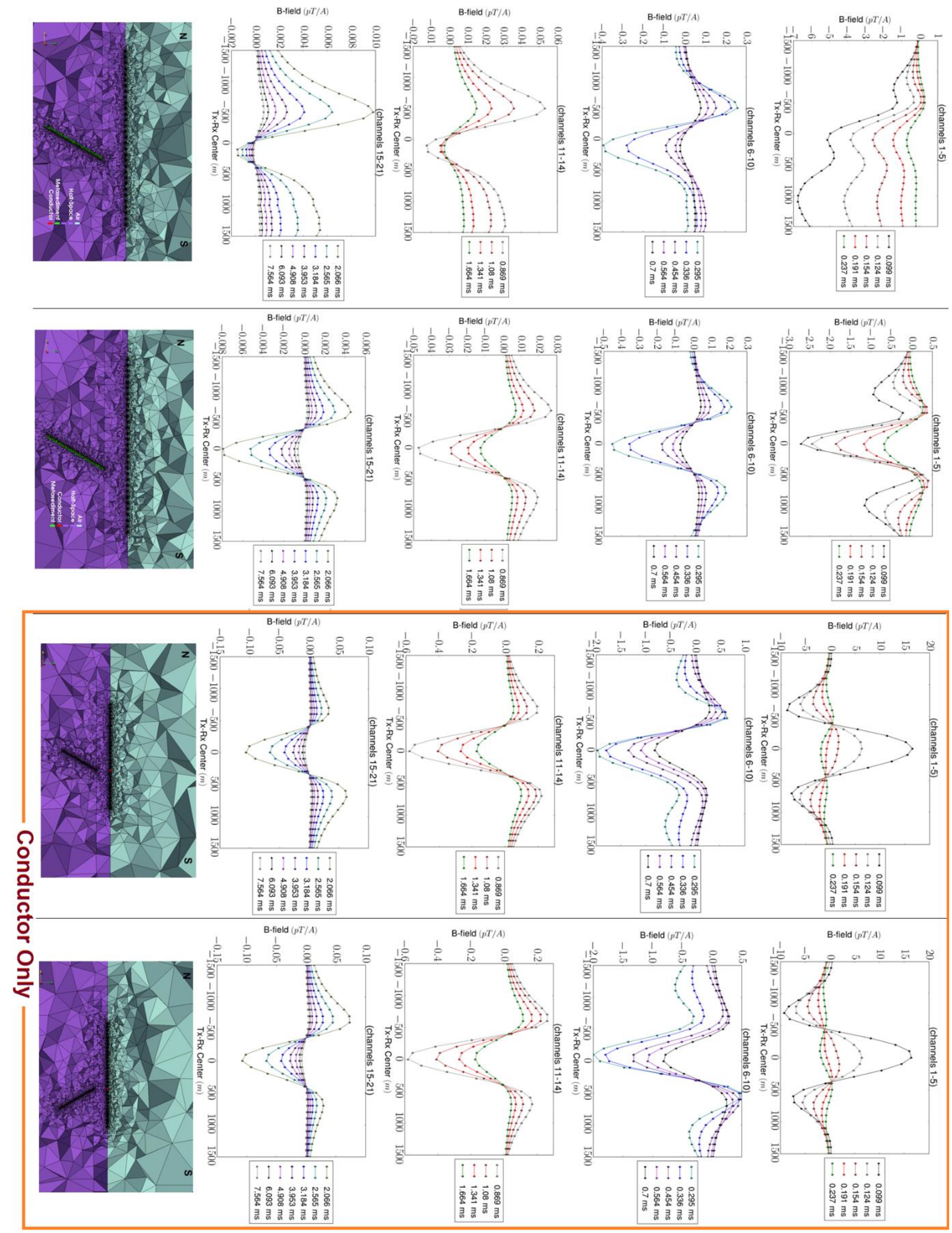

Figure 6.15: See page 158 for full caption.

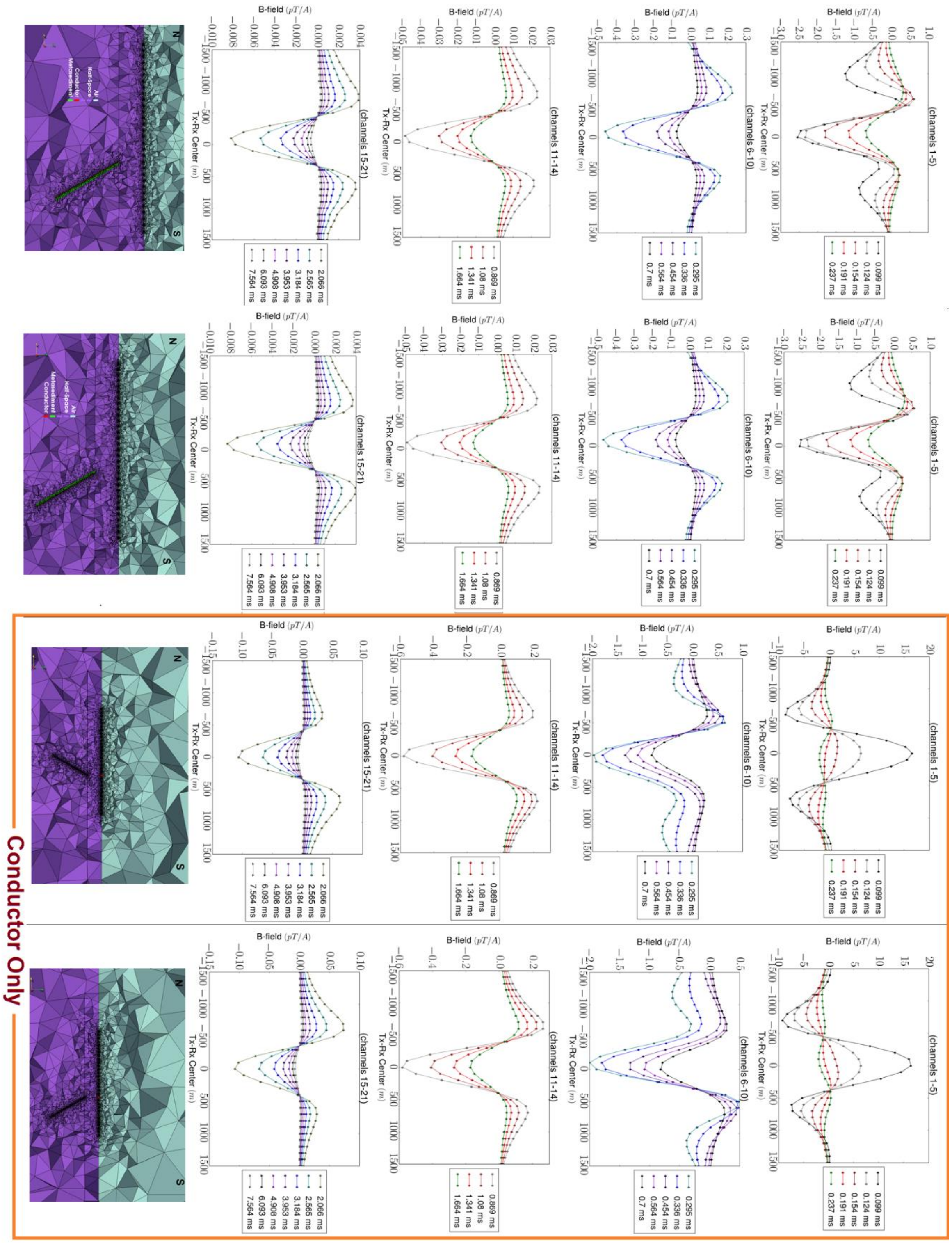

Figure 6.16: See page 158 for full caption.

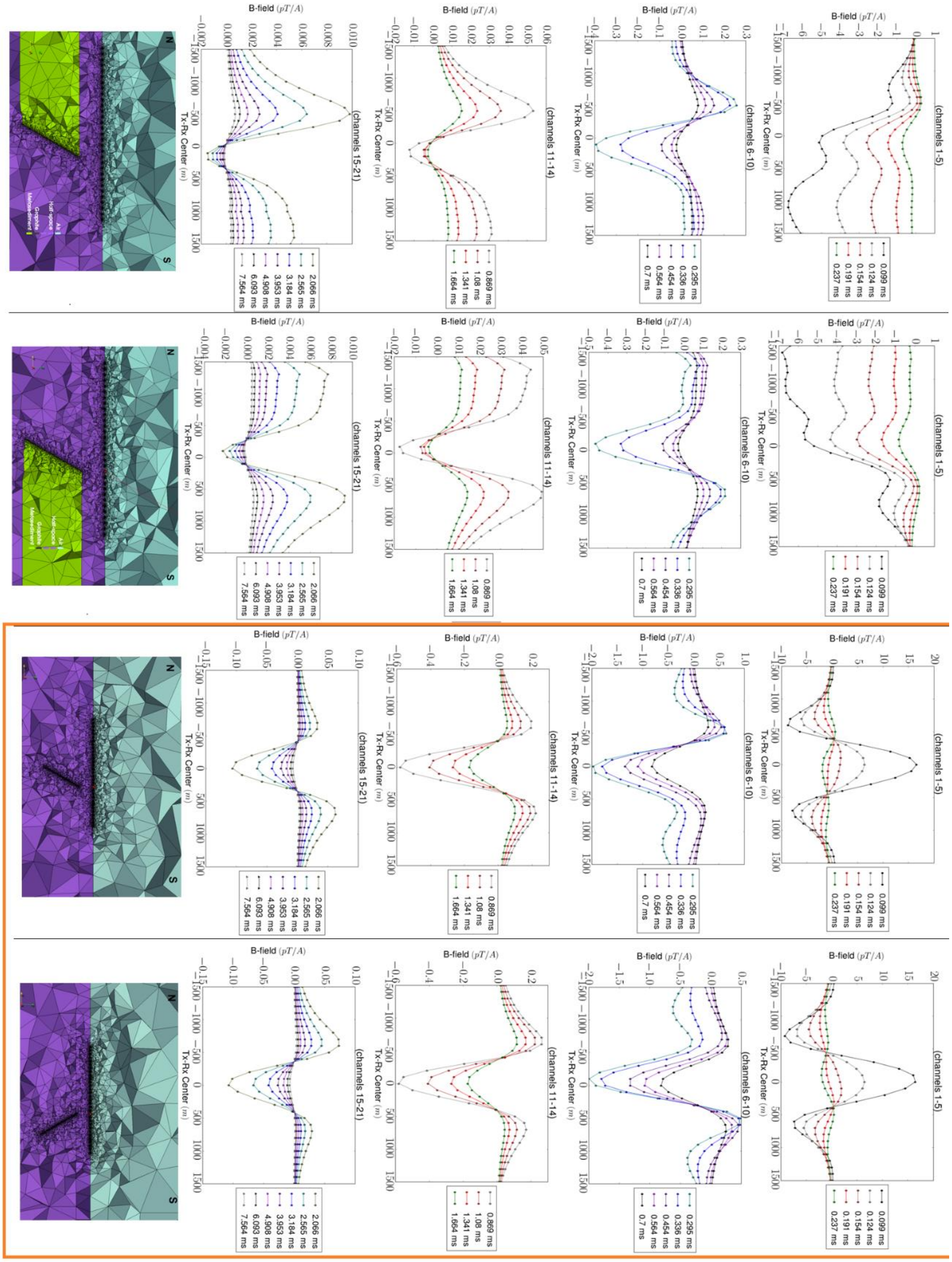

Figure 6.17: See page 158 for full caption.

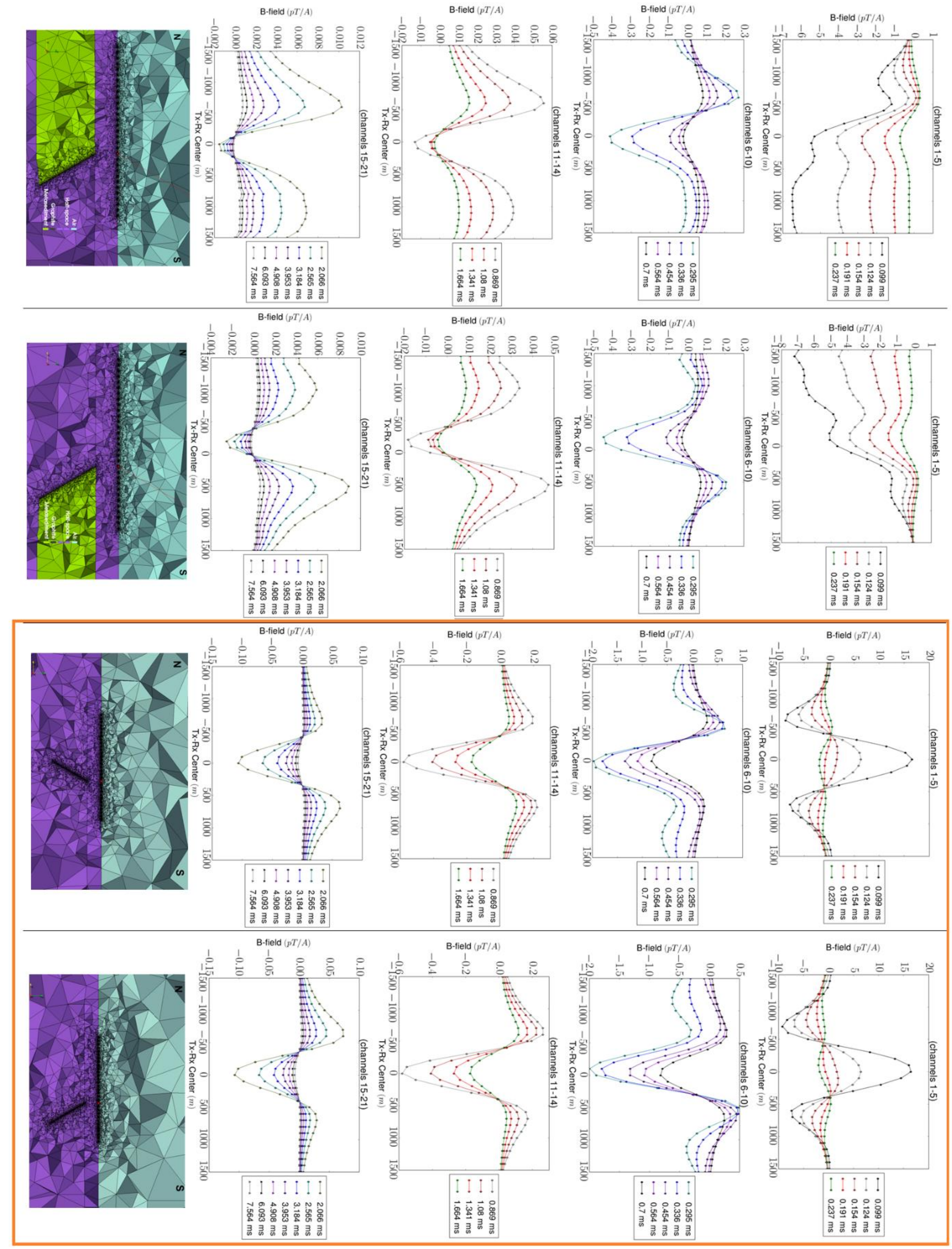

Figure 6.18: See page 158 for full caption.

Figure 6.15: Z-component time-domain secondary **B**-field vs. distance plots for the two *north dipping*, *thin* metasediment and conductor models at left, and the north and south dipping conductor-only models at right for comparison.

Figure 6.16: Z-component time-domain secondary **B**-field vs. distance plots for the two *south dipping, thin* metasediment and conductor models at left, and the north and south dipping conductor-only models at right for comparison.

Figure 6.17: Z-component time-domain secondary **B**-field vs. distance plots for the two *north dipping*, *thick* metasediment and conductor models at left, and the north and south dipping conductor-only models at right for comparison.

Figure 6.18: Z-component time-domain secondary **B**-field vs. distance plots for the two *south dipping*, *thick* metasediment and conductor models at left, and the north and south dipping conductor-only models at right for comparison.

6.3.4 Faulted vs. Folded Conductor

Another question faced by ARC geophysicists in the Athabasca Basin is the possible effect on the time-domain response of a conductor that has undergone faulting or folding along its strike length. Although specific details are intentionally not discussed here, large conductive units in parts of the Athabasca Basin important to ARC are sometimes offset along strike-slip style faults, and it is not known whether the conductor is truly offset or if the movement was more ductile and the conductor simply folded and is still a continuous unit. Figure 6.19 shows a much simplified schematic plan map based on Athabasca Basin geology and used in the design of the fold vs. fault models, better illustrating the problem faced in this case.

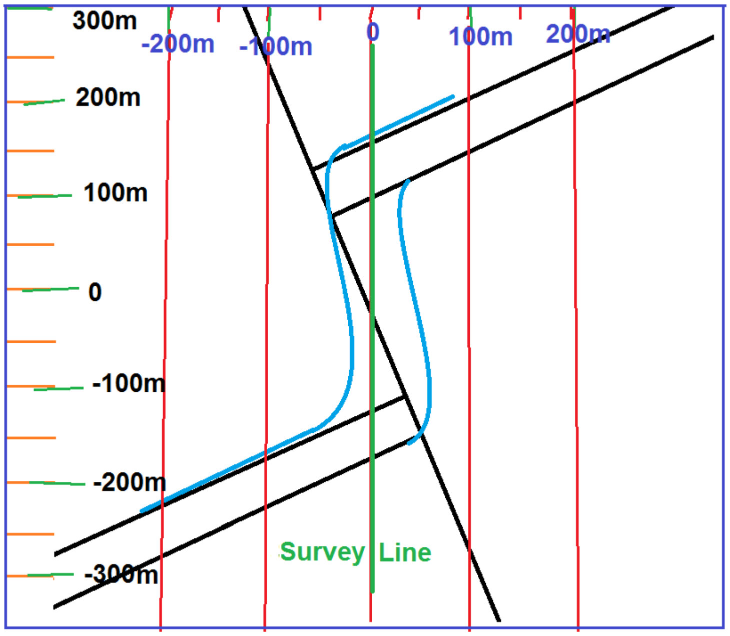

Figure 6.19: Schematic plan map used in the design of the fold vs. fault model meshes

Figure 6.20 shows views of the 3D model meshes for the fold and fault models. At upper and lower right are views looking up on the conductor and the unconformity from deeper within the model, the basement cells having been removed to allow for this view. At upper and lower left are cross-sections along the y-axis of the fault and fold models, again with basement cells removed for a better view. The conductor is approximately 50 m thick and in the case of the faulted conductor, the two sections are offset by approximately 200 m along the NW-SE fault. The fault itself was not specifically represented in the model. As in most other cases in this research, the conductor is 30 Ohm-m and at a depth of 400 m in a resistive half-space. A second version includes a 3500 Ohm-m sediment layer which is more accurate for the Athabasca Basin. Figure 6.21 shows a comparison of z-component d$\mathbf{B}$/dt and $\mathbf{B}$-field

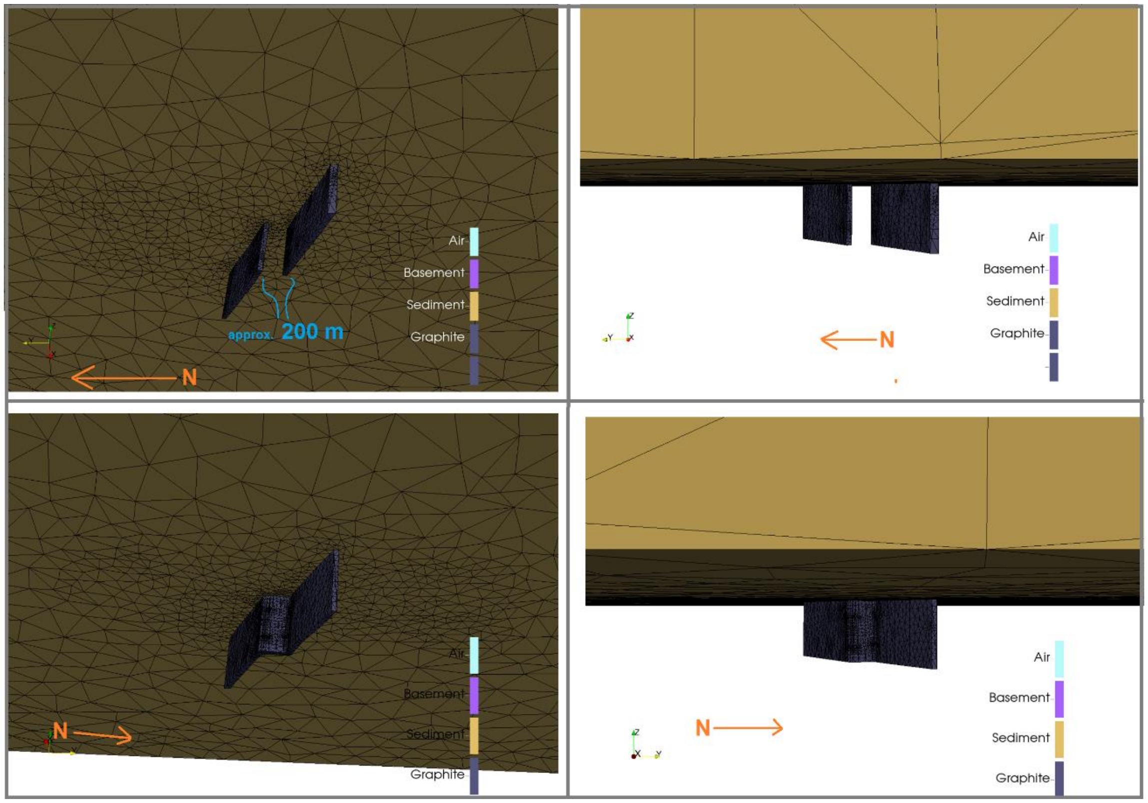

Figure 6.20: Views of the 3D model meshes for the fold and fault models. At upper and lower right are views looking up on the conductor and the unconformity surface for the fault and fold models respectively, the basement cells having been removed from view. At upper and lower left are cross-sections along the y-axis of the fault and fold models, again with basement cells removed for a better view.

vs. distance plots for the fault and fold models; here the 30 Ohm-m conductors are in half-space only to better observe any possible differences between the responses. Figure 6.22 shows the same comparison except in this case the 3500 Ohm-m sediment layer is included in the secondary field response. These figures also show cutaway views of the model mesh and the location of the receivers along the survey line.

In this case, there is no significant difference in the response of the fault and fold models, and it is apparently not possible using these survey parameters to detect whether the conductor is continuous or offset along the fault. Despite these relatively dull results, they are important in that they again show the limitations of large offset

Slingram-style surveys. Again, this is a simplified case, and more could be done to better investigate this situation such as adding in some zone of alteration that would very likely occur along the fault, and may do better to distinguish the offset in the conductor. Also, it is possible that additional survey lines more distant from the conductor or a change in the survey line orientation would better define the offset conductor. However very likely the transmitter-receiver offset plays the most significant role in cases where measuring responses of closely space geologic features is desired.

.

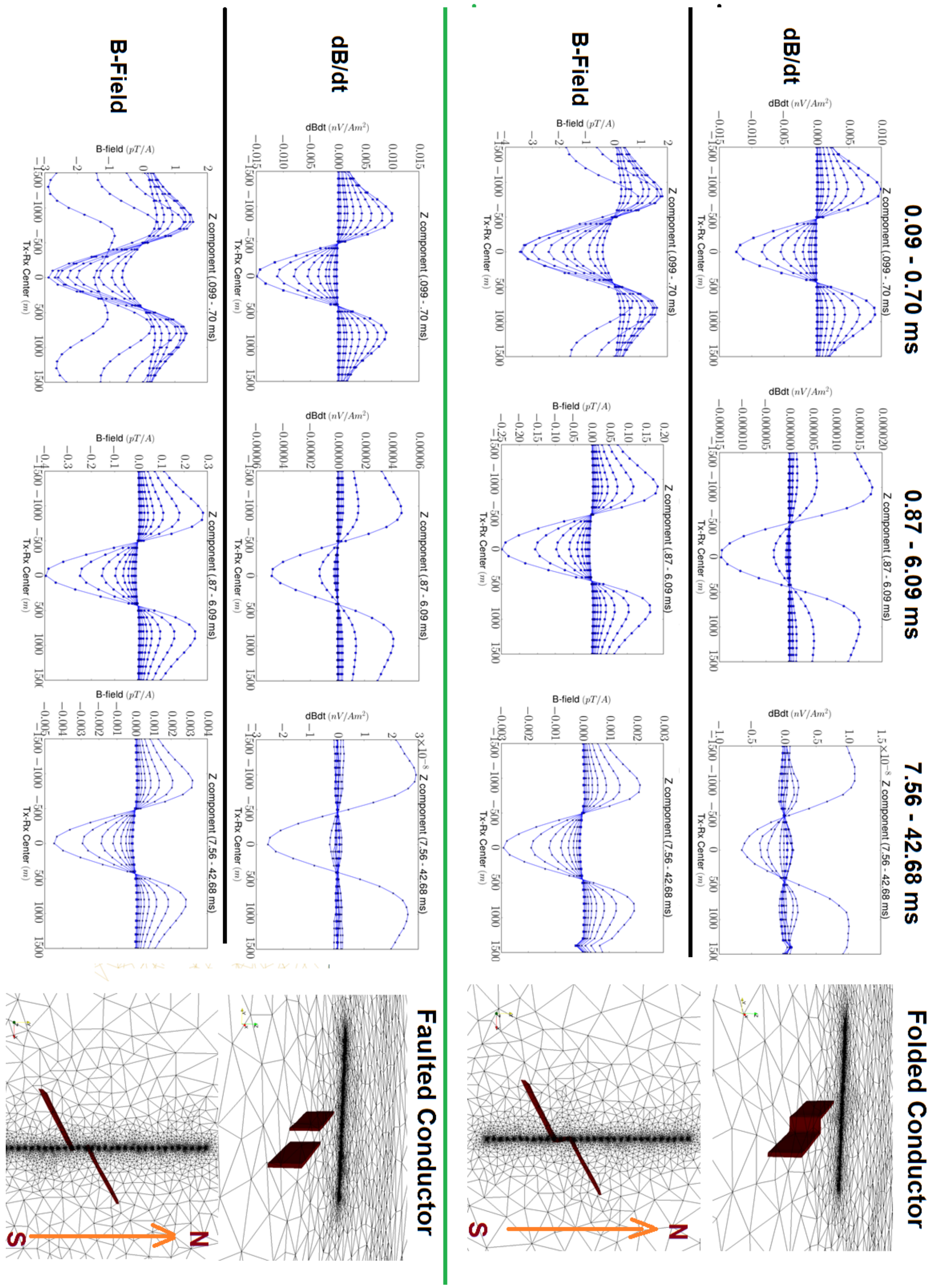

Figure 6.21: See page 164 for full caption.

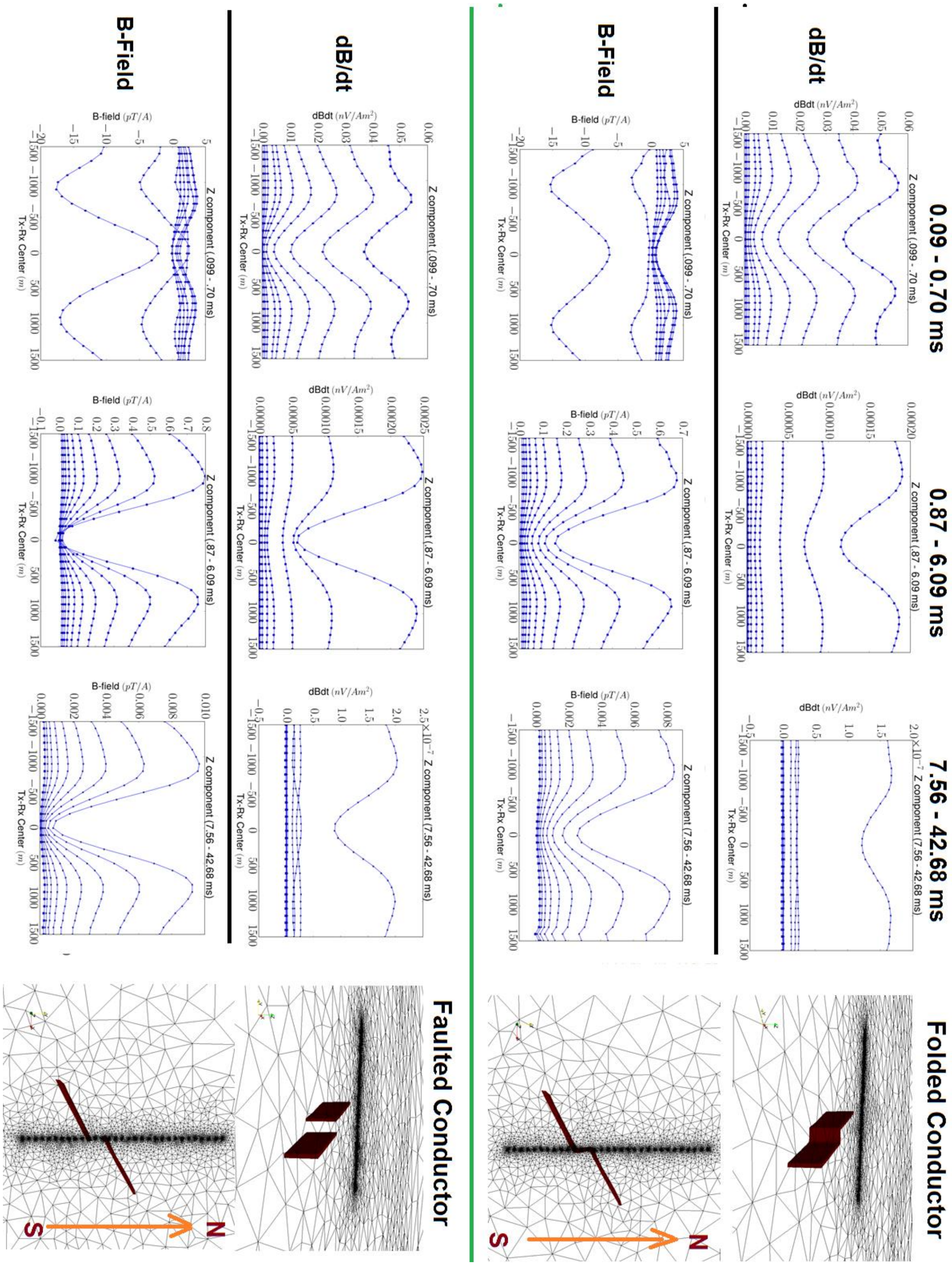

Figure 6.22: See page 164 for full caption.

Figure 6.21: Comparison of z-component time-domain d$\mathbf{B}$/dt and $\mathbf{B}$-field vs. distance plots for the fault and fold models, 30 Ohm-m conductors *in half-space only.*

Figure 6.22: Comparison of z-component time-domain d$\mathbf{B}$/dt and $\mathbf{B}$-field vs. distance plots for the fault and fold models 30 Ohm-m conductors, *and 3500 Ohm-m sediment layer in half-space.*

6.3.5 Classic Athabasca Uranium Exploration Cross-section Model

Next, to more fully explore the potential for model design and begin to divert from single conductor situations, the classic Cigar Lake uranium deposition cross-section cartoon, commonly used by ARC in their examples (per. comm. Robert Hearst, 2016), was recreated in 3D. Figure 6.23 shows, at left, the cartoon cross-section used in the model design and, at right, views of the model mesh shown with and without the metagranite basement cells for clarity. Although simple, the model does contain features such as the alteration halo and ore zone that are of great importance in real exploration and had not previously been modeled in this project. Figures 6.24 and 6.25 show respectively the z-component d$\mathbf{B}$/dt and $\mathbf{B}$-field vs. distance plots for four versions of the cross-section model. From left to right in the figures, regions have been progressively changed to background. At the far left is the secondary field response of the full model including the sediment layer. In the other models, the sediment and overburden have been changed to resistive background effectively giving just the secondary field response of the remaining units in the model. Both the $\mathbf{B}$-field, and d$\mathbf{B}$/dt responses are again primarily that of a vertical conductor, and effects of the various regions, perhaps as expected, are manifested primarily as changes in response amplitude. As in other models, the

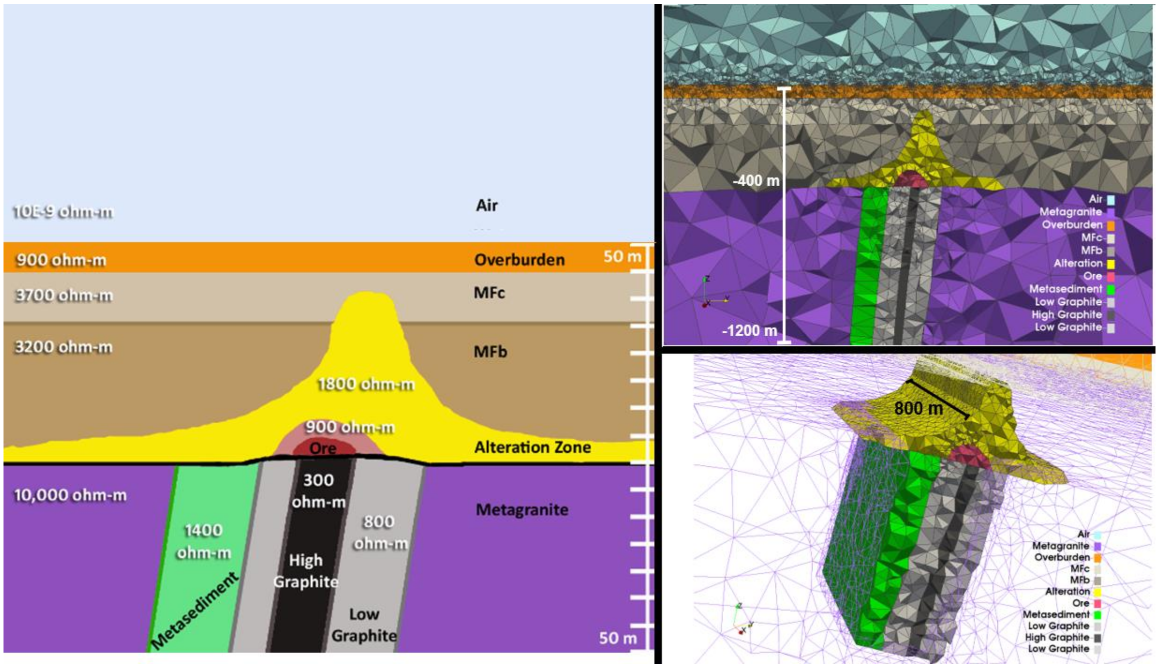

Figure 6.23: At left is a cartoon cross-section showing a typical, and simplified, Athabasca Basin uranium exploration scenario inspired by ARC. At right are views of the model mesh shown with and without the metagranite cells for clarity.

d**B**/dt response undergoes sign reversals at varied times, depending on what regions are present in the model. Interestingly there is an indication in the total-field response for the **B**-field that the blocky nature of the conductor package within the model is affecting the response. This makes sense as the package is on the order of 400 m thick and so within the resolution limits for the survey. In reality, the geology around the conductor package would itself be complex and varied, and would likely not produce a similar response.

When including realistic regions in the model mesh, the limit on factors such as the extents of regions, presence of curves, the thickness of regions, etc. is the number of model cells. This model, if refined using the same method as all previous models, is composed of roughly 1.7 million cells, which is too many for the current direct solve version of the CESM3DFWD code running on a 64 GB computing node.

By easing the mesh quality requirement in TetGen to the default setting, the mesh was reduced to approximately 600,000 cells and could run successfully. Appendix E shows a comparison for two of the multi-conductor models seen in the next section of this chapter, computed with the standard mesh quality setting and the default quality setting. The comparison demonstrates that responses for that model are not greatly affected by the decrease in mesh refinement, and so by extension, the results of the classic cross-section model are valid even though a reduction in well over half of the mesh cells was necessary to compute the model.

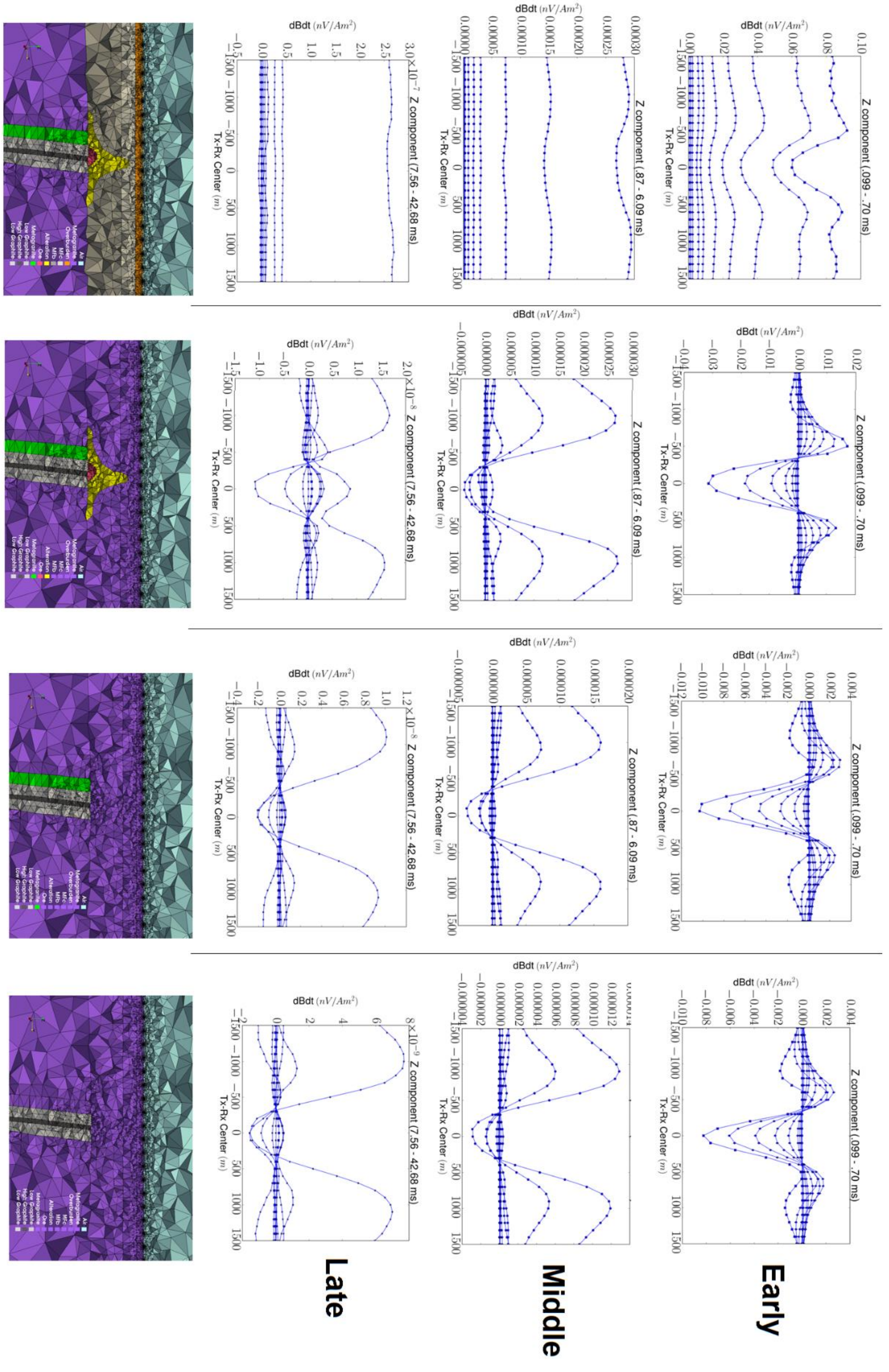

Figure 6.24: See page 169 for full caption.

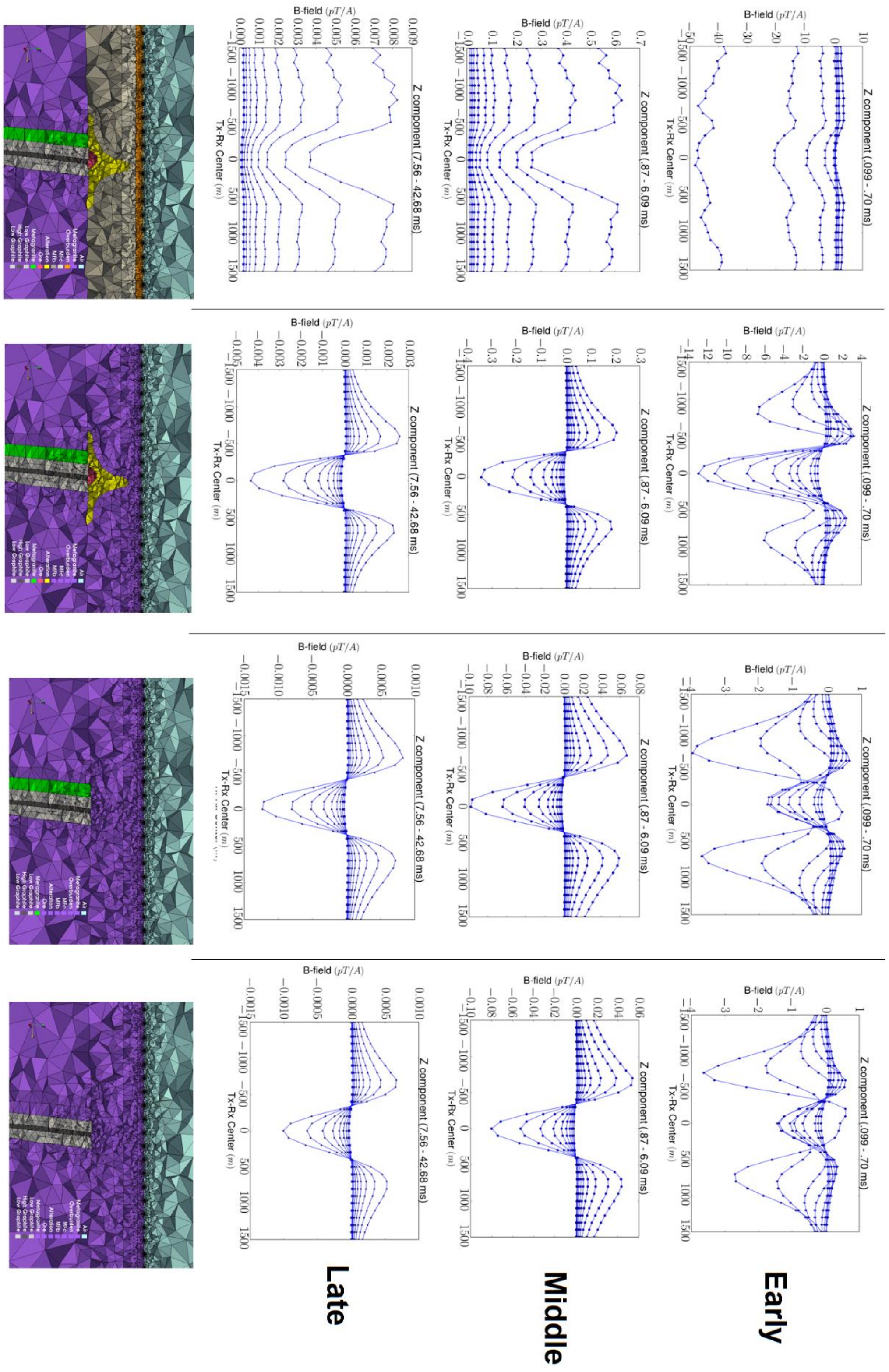

Figure 6.25: See page 169 for full caption.

Figure 6.24: Comparison of z-component time-domain d$\mathbf{B}$/dt vs. distance plots for four versions of the cross-section model, from left to right progressive regions have been changed to the background.

Figure 6.25: Comparison of z-component time-domain $\mathbf{B}$-field vs. distance plots for four versions of the cross-section model, from left to right progressive regions have been changed to the background.

6.3.6 Realistic Multi-Conductor Model

For the final demonstration of the effectiveness of the forward modeling method investigated and developed in this thesis, a realistic, multi-conductor model was created based on an ARC cross-section created from actual drill log geologic data. Actual SQUID **B**-field ground TDEM data was collected over the area modeled in the cross-section and so could be compared directly to the responses generated from the forward models. Figure 26 shows at the top, the geologic cross-section and ARC **B**-field response that served as the inspiration for the multi-conductor model. At the bottom of this figure is a cross-section along the y-axis of the corresponding model mesh with the resistivity values of the geologic regions indicated on the model. The resistivity values were taken directly from the average values measured in the ARC drill logs and so this model, although simplified, is as accurate geologically as possible.

The ARC drill holes did not penetrate further than about 100 m below the unconformity, and so the 100 m depth extent of the conductor package seen in the cross-section is somewhat realistic, but the package likely extends to greater depths. For this reason, three initial versions of the model were created, as seen in Figure 6.27, each with different depth extents for the conductor package, namely 100 m like that in the cross- section, and additionally 300 m and 1000 m versions. Two regions of the model, colored white and labeled unknown, are in areas where there is no drill hole data, and so the geology of the region is not known by ARC. For an initial test, these regions were assumed to be pelitic gneiss, colored aqua in the cross-section, which is not unrealistic and serves as a good initial baseline response for investigation.

Figure 6.28 shows the z-component, total **B**-field vs. distance plots for the three versions of the multi-conductor model with varied depth extent. The response of the model with the 300 m depth extent shows the best agreement with the ARC response over the entire time window, and so was selected for all further testing. The 100 m depth extent model is also in agreement with the ARC response, but it is clear that a greater depth extent is required. The 1000 m depth extent model, interestingly appears to be too much, as the late time response is seen to change form and no longer match the ARC response, yet at early and mid-times the response is perhaps the closest match. Although it is both possible and very likely that the graphitic conductors and other units do extend to at least a kilometer beneath the unconformity, merely extending the cross-section in this manner has an adverse effect on the late-time response, and so is not a good approximation overall.

Next, many versions of the model were computed substituting the various rock types present into the unknown regions to obtain the closest possible match to the ARC response. Figure 6.29 shows a comparison of the z-component **B**-field response vs. distance plots at six selected time gates from upper left to lower right

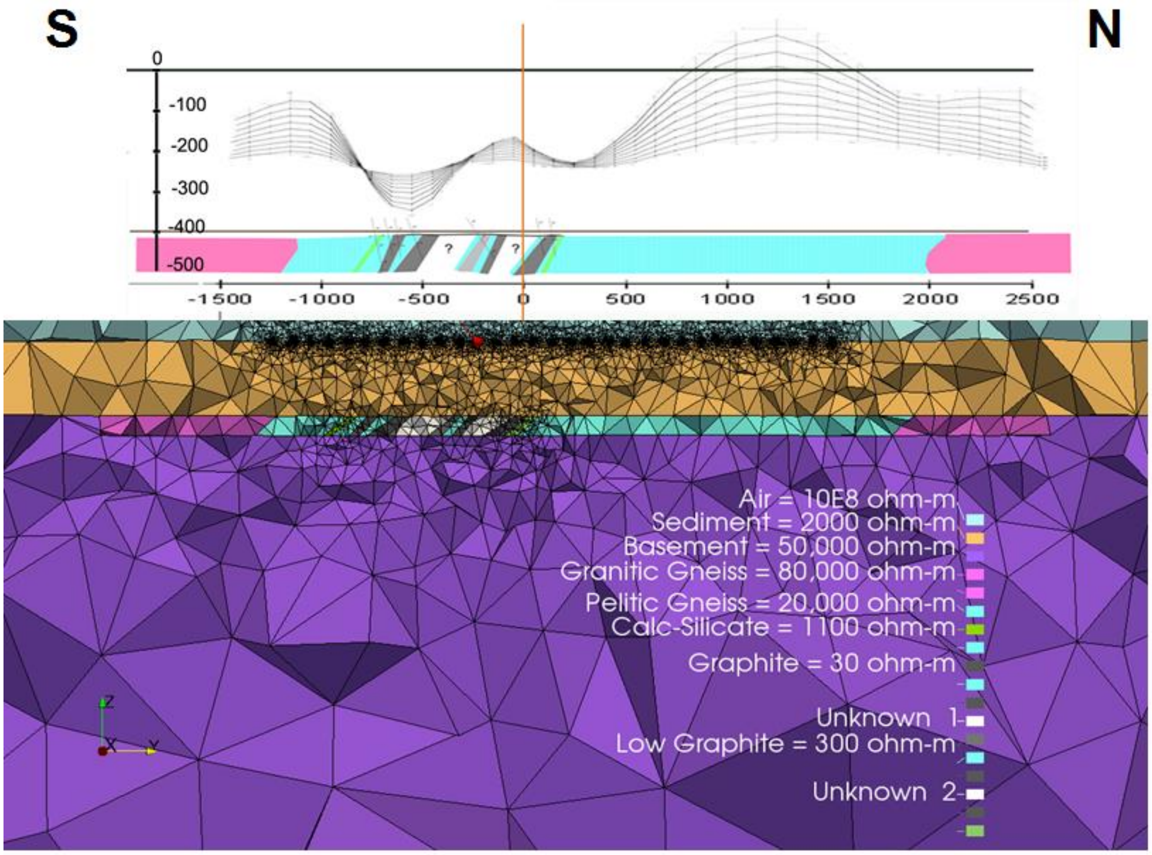

Figure 6.26: At top is the geologic cross-section and ARC **B**-field response that served as the inspiration for the multi-conductor model. Below is a cross-section along the *y*-axis of the model mesh and the region resistivity values.

for seven variations of the multi-conductor model. The names seen in the legend correspond to the rock type used for sections *unknown one* and *unknown two* respectively. It can be seen that a fair amount of these responses appear to be close matches to the ARC response, and Figure 6.30 includes a scaled version of the ARC data over the same six time gates seen in Figure 6.29 for comparison. The ARC data was of higher amplitude than the forward response and so was scaled by a factor of 10^{-3} for this comparison. This scaling factor is required due to the inexact match of the background response used to calculate the secondary field. Specifically, the

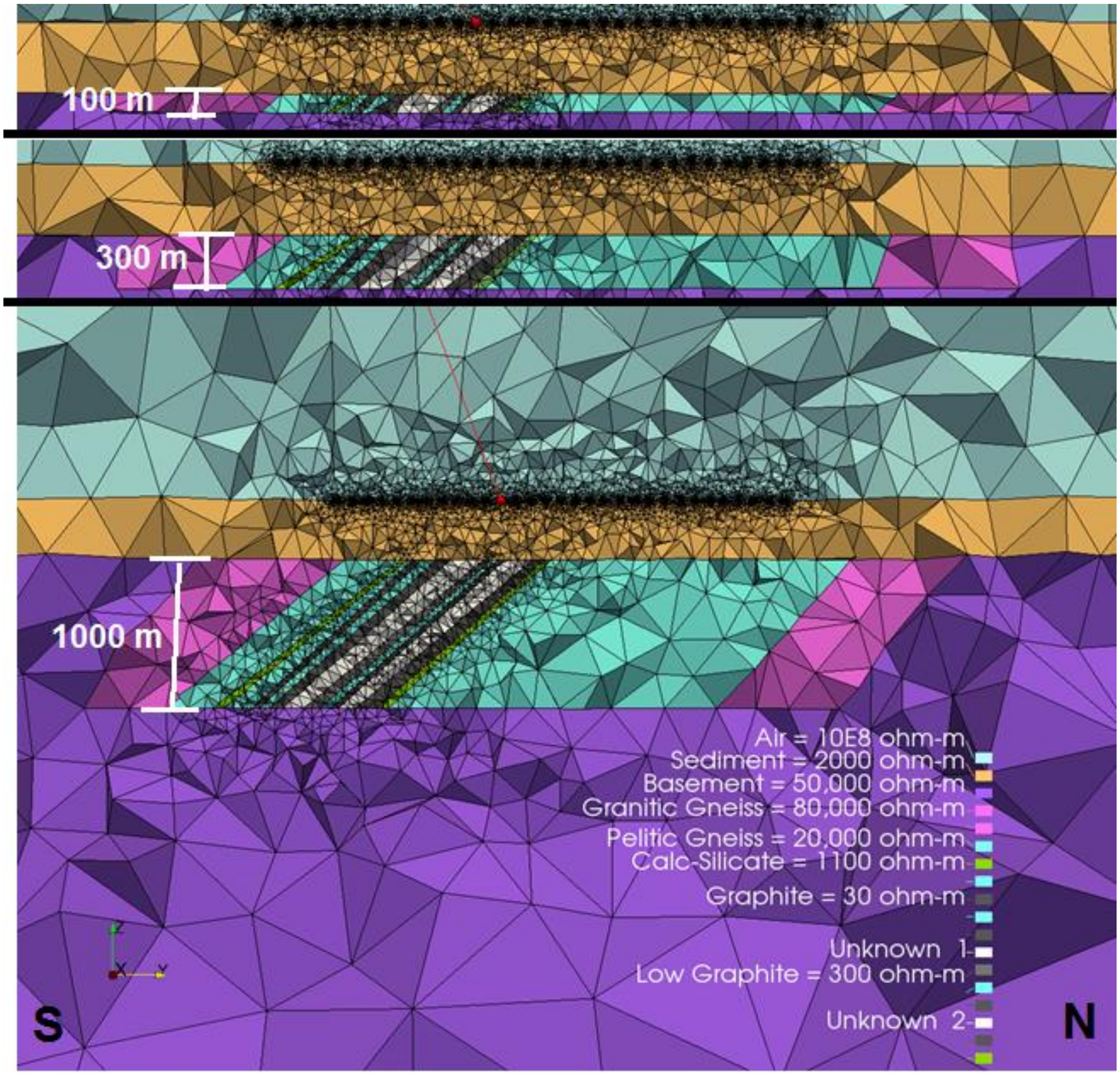

Figure 6.27: From top to bottom are cross-sections along the y-axis of the model mesh for three versions of the multi-conductor model, each with different depth extents for the conductor package.

scaling value was selected to best match the highlighted time gate in Figure 6.30, and so the fit between responses can be seen to degrade away from this time gate. However, this serves as a good illustration of the agreement in the responses, and for the most part rules out the three versions of the model containing the highly conductive (30 Ohm-m) graphite in the two unknown regions. The other models give good fits with the best two being possibly the low-graphite – low-graphite, and

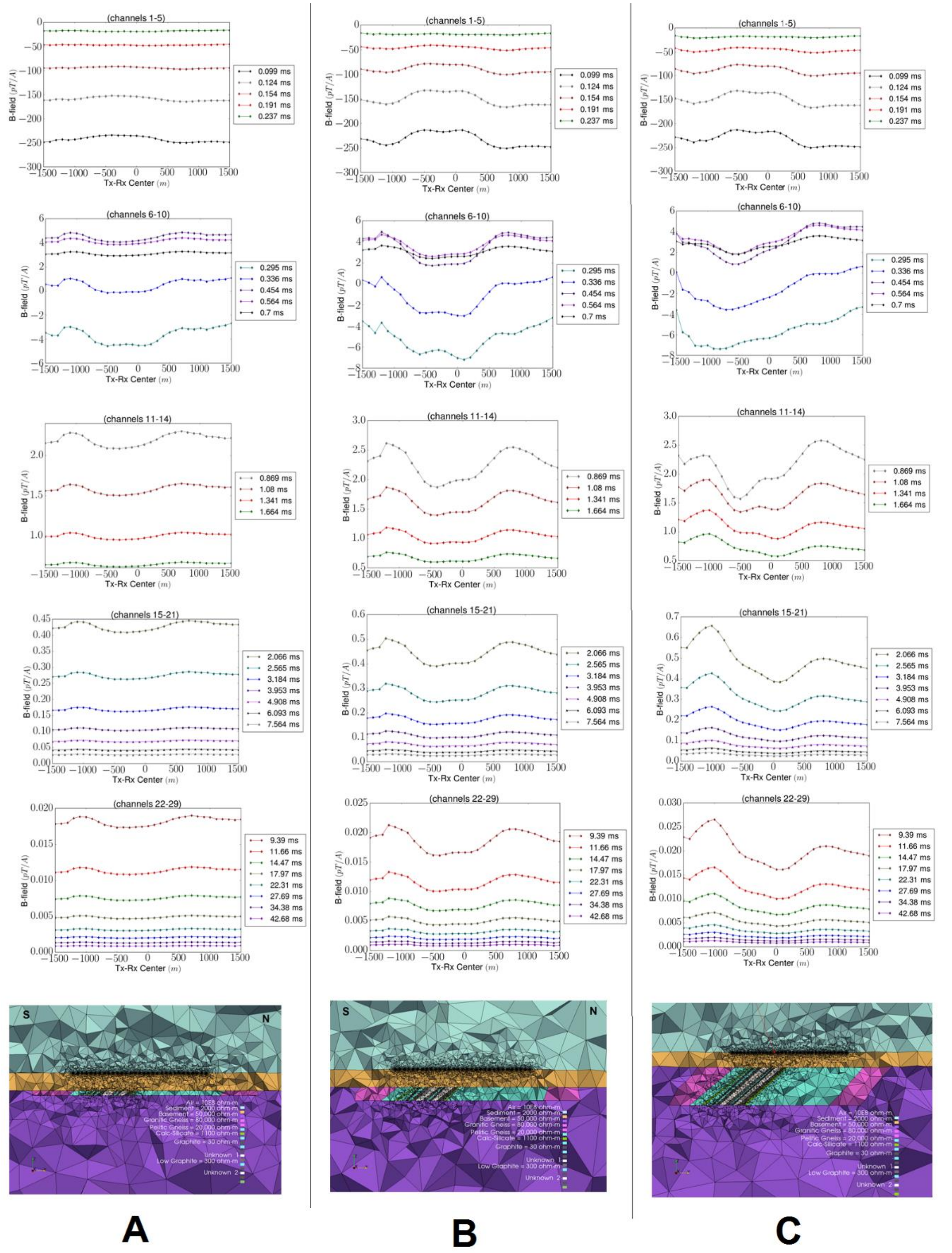

Figure 6.28: Z-component time-domain **B**-field vs. distance plots for the three versions of the multi-conductor model with varied depth extent. A) 100 metres. B) 300 m. C) 1,000 m.

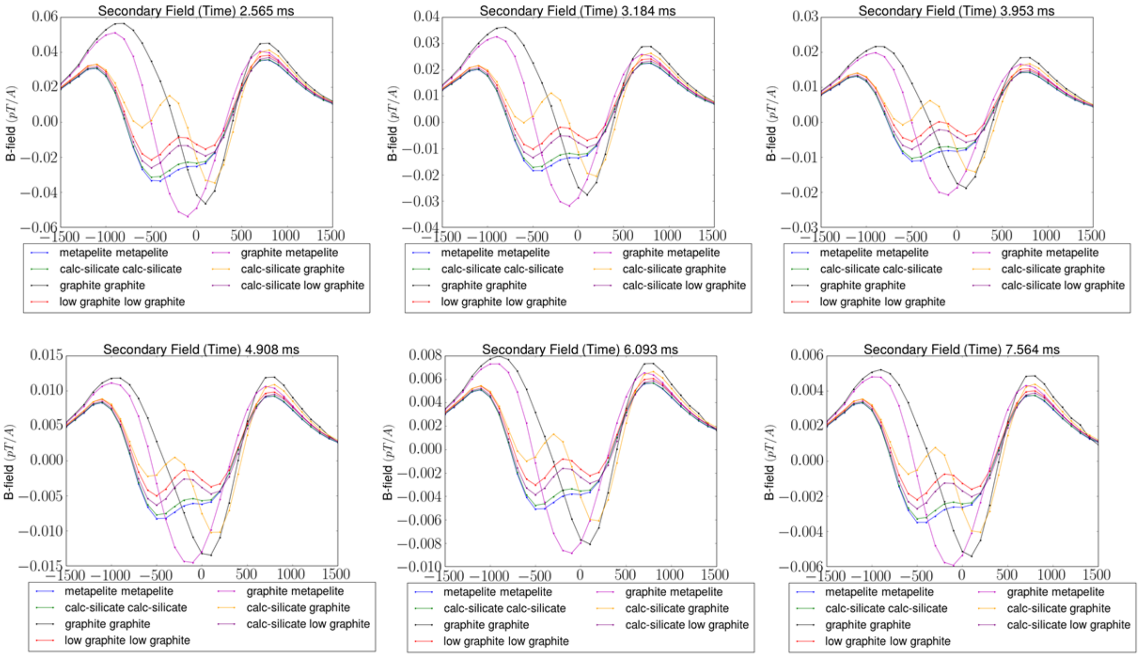

Figure 6.29: Comparison of the time-domain z-component $\mathbf{B}$-field response vs. distance plots at six selected time gates from upper left to lower right for seven variations of the multi-conductor model. The names in the legend correspond to the rock type used for sections *unknown one* and *unknown two* respectively.

calc-silicate – low-graphite versions. Outputs of all versions can be found in Appendix I.

Figure 6.31 shows the Z-component **B**-field vs. distance plots for the version of the multi-conductor model with calcium silicate in both unknown regions alongside the full ARC response over three time windows. This figure includes the total-field response calculated with the sediment layer present and the secondary field response without the sediment layer calculated to better observe the response of just the units of interest. The agreement of the forward-modeled data with the actual ground TDEM data is quite good for such a simplified model. Differences, however, do arise particularly that of the background level of the response amplitude being less for the

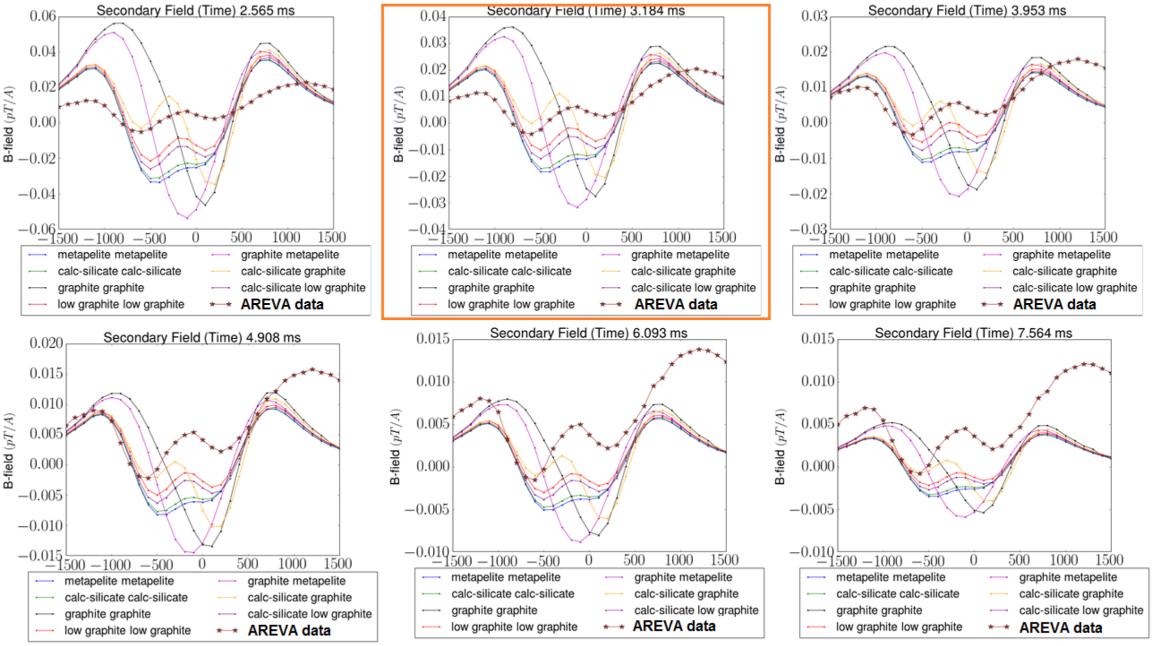

Figure 6.30: Comparison of the time-domain z-component **B**-field response vs. distance plots at six selected time gates from upper left to lower right for seven variations of the multi-conductor model, along with the ARC ground TDEM data collected in the Athabasca Basin. The ARC data was scaled by 10^{-3} pT/A to match the highlighted time gate as close as possible.

forward-modeled data. The fact that the ARC response seems to lie somewhat between the forward modeled total-field and secondary field responses prompted more testing to be carried out to understand the effect of the background resistivity, and the sediment layer resistivity on the response amplitude. For these tests, the version of the model with calcium silicate in both unknown regions (Figure 6.31) was used as a starting point. In the first test, the response was recomputed with sediment resistivities of 2500, 5000, 7000, and 10,000 Ohm-m, and compared to the standard 3500 Ohm-m sediment model. Figure 6.32 shows, in two parts, the Z-component **B**-field vs. distance plots for five versions of the multi-conductor model with, from top to bottom, increasing sediment layer resistivities, and at the bottom the ARC ground

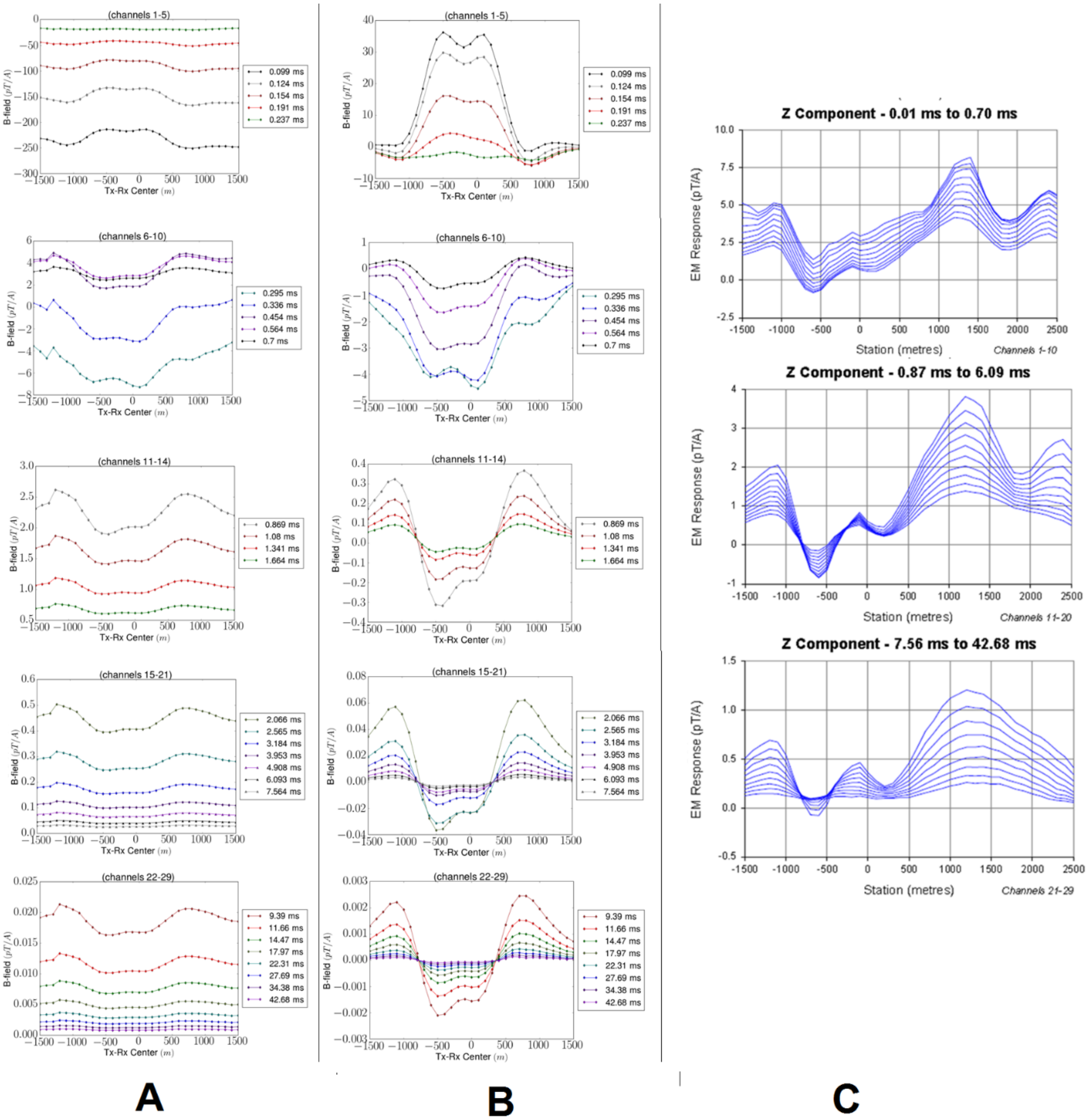

Figure 6.31: Z-component time-domain **B**-field vs. distance plots for the version of the multi-conductor model with calcium silicate in both unknown regions. A) Sediment layer included in the secondary field. B) Sediment layer *not* included in the secondary field. C) ARC ground TDEM response over similar geology.

TDEM results for comparison. The results highlighted in orange are the standard 3500 Ohm-m meter sediment layer based on the average of ARC measurements. The very early times show sign reversal, but the results are a good match to the ARC response at middle and late-time gates, and overall this resistivity gives the best match and confirms in a way the average of the drill hole measurements for the sediment layer. Highlighted in blue, the 5000 Ohm-m half-space shows the best match to the ARC early time response, however by middle and late times the curve has changed.

For the second test, the model was computed as usual but instead of obtaining the secondary field by subtracting a half-space model with the resistivity of the basement, a range of half-spaces with other resistivity values were used: 5000, 10,000, 18,000, and 25,000 Ohm-m. The standard basement resistivity is 50,000 Ohm-m, obtained as an average of the granitic and pelitic gneiss units that are dominant in the region. The value was chosen to be lower than the maximum resistivity so that some effect of the highly resistive granitic gneiss would still be present in the response, as it is a region of interest in the model. A comparison of **B**-field vs. distance plots at middle-times for three of these models with the 5000, 18,000, and 50,000 Ohm-m backgrounds is shown in Figure 6.33.

As seen at the top of Figure 6.33, by calculating the secondary field with a half-space much lower than the maximum resistivity the amplitude of the response overall is decreased, and at the same time, the difference in peak-to-trough amplitude is increased. This is thought to be because the 5000 Ohm-m background is approaching the resistivity of the sediment layer, and like in the center of Figure

6.31 where the sediment is not included in the secondary field, the peak-to-trough amplitude increases as the effect of the sediment is removed. The increase in overall response amplitude for secondary fields computed with the more restive half-spaces is due to the fact that more of the effect of the very resistive regions of the model are removed. However, the sediment is still present which is why the peak-to-trough amplitude is not seen to change when the half-space resistivity is above 18,000 Ohm-m.

Half-spaces with resistivities above 50,000 Ohm-m were not computed for comparison. However, it is thought that by using an even more resistive half-space to compute the secondary field, the forward response could be brought closer to the ARC response, which is currently off by approximately 10^3. To more closely match the ARC response more work in fine tuning the effect of the sediment layer is likely necessary. The effect of the sediment layer is important in the model response and can not be eliminated entirely, but more considerations may need to be accounted for to obtain a better result. Also, the unknown regions in the model could be further separated to get an even closer match to the ARC data, but due to limited information, this was not pursued further.

The results of this modeling effort demonstrate the ability of this forward method to reproduce actual ground TDEM responses over realistic geologic scenarios. Many complications must be considered, and careful attention and experimentation are necessary to fine tune the results, but even a quick series of models like those presented here can provide a wealth of valuable information, and could aid in the further planning of exploration activities.

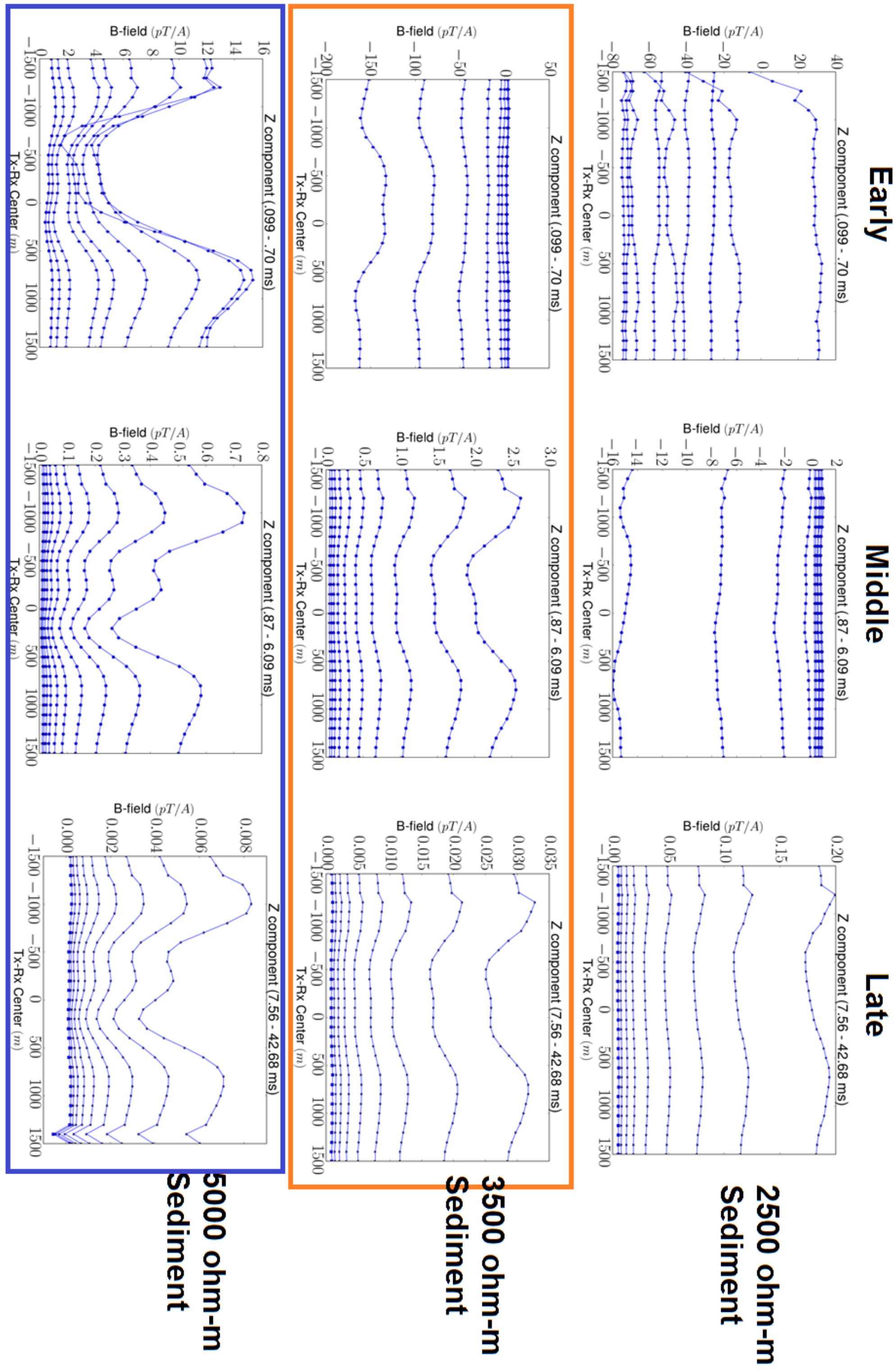

Figure 6.32: See page 182 for full caption.

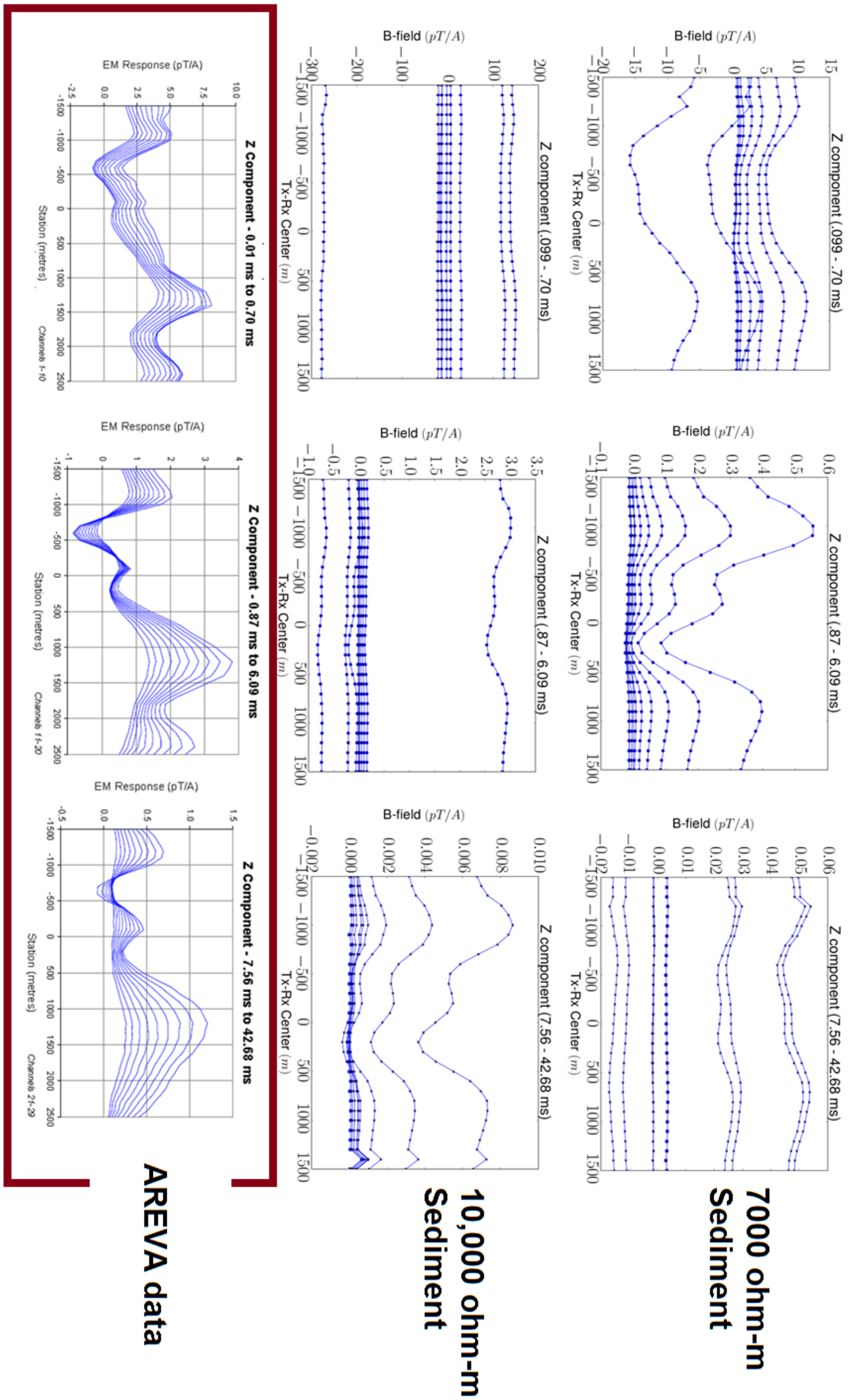

Figure 6.32 continued.

Figure 6.32: Z-component time-domain **B**-field vs. distance plots for five versions of the multi-conductor model with, from top to bottom, increasing sediment layer resistivities. In all cases, both unknown regions had the resistivity of the calcium silicate. At the bottom are the ARC ground TDEM results for comparison.

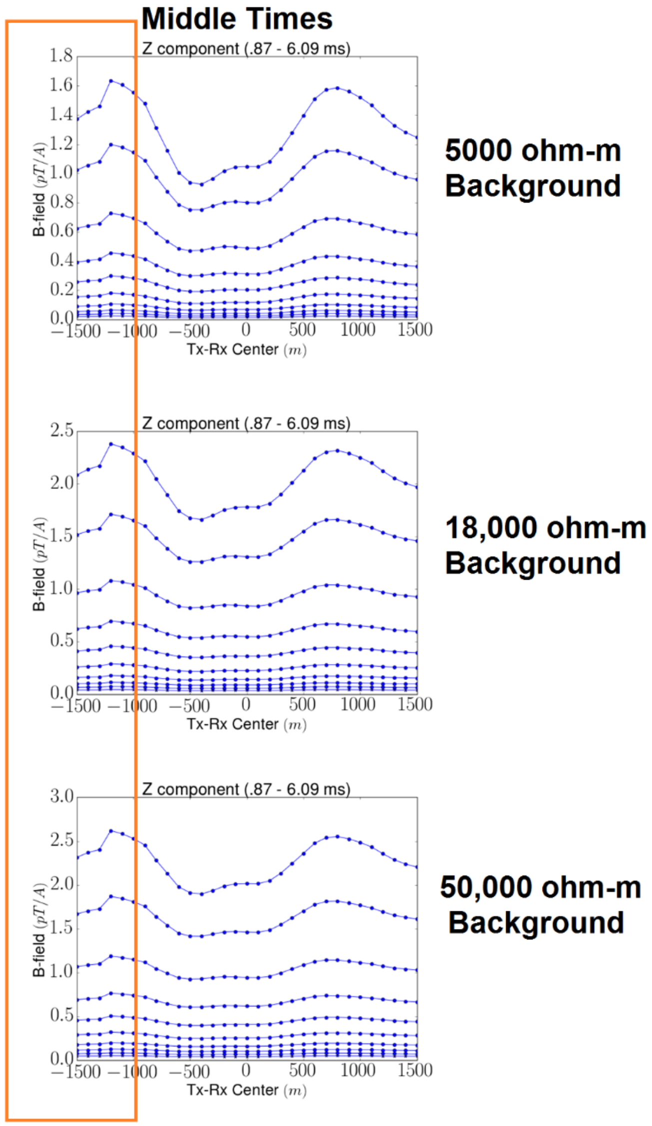

Figure 6.33: Z-component time-domain **B**-field vs. distance plots at middle-times for three versions of the multi-conductor model with, from top to bottom, increasing background resistivities. In all cases both unknown regions had the resistivity of the calcium silicate.

6.4 Conclusions

The results presented in this chapter demonstrate the effect on the time-domain magnetic field response of a variety of realistic exploration situations and prove the usefulness of this forward modeling method. The three-conductor model again indicated the inability of the large offset Slingram-style survey to distinguish multiple closely spaced conductors, but the response was distinguished to some degree from the single dipping conductor model. The Paleoweathering model established the effect of a moderately conductive/resistive layer above the conductor, something that is important not only for understanding the effect of paleoweathering, but also more broadly the effect of the sediment layer present in the Athabasca Basin. The set of dipping metasediment and conductor models answered a specific and interesting exploration question regarding apparent reversals of conductor dip in the **B**-field response and laid out a set of instances by which the phenomenon may occur. The fault vs. fold models, while interesting in theory, showed no significant differences between themselves or a simple vertical conductor, and suggest more investigation into transmitter-receiver offset is necessary to better resolve closely spaced features. The classic cross-section model illustrates the ability to design models that contain more than a few simple conductors and with regions of complex curving shape. This set of models also demonstrates the possible effect of a simple alteration halo and ore body on the standard vertical conductor response. Finally, the multi-conductor model demonstrates the effectiveness of this forward modeling method in modeling complex, realistic geologic situations and obtaining meaningful results. The result of these models show what rock types ARC may encounter if they drill into the previously unknown regions in their geologic section. The results also answer specific questions necessary for obtaining a truly accurate match to TDEM data collected in the field. Although more work is necessary to fully understand the many complex parameters in such a model, the initial effort shows that even simplified versions of actual geology may be modeled to provide answers to complicated exploration questions.

Chapter 7

Conclusion

7.1 Discussion

The fact that the results of the multi-conductor model to not perfectly match the response of the SQUIDTEM data collected by ARC at the Waterbury-Cigar Lake site is a topic that was discussed to some detail after the initial submission of the thesis for its external review. It is noted that ARC chief geophysicists Robert Hearst has mentioned his concern not only with the mismatch in the data but with the early-time sign reversals seen in this model and in a few other models created during this project.

First, the fact that the modeled results presented in this thesis for the multi-conductor model do not perfectly match the ARC data, to the author at least, seems clear. It is admitted that the process by which the region resistivities are chosen for the model and accompanying background model used to compute the secondary B-field and dB/dt responses is still currently developing. The removal of a background field can affect such things as the response amplitude but does not cause early-time sign reversals as they are present in the total field response for all models where the reversal occurs, except when using a coincident TX-RX layout as seen in Appendix J.

The multi-conductor model was created from a highly simplified 2D geologic cross-section provided by ARC that was simply extended along its strike length to create a 3D model. The geologic cross-section, created based on drill data, extended only roughly 100 m beneath the unconformity surface (located at a depth of roughly 400 m) and so all modeled regions deeper than that were strictly based on the speculation that the units continued at depth. The units do likely extend to considerable depth but the geometry of the units can not be confirmed below the existing drill holes. The idea of simply extending the 2D cross-section into 3D is also problematic as the geology at Waterbury-Cigar Lake is known to be highly variable over a scale of 10's to 100's of metres making a simple extension of the conductor package to 800 m along strike, or 2400 m as seen in Appendix J, a vast oversimplification. Finally, the resistivities used for modeling were based on average measured resistivities of the common rock types found on ARC properties in the Athabasca Basin and so not exactly correct for the particular location of the 2D geologic cross-section. Although these values are close to what is likely to be measured at the exact site of the cross-section, the ARC resistivity data varies widely and the average resistivity value for any given rock type tends to be far from its maximum and minimum measured values. Given all this information it is believed by the author that the results for the multi-conductor model presented in Chapter 6 actually do present a good initial match to the ARC data with the exception of the early-time sign reversals. The multi-conductor model was never meant to produce an exact match to the ARC SQUIDTEM data and was primarily created to showcase the ability of the method to create more complex models that represent realistic geologic situations. It is certainly not believed by the author that the validity of this method is dependant on the success of this model alone, and certainly a better result could be produced with additional geologic and rock property information as well as more considerate model construction.

As for the issue with the early-time sign reversals, much additional modeling work was done after initial submission of the thesis using the multi-conductor model and variations of it, in attempt to correct for the problem. These results are presented in Appendix J and demonstrate the effects of such things as: increasing the strike-length and depth extent of the conductor package, varying the resistivity of the sediment layer in the model, changing all non-conductive regions of the model to free-space values to attempt to match the Maxwell® modeling program by EMIT, reducing the frequency range in the forward modeled data, and many more. However, at the time of the final submission of this thesis the exact answer to the early-time reversal issue is still unknown. It is believed by the author that the early-time reversals are dependant on variations in resistivity of the sediment layer, as shown in Appendix J, as well as the resistivity of the other model regions but to a lesser extent. The author acknowledges that the early-time reversals are a problem but does not believe that it discounts the accuracy of this method which has been shown in early chapters to successfully reproduce published results. The author believes that this issue is due to the complexity of the multi-conductor model and the fact that until now, forward models with so many varied regions of resistivity have not been created or compared with ARC data. Problems like the early-time reversals in synthetic TDEM data, to the authors knowledge, have simply not been encountered and more work is necessary to understand their origin and how to correct for them. It is encouraged that the reader look through the results presented in Appendix J as they are informative and shed light on early-time reversals and their dependence on model resistivity.

7.1 Conclusion

This study has shown that the idea of using many 3D frequency-domain EM responses to construct a single time-domain EM response, first proposed by Newman et al. (1986), and updated to incorporate the 3D finite element frequency-domain forward modeling code of Ansari and Farquharson (2014), is successful in producing accurate time-domain magnetic field responses and able to answer specific questions faced in modern geophysical exploration for structurally thin and complex uranium deposits in the Athabasca Basin, Canada.

The forward modeling process, although perhaps more time consuming and computationally intensive than methods currently used in uranium exploration, through a series of synthetic and realistic examples, has shown the ability to generate forward data for models that would not be possible to compute using simpler approximation methods, such as thin plates, and in a reasonable amount of time.

A major component of this project was the question of whether individual graphitic conductors could be detected at depth within a broader unit of resistive and moderately conductive rock types. The results have shown that when using large offset (i.e. 800 m) Slingram-style ground TDEM surveys, it is not possible to detect individual conductors directly at separations less that a few hundred metres. However, the results of the final multi-conductor model show that it is possible to model a complex section with many individual units, and through trial and error determine not only if multiple conductors are present, but also the rock types likely present in unknown regions.

Beyond the Athabasca Basin inspired models, the process was shown to accurately reproduce the previously published results of Newman et al. (1986), and Ogilvy (1986), both of which had varied survey designs, transmitter-receiver spacing, and depths of conductors. These successes suggest that many different possible exploration situations could be modeled using this method, and it is by no means limited to the search for graphitic conductors alone.

References

Amestoy, P. R., A. Guermouche, J.-Y. L'Excellent, and S. Pralet, 2006, Hybrid scheduling for the parallel solution of linear systems: Parallel Computing, 32, 136–156.

Ansari, S. & Farquharson, C.G., 2014. 3D finite-element forward modeling of electromagnetic data using vector and scalar potentials and unstructured grids. *Geophyics*, 79(4), pp.E149–E165.

Ansari, S. & Farquharson, C.G., 2013. Numerical modeling of geophysical electromagnetic inductive and galvanic phenomena. , pp.669–674.

Bruneton, P., 1993. Geological environment of the Cigar Lake uranium deposit. *Canadian Journal of Earth Sciences*, 30, pp.653–673.

Coggon, J.H., 1971. Electromagnetic and Electrical Modeling by the Finite Element Method. , 36.

Crowe, M., Heinson, G. & Dhu, T., 2013. Magnetotellurics and Airborne Electromagnetics – a combined method for assessing basin structure and exploring for unconformity-related uranium. , 7000201(August), pp.11–14.

Foley, C.P. & Leslie, K.E., 1998. Potential use of high Tc SQUIDS for airborne electromagnetics. *Expl. Geophys.*, 29(1/2), pp.30–34.

Foley, C.P., Leslie, K.E. & Binks, R.A., 2006. A history of the CSIRO's development of high temperature superconducting rf SQUIDs for TEM prospecting. *ASEG Extended Abstracts*, (1).

Grant, F S., and G F. West. *Interpretation Theory in Applied Geophysics*. Mc Graw-Hill, 1965.

Hautot, S., Goldak, D., Tarits, P., Kosteniuk, P., 2011. Three-dimensional magnetotelluric inversion of large data sets : Case study of Pasfield Lake (Saskatchewan) for mineral exploration. , pp.3–6.

Ipsen, I.C.F. & Meyer, C.D., 1998. The idea behind Krylov methods. *American Mathematical Monthly*, 105(10), pp.889–899.

Irvine, R. & Witherly, K., 2006. Advances in airborne EM acquisition and processing for uranium exploration in the Athabasca Basin, Canada. , pp.2042–2046.

Jahandari, H. & Farquharson, C.G., 2014. A finite-volume solution to the geophysical electromagnetic forward problem using unstructured grids. *Geophysics*, 79(6), pp.E287–E302.

Jefferson, C., Thomas, D., Gandhi, S., Ramaekers, P., Delaney, G., Brisbin, D., Cutts, C., Quirt, D., Portella, P., Olson, R., 2007. Unconformity-associated uranium deposits of the Athabasca basin, Saskatchewan and Alberta. *Bulletin of the Geological Survey of Canada*, (5), pp.23–67.

Keller, G. V., 1997. Principles of time-domain electromagnetic (TDEM) sounding. *The Leading Edge*, 16, p.355.

Lamontagne, Y., 1975. *Applications of WideBand, Time-Domain EM Measurements in Mineral Exploration.*

Prikhodo, A., Morrison, E., Bagrianski, A., Kuzmin, P., Tishin, P., Legault, J.,

2010. Evolution of VTEM – technical solutions for effective exploration. *ASEG Expanded Abstracts*, 1, pp.1–4.

Legault, J.M., Kumar, H., Milicevic, B. & Hulbert, L., 2009. ZTEM airborne tipper AFMAG test survey over a magmatic copper-nickel target at axis lake in northern saskatchewan. *SEG Technical Program Expanded Abstracts*, 28, pp.1272–1276. Available at: http://www.scopus.com/inward/record.url?eid=2-s2.0-84863138594&partnerID=tZOtx3y1.

Legault, J.M., Kumar, H., Milicevic, B. & Wannamaker, P., 2009. ZTEM tipper AFMAG and 2D inversion results over an unconformity uranium target in northern saskatchewan. *SEG Technical Program Expanded Abstracts*, 28, pp.1277–1281. Available at: http://www.scopus.com/inward/record.url?eid=2-s2.0-84863180043&partnerID=tZOtx3y1.

Lelièvre, P., Carter-McAuslan, A., Farquharson, C., Hurich, C., 2012. Unified geophysical and geological 3D Earth models. *The Leading Edge*, 31 No.3(March), pp.322–328.

Lelievre, P., Zheglova, P., Danek, T., Farquharson, C., 2012. Geophysical inversion for contact surfaces. , pp.1–5.

Lo, B., Legault, J. & Kuzmin, P., 2008. Z-TEM (airborne AFMAG) tests over unconformity uranium deposits.

Mccracken, K.G., 1986. A comparison of electromagnetic exploration systems. , 51(3), pp.810–818.

Nabighian, M.N. *Electromagnetic Methods in Applied Geophysics*. Vol. 1, Society of Exploration Geophysicists, 1988.

Nabighian, M., & Macnae J. "Time Domain Electromagnetic Prospecting Methods." In *Electromagnetic Methods in Applied Geophysics*, edited by Nabighian M., Vol. 2. Tulsa, OK: Society of Exploration Geophysicists, 1991.

Newman, G.A. & Hohmann, G.W., 1988. Transient electromagnetic responses of high-contrast prisms in a Layered Earth Model. *Geophyics*, 53(5), pp.691–706.

Newman, G.A., Hohmann, G.W. & Anderson, W.L., 1986. Transient electromagnetic response of a three-dimensional body in a Layered Earth. *Geophysics*, 51(8), pp.1608–1627.

Ogilvy, R.D., 1986. Theoretical transient EM response curves over a thin dipping dyke in freespace - separated inline loop configuration. *Geophysical Prospecting*, (November 1984), pp.769–788.

Osmond, R., Watts, A., Ravenhurst, W., Foley, C., Leslie, K., 2002. Finding Nickel from the B field at Raglan — " To B or not dB ." *SEG Technical Program Expanded Abstracts 2002*, pp.404–407. Available at: http://library.seg.org/doi/abs/10.1190/1.1817265.

Peltoniemi, M., 1998. Depth of Penetration of Frequency-Domain Airborne Electromagnetic Methods. *Exploration Geophysics*, 29, pp.Session:10–23.

Pouliot, J., Bedard, K., Kirwood, D., Lachance, B., 2008. Reasoning about geological space: Coupling 3D GeoModels and topological queries as an aid to spatial data selection. *Computers and Geosciences*, 34, pp.529–541.

Powell, B. & Wood, G., 2007. Advances in Geophysical Exploration for Uranium

Deposits in the Athabasca Basin. *Ore Deposits and Exploration Technology*, pp.771–790.

Puzyrev, V., Koldan, J., de la Puente, J., Houzeaux, G., Vazquez, M., Cela, J.M., 2013. A parallel finite-element method for three-dimensional controlled-source electromagnetic forward modelling. *Geophysical Journal International*, 193(2), pp.678–693.

Reid, J.E. & Howlett, A., 2001. Application of the EM-31 terrain conductivity meter in highly-conductive regimes. *Exploration Geophysics*, 32(4), pp.219–224.

Reid, J.E. & Macnae, J.C., 1999. Doubling the effective skin depth with a local source. *Geophysics*, 64(3), p.732.

Reid, K.D., Ansdell, K., Jiricka, D., Witt, G., Card, C., 2014. Regional setting, geology, and paragenesis of the centennial unconformity-related uranium deposit, Athabasca Basin, Saskatchewan, Canada. *Economic Geology*, 109, pp.539–566.

Ren, Z., Kalscheuer, T., Greenhalgh, S., Maurer, H., 2014. A finite-element-based domain-decomposition approach for plane wave 3D electromagnetic modeling. *Geophysics*, 79(6), pp.E255–E268. Available at: http://library.seg.org/doi/abs/10.1190/geo2013-0376.1.

Schwarzbach, C., Borner, R.U. & Spitzer, K., 2011. Three-dimensional adaptive higher order finite element simulation for geo-electromagnetics-a marine CSEM example. *Geophysical Journal International*, 187(1), pp.63–74.

Smith, R., Fountain, D. & Allard, M., 2003. The MEGATEM fixed-wing transient em system applied to mineral exploration: A discovery case history. *First Break*, 21(July), pp.73–77.

Smith, R.S. & Koch, R., 2006. Airborne EM measurements over the Shea Creek Uranium prospect , Saskatchewan , Canada. , pp.1263–1267.

Smith, R.S. & Lemieux, J., 2003. Examples showing characteristics of the MEGATEM airborne electromagnetic system.

Tuncer, V., Unsworth, M., Siripunvaraporn, W., Craven, J., 2006. Exploration for unconformity-type uranium deposits with audiomagnetotelluric data: A case study from the McArthur River mine, Saskatchewan, Canada. *Geophysics*, 71(6), p.B201.

Tuncer, V. & Unsworth, M.J., 2006. Audiomagnetotelluric exploration for unconformity uranium deposits in the Athabasca Basin, Saskatachewan, Canada. , pp.2042–2046.

Um, E.S., Harris, J.M. & Alumbaugh, D.L., 2010. 3D time-domain simulation of electromagnetic diffusion phenomna: a finite-element electric-field approach. *Geophyics*, 75(4).

West, G.F., Macnae, J.C. & Lamontagne, Y., 1984. A time-domain electromagnetic system measuring the step-response of the ground. *Geophysics*, 49(07), pp.1010–1026.

Witherly, K., 2009. The search for uranium deposits using airborne EM in the Athabasca Basin, Saskatchewan Canada; experience of the last five years.

Witherly, K. & Irvine, R., 2006. The VTEM airborne electromagnetic system-benchmarking continuous improvement via repeat surveys over time. , pp.2042–2046.

Witherly, K., Irvine, R. & Morrison, E., 2004. The Geotech VTEM time-domain helicopter EM system. *74th Ann. Internat. Mtg.*, pp.1217–1220.

Witherly, K. & Kosteniuk, P., 2010. An assessment of EM and potential field data at Pasfield Lake , Saskatchewan-a suspect astrobleme Pasfield Lake SK-a suspect astrobleme. *Geophysics*, pp.1122–1126.

Won, I., Keiswetter, D., Fields, G., Sutton, L., 1996. GEM-2: A New Multifrequency Electromagnetic Sensor. *Journal of Environmental and Engineering Geophysics*, 1(2), pp.129–137. Available at: http://link.aip.org/link/?JGX/1/129/1.

World Nuclear Association. (2015). *Uranium in Canada*. Retrieved February 25, 2015, www.world-nuclear.org

Appendix

Due to the length of the appendix, this section is available only in the digital version of the thesis.